Measurements of the Tau Lepton Polarisation Asymmetries Using $\tau \rightarrow \mu \overline{\nu}_\mu \nu_\tau$ Decays Identified in the OPAL Detector At LEP

Clive M. Lewis

Department of Physics and Astronomy

University College London

Submitted for the degree of

Doctor of Philosophy

December 1996

Abstract

The analysis presented in this thesis is a measurement of the τ lepton asymmetries $\langle P_\tau \rangle$ and A_{pol}^{FB} at the Z^0 resonance using the $\tau \rightarrow \mu \overline{\nu}_\mu \nu_\tau$ decay channel. For this, a total sample of 141164 $e^+e^- \rightarrow \tau^+\tau^-$ events identified by the OPAL detector between the years 1990 to 1994 has been used.

Separate $\tau \rightarrow \mu \overline{\nu}_\mu \nu_\tau$ selections identifying candidates in the barrel and endcap regions of the detector are applied to a preselected sample of $e^+e^- \rightarrow \tau^+\tau^-$ events, where this is the first OPAL polarisation measurement to include the endcap region as part of the analysis. A binned maximum likelihood fit is applied to the resulting samples in each of the regions to extract $\langle P_\tau \rangle$ and A_{pol}^{FB}, and then these results are combined to give the following single measurements for the τ asymmetries:

$$\langle P_\tau \rangle = -0.142 \pm 0.031$$
$$A_{pol}^{FB} = -0.097 \pm 0.028.$$

These values compare very favourably with existing τ polarisation studies performed at OPAL using only $\tau \rightarrow \mu \overline{\nu}_\mu \nu_\tau$ decays. In addition, these results may be re-expressed in terms of the ratio of the effective vector and axial-vector couplings for the electron and τ to the Z^0 boson:

$$\frac{\hat{v}_\tau}{\hat{a}_\tau} = 0.072 \pm 0.016 \qquad \text{and} \qquad \frac{\hat{v}_e}{\hat{a}_e} = 0.065 \pm 0.019.$$

These values are consistent with one another and therefore with the hypothesis of lepton universality. Hence the results for the e and τ leptons may be combined under the assumption of lepton universality to give the following measurement for effective electroweak mixing angle for leptons,

$$\sin^2\theta_{\mathrm{eff}}^{\mathrm{lept}} = 0.2322 \pm 0.0031$$

This is in good agreement with the current world average value for all electroweak measurements.

Contents

Acknowledgements

Now that this beast is finally finished, may I first express my apologies to all the people mentioned below for changes that might have occurred to my disposition while I've had this 200-page spawn of satan nibbling on my grey cells.

I'd like to thank first and foremost my parents for their fine efforts in procreation. Hopefully, having a copy of this thesis to impress her mates with at coffee mornings will go some way to compensate my mother for the pain and suffering she endured during the act of bearing. Thanks too to my fellow bearees David, Andy, and, in particular, Skid for the many correspondences he sent while I was in "the 'Neve".

Over the last three years many hours of boozing have been whiled away, both home and abroad, and a great deal of my meagre funding has been spent on substances that have merely been sprayed into a porcelein bowl some minutes later. Nevertheless, were it not for the ritual act of going to the pub I'd have completely lost the plot long ago, and so I've made a list of the people who've been in regular attendance whilst I've grizzled and dribbled my way into oblivion. I've graciously devoted to each and every very one of them a whole line of their own, and mentioned in it why:

The Fly - hatfuls of banter

JP - oracle of information

Danny - source of amusement

Steve - mad as a bucket of snakes

Titan - depravity; a horrible, horrible man

Adam - fellow instrumentalist and Camden kid

John - general best-mate-type behaviour

Sean - all-round diamond geezar and good reason to visit Windsor

Simon C. - guitar sound and Safeways banter

David Reynolds. - witnessing the Realm's finest 90 minutes in 30 years with me

Ali F. - being top bird

David Ringpiece - talking a**e at coffee breaks, and filth-trawling on the Net

James - web-meister

Doug - herbal remedies and Alpine trips

Nick - prodder

Galloni - pleasurer of Scandinavian women using small spoons

Mike - fine poster collection and general loutishness

(Jamie) Lee Curtis - skin spanker and exposure in Trading Places

Warren - roaring and bass donation

Jason - FD bible

Ollie - advice on older, more-experienced women

Jim - drinking $\times 10^6$ for example?

Lian - lack of bladder control, and for not waking up

Sweary Mary - swearing a lot

Amy - fruitcake

Michaela - demonstrations of black belt judo holds

Liz - wound-tending, cooking, roof-provider ...etc etc. Ta!

Roz - legacy of artistic photograhic material

Of course, this thesis would have been impossible but for the superb guidance I received from Peter Clarke and Mark Thomson - I'm deeply grateful to both of them. Thanks also to everyone in the UCL HEP group and all the other people I met whilst at CERN. Finally, I'm obliged to doff my hat in the direction of PPARC, and their two charming CERN residents Sue and Mary Elizabeth.

Chapter 1

Introduction to the Standard Model

This thesis describes measurements made using data from the OPAL experiment at LEP. The LEP detector was designed to collide beams of $e^+$and e^-particles at centre of mass energies at and just either side of the mass of the Z^0 boson. In this way precision measurements and tests have been made of the various parameters used in the current best description of the fundamental forces and particles at work in nature: the Standard Model [1, 2, 3]. This chapter aims to provide a brief theoretical overview of the Standard Model, since the measurements made in this thesis are used to directly test various predictions made by the theory.

After this theoretical introduction has been made the structure for the rest of the thesis is as follows. First, the importance of certain electroweak variables (including $\langle P_\tau \rangle$ and A^{FB}_{pol}) is explained within the context of precision Standard Model tests performed at LEP. There then follows a description of the OPAL detector and how it is used to select a sample of $\tau \rightarrow \mu \overline{\nu}_\mu \nu_\tau$ decays from a larger sample of Z^0 decays collected at the Z^0 resonance. There is a discussion of the various checks that have been performed to ensure that the simulated Monte Carlo data used extensively throughout the analysis accurately replicates the $\tau \rightarrow \mu \overline{\nu}_\mu \nu_\tau$ sample obtained from real OPAL data. Finally the extraction of $\langle P_\tau \rangle$ and A^{FB}_{pol}

using a binned maximum likelihood fit is described in some detail before the final presentation of results and discussion.

1.1 Introduction

The Standard Model (SM) provides a theoretical framework to describe in a quantitative, calculable way the interactions of all "elementary" particles that are believed to exist. Within the model these elementary particles are therefore structureless and point-like, and fall into one of two basic categories: fermions and bosons. Fermions (bosons) refer to particle states whose intrinsic spin is given by $J = n(\hbar/2)$, where n is an odd (even) integer.

Within the SM, the fundamental fermions make up the basic constituents of matter, and possess spin-$\frac{1}{2}$. This means they have an intrinsic angular momentum of magnitude $S = \sqrt{\frac{1}{2}(\frac{1}{2}+1)}\hbar$ and can only exist in one of two quantized spin (or **helicity**) states.[1] The helicity $S_z = \pm\frac{1}{2}\hbar$ gives the longitudinal component of a fermion's spin, where those with negative (positive) helicity are said to be "left (right)-handed".

In the quantum field theory that underpins the SM, the interactions between fermions are mediated by the exchange of virtual quanta of so-called gauge fields. These quanta are essentially the "force-carriers", which, within the SM, are intermediate vector (that is, spin-1) bosons. Vector bosons can have three-fold spin degeneracy, with two states where the spin is said to be longitudinally polarised ($S_z = \pm\hbar$), and a third where it is said to be transversely polarised ($S_z = 0$).

[1]The two states arise from the degeneracy of solutions for free-particles in the relativistic Dirac equation.

1.2 The forces and gauge bosons

The electromagnetic, weak, strong and gravitational forces govern all known interactions. The gravitational force is not significant in the high energy reactions of sub-atomic particles such as those at LEP (although gravitational distortions of the LEP ring due to the sun and moon do affect beam energy calibrations [4]). This is just as well, since there is no universally-accepted field theory that adequately describes the intimate connection between gravitation and the relativistic description of space-time. Gravitation is therefore excluded from the discussions of the Standard Model presented here.

The remaining three forces are described within the SM by gauge field theories, with each interaction mediated by the exchange of different vector bosons: the electromagnetic force is propagated by the photon (γ), the weak force by the $W^{\pm}$ and Z^0 bosons, and the strong force by 8 neutrally-charged gluons. Unlike the massless photon and gluons, the $W^{\pm}$ and Z^0 bosons are heavy ($M_W \simeq 80.4$ GeV and $M_Z \simeq 91.2$ GeV), causing the weak interaction to only act over very short distances, typically $\mathcal{O}(10^{-17}\text{m})$.

1.3 Elementary fermions

The strong force only acts on particles that possess **colour charge**, where colour charge is exchanged between particles in a strong interaction by the gluons. The elementary fermions described by the SM fall into two classes: leptons, which carry no colour charge and experience only the electromagnetic and weak forces, and quarks, which do carry colour charge and are subject to all three types of interaction.

For both leptons and quarks, there are three "generations" of particles. The three generations of quark each contain an up-type quark of electromagnetic charge $+\frac{2}{3}$ (u,c and t - referred to as up, charm and top respectively), and a down-type

Generations		
I	II	III
$\begin{pmatrix} \mathrm{u} \\ \mathrm{d} \end{pmatrix}$	$\begin{pmatrix} \mathrm{c} \\ \mathrm{s} \end{pmatrix}$	$\begin{pmatrix} \mathrm{t} \\ \mathrm{b} \end{pmatrix}$
$\begin{pmatrix} \nu_{\mathrm{e}} \\ \mathrm{e}^- \end{pmatrix}$	$\begin{pmatrix} \nu_\mu \\ \mu^- \end{pmatrix}$	$\begin{pmatrix} \nu_\tau \\ \tau^- \end{pmatrix}$

$\Leftarrow$ quark generations

$\Leftarrow$ lepton generations

Table 1.1: The quark and lepton generations within the Standard Model.

quark of charge -$\frac{1}{3}$ (d, s and b - down, strange and bottom). Each lepton generation contains a massive electromagnetically-charged e^-, μ^- or τ^-, and its corresponding neutral neutrino. All particle types are shown in table 1.1, where every particle in the table also possesses an anti-particle partner of identical mass but opposite assignments for all quantum numbers. For a quark q or neutrino ν, its anti-matter partner is denoted by $\overline{\mathrm{q}}$ or $\overline{\nu}$ respectively, whilst, for leptons, ℓ^+ is used to denote the anti-matter equivalent of lepton ℓ^-.

It is assumed within the SM and throughout this analysis that only left(right)-handed (anti-)neutrinos can exist. A result of this is that neutinos are necessarily massless, and indeed there is no experimental evidence to the contrary, with the current world averages [5] giving the following 95% confidence limits on the masses as: $m_{\nu_{\mathrm{e}}}<15\,\mathrm{eV}$, $m_{\nu_\mu}<0.17\,\mathrm{MeV}$ and $m_{\nu_\tau}<24\,\mathrm{MeV}$.

Apart from the massless neutrinos, the leptons and quarks in successive generations are arranged in order of ascending mass. For leptons, the number of particles observed within a given generation is conserved in all reactions, as, for example, in the case of the muon decay process $\mu^-\rightarrow \mathrm{e}^-\overline{\nu}_{\mathrm{e}}\nu_\mu$.

For quarks, quantum numbers associated with each quark type (not generation) are conserved only in strong interactions. However, for weak interactions involving quarks, the mass eigenstates (d,s and b) must be replaced by corresponding weak eigenstates (d$'$,s$'$ and b$'$) to achieve the correct prescription of the couplings. The weak eigenstates are linear combinations of the mass eigenstates described by the Cabibbo-Kobayashi-Maskawa (CKM) mixing matrix. The terms in the CKM matrix have to be determined experimentally, and influence the relative branching fractions of hadronic τ decays. For example, the $\tau \rightarrow K\nu_\tau$ decay channel ($\sim 0.65\%$) is said to be Cabibbo-suppressed in relation to the $\tau \rightarrow \pi\nu_\tau$ channel ($\sim 11.8\%$).

1.4 Gauge field theories

The evidence for the fact that there only three interactions within the SM (ignoring gravity) comes from the fact that each can be successfully described using a single universal coupling strength. As in classical mechanics, a Lagrangian, $\mathcal{L}$, can be used to describe the dynamics of particles in a system. However, within field theories, particles are described as quantized perturbations of physical fields, and so terms in $\mathcal{L}$ are constructed from operators. These operators come from the quantum mechanical descriptions of spin-$\frac{1}{2}$ or spin-1 particles, and obey certain (anti-)commutation relations accordingly.

1.4.1 Local gauge invariance

Interactions are introduced into the theories under the requirement that $\mathcal{L}$ is invariant under local (space-time-dependent) gauge transformations. A Lagrangian containing only free-particle terms is not invariant under such transformations. However, a compensating field can be introduced with transformational properties which exactly cancel the derivatives of the local phase, and which restore the invariance of $\mathcal{L}$. This is the "gauge principle" (for example, see [3] for a more detailed discussion), where interactions are brought into the theory as fields which maintain local gauge invariance.

For the field theory description of the SM, the gauge principle has been used as a basic postulate, and then the three interactions have been introduced using a choice of symmetry group for each which best agrees with experimental observations. For example, quantum electrodymanics (QED) has been used very successfully to provide a mathematical description of the electromagnetic interaction. Such interactions in QED lead to transformations of complex phase, where these transformations are given by the symmetry group, U(1). Applying the gauge principle to weak and strong interactions has led to both being successfully described using more complex mathematical groups. In each case, the form of the symmetry predicts the existence of the $\gamma, \mathrm{W}^{\pm}, \mathrm{Z}^0$ and gluons, and reveals certain properties about each.

1.4.2 Renormalisation

Besides local gauge invariance, a further requirement used in describing the SM is that the theories are **renormalisable**. This ensures that the amplitudes of the various processes remain calculable under the perturbative expansion of the underlying field theory.

Richard Feynman developed a calculational formalism for such expansions, in which each term in the perturbative series is represented by one or more unique "Feynman diagrams". For example, the **lowest order** term in the perturbation series for the QED annihilation process $\mathrm{e^+e^-} \to \gamma \to \mu^+\mu^-$ is represented in figure 1.1.

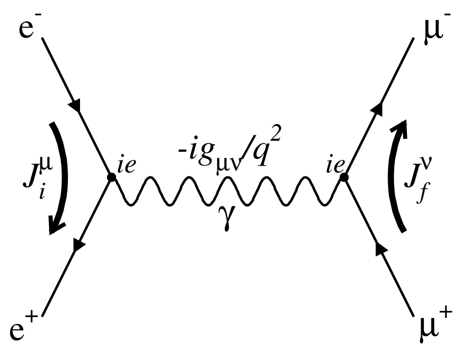

Figure 1.1: Born-level Feynman diagram for the process $\mathrm{e^+e^-} \to \gamma \to \mu^+\mu^-$.

The amplitude $\mathcal{M}$ for such first-order (or so-called "Born-level") diagrams can be calculated using the following general expression:

$$\mathcal{M} = iJ_f^{\mu}\Delta_{\mu\nu}^{\mathrm{X}}J_i^{\nu} \tag{1.1}$$

where $\Delta_{\mu\nu}^{\mathrm{X}}$ is the propagator term for boson X, and J_i^{μ} and J_f^{ν} are the fermion transition currents in the initial and final states respectively. The coupling strength for the process arises from coupling strengths that are assigned to each vertex in the diagram. For the pure QED diagram in figure 1.1, the intermediate vector boson is a photon (X$=\gamma$), and so the coupling strengths at each vertex are $\propto e$, where e is the charge of an electron and is used to define the fine-structure constant, $\alpha = e^2/4\pi$. Furthermore, the propagator term is given by $\Delta_{\mu\nu}^{\gamma} = -ig_{\mu\nu}/q^2$, where q is the four-momentum of the photon determined by four-momentum conservation at the vertices. Since $q^2 \neq 0$ the photon is said to be "virtual" or "off-mass shell".

The same Feynman rules can be applied to higher-order terms in the perturbation expansion. Each successive order in the series will contain a greater number of vertices and propagators, and so its amplitude acquires an extra factor of α. This leads to the overall coupling strength being much smaller than that for the preceding order since $\alpha \ll 1$. However, a problem arises from vacuum polarisation diagrams such as the $\mathcal{O}(\alpha)$ process shown in figure 1.2

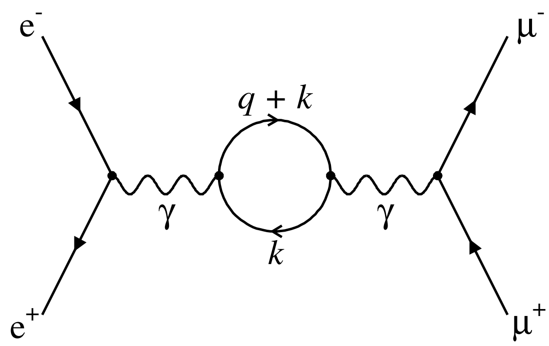

Figure 1.2: $\mathcal{O}(\alpha)$ vacuum polarisation diagram for the process $\mathrm{e^+e^-} \to \gamma \to \mu^+\mu^-$.

Such diagrams lead to infinite amplitudes since the integrals over all momenta k for virtual particles circulating within the loop are divergent. The basis of renormalisation is that, to get around this difficulty, coupling strengths are used which combine the dominant coupling strength of the Born-level process with those from all higher-order divergent diagrams. Since the Born-level process can never be observed in isolation, the bare charge e_0 that governs its coupling strength cannot be determined. However, a physical charge e can be defined by the equation $e = e_0 + \delta e$, where e is the finite residual of an infinite bare charge and an opposing infinite counterterm, which is dependent on the energy of the interaction. In such a way the bare charge has been chosen so as to lead to the cancellation of all divergences arising from higher order diagrams.

If the cancellation of divergences to **all** orders can be achieved using a finite number of counterterms then the theory is said to be renormalisable, where local gauge invariance is a necessary requirement for non-Abelian gauge theories to be renormalisable. QED is a renormalisable theory where a consequence of this is that α, defined by the physical charge e, becomes a "running" coupling constant which varies from $\sim$1/137 for very low energy Thomson scattering to $\sim$1/129 at $\sqrt{s}$=$\mathrm{M_Z}$.

1.5 Electroweak Theory

Within the Glashow-Salam-Weinberg (GSW)[1] model that was developed in the late 1960's the electomagnetic and weak forces can be jointly described by the non-Abelian product group SU(2)×U(1). Prior to this, it had already been observed that the charged weak current only couples to left-handed fermions. This can be explained in terms of a weak isospin current by which a left-handed fermion is transformed into its left-handed partner in a weak isospin doublet under the rotation symmetry group $\mathrm{SU}(2)_L$[2] (L, R will be used to denote left- or right-handedness). The following doublets are defined, each with weak isospin $T = \frac{1}{2}$,

$$\begin{pmatrix} \nu_{\mathrm{e}} \\ \mathrm{e} \end{pmatrix}_L \begin{pmatrix} \nu_{\mu} \\ \mu \end{pmatrix}_L \begin{pmatrix} \nu_{\tau} \\ \tau \end{pmatrix}_L \quad \& \quad \begin{pmatrix} \mathrm{u} \\ \mathrm{d} \end{pmatrix}_L \begin{pmatrix} \mathrm{c} \\ \mathrm{s} \end{pmatrix}_L \begin{pmatrix} \mathrm{t} \\ \mathrm{b} \end{pmatrix}_L$$

Within each doublet, each particle has a different "third isospin component", denoted by the quantum number T_3. For the neutrinos and left-handed up-type

[2]The rotation group SU(2) is non-Abelian and so its generators do not commute.

quarks this takes the value $T_3 = \frac{1}{2}$, whilst the ℓ_L^- and down-type quarks are assigned $T_3 = -\frac{1}{2}$. All right-handed fermions have $T = 0$ and are in isospin singlets. In order to maintain local gauge invariance under $\mathrm{SU}(2)_L$ transformations three weak fields must be introduced: W_i^μ (i=1,2,3), where the choice of labels here stem from the use of Pauli matrices in the transformations.

With the unification of the weak and electromagnetic interactions the symmetry group is extended to $\mathrm{SU}(2)_L \times \mathrm{U}(1)_Y$. Just as the electromagnetic charge operator Q generates the $\mathrm{U}(1)_{em}$ group in QED, so the hypercharge generator Y generates the symmetry group $\mathrm{U}(1)_Y$, where Y is defined by the following expression:

$$Q = T_3 + \frac{Y}{2}$$

The $\mathrm{U}(1)_Y$ symmetry describes the so-called "weak hypercharge current", where local gauge invariance is maintained in this case by the introduction of the weak hypercharge field B^μ. Furthermore the so-called Higgs field [6] is introduced to the theory giving rise to terms in $\mathcal{L}$ which can interpreted as mass terms for the electroweak gauge bosons, and an extra term which predicts the existence of the scalar Higgs (H^0) boson. The choice of a non-zero expectation value v for the Higgs field means that, whilst the Higgs field still respects the $\mathrm{SU}(2)_L \times \mathrm{U}(1)_Y$ symmetry, the symmetry becomes hidden ("spontaneously broken").

The inclusion of the Higgs field allows the physical gauge bosons of the electroweak theory to be identified as orthogonal linear combinations of the weak isospin fields W_i^μ and the weak hypercharge field B^μ:

$$\begin{aligned} W^{\pm\mu} &= \frac{1}{\sqrt{2}}(W_1^\mu \pm W_2^\mu) \\ Z^{0\mu} &= W_3^\mu \cos\theta_W - B^\mu \sin\theta_W \\ A^\mu &= W_3^\mu \sin\theta_W + B^\mu \cos\theta_W \end{aligned} \tag{1.2}$$

where A^μ is identified as the massless photon field. The quantity θ_W used in equation 1.2 is known as the weak mixing angle, and is defined as:

$$\sin^2\theta_W = 1 - \frac{M_{\mathrm{W}}^2}{M_{\mathrm{Z}}^2} = \frac{g_1^2}{g_1^2 + g_2^2} \tag{1.3}$$

Defining the weak mixing angle this way leads to the following relations for the masses of the $W^{\pm}$ and Z^0 bosons:

$$M_{\mathrm{W}} = \frac{v}{2} g_2 \qquad \& \qquad M_{\mathrm{Z}} = \frac{v}{2}\sqrt{g_1^2 + g_2^2} \tag{1.4}$$

where the terms g_1 and g_2 are the gauge coupling constants for the $\mathrm{U}(1)_Y$ and $\mathrm{SU}(2)_L$ fields respectively, and, since A^{μ} is identified as the photon field, these may be expressed in terms of the electric charge of the electron:

$$g_1 = \frac{e}{\cos\theta_W} \qquad \& \qquad g_2 = \frac{e}{\sin\theta_W} \tag{1.5}$$

1.6 Quantumchromodynamics (QCD)

The gauge symmetry of QCD is based on the non-Abelian rotation group $\mathrm{SU}(3)_C$. This introduces the three-valued "colour charge" for quarks, to which the strong interaction couples. It is an experimental observation that quarks are only seen to exist within hadrons, which are either $\mathrm{q\overline{q}}$ (mesons) or qqq (baryons) bound states whose net colour charge is zero. For the q and $\mathrm{\overline{q}}$ in a meson the colour charges are equal and opposite; whilst, for the baryons, each of the three constituent ("valence") quarks take a different colour charge value. The analogy to colour is drawn from the fact that the net sum of the three colour charges is zero in much the same way that white light is composed of the red, green and blue primary colours.

In addition to the valence quarks that exist in hadronic states, deep inelastic scattering experiments have revealed that the valence quarks in hadrons exist within a "sea" of gluons and virtual quark-antiquark pairs. There is an apparent paradox here in that the quarks appear to be loosely bound within the hadrons and yet are never observed in isolation. This is accounted for by the concept of asymptotic freedom, whereby the colour charge of the valence quarks is effectively hidden at short distances (high energy) by the spatial distribution of its net colour charge throughout the surrounding gluonic sea. This leads to the strong coupling constant α_s decreasing ("running") with energy. However, at $\sqrt{s} = M_{\mathrm{Z}}$, $\alpha_s \simeq 0.12$

(compared to $\alpha \simeq 1/129$ for the QED coupling constant at the same energy), and so the coupling strength is relatively large. This makes the perturbative QCD expansion more sensitive to higher orders than is the case for QED at these energies, whilst at low energies perturbative QCD must be abandoned altogether in favour of a more empirical approach.

1.7 The Standard Model at LEP

The e^+e^-colliders at LEP and the SLD opened up for the first time the opportunity to study the electroweak Standard Model to a very high level of precision. Both machines have run at energies in the region of $\sqrt{s} \simeq M_Z$. This energy corresponds to a huge rise in cross section for the process $e^+e^- \rightarrow f\overline{f}$ due to the strong resonance of the weak neutral current, and between the years 1989 and 1995 several million Z^0 decays have been collected by OPAL alone (with around 16 million in total for all four LEP experiments). A result of this is that certain observables have been very precisely determined and have enabled the Standard Model to be very closely scrutinised.

In particular the loop effects and the treatment of radiative corrections play a vital role in testing the validity of the electroweak unification [13], and represent also a "window to new physics". This arises from the fact that the decoupling theorem [8] does not hold automatically for theories in which the gauge symmetry is spontaneously broken. A consequence of this is that very heavy particles ($m \gg M_Z$ can still affect physics events for which $\sqrt{s} < m$. Hence, the virtual presence of the Higgs boson and top quark must be accounted for in the treatment of higher order corrections through renormalisation.

The minimal set of input parameters for the Standard Model is given by the fermion masses, the vacuum expectation value of the Higgs field (v), the values of the three gauge couplings (g_1 and g_2 for the $U(1)_R$ and $SU(2)_L$ fields, and α_s for the strong interaction) and the parameters in the CKM matrix. All of these parameters have to be determined experimentally. The Fermi constant G_μ (muon lifetime), electromagnetic fine structure constant α (from Thomson scattering) and M_Z (from the Z^0 lineshape), however, are already known to a very high degree of statistical precision and so these are used at LEP/SLD as theoretical inputs from which predictions can be made for the Standard Model electroweak parameters, although M_H and M_{top}, which enter as higher order weak corrections, must also be included as free parameters. This can be done using the "on-shell"[13] renormalization scheme at LEP/SLD, the details of which will be discussed in the next chapter.

Using the on-shell scheme, the statistical precision at LEP and SLD is now such that it has been possible to place experimental limits on the Higgs boson and top masses (M_H and M_{top}) by observing the effect that radiative corrections have upon electroweak observables. In particular the indirect M_{top} measurements at LEP/SLD [10] agree very well with direct measurements made by the CDF/DØ experiments on the $p\overline{p}$ collider at Fermilab [12]:

- Indirect LEP+SLD results: $M_{top} = 177^{+7}_{-8}{}^{+17}_{-19}\,\mathrm{GeV}$
- Direct $p\overline{p}$ results: $M_{top} = 175 \pm 6\,\mathrm{GeV}$

The first error on the LEP/SLD result is the error on the central value given an input value of M_H=300 GeV, whilst the second error shows the variation of the central value for a Higgs mass in the interval $60 < M_H < 1000\,\mathrm{GeV}$. Figure 1.3 shows the variation of χ^2 constructed from an electroweak fit to obtain M_{top} for various input values of M_H. This combines electroweak measurements made using e^+e^-data at LEP and SLD with precision electroweak measurements from $p\overline{p}$ colliders and νN scattering experiments.

To constrain the Higgs mass it is possible to perform a fit to all LEP data. The latest results from such a fit made by the LEP Electroweak Working Group [10] are given in table 1.2. This fit appears to favour a light Higgs mass although the errors on the central value are very large. The strongly asymmetric errors occur since, to lowest order, M_H enters radiative corrections in terms proportional to

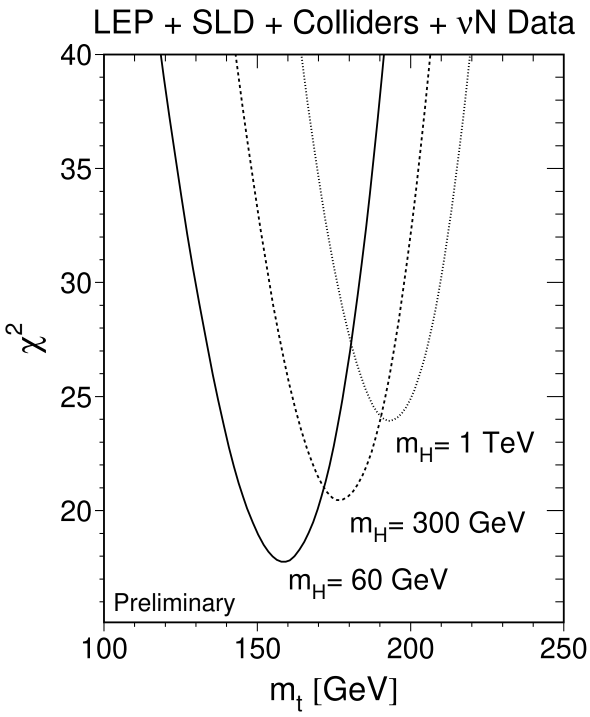

Figure 1.3: Variation of χ^2 resulting from an electroweak fit to parameters of the Standard Model using results from LEP, SLD, $p\overline{p}$ colliders and νN scattering experiments.

$\ln(M_{\rm H})$(see next chapter). Including the direct CDF/DØ measurements for $M_{\rm top}$ results in a reduction in the correlation between $\ln(M_{\rm H})$ and $M_{\rm top}$ in the fit and increases the central values to those shown in the right-hand column.

This thesis is concerned with measurements of the τ polarisation asymmetries ($\langle P_\tau \rangle$ and A^{FB}_{pol}) from $e^+e^- \rightarrow \tau^+\tau^-$events at LEP1 (that is, at centre of mass energies, $\sqrt{s} \simeq M_Z$). These are among the electroweak observables used as inputs to the above fits performed by the LEP Electroweak Working Group. In addition, they are used to provide a test of lepton universality and (then assuming universality) a measurement of the effective weak mixing angle, $\sin^2\theta^{\rm lept}_{\rm eff}$. The significance of all these terms will made apparent by the end of the next chapter.

	LEP	LEP + SLD + $p\overline{p}$ & νN data + M_{top}
M_{top}(GeV)	155^{+18}_{-13}	172^{+18}_{-13}
M_{H}(GeV)	86^{+202}_{-51}	149^{+148}_{-82}
$\ln(M_{H})$	$1.93^{+0.52}_{-0.39}$	$2.17^{+0.30}_{-0.35}$
$\alpha_s(M_Z^2)$	0.121±0.003	0.120±0.003
χ^2/d.o.f.	9/8	19/14

Table 1.2: The results of fits to LEP data alone and then to all electroweak data as well as the direct M_{top} from Fermilab. The logarithmic dependence of M_{H} to lowest within radiative corrections in the Standard Model means that both M_{H} and $\ln(M_{H})$ have been given.

Chapter 2

Theoretical description of $e^+e^- \rightarrow \tau^+\tau^-$ at LEP and the τ asymmetries

This chapter describes the significance of the $\langle P_\tau \rangle$ and A^{FB}_{pol} measurements at LEP. This shall be done by first introducing the concept of polarisation for the Born-level process at the Z^0 resonance (where γ-exchange in the s-channel is also ignored). Radiative corrections and interference effects are then introduced along with the effects of renormalisation.

2.1 Born-level description of $e^+e^- \rightarrow \tau^+\tau^-$

We have already seen in the previous chapter how the total amplitude for the pure QED process $e^+e^- \rightarrow \mu^+\mu^-$ is calculated using a perturbation series expansion, and that for each order in the expansion there are one or more corresponding Feynman diagrams whose individual amplitudes can be calculated using Feynman rules. The first-order diagrams in the expansion are called the Born-level processes, and for perturbation theory to work it is required that these form the dominant contribution to the overall amplitude for the process.

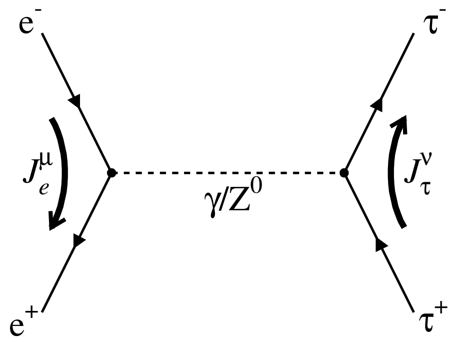

Figure 2.1: Born-level Feynman diagram for the process $e^+e^-\to\tau^+\tau^-$.

Consider now the Born-level diagram for the process $e^+e^-\to\tau^+\tau^-$. An expression for its amplitude can be gained by adapting the general expression given by equation 1.1 to obtain,

$$\mathcal{M} = iJ^\mu_\tau \Delta^{\mathrm{X}}_{\mu\nu} J^\nu_{\mathrm{e}} \tag{2.1}$$

where $\Delta^{\mathrm{X}}_{\mu\nu}$ is the propagator term for boson X, and J^μ_{e} and J^ν_τ are the fermion transition currents in the initial ($e^\pm$) and final ($\tau^\pm$) states respectively. Electroweak processes such as $e^+e^-\to\tau^+\tau^-$are mediated in the s-channel[1] at LEP1 energies by either a γ or Z^0 of 4-momentum q. Applying Feynman Rules to equation 2.1 gives the invariant amplitudes for each possibility as,

$$\mathcal{M}_\gamma = -e^2\langle\overline{\mathrm{u}}_\tau|\gamma^\mu Q_\tau|\mathrm{v}_\tau\rangle\left(\frac{g_{\mu\nu}}{q^2}\right)\langle\overline{\mathrm{v}}_{\mathrm{e}}|\gamma^\nu Q_{\mathrm{e}}|\mathrm{u}_{\mathrm{e}}\rangle \tag{2.2}$$

$$\mathcal{M}_{\mathrm{Z}} = -\frac{e^2}{4\sin^2\theta_W\cos^2\theta_W}\langle\overline{\mathrm{u}}_\tau|\gamma^\mu\left(v_\tau - a_\tau\gamma^5\right)|\mathrm{v}_\tau\rangle\left(\frac{g_{\mu\nu}-\frac{q_\mu q_\nu}{M_{\mathrm{Z}}^2}}{q^2-M_{\mathrm{Z}}^2}\right)\langle\overline{\mathrm{v}}_{\mathrm{e}}|\gamma^\nu\left(v_{\mathrm{e}}-a_{\mathrm{e}}\gamma^5\right)|\mathrm{u}_{\mathrm{e}}\rangle \tag{2.3}$$

where the terms $\langle\overline{\mathrm{u}(\mathrm{v})}_{\tau(\mathrm{e})}|$ and $|\mathrm{u}(\mathrm{v})_{\tau(\mathrm{e})}\rangle$ each contain a Dirac spinor used to represent the spin component of the fermion (u_ℓ) and anti-fermion (v_ℓ) wave functions. For the γ and Z^0 respectively, $Q_{\mathrm{e},\tau}$ (the electric charge) and $v_{\mathrm{e},\tau}$ are scalar constants which represent the vector coupling strengths to the e and τ leptons, whilst the $a_{\mathrm{e},\tau}$ constants represent the "axial-vector" coupling strengths to the Z^0. For

[1]Higgs exchange can be neglected due to the small Yukawa coupling to the electron.

electromagnetic interactions parity is always conserved, whilst for weak interactions this is not the case. Indeed, under the assumption of V-A theory, parity is maximally violated for the charged weak current.

At Born-level, the couplings for a lepton ℓ to the Z^0 boson are given by the following expressions:

$$a_\ell = T_3^\ell \quad \text{and} \quad v_\ell = T_3^\ell - 2Q_\ell \sin^2\theta_W \tag{2.4}$$

where $Q_{\ell^\pm} = \pm 1$, T_3^ℓ is the third component of isospin, and $\sin^2\theta_W$ is the weak mixing angle.

Although the invariant amplitudes $\mathcal{M}_\gamma$ and $\mathcal{M}_Z$ have been written separately above, electroweak mixing at the quantum level means that the γ and Z^0 are prohibited from propagating independently. The Born-level differential cross-section for the process $e^+e^- \rightarrow \tau^+\tau^-$ in the centre-of-mass frame is can be shown to be (see [2] for example),

$$\frac{d\sigma}{d\Omega} = \frac{1}{64\pi^2 s}\frac{|\vec{p_\tau}|}{|\vec{p_e}|}\overline{|\mathcal{M}|^2} \tag{2.5}$$

where the amplitude term is given by

$$\overline{|\mathcal{M}|^2} = \overline{|\mathcal{M}_\gamma + \mathcal{M}_Z|^2} \tag{2.6}$$

This term has been averaged over fermion spin states and contains γ^2, Z^2 as well as γZ interference terms.

If the expressions 2.2 and 2.3 are put into equation 2.6, and this in turn is substituted into equation 2.5 without excluding mass terms for the final state τ leptons ($\mu_\tau = M_\tau^2/s$), then the full Born-level differential cross section can be written as ($\theta = \angle(e^-, \tau^-)$):

$$\begin{aligned}\frac{d\sigma}{d\Omega} &= \frac{\alpha^2}{4s}\sqrt{1-4\mu_\tau}\,\cdot \\ &\cdot\left[G_1(s)(1+\cos^2\theta) + 4\mu_\tau G_2(s)\sin^2\theta + \sqrt{1-4\mu_\tau}\,G_3(s)\cdot 2\cos\theta\right]\end{aligned} \tag{2.7}$$

where the $G_\mu(s)$ functions are given by:

$$\begin{aligned}
G_1(s) &= Q_e^2 Q_\tau^2 - 2v_e v_\tau Q_e Q_\tau \Re e\left[\chi_0(s)\right] + \left(v_e^2 + a_e^2\right)\left(v_\tau^2 + a_\tau^2 - 4\mu_\tau a_\tau^2\right)|\chi_0(s)|^2 \\
G_2(s) &= Q_e^2 Q_\tau^2 - 2v_e v_\tau Q_e Q_\tau \Re e\left[\chi_0(s)\right] + \left(v_e^2 + a_e^2\right) v_\tau^2 |\chi_0(s)|^2 \\
G_3(s) &= -2a_e a_\tau Q_e Q_\tau \Re e\left[\chi_0(s)\right] + 4v_e a_e v_\tau a_\tau |\chi_0(s)|^2 \qquad (2.8)
\end{aligned}$$

and

$$\chi_0(s) = \frac{s}{s - M_Z^2} \qquad (2.9)$$

The quantity $\chi_0(s)$ is the propagator term in the Born approximation. With the inclusion of weak corrections (in the improved Born approximation), $\chi_0(s)$ adopts an imaginary component. Hence, the form-factors $G_i(s)$ are defined above in terms of a complex definition for the propagator term.

2.2 The Born-level τ asymmetries at the Z^0 resonance

The expression for the Born-level differential cross section may be simplified if one assumes that the $e^+e^- \to \tau^+\tau^-$ events to be studied are collected at $\sqrt{s} = M_Z$. Furthermore, if one assumes that $M_\tau \ll M_Z$, then, in this limit, $\mu_\tau \simeq 0$ and the operators $\frac{1}{2}(1 \pm \gamma^5)$ can be used to pick out left(right)-handed components within the differential cross section. For this, the vector and axial-vector ℓ-Z ($\ell = \tau$,e) coupling strengths, v_ℓ and a_ℓ, may be substituted by left- and right-handed ℓ-Z coupling strengths, l_ℓ and r_ℓ, where the latter are defined using,

$$l_\ell \cdot \frac{1}{2}(1-\gamma^5) + r_\ell \cdot \frac{1}{2}(1+\gamma^5) = v_\ell - a_\ell \gamma^5 \qquad (2.10)$$

Picking out the vector and axial-vector (γ^5) coefficients in this expression gives the following:

$$l_\ell = v_\ell + a_\ell \quad \text{and} \quad r_\ell = v_\ell - a_\ell \qquad (2.11)$$

If the simplifying assumptions outlined above are now applied to equation 2.7 and, in addition, v_ℓ and a_ℓ are replaced with l_ℓ and r_ℓ using the expressions in equations 2.11, then the total Born differential cross section at the Z^0 resonance can be expressed as:

$$\begin{aligned}\frac{d\sigma}{d\Omega} &\simeq \frac{\alpha|\chi_0|^2}{16s}\Big[l_e^2 l_\tau^2\left(1+\cos^2\theta+2\cos\theta\right)+l_e^2 r_\tau^2\left(1+\cos^2\theta-2\cos\theta\right)\\ &\qquad +r_e^2 l_\tau^2\left(1+\cos^2\theta-2\cos\theta\right)+r_e^2 r_\tau^2\left(1+\cos^2\theta+2\cos\theta\right)\Big] \quad (2.12)\\ &= \frac{d\sigma_{LL}}{d\Omega}+\frac{d\sigma_{LR}}{d\Omega}+\frac{d\sigma_{RL}}{d\Omega}+\frac{d\sigma_{RR}}{d\Omega} \quad (2.13)\end{aligned}$$

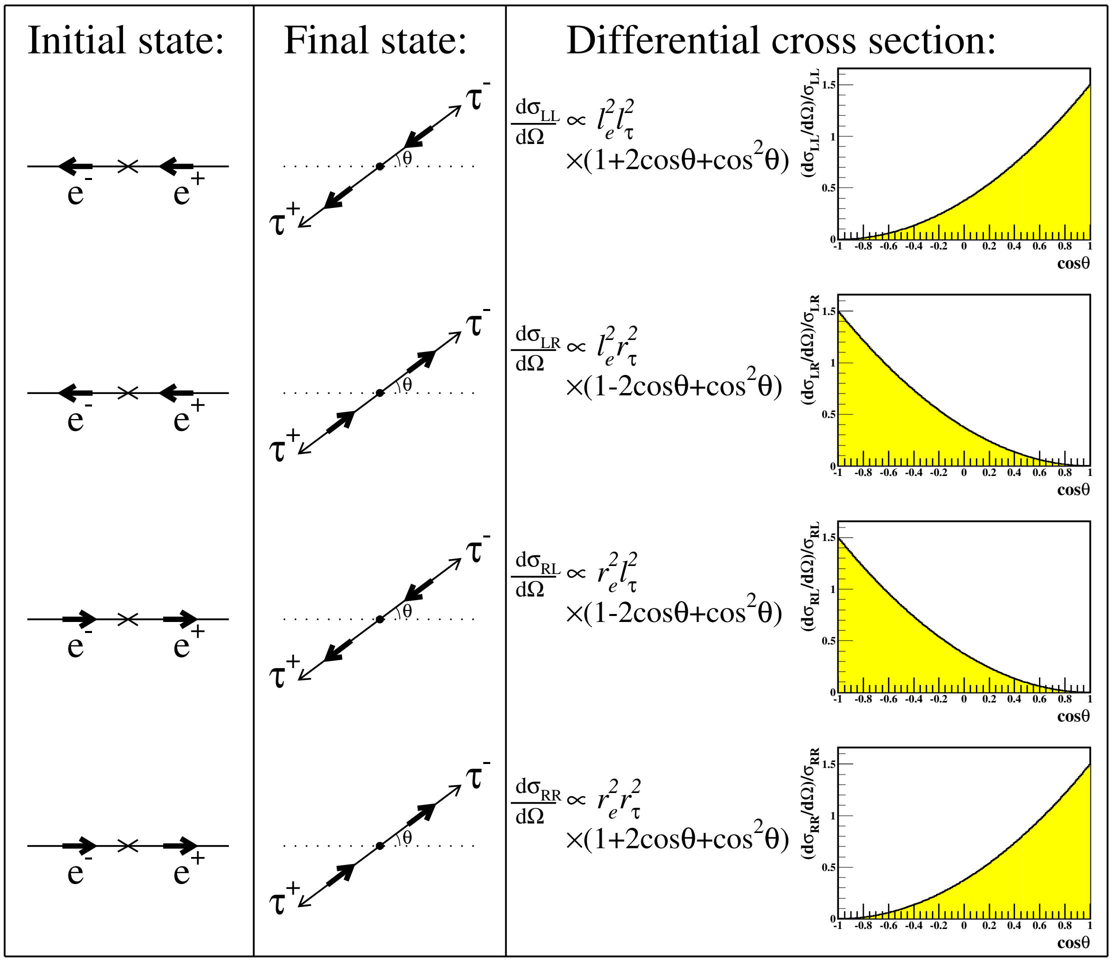

Figure 2.2: Diagram showing the four possible spin states for the process $e^+e^-\to\tau^+\tau^-$and the forms of the differential cross sections for each.

Hence the cross-section at any particular production angle θ for the τ^- is clearly given by the sum of four possible helicity combinations, where, for example, the term $\frac{d\sigma_{RL}}{d\Omega}$ gives the differential cross section in the case where the initial state e^- is right-handed and the final state τ^- is left-handed. The fact that the intermediate vector boson is a spin-1 particle places a constraint on the helicities of the e^+ and τ^+ in the event and so there are only four possible helicity configurations (see figure 2.2), where the differential cross section for each may be taken from equations 2.12 and 2.13.

The polarisation of the τ comes from the fact that $l_\ell \neq r_\ell\,(\ell = \mathrm{e}, \tau)$ and so the two helicity states of the final $\tau^\pm$ will be produced at different rates in $e^+e^- \to \tau^+\tau^-$ events. The τ polarisation is a measure of this, and in this analysis the quantity determined is $\langle P_\tau \rangle$, which is averaged over an angular range symmetric about $\cos\theta = 0$, and which by convention is taken to the polarisation for the τ^-. The polarisation $\langle P_\tau \rangle$ is defined as:

$$\langle P_\tau \rangle \equiv \frac{\sigma_R - \sigma_L}{\sigma_R + \sigma_L} \tag{2.14}$$

where

$$\sigma_L = \int \left(\frac{d\sigma_{LL}}{d\Omega} + \frac{d\sigma_{RL}}{d\Omega} \right) d\Omega \quad \& \quad \sigma_R = \int \left(\frac{d\sigma_{LR}}{d\Omega} + \frac{d\sigma_{RR}}{d\Omega} \right) d\Omega$$

The form of the individual differential cross sections and their relative strengths in terms of v_ℓ and a_ℓ are known from equations 2.11-2.13, and so this gives,

$$\langle P_\tau \rangle \simeq -\frac{2 v_\tau a_\tau}{v_\tau^2 + a_\tau^2} = -\mathcal{A}_\tau \tag{2.15}$$

Here the expression is not expressed as an exact equality as a reminder that its derivation has been made using a number of simplifying assumptions. The expression becomes exact only if corrections are made to $\langle P_\tau \rangle$ to account for contributions from γ^2 and γZ terms in the cross-section, other photonic corrections (QED initial and final state bremsstrahlung) and the effect of helicity-flip configurations brought about by the mass of the τ leptons in the final state. This arises since the $\frac{1}{2}(1 \pm \gamma^5)$ operators fail to pick out the two helicity states exactly. This effect is only really significant in the case of $\mathrm{b\bar{b}}$ (and heavier) final states, but is nevertheless corrected for in this analysis.

In addition to $\langle P_\tau \rangle$, a number of other so-called "asymmetries" can be measured using $e^+e^- \to \tau^+\tau^-$ events at LEP1, and these also depend upon the couplings of the e and τ leptons to the Z^0 boson. The most simple of these is A_{FB}, the forward-backward asymmetry, which is a measure of the different production rates for τ^- leptons in the forward and backward hemispheres. It is defined for the τ^- as:

$$A_{FB} \equiv \frac{\sigma_F - \sigma_B}{\sigma_F + \sigma_B} \simeq \frac{3}{4} \cdot \frac{2v_e a_e}{v_e^2 + a_e^2} \cdot \frac{2v_\tau a_\tau}{v_\tau^2 + a_\tau^2} = \frac{3}{4}\mathcal{A}_e \mathcal{A}_\tau \tag{2.16}$$

where

$$\sigma_F = \int_0^1 \frac{d\sigma}{d\cos\theta} d\cos\theta \quad \& \quad \sigma_B = \int_{-1}^0 \frac{d\sigma}{d\cos\theta} d\cos\theta$$

Finally A_{pol}^{FB} is a measure of the forward-backward asymmetry of $\langle P_\tau \rangle$ itself, where for the τ^- it is defined as:

$$A_{pol}^{FB} \equiv \frac{(\sigma_R^F - \sigma_L^F) - (\sigma_R^B - \sigma_L^B)}{\sigma_R^F + \sigma_L^F + \sigma_R^B + \sigma_L^B} \simeq -\frac{3}{4}\frac{2v_e a_e}{v_e^2 + a_e^2} = -\frac{3}{4}\mathcal{A}_e \tag{2.17}$$

2.3 Radiative corrections

The Born-level approximation detailed in the previous section contains the profound simplification that only lowest-order diagrams are considered. In practice radiative corrections are numerically significant and must be accounted for in studies of electroweak observables such as $\langle P_\tau \rangle$ and A_{pol}^{FB}.

For the electroweak measurements performed at LEP, the on-shell renormalization scheme is in general used, the details of which are discussed in [13]. This gives clear physical significance to inputs used in describing the internal structure of the electroweak theory, these being $\alpha, M_W, M_Z, M_{top}$ and M_H. Values of α that are exact to all orders of perturbation theory are known at $\sqrt{s} \simeq 0$ from the Thomson Cross Section, and so are used in the on-shell scheme with the appropriate rescaling to $\sqrt{s} \simeq M_Z$ according to:

$$\alpha(s) = \frac{\alpha(0)}{1 - \Delta\alpha(s)} \quad \left(\alpha = \frac{e}{4\pi}\right) \tag{2.18}$$

Also M_W is replaced as an input by the muon decay constant G_μ since the muon lifetime on which it depends is known very precisely, although again a term is included as part of the treatment of radiative corrections to account for the difference in scale between the muon lifetime measurement ($\sqrt{s} \simeq 0$) and LEP1 energies ($\sqrt{s} \simeq M_Z$).

For the $e^+e^- \to f\overline{f}$ process, radiative corrections fall into the following three categories:-

- **QED corrections** - these arise from processes with an extra photon added to the Born diagrams or a virtual photon loop.
- **Weak corrections** - these contain all other single loop diagrams: propagator corrections, vertex corrections and box diagrams (see figure 2.3 to see the distinction between each of these).
- **QCD corrections** - these are processes which contain radiated or virtual gluons. Such processes need only be considered in the case of hadronic final states and so will not be discussed further here.

The lowest order diagrams which lead to these corrections are displayed in figure 2.3, and the effects that these have on the electroweak observables at or near the Z^0 resonance are discussed below.

In general, the results of the renormalisation for weak and QED corrections can be summarized in terms of dressed renormalized gauge boson propagators and gauge boson-fermion vertices.

QED corrections

The $\mathcal{O}(\alpha)$ QED corrections to the process $e^+e^- \to \tau^+\tau^-$ include the effects of initial and final state radiation (figure 2.3(a)). Both involve the emission of a real photon and affect the kinematics of the event. The degree to which this may influence a sample of τ decays depends to a certain extent upon the experimental acceptance. In addition, initial state radiation affects the centre-of-mass energy in an interaction, and so this this has a direct effect upon the τ asymmetries. Such QED

QED CORRECTIONS

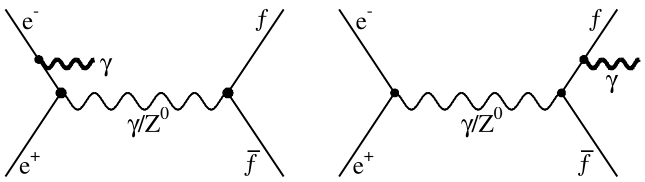

2.3(a): Initial and final state radiation

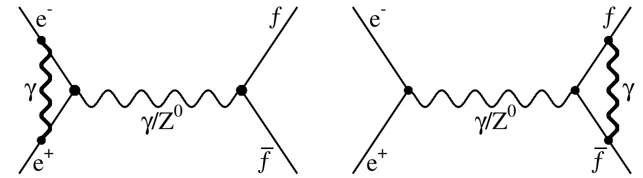

2.3(b): Virtual photon loop corrections

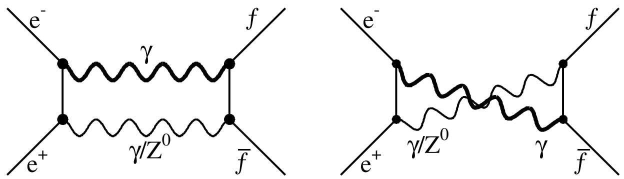

2.3(c): Virtual photon box corrections

WEAK CORRECTIONS

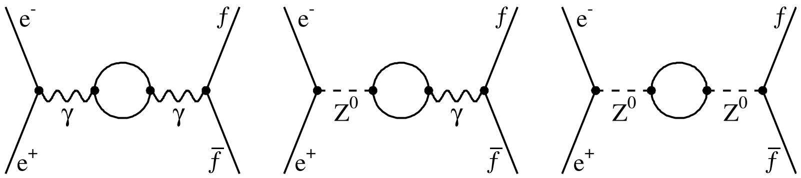

2.3(d): Propagator corrections

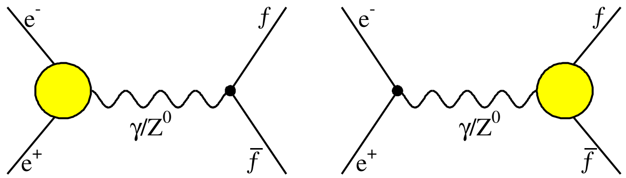

2.3(e): Vertex corrections

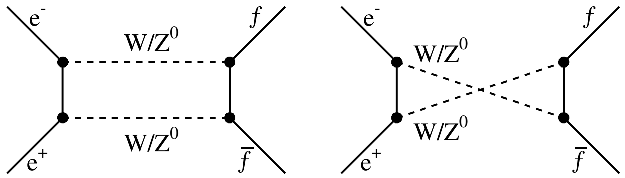

2.3(f): Box corrections

Figure 2.3: Feynman diagrams showing the different processes which contribute to lowest order QED ((a)-(c)) and weak ((d)-(f)) corrections in the process $e^+e^- \rightarrow f\overline{f}$. For the QED processes the additional photon is indicated in bold.

corrections are therefore important and are discussed in detail nearer the end of the chapter.

However, there are also QED contributions involving the exchange of virtual photons in loops (such as the processes in figures 2.3(b,c)), and these are unaffected by any kinematic cuts used in event selection. The photonic part of the processes shown in figure 2.3(e) lead to QED corrections which form a finite gauge-invariant subset after renormalization, and which are independent of the non-electromagnetic part of the theory. Generally they are large around the Z^0 peak and need careful treatment, with leading higher order terms also requiring consideration.

Weak corrections

The weak corrections to $e^+e^- \to f\overline{f}$ processes feature virtual states only and so are largely independent of the experimental cuts used in the detector. The weak corrections depend on the internal structure of the Standard Model theory, and so are sensitive to the masses of the top quark and Higgs boson. For light final state particles (that is $f \neq$b,t), the improved Born approximation is used in which the structural simplicities of the Born-level desription of $e^+e^- \to f\overline{f}$ processes are maintained by absorbing the leading term radiative effects into "effective" coupling strengths. In general the corrections are s-dependent and this leads to the so-calling "running" of the couplings.

In the on-shell scheme the propagator corrections (figure 2.3(d)) are treated separately from the vertex and box diagrams (figure 2.3(e,f)), which depend on the final state fermion. The former are treated by introducing renormalised self-energy terms into the propagator terms used for calculation of the invariant amplitudes. This is discussed in depth in [13] and so shall not be dwelled upon here. However, most of the leading order effects of propagator corrections may be introduced by use of a single finite quantity $\Delta\rho$ which depends explicitly on M_{top} and M_{H}:

$$\rho = 1 + \Delta\rho = 1 + \frac{3G_\mu}{8\sqrt{2}\pi^2} \cdot M_{top}^2 + \cdots - \frac{\alpha}{4\pi} \ln \frac{M_{\mathrm{H}}}{M_{\mathrm{Z}}} + \cdots \qquad (2.19)$$

The value of $\Delta\rho$ has a direct influence upon the ℓ–Z^0 couplings (defined for the Born approximation in equation 2.4), through the following redefinition of the weak mixing angle:

$$\sin^2\overline{\theta}_W \simeq \sin^2\theta_W + \cos^2\theta_W\Delta\rho \tag{2.20}$$

Meanwhile, the imaginary parts of the Z^0 self-energy contribute to a "physical" definition of the Z^0-width, Γ_Z. This is incorporated into the propagator term $\chi(s)$ defined for the Born-level in equation 2.9. This is defined now to be,

$$\chi_0(s) = \frac{s}{s - M_Z^2 - is\Gamma_Z/M_Z} \tag{2.21}$$

Redefining $\chi(s)$ in this way allows the Born-like structure of the Z^0 exchange amplitude to remain intact, whilst allowing for a physical description of the $e^+e^- \to f\overline{f}$ cross section at $\sqrt{s} = M_Z$.

Aside from the propagator corrections, the weak vertex and box corrections have also been mentioned and, unlike the propagator corrections, these lead to corrections which depend on the type of fermion-antifermion pair produced in the final state. Illustated in figure 2.3(e), the vertex corrections involve the exchange of additional fermions, gauge bosons or scalars at a vertex, and are accounted for in the definition of the effective weak mixing angle:

$$\sin^2\theta^f_{\text{eff}} = \sin^2\overline{\theta}_W(1 + \Delta\kappa_f) \tag{2.22}$$

where the f subscript on $\Delta\kappa_f$ (superscript on $\sin^2\theta^f_{\text{eff}}$) indicates the dependence on the type of final state particle produced. For final-state leptons the correction is significant but contains no strong dependence on M_{top} or M_H. Also the correction is only weakly dependent upon the type of final state lepton produced.

Finally, the weak box corrections shown in figure 2.3(f) also contribute to the $\Delta\kappa_f$ factor used in the definition of $\sin^2\theta^f_{\text{eff}}$. These depend on fermion species and the scattering angle but are almost negligible close to the Z^0 resonance. Also any box diagrams containing one or more exchanged photons are included as part of the QED radiative correction procedure detailed above, rather than as a weak correction.

2.4 The τ asymmetries in the improved Born-level approximation

The previous section showed how leading-term weak corrections can be absorbed into "effective" quantities. These can then be used to give good approximations for observables such as cross sections and asymmetries in such a way that the structural simplicity of the Born-level expressions is retained. Therefore, in the improved Born approximation, the cross section for the process $e^+e^- \to \tau^+\tau^-$ may be expressed by taking the lowest-order expression (equations 2.7-2.9) and making the following substitutions:

$$\begin{aligned}
\alpha &\to \alpha(s) = \frac{\alpha(0)}{(1-\Delta\alpha(s))} \\
\frac{e^2}{4\sin^2\theta_W \cos^2\theta_W} &\to \sqrt{2}G_\mu M_Z^2(1+\Delta\rho) \\
\frac{s}{s-M_Z^2} &\to \frac{s}{s-M_Z^2+is\Gamma_Z/M_Z} \\
\sin^2\theta_W &\to \sin^2\theta_{\rm eff}^{\rm lept} = \sin^2\overline{\theta}_W(1+\Delta\kappa_\ell)
\end{aligned} \tag{2.23}$$

Also the vector and axial couplings of the leptons to the Z^0 boson are replaced by their effective quantities, where these are given by,

$$\hat{a}_\ell = \sqrt{\rho}T_3^\ell \quad \text{and} \quad \hat{v}_\ell = \sqrt{\rho}\left(T_3^\ell - 2Q_\ell \sin^2\theta_{\rm eff}^{\rm lept}\right) \tag{2.24}$$

such that the coupling combinations $\mathcal{A}_\ell$ also become,

$$\mathcal{A}_\ell = \frac{\hat{a}_\ell \hat{v}_\ell}{\hat{v}_\ell^2 + \hat{a}_\ell^2} \tag{2.25}$$

The values of $\langle P_\tau \rangle$ and A_{pol}^{FB} quoted in measurements made at LEP [11] have been corrected so that they correspond to the centre-of-mass energy, $\sqrt{s}=M_Z$. Also small corrections are applied to correct for the following effects using a program called ZFITTER [17]:

- Direct Born-level γ and γZ^0 terms, which are dependent upon $\sqrt{s}$. The results, therefore, are corrected to correspond to $\langle P_\tau \rangle$ and A_{pol}^{FB} at $\sqrt{s}{=}M_{\rm Z}$ with no γ-exchange in the s-channel.

- Electomagnetic radiative corrections for initial and final state radiation from the beam particles and $\tau^\pm$ respectively.
- Born-level mass terms leading to helicity-flip configurations.

If measured values of $\langle P_\tau \rangle$ and A_{pol}^{FB} are corrected for the above effects then the following expressions become exact:

$$\langle P_\tau \rangle = -\mathcal{A}_\tau \quad \text{and} \quad A_{pol}^{FB} = -\frac{3}{4}\mathcal{A}_{\rm e} \tag{2.26}$$

where the sensitivity of $\langle P_\tau \rangle$ and A_{pol}^{FB} to higher-order weak corrections comes through the term $\Delta\kappa_\ell$ since, as can be seen from equations 2.24, 2.25 and 2.26, the $\sqrt{\rho}$-dependence will cancel from the expressions for the asymmetries.

2.5 Measurement of $\langle P_\tau \rangle$and A_{pol}^{FB}

The spin-properties of particles can never be observed directly in the detector. However, in the case of the τ lepton, final state polarisation is measurable from the kinematic properties of its decay products. The $\tau^\pm$ itself is very short-lived ($\tau_\tau \simeq 290\,$fs) and so, for $\rm e^+e^- \rightarrow \tau^+\tau^-$events at OPAL, only the decay products of the τ^- and τ^+ will be observed in the subcomponents of the OPAL detector used within this analysis.

The method for measuring $\langle P_\tau \rangle$ is best introduced by explaining it in terms of the $\tau \rightarrow \pi\nu_\tau$ decay channel, since there are only two bodies in the final state. Consider the rest frame in which a τ^- lepton decays under the assumption of pure V-A theory to give a spin-0 π^- and a spin-$\frac{1}{2}$ ν_τ. The direction in which the π^- will be produced is constrained by the fact that the ν_τ is required by the Standard model to be left-handed. Therefore the back-to-back ν_τ and π^- will be produced such that the preferred direction of the ν_τ is one in which its spin is aligned with that of the τ^-.

The τ^- rest frame is highly boosted with respect to the detector ("lab.") frame, where the spin of the τ^- is aligned or anti-aligned with the direction of the boost depending on whether the τ^- is right- or left-handed respectively. If ω is defined in the rest frame to be the decay angle of the π^- with respect to the boost direction then, depending on the helicity of the τ^-, the angular distribution of pions produced in the rest frame will take one of the two forms shown in figure 2.4:

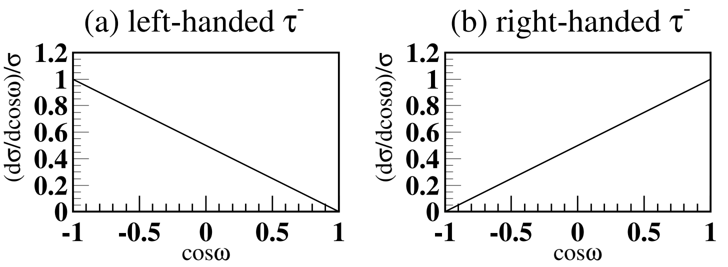

Figure 2.4: Angular distribution of the π^- in the rest frame of the decay process $\tau \rightarrow \pi\nu_\tau$. The distribution depends on the helicity of the τ^- as shown.

Under the Lorentz boost of the rest frame with respect to the lab. frame, the production angle ω is related to the energy of the π^- observed in the OPAL detector by the relation:

$$E_\pi \simeq \frac{E_\tau}{2}(1 + \cos\omega) \tag{2.27}$$

where the expression is not exact since the assumption that $(M_\pi/M_\tau)^2 \ll 1$ has been made. This expression can be re-expressed if the beam energy is taken to be $E_{beam} = E_\tau$ and the energy of the π^- is expressed as a fraction of its kinematic maximum:

$$x_\pi = \frac{E_\pi}{E_{beam}} \simeq \frac{1}{2}(1 + \cos\omega) \tag{2.28}$$

Therefore, the distributions shown in figure 2.4 can be transformed under this relation to give corresponding distributions in x_π for each of the two helicity states of the τ^-. These are shown schematically in figure 2.5.

Consider now π^+ particles produced in τ^+ decays. From the plots shown in figure 2.2 it can be seen that, for every τ^- produced at a production angle θ, there

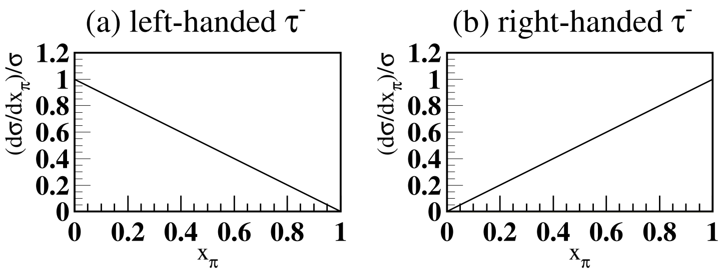

Figure 2.5: Schematic lab. frame energy distributions for π^- particles from the decay process $\tau \rightarrow \pi\nu_\tau$. The distributions depend on the helicity of the τ^- as shown.

is a τ^+ produced whose helicity state is opposite to that of the τ^- and for which $\cos\theta_+$=-$\cos\theta_-$. However, since for τ^+ decays there is a right-handed $\overline{\nu}_\tau$ produced in place of the left-handed ν_τ for τ^- decays, the two distributions shown in figures 2.4 and 2.5 for τ^- decays are reversed for the two helicity states of the τ^+. This means that in $e^+e^- \rightarrow \tau^+\tau^-$decays the τ^- and τ^+ will have opposite helicities but, if they both decay by the process $\tau \rightarrow \pi\nu_\tau$, the expected momentum distributions of the π^- and π^+ in the event will be exactly the same. The consequence of this is that the τ asymmetries defined earlier for the τ^- are of opposite sign for τ^+ leptons (for example, to very good approximation, $\langle P_{\tau^+}\rangle$=-$\langle P_{\tau^-}\rangle$). Also, when collecting a sample of τ decays for a polarisation analysis, all those which are measured to be positively-charged are treated as if they were negatively-charged τ decays from the opposite hemisphere (that is, the sign of $\cos\theta$ is reversed). For the rest of the chapter only the τ^- decay will be discussed.

The analysis presented in this thesis does not use the $\tau \rightarrow \pi\nu_\tau$ decay, but instead the purely leptonic decay channel $\tau \rightarrow \mu\overline{\nu}_\mu\nu_\tau$. The additional presence of the $\overline{\nu}_\mu$ in such a 3-body decay means that, in the rest frame of the τ^-, there is less constraint placed upon the direction in which the daughter μ^- can travel. This results in the energy distributions of μ^- particles from negative and positive helicity τ^- leptons being less distinct from from one another than is the case in figure 2.5 for daughter π^- particles. Figure 2.6 shows the momentum distributions of daughter μ^- particles for the different helicity states of the τ^-.

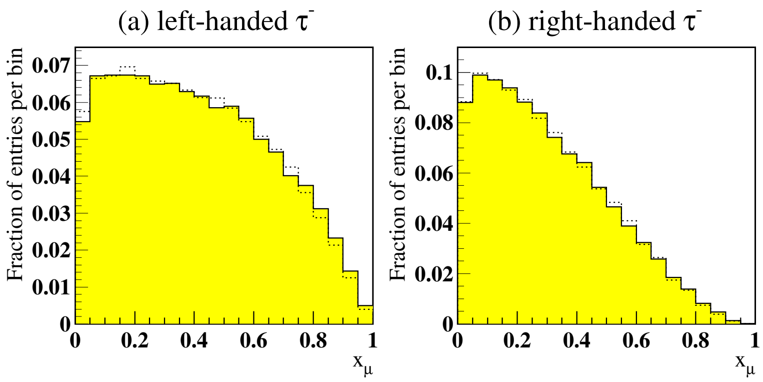

Figure 2.6: Energy distributions of daughter μ^- leptons from the decay process $\tau \rightarrow \mu\overline{\nu}_\mu\nu_\tau$, where each distribution is for the two helicity states of the τ^-. The solid line respesents the distributions for the case where all bremsstrahlung effects are switched off, whilst the dotted lines are for when the effects of initial state radiation are included up to $\mathcal{O}(\alpha^2)$.

These plots have made using a sample of 100,000 $\tau \rightarrow \mu\overline{\nu}_\mu\nu_\tau$ decays generated by the Monte Carlo (MC) simulation program KoralZ3.8 [19]. For direct comparisons with $\tau \rightarrow \mu\overline{\nu}_\mu\nu_\tau$ decays taken from real data events at OPAL, such MC events can be passed to a full simulation program which can be used to predict the passage of the decay products through the detector. In such a way it is possible to estimate the energy distributions for muons after a wide number of different effects have been taken into account. These include the effects of detector resolution, biasing due to event selection as well as physics effects, such as the emission of QED bremsstrahlung.

Suppose now that a sample of $\tau \rightarrow \mu\overline{\nu}_\mu\nu_\tau$ decays can be selected from real data accumulated at the Z^0 resonance in a region of the detector that is symmetric about $\cos\theta$=0 (see appendix A). The momentum distribution of this sample will therefore depend on the relative fractions of muons that come from negative and positive helicity τ^- leptons, or, in other words, $\langle P_\tau \rangle$. If Monte Carlo events can be used to predict the shape of the x_μ distributions for the negative and positive helicity $\tau \rightarrow \mu\overline{\nu}_\mu\nu_\tau$ decays then, by fitting linear combinations of these to the data distribution, it is possible to extract a measurement of $\langle P_\tau \rangle$. By extending the fit into two dimensions to take into account $\cos\theta$-dependence it is possible to extract both $\langle P_\tau \rangle$ and A^{FB}_{pol} simultaneously. The fitting method for this is explained in detail in chapter 9.

Clearly such a method relies on the Monte Carlo being able to predict the distributions in x_μ and $\cos\theta$ correctly, and indeed much of this thesis is concerned with ensuring that this is the case. In addition, a variety of different non-$\tau^+\tau^-$ Monte Carlo events are also used to estimate the backgrounds that enter the sample from which $\langle P_\tau \rangle$ is measured. The subject of backgrounds will therefore be studied in greater depth later in the analysis.

The advantage of this method is that it is relatively insensitive to the indirect effects of QED bremsstrahlung. Initial state radiation has a direct effect upon the $\langle P_\tau \rangle$ since it causes a change in $\sqrt{s}$. However, both initial-state and final-state radiation can indirectly influence a polarisation measurement since they affect the momentum spectra of the final τ decay products. Figure 2.6 illustrates what happens to the momenta spectra (at generator-level) when the effects of initial-state radiation are included up to $\mathcal{O}(\alpha^2)$ when generating events using KoralZ3.8. Figure 2.7 illustrates the additional effect of final state bremsstahlung ($\mathcal{O}(\alpha)$ only). Clearly both result in a downward migration between bins for the two spectra. The $e^+e^- \rightarrow \tau^+\tau^-$MC events used for this analysis (generated by KoralZ4.0 [19]) include the effects of QED bremsstrahlung in the initial and final-state up to $\mathcal{O}(\alpha^2)$, where the treatment of each is well-understood. KoralZ4.0 also includes the effect of bremsstrahlung radiation up to $\mathcal{O}(\alpha)$ in leptonic decays of the τ. Therefore the indirect effects that QED bremsstrahlung have upon the measured asymmetry values through alterations in the momentum spectra are already taken care of by the Monte Carlo simulation.

However, the direct effects of QED initial state radiation have to be accounted for since initial state radiation causes $\sqrt{s}$ to fall below the Z^0 resonance. This means that γ exchange and γZ interference terms become significant and effect the measured polarisation. Fortunately this does not affect $\langle P_\tau \rangle$ or A^{FB}_{pol} strongly for the following two reasons: first, both depend weakly on $\sqrt{s}$; and second, the $e^+e^- \rightarrow f\overline{f}$ cross section drops off very sharply below the Z^0 resonance the s-channel

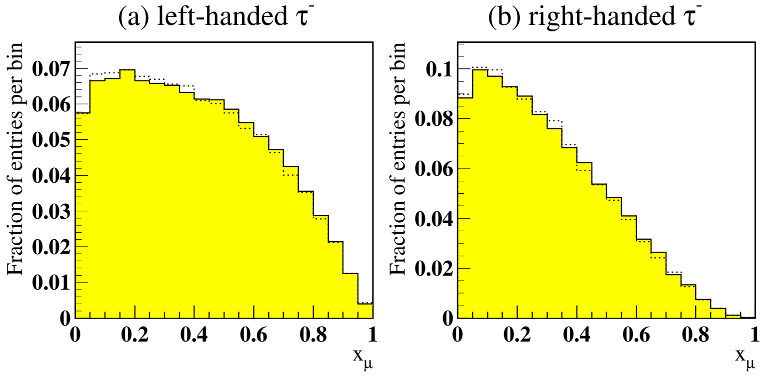

Figure 2.7: Energy distributions of daughter μ^- leptons from the decay process, where each distribution is for the two helicity states of the τ^-. The solid line respesents the distributions for the case where initial state QED bremstrahlung is included up to $\mathcal{O}(\alpha^2)$, whilst the dotted lines show the momenta spectra obtained when final state radiation is also included up to $\mathcal{O}(\alpha)$.

process $e^+e^- \rightarrow f\overline{f}$ less likely to occur between beam particles which have emitted a bremsstrahlung photon.

2.6 Comparison with other asymmetries

The fact that the asymmetries $\langle P_\tau \rangle$ and A_{pol}^{FB} are obtained using the kinematic properties of τ decay products means that they are less easy to measure than the forward-backward asymmetries, A_{FB}. However, whilst the statistical errors obtained on the A_{FB} measurements are smaller (particularly in the $Z^0 \rightarrow \mu^+\mu^-$ channel), the asymmetries themselves exhibit a strong $\sqrt{s}$-dependence. Because of this, more care is required in the treatment of QED corrections when extracting measurements of the forward-backward asymmetries at the Z^0 resonance, A_{FB}^0. This dependence is illustrated in figure 2.8 which also illustrates the increased sensitivity of $\langle P_\tau \rangle$ and A_{pol}^{FB} to $M_{\rm top}$ and $M_{\rm H}$ compared to A_{FB}.

A symmetry that has not been mentioned so far is the A_{LR} [31] measurement made exclusively at the linear e^+e^- collider at SLD. This machine runs at similar energies to those at LEP1 but with polarised beams. The asymmetry depends on

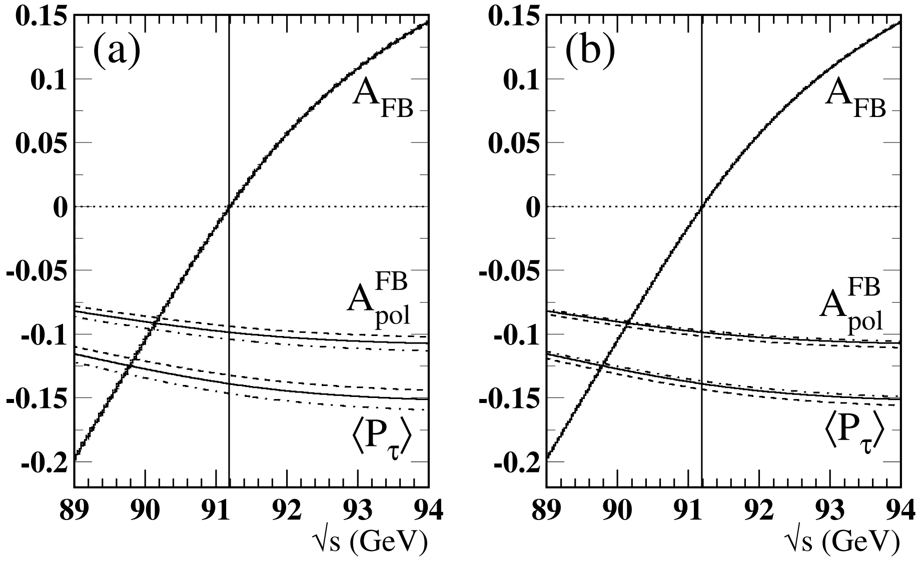

Figure 2.8: The variation of the tau asymmetries $\langle P_\tau \rangle$, A_{pol}^{FB} and A_{FB} with centre-of-mass energy around the Z^0 resonance. The values of each are obtained using the program ZFITTER, where the solid lines show the variation of the asymmetries given the following inputs: M_{Z}=91.1863 GeV, M_{top}=175 GeV, M_{H}=300 GeV and α_s=0.118. In addition, plot (a) shows the asymmetries when M_{top}=150 GeV (dashed lines) and M_{top}=200 GeV (dot-dashed lines); whilst plot (b) shows the asymmetries when M_{H}=100 GeV (dashed lines) and M_{H}=500 GeV (dot-dashed lines).

the e-Z couplings, and is largely independent of the final state. Like $\langle P_\tau \rangle$ and A_{pol}^{FB} (and unlike A_{FB}) it is relatively insensitive to changes in $\sqrt{s}$.

2.7 The use of asymmetries in precision tests of the Standard Model

The latest summary of the LEP and SLD electroweak measurements and constraints upon the Standard Model are to be found in [10]. This includes details of the electroweak fit described at the end of the last chapter in which various electroweak observables measured at LEP (and other experiments) are used to make indirect measurements of the top mass, M_{top}, and place limits upon the mass of the as-yet undiscovered Higgs boson, M_{H}. Values of $\mathcal{A}_{\mathrm{e}}$ and $\mathcal{A}_\tau$ from LEP τ polarisation measurements are used as inputs to the fits made by the LEP Electroweak Working Group. The LEP τ polarisation measurements are a combination of those made at each of four experiments, where these have been obtained using analyses which involve the following τ decay channels: $\tau \rightarrow \mathrm{e}\overline{\nu}_{\mathrm{e}}\nu_\tau$, $\tau \rightarrow \mu\overline{\nu}_\mu\nu_\tau$, $\tau \rightarrow \pi(\mathrm{K})\nu_\tau$, $\tau \rightarrow \rho\nu_\tau$ and $\tau \rightarrow \mathrm{a}_1\nu_\tau$.

In addition, the LEP-averaged values of $\mathcal{A}_{\mathrm{e}}$ and $\mathcal{A}_\tau$ from the τ polarisation asymmetry measurements are used in other precision tests of the Standard Model.

First they may be combined with values of A_{FB}^0 in each lepton channel and the leptonic partial widths of the Z^0 ($\Gamma_{\ell\ell}$) to provide measurements of the effective vector and axial couplings. The asymmetries determine the ratio $\hat{v}_\ell/\hat{a}_\ell$ whilst the values for $\Gamma_{\ell\ell}$ give the quadratic sum of $\hat{v}_\ell$ and $\hat{a}_\ell$. The combined LEP measurements are displayed in figure 2.9. These provide a test of lepton universality and indicate that Standard Model predictions are consistent with LEP data.

The LEP τ polarisation asymmetry results are also used to obtain a measurement of the effective electroweak mixing angle ($\sin^2\theta_{\mathrm{eff}}^{\mathrm{lept}}$) which is given by the

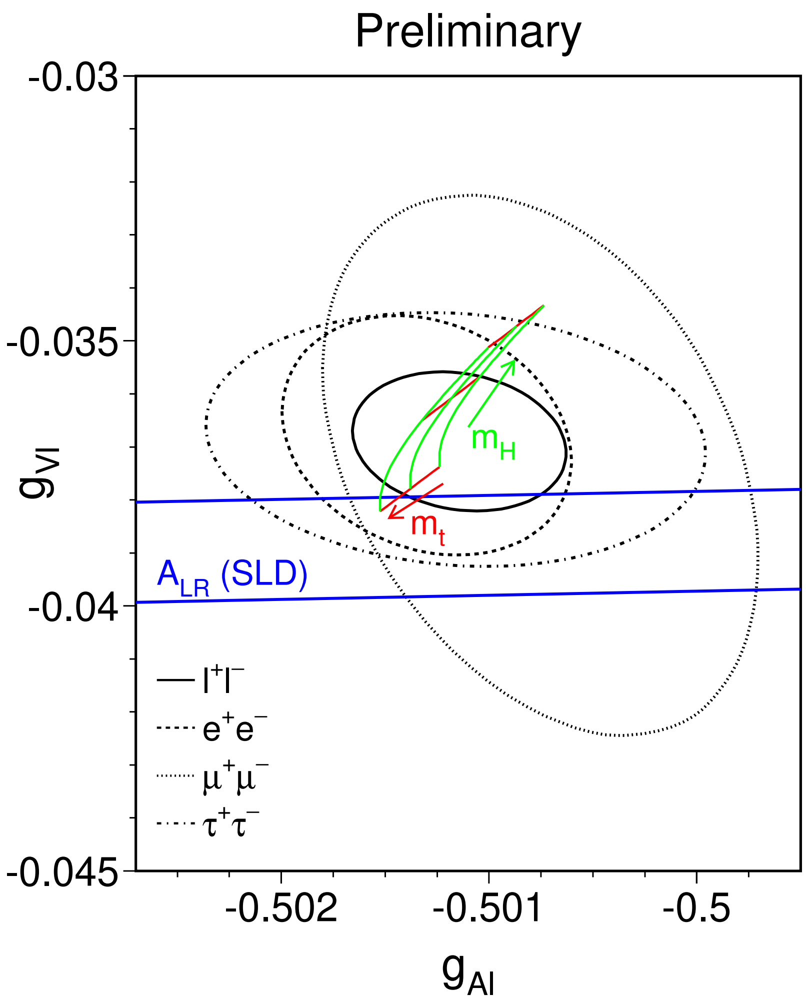

Figure 2.9: Contours of 68% probability in the $\hat{v}_\ell - \hat{a}_\ell$ (in figure, $g_{V_\ell} - g_{A_\ell}$) plane from LEP electroweak measurements. The solid contour results from a fit assuming lepton universality. Also shown is the $\pm 1\sigma$ band resulting from the A_{LR} measurement at SLD. The grid corresponds to the Standard Model prediction for $M_{\rm top} = 175 \pm 9\,\rm GeV$ and $M_{\rm H} = 300^{+700}_{-240}\,\rm GeV$. The arrows point in the direction of increasing values of $M_{\rm top}$ and $M_{\rm H}$.

expression,

$$\sin^2\theta_{\text{eff}}^{\text{lept}} = \frac{1}{4}\left(1 - \frac{\hat{v}_\ell}{\hat{a}_\ell}\right) \tag{2.29}$$

A combined average for $\sin^2\theta_{\text{eff}}^{\text{lept}}$ is obtained under the assumption of lepton universality by combining the LEP values for $\mathcal{A}_{\text{e}}$ and $\mathcal{A}_\tau$ (from τ measurements) with the A_{FB}^0 pole asymmetries (including $A_{FB}^{0,\text{b}}$ and $A_{FB}^{0,\text{c}}$) and A_{LR} (from SLD) measurements to give,

$$\sin^2\theta_{\text{eff}}^{\text{lept}} = 0.23165 \pm 0.00024$$

This result is displayed in figure 2.10 with measurements of $\Gamma_{\ell\ell}$ to show that again the Standard Model predictions are consistent with data.

By convention [11], the τ polarisation asymmetries are presented by each experiment in a way that combines the measurements from each of the decay channels to give values for $\hat{v}_{\text{e}}/\hat{a}_{\text{e}}$ and $\hat{v}_\tau/\hat{a}_\tau$. In measurements of $\langle P_\tau\rangle$ and A_{pol}^{FB} made at OPAL a global fit has been performed to all decay channels simultaneously ($\tau\rightarrow$e,μ,π,ρ,a$_1$,unknown) which accounts for correlations between decays in $\text{e}^+\text{e}^-\rightarrow\tau^+\tau^-$events. However, independent fits to each of the decay channels are also performed, and from these the weighted means of $\langle P_\tau\rangle$ and A_{pol}^{FB} are obtained and used to check for consistency between the two methods. Since the values of $\langle P_\tau\rangle$ and A_{pol}^{FB} are largely independent in the fitting methods used the assumption of lepton universality may be used to get measurements of $\hat{v}_\ell/\hat{a}_\ell$ and hence $\sin^2\theta_{\text{eff}}^{\text{lept}}$. The values of $\sin^2\theta_{\text{eff}}^{\text{lept}}$ using the latest τ polarisation results [10] from each of the LEP experiments are as follows:

$$\sin^2\theta_{\text{eff}}^{\text{lept}} = \begin{cases} 0.2334 \pm 0.0012 & \text{(OPAL)} \\ 0.2332 \pm 0.0014 & \text{(ALEPH)} \\ 0.2320 \pm 0.0021 & \text{(DELPHI)} \\ 0.2309 \pm 0.0016 & \text{(L3)} \end{cases} \tag{2.30}$$

where some of these of values have been updated since the last τ polarisation publications [28, 29, 27, 30].

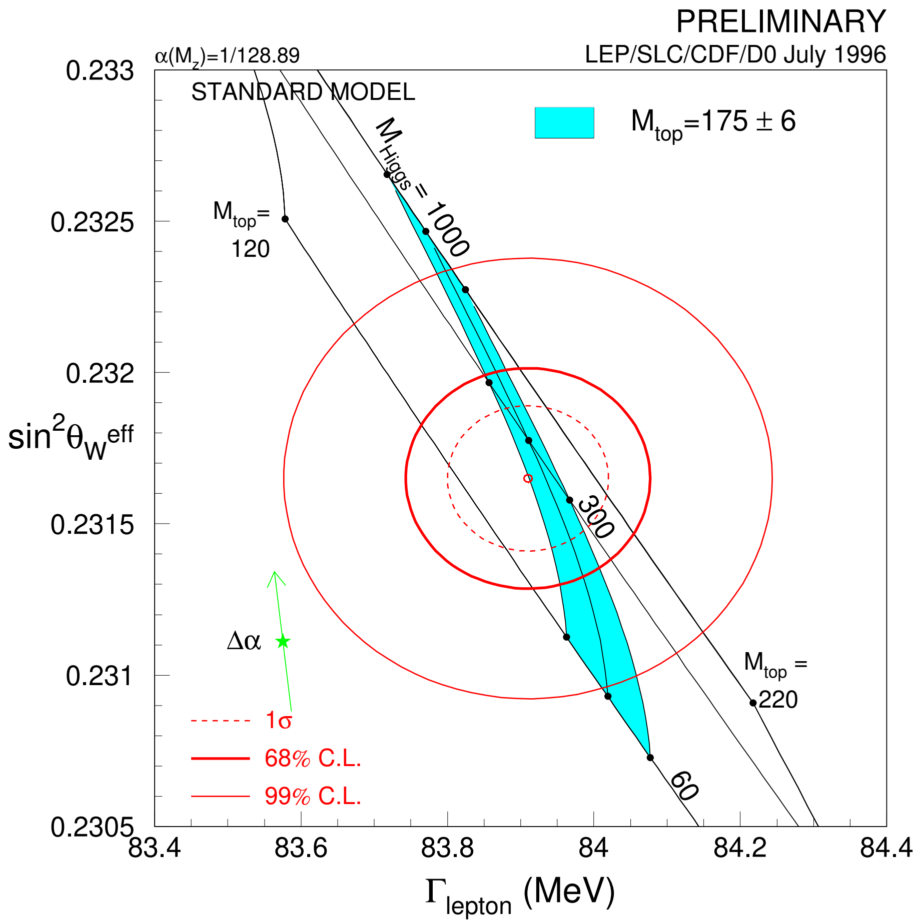

Figure 2.10: The LEP/SLD measurements of $\sin^2\theta_{\rm eff}^{\rm lept}$ and $\Gamma_{\ell\ell}$ along with the Standard Model predictions. The star shows the Standard Model predictions if only photon vacuum polarisation is included out of all the electroweak radiative corrections. The corresponding arrow shows the variation of this prediction if $\alpha(M_Z^2)$ is changed by one standard deviation. The variation gives an additional uncertainty to the Standard Model prediction as shown.

The analysis presented in this thesis is a measurement of $\langle P_\tau \rangle$ and A^{FB}_{pol} using samples of $\tau \rightarrow \mu\overline{\nu}_\mu\nu_\tau$ decays identified in the barrel ($|\cos\theta| < 0.72$) and, for the first time, endcap ($0.72 < |\cos\theta| < 0.90$) regions of OPAL. Therefore, the values of $\langle P_\tau \rangle$ and A^{FB}_{pol} obtained are to be compared with similar measurements made using the same decay channel, since measurements which combine all decay channels will clearly have much lower errors.[2] The most recent OPAL measurements of $\langle P_\tau \rangle$ and A^{FB}_{pol} [27] made using $\tau \rightarrow \mu\overline{\nu}_\mu\nu_\tau$ decays are as follows:

$$\begin{aligned} \langle P_\tau \rangle &= -0.138 \pm 0.033\,(stat.) \pm 0.022\,(syst.) \\ A^{FB}_{pol} &= -0.143 \pm 0.038\,(stat.) \pm 0.005\,(syst.) \end{aligned} \tag{2.31}$$

where these measurements have been made by applying a binned maximum likelihood fit to samples of $\tau \rightarrow \mu\overline{\nu}_\mu\nu_\tau$ decays identified in the barrel region of OPAL only ($|\cos\theta| < 0.68$). The anaylsis included in this thesis employs similar extraction techniques but uses an extended range of angular acceptance in the OPAL detector. In addition this analysis uses a significantly larger amount of Monte Carlo data as well as improved selection techniques. Both of these have allowed a number of improvements to be made to the methods used in evaluating the systematic errors.

[2] Also, since the $\tau \rightarrow \pi(\mathrm{K})\nu_\tau$ and $\tau \rightarrow \rho\nu_\tau$ channels are more sensitive to the τ polarisation asymmetries, they are more strongly weighted for analyses in which the main τ decay channels are combined [27].

Chapter 3

The OPAL detector at LEP

In order to fully understand the techiques employed in selecting the data-set used for this analysis, some time should be spent in describing the Large Electron Positron (LEP) [32] collider at CERN and the OPAL (Omni-Purpose Apparatus at LEP) [33] detector.

The LEP collider was designed to scan an energy range around the Z^0-resonance, thus allowing precision measurements to be made of the Z^0 mass and decay width, as well as its couplings to quarks and leptons. OPAL is one of the large detectors situated at the four interaction points of the LEP storage ring (the others being ALEPH [34], DELPHI [35] and L3 [36]), and fundamental to its design was the need to efficiently reconstruct and identify every type of event possible in e^+e^-collisions with minimal ambiguity. The first phase of LEP running (LEP1) ran from August 1989 until the end of June 1995 during which each of the four experiments saw around 4 million Z^0 decays close to the Z^0-resonance. An intermediate stage of LEP (LEP1.5) running between July and December 1995 saw the machine running at centre of mass energies in excess of 130 GeV. The second full phase of LEP running (LEP2) began in June 1996 after further upgrades which allow the machine to presently run at energies at which W^+W^- pair production can be observed. Further tests of Standard Model predictions can thus be made by measuring the couplings at the ZWW and γWW vertices and by significantly reducing our uncertainty in the knowledge of the W mass.

3.1 LEP

The LEP collider is contained within a large near-circular tunnel that is 26.7 km in length and runs beneath the Swiss-French countryside at depths of between 80 and 170 m below the surface. The large size of the LEP ring is to minimise the energy lost through synchrotron radiation by the beam particles, since the energy radiated per cycle is given by,

$$\Delta E = \frac{4\pi}{3}\frac{e^2\beta^2\gamma^4}{R}$$

where R is the radius of the ring, β is the velocity ($\beta = v/c$), and $\gamma = (1-\beta^2)^{-\frac{1}{2}}$. ΔE ~124 MeV for 46 GeV $e^{\pm}$beams.

The ring consists of eight arcs and eight straight sections. The LEP experiments are situated symmetrically along four of the straight sections, and during most of LEP1 it was the L3 and OPAL sections that housed the accelerating RF cavities used to compensate for the energy lost through synchrotron radiation. For the LEP2 energy upgrade superconducting cavities were required to cope with the increased synchrotron radiation loss at higher beam energies. 192 of these were installed in four of the straight sections around the LEP ring close to the experimental zones, along with a large cold box in each section to supply liquid helium.

At LEP1 a bending field of 0.133 T was provided along the eight arced sections of the ring by concrete-core steel-laminate dipole magnets. Along each arc there were 31 standard magnet cells, consisting of focussing and defocussing quadrupoles and sextupoles, orbit correctors and 12 bending dipoles.

A non-evaporable getter strip pumping system is used to create an ultra-high vacuum of 8×10^{-12} Torr in which 46GeV beams could be maintained for over twenty hours with low backgrounds from beam-gas interactions.

The first stage of the acceleration process involves electrons being thermally ejected from a heating element and accelerated to 200 MeV in a linear accelerator. A proportion of these are then collided with a fixed target in order to produce bremsstrahlung photons. The positrons are obtained through e^+e^-pair production from these photons. The beam current is built up in a 600 MeV electron-positron accumulator ring before injection in the Proton Synchrotron which operates as a 3.5 GeV e^+e^- storage ring. The beams are then delivered to the larger Super Proton Synchrotron where they are accelerated further to 20 GeV before the final injection into the LEP ring.

The beams are raised to the full beam energy within the LEP ring by the accelerating RF cavities. For the data used in this analysis (taken up to the end of the 1994 run), the beams away from the crossing points were kept apart using a "pretzel orbit" system employing electrostatic separators. The beam particles themselves were maintained within well-defined bunches of $\sim 4 \times 10^{11}$ electrons or positrons, where a typical bunch at LEP1 was $150\,\mu$m(horizontal)$\times 10\,\mu$m(vertical)$\times 10$ mm(length) in size with a relative energy spread of $\sim$0.1%. When LEP started running beam-crossings occurred every $22\,\mu$s with 4 bunches of electrons colliding with 4 bunches of positrons (4×4 mode). In 1992 this was upgraded to 8×8 mode with the beam-crossing time reduced to $11\,\mu$s.

3.2 OPAL

The OPAL detector [33] was designed to efficiently identify and measure final state particles from $Z^0 \rightarrow f\overline{f}$ decays over as large a range of solid angle as possible. To achieve this a sequence of subdetectors surrounds the interaction region. This section will give a overview of the general principles behind the design of OPAL, detailing why the subdetectors are arranged the way they are and the tasks performed by each of its principal components. The following section will discuss the subdetectors on a more technical level and explain how they operate.

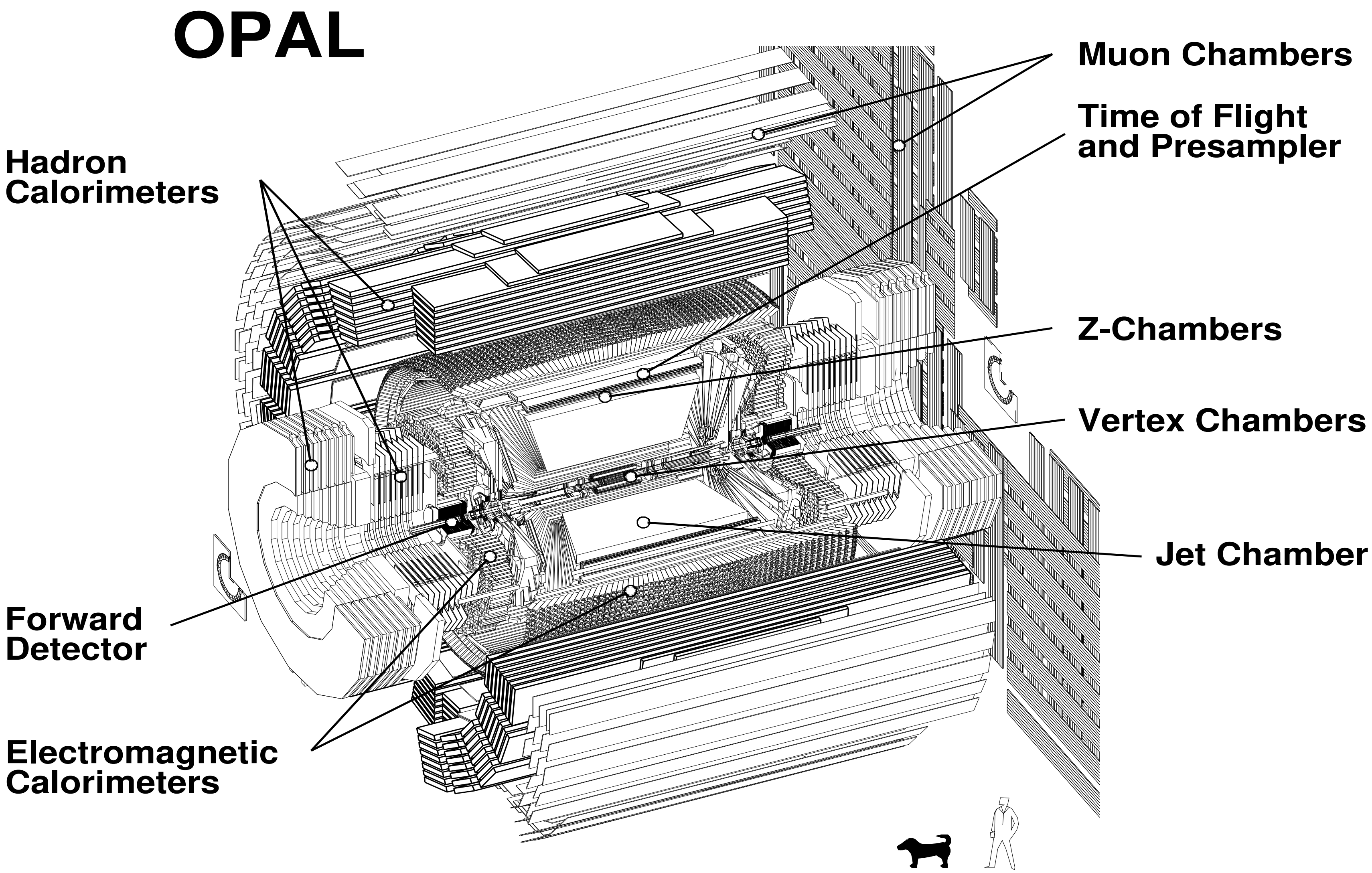

Figure 3.1: A perspective view of the OPAL detector showing the principal sub-detectors

Most particles created in physics events will first travel through the central tracking detector. This is to accurately measure the positions and momenta of charged tracks using a silicon microvertex detector and a series of drift chambers. The central tracking chamber is housed within a solenoidal magnet so as to provide a uniform axial magnetic field across the drift chambers. The momentum and charge of charged tracks is thus obtained from their curvature in this magnetic field. The silicon microvertex detector forms the innermost part of the central tracking detector and allows for the precise 3D reconstruction of decay vertices close to the beam axis. It is therefore used particularly for analyses measuring the lifetimes of short-lived particles, such as the τ lepton.

Beyond the magnet lies the following sequence of subdetectors designed to distinguish between different particle types: the electromagnetic calorimeter, the hadronic calorimeter and the muon chambers. Each of these types of subdetector has separate "barrel" and "endcap" components (see figure 3.1), where the barrel is composed of concentric cylindrical layers and the endcap components plug the remaining gaps in acceptance.

The electromagnetic calorimeter comprises over 10000 lead glass blocks which almost fully surround the interaction region. These blocks are designed to be thick enough to fully absorb the electromagnetic showering that occurs within the material due to the passage of a high energy electron or photon. This response contrasts with that for muons and hadrons, since muons interact very weakly and so pass straight through, whilst hadronic showering develops more slowly than electromagnetic showering and so is rarely fully contained within the lead glass. Electrons can therefore be distinguished from other charged particles by their shower shape in the calorimeter and by the fact that the energy deposited there will be approximately equal to the momentum of the associated electron track observed in the central tracking detector.

Detectors are positioned between layers of the large iron magnet return yoke that surrounds the electromagnetic calorimeter. These are used to sample any showering that develops within the iron, and so this forms the basis of the hadron calorimeter. It is designed to fully contain any hadronic showering initiated in the electromagnetic calorimeter, so that any particles getting beyond it and into the muon chambers should virtually all be muons. Muons will therefore leave hits in most of the layers of the hadron calorimeter since they pass straight through with little deviation. Also, since generally very few shower particles are produced, very few hits in each layer will be observed. On the other hand hadrons produce showering and are usually totally absorbed, leading to a much larger number of hits being observed in fewer layers of the calorimeter.

The muon chambers are positioned furthest away from the interaction point and give precise position measurements for charged particles which manage to penetrate through both calorimeters. These will be made up of mostly muons, although it will be shown in later chapters that there are several mechanisms by which hadronic tracks can also lead to hits in the muon chambers. In the detection of muons it is possible by extrapolation to assign hits observed in the muon chambers to a charged track measured in the central tracking detector. If a probability is constructed that the two signals are matched then it is possible to distinguish between muons and hadrons observed in the muon chambers. This principle forms the basis of the muon detection scheme used within this analysis.

In discussing the various subcomponents of the OPAL in this and later chapters the standard two-letter codes listed in table 3.1 will be used. In addition the following groups of subdetector components are grouped together as higher-level systems: the **central tracking detector**, CT comprises SI,CV,CJ and CZ; the **electromagnetic calorimeter**, ECAL, is composed of PB,EB,PE and EE; and HB,HE and HP are subcomponents of the **hadron calorimeter**, HCAL.

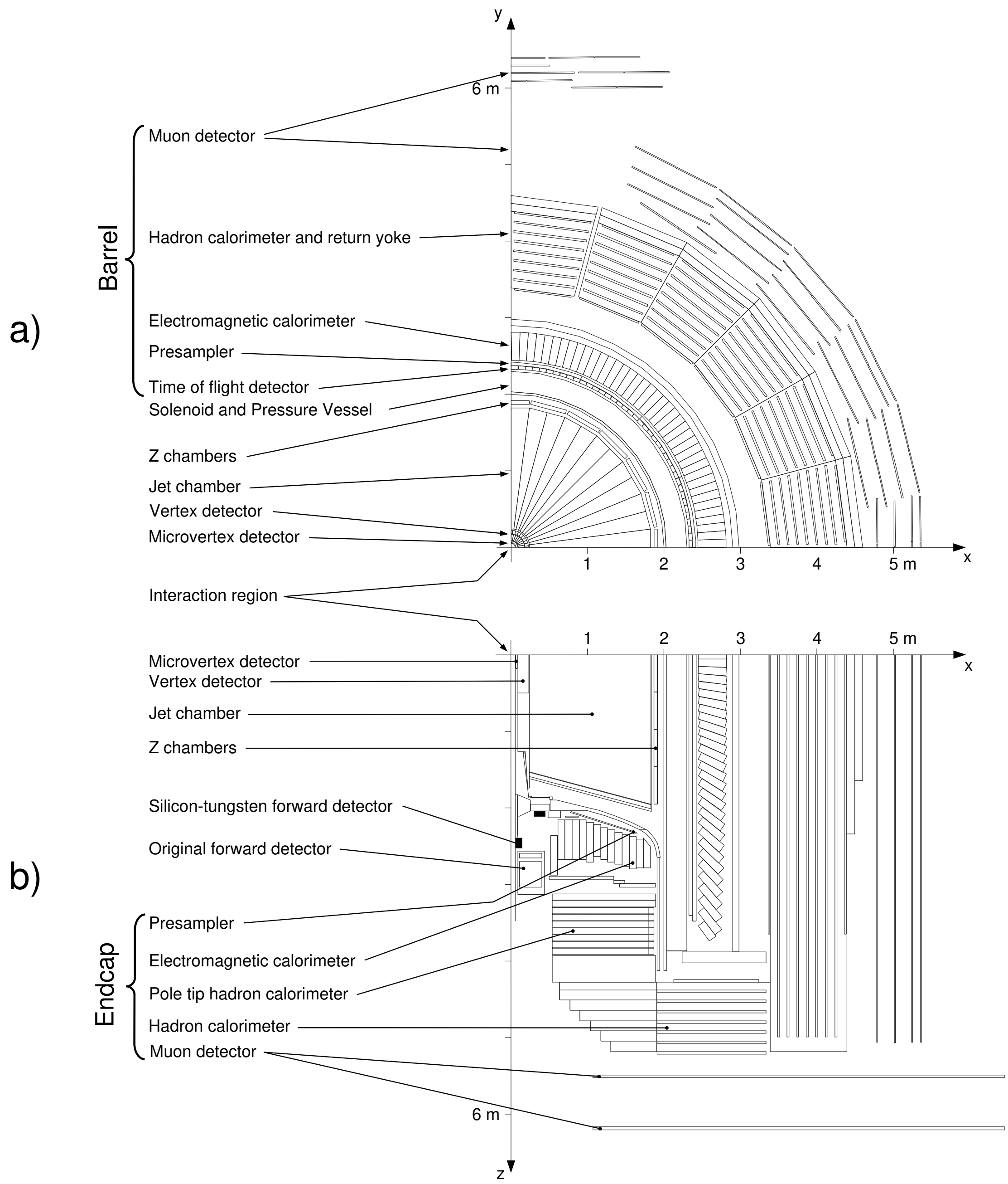

Figure 3.2: Cut-off views of the OPAL detector in **a)** the x-y plane and **b)** the x-z plane

Code	Subdetector
CV	Central tracking detector vertex chamber
CJ	Central tracking detector jet chamber
CZ	Central tracking detector Z-chambers
TB	Time-of-flight, barrel
PB	Presampler, barrel
EB	Electromagnetic calorimeter, barrel
PE	Presampler, endcap
EE	Electromagnetic calorimeter, endcap
HB	Hadron calorimeter, barrel
HE	Hadron calorimeter, endcap
HP	Hadron calorimeter, poletip
MB	Muon chambers, barrel
ME	Muon chambers, endcap
FD	Forward detector
SI	Silicon microvertex detector
SW	Silicon tungsten luminometer

Table 3.1: OPAL subdetector reference codes.

3.3 The OPAL subdetectors

3.3.1 Central tracking detector (CT)

The central tracking detector consists of the silicon microvertex detector (installed in 1991) and three drift chamber devices: the vertex detector (CV), the jet chamber (CJ) and the Z-chambers (CZ). The entire central detector is housed within a pressure vessel located between the beam pipe and the coil of the OPAL magnet.

The drift chambers work on the following principle. Alternate planes of cathode and anode sense wires are set up an electric field within a volume of gas. The passage of a charged particle through the gas liberates ionization electrons which drift towards the nearest anode wire. The drift times are used to infer the distance between the sense wires and the path of the particle, and charge division or the timing difference of the signal between the two ends of the sense wire are used to infer the coordinate along the wire. A series of space points along the trajectory of the particle are thus reconstructed. The pressure vessel is used to maintain a gas mixture consisting of 88.2% argon, 9.8% methane and 2.0% isobutane at a pressure of 4 bar. This same gas mixture and pressure is used in CV, CJ and CZ.

Vertex detector (CV)

This was designed to give precise position measurements for charged tracks close to the interaction region. This aids the identification of secondary vertices and hence also the impact parameter, d_0. The detector is a high precision drift chamber of radius 235 mm and length 1 m, situated between the microvertex detector and the jet chamber, and consists of two concentric layers. Both layers contain 36 "cells" which are equally spaced in ϕ and are defined by the positions of successive planes of cathode wires (with radial wire separation 1 mm). Anode planes lie at the centre of each cell, where each consists of anode signal wires interspersed with potential wires. The 12 anode wires per cell in the inner layer (known as "axial wires") run parallel to the z-axis, whilst the outer layer has 6 anode wires per cell ("stereo wires") inclined at 4° with respect to the z-axis. The axial and stereo wires cover the polar angle ranges $|\cos\theta| \leq 0.95$ and $|\cos\theta| \leq 0.92$ respectively.

The axial wires provide precise position measurements in the $r-\phi$ plane with a resolution of $55\,\mu$m, while a coarse z-coordinate measurement is also possible by measuring the relative arrival times of signals at opposite ends of an anode wire. The additional use of the stereo information improves the resolution of the z measurement from 40 mm to 0.7 mm.

Jet chamber (CJ)

The jet chamber is a 4 m long cylindrical drift chamber designed for the reconstruction and measurement of charged tracks within a solid angle close to 4π. It has inner and outer radii of 25 cm and 185 cm respectively, and is divided into 24 identical sectors in ϕ by the positions of radial planes of cathode wires. A plane of 159 anode signal wires lies centrally in each sector, where these signal wires run axially with a radial spacing of 10 mm and are interspersed with potential wires. To resolve left-right ambiguity the potential wires are coplanar whilst the signal wires are staggered alternately at $\pm 100\mu$m with respect to this plane. The jet chamber provides full 159-wire coverage for the polar angle range $|\cos\theta| < 0.73$ but beyond this the coverage drops off steadily to around 8 wires for a polar angle of $|\cos\theta| = 0.98$.

For each space point measured in CJ the radius is given by the wire position and the azimuthal angle by the drift time to give a spatial resolution in the $r-\phi$ plane of 135μm. Charge division of the integrated signal arriving at each end of the signal wires gives a z-measurement of resolution 60 mm. Detailed studies using $e^+e^- \rightarrow \mu^+\mu^-$ and $e^+e^- \rightarrow q\,\overline{q}$ events have been made to calibrate and correct the response of CJ. In conjunction with other CT components, the transverse momentum resolution (σ_{p_t}) is measured to be $\sigma_{p_t}/p_t = \sqrt{(0.02)^2 + (0.015 \cdot p_t)^2}$. The impact parameter ($d_0$) resolution using only CJ is 113μm, or 40μm when the measurement is combined with that from CV.

By summing the charge collected at the ends of each signal wire, CJ is also able measure the rate of energy loss along the particle trajectory, dE/dx, to a precision of $\pm 3.8\%$ for minimum ionizing pions in hadronic events (with at least 130 measured space points). As a result, e-π separation is possible with a significance of at least 2σ for momenta up to 13 GeV/c, and π-K or π-p separation up to 20 GeV/c.

Z-chambers (CZ)

The 24 z-chambers, which form a barrel layer around the jet chamber as shown in figures 3.1 and 3.2, are designed to make precise z-coordinate measurements for charged tracks as they emerge from CJ. This results in an improvement in resolution for the polar angle measurement, which is combined with the transverse momentum measurement from CJ to obtain the total momentum of charged tracks. Thus the momenta of tracks with CZ hits are more precisely defined, enabling the better reconstruction of the invariant mass.

The 24 z-chambers cover 94 % of the azimuthal angle within a polar angle range of $|\cos\theta| < 0.72$, where the gaps in ϕ between adjacent z-chambers coincide with the position of an anode plane in CJ. Each chamber is 50 cm wide and 5.9 cm thick, and is divided along its 4.0 m length into 8 bidirectional cells to limit the maximum drift distance in the z-direction to 25 cm. Each cell has 6 anode wires running azimuthally at increasing radii (4 mm spacing) and with a stagger of $\pm 250\,\mu$m in z to resolve the left-right ambiguity. Amplifiers at each end of the wires enable the use of charge division to measure ϕ with a resolution of 15 mm. The intrinsic z resolution for minimum ionising particles travelling normal to the drift direction is 100-200 μm (depending on the drift distance), whilst the absolute resolution is estimated to be around 300 μm.

Silicon microvertex detector (SI)

In 1991 a microvertex detector [37] was added to OPAL consisting of two barrel layers of silicon microstrip devices at radii of 6.1 and 7.5 cm. Prior to this the OPAL beam pipe had been the inner wall of the pressure vessel (radius 7.8 cm) consisting of 0.13 cm thick carbon fibre with a 100 μm aluminium inner lining. In order that the microvertex detector be as close as possible to the interaction point, a second beam pipe made of 0.11 cm thick beryllium ($\sim 0.003X_0$ of material) was added at a radius of 5.35 cm.

The inner layer of SI consists of 11 "ladders", whilst the outer comprises 14. Each of these ladders is 18 cm long and is made up of three single-sided wafers (6 cm long and 3.3 cm wide) daisy-chained together. In its original form the detector gave readouts in the $r-\phi$ plane only, although reconstruction in 3-dimensions was made possible after an upgrade in 1993 for which $r-\phi$ and $r-z$ wafers were glued back-to-back. Further upgrades were made for 1995 LEP running, before which the active length of the detector was 16 cm with a two-layer acceptance in the range $|\cos\theta| < 0.76$.

The $r-\phi$ measurement has a single-hit resolution of less than $8\,\mu$m (including alignment uncertainties), and so, when this information is combined with that from the rest of CT, the impact parameter (d_0) resolution has been estimated as $16\,\mu$m using samples of dimuon events. The resolution of z_0, the z-coordinate of a charged track at the point of closest approach, is estimated to be around $75\,\mu$m. Such precision and the fact that the two layers are some 1.4 cm apart allows for the precise reconstruction of decay vertices. The detector is therefore used extensively in the tagging of short-lived heavy-flavour quark events and the measurement of particle lifetimes (such as for that of the τ lepton). It is not used explicitly in this analysis, although information from SI is used in the reconstruction of charged tracks.

3.3.2 OPAL magnet

The magnet consists of a solenoidal coil and an iron yoke. The solenoidal coil lies inbetween CT and the electromagnetic calorimeter so as to provide a magnetic field of adequate strength that is uniform across the volume of CJ. At the same time time it has been designed to contain as few radiation lengths of material as possible to minimise the showering of particles before they enter the calorimetry. The magnet is able to provide a field of 0.435 T that is measured to be uniform to within $\pm 0.5\%$. In terms of thickness, 96 mm of aluminium and 54 mm of glass-epoxy amount to $\sim 1.7X_0$ of material (including also the pressure vessel). The coil had also been designed such that field leakage into the calorimeter is low and so does not interfere with the photomultipliers used there.

3.3.3 Time-of-flight counters

The time-of-flight system covers the polar angle range $|\cos\theta| < 0.82$, and forms a barrel layer comprising 160 plastic scintillator strips lying at a mean radius of 2.360 m (just outside the solenoidal coil). These strips provide precision timing for charged particles and photons, with a resolution of $\pm 460\,\mathrm{ps}$ estimated using $Z^0 \to \mu^+\mu^-$ events. The detector is used mostly to trigger data events and reject the background from cosmic rays, although particle identification is also possible in the range 0.6 to 2.5 GeV.

3.3.4 Electromagnetic calorimeter (ECAL)

The electromagnetic calorimeter consists of presamplers (PB and PE) and total absorption calorimeters (EB and EE) made up of large numbers lead glass blocks, and its purpose is to detect and identify electrons and photons. Both cause electromagnetic showering which is usually totally contained within the lead glass, enabling their full energies to be determined. However, most electromagnetic showers are initiated in the $2.08\,X_0$ of material that is estimated (for the barrel region) to lie in front of the lead glass. The presamplers (PB and PE) measure the position and sample the energy of this showering, so that the raw energy response seen in the lead glass can be corrected.

Electromagetic presamplers (PB/PE)

The barrel presampler covers the polar angle range $|\cos\theta| < 0.81$ and consists of two layers of streamer tubes, whilst the endcap presampler covers the range $0.83 < |\cos\theta| < 0.95$, and consists of an array of 32 thin (7 mm) multiwire proportional chambers operating in high-gain mode. For electrons in the barrel region with energies between 6 and 50 GeV, PB is estimated to recover $\sim$50% of the energy resolution degradation that occurs due to showering in front of the lead glass.

Lead glass calorimeters (EB/EE)

The barrel lead glass calorimeter (EB) covers the polar angle range $|\cos\theta| < 0.82$ and is located at an inner radius of 2.455 m. It consists of a cylindrical array of 9440 optically-isolated lead glass blocks, each arranged so that its longtudinal axis points roughly towards the interaction point (see figures 3.1 and 3.2). This minimises the number blocks traversed by a single particle, and so allows the response of particles travelling in close proximity to one another to be more easily resolved. However, the pointing geometry is not exact so as to prevent the escape of neutral particles between two adjacent blocks. The endcap lead glass calorimeter (EE) consists of two dome shaped arrays of 1132 optically-isolated lead glass blocks, and covers the angular range $0.81 < |\cos\theta| < 0.98$.

For EB, each lead glass block is 37 cm in depth ($24.6\,X_0$), whilst those in EE contain at least $20.5\,X_0$. Incident electrons entering the blocks emit bremsstrahlung photons which produce a rapidly multiplying shower of e^+e^-pairs. These produce Čerenkov light within the lead glass, where the total intensity of the Čerenkov light observed in a block is proportional to the number of e^+e^-pairs produced, which itself is proportional to the energy of the incident particle. Thus the shower energy is instrumented by the use of phototubes that are tolerant to magnetic fields (more so in the endcap). The intrinsic energy resolutions (σ_E/E) of the lead-glass calorimeters are $0.2\%+6.3\%/\sqrt{E}$ (EB) and $5\%/\sqrt{E}$ (EE), although the actual resolutions are degraded by the presence of the material that lies in front of each calorimeter.

3.3.5 Hadron calorimeter (HCAL)

The HCAL is used to measure the energies of hadrons emerging from the ECAL and to assist in the identification of muons. The iron return yoke for the OPAL magnet provides at least $4\,X_0$ of absorber material over 97% of the 4π solid angle. The yoke is segmented into layers with plastic streamer tubes (or thin high multi-wire proportional chambers for HP) placed between them. This forms a cylindrical sampling calorimeter of ~ 1 m in depth, that is composed of three different sub-components, each covering a different polar angle range in the OPAL detector. The barrel, endcaps and pole-tips (HB, HE and HP) roughly cover the angular ranges $|\cos\theta| <\sim 0.81$, $\sim 0.81 < |\cos\theta| < 0.91$ and $0.91 < |\cos\theta| < 0.99$ respectively.

Being a sampling calorimeter, the intrinsic energy resolutions are poor compared to the ECAL. However, the resolution of the detector is improved by combining the response of ECAL with that of the HCAL using a parametrization to account for the hadronic showering that has already developed in front of the HCAL.

Barrel and endcap hadron calorimeter (HB/HE)

The barrel and endcap hadron calorimeters are similar to one another in design. The 100 mm layers of iron magnet yoke are interspersed with 25 mm (35 mm for HE) gaps in which limited streamer mode chambers (of the same design as those used in PB) are positioned. The barrel uses 9 layers of detector with 8 layers of absorber, one more of each than is used in the endcaps. The readout of the streamer tubes is carried out by a combination of pads (typically 500 mm square) on one side and strips on the other. Pads are grouped together through the layers of the detector to form towers, where the pads signals within a tower are used to provide an measure of the deposited shower energy (with an estimated resolution of $\sigma_E/E \simeq 120\%/\sqrt{E}$). The number of strip hits forms an alternative measure of the energy of an incident hadron, since the number of particles in a shower is proportional to the energy (there is some strip saturation for hadrons of above 10 GeV). A typical 10 GeV pion, for example, typically produces about 25 strip hits across a number of layers. This response is quite different from that for muon tracks, which pass through the HCAL usually leaving single hits in most of the layers. For this analysis, only the strip hit information is used.

Pole-tip hadron calorimeter (HP)

The annular pole-tips cover a region of the detector in which the tracking in CT is much poorer. It is designed therefore to give better energy resolution than HB and HE. The sampling interval is reduced to 80 mm, whilst the number of sampling layers is increased to 10. Thin proportional chambers operate in the 10 mm spacings between successive layers of the iron yoke pole-tips, where these spacings are small to reduce perturbations in the magnetic field. Again the readout is performed by pads and strips.

3.3.6 Muon detector

The muon detector provides precise position measurements of charged particles emerging from the hadron calorimeter. The probability of a pion passing through 1.3 m of iron (over 7 interaction lengths) without interacting is less than 0.1%, whilst muons with energy 3 GeV or more have essentially a 100% chance of emerging from the HCAL and being detected by the muon chambers (if within the acceptance). The muon detector covers 93% of the 4π solid angle, and comprises separate barrel and endcap components which operate quite differently from each other.

Muon identification relies on extrapolating the trajectories of charged tracks through the magnet and calorimetry (accounting for energy loss and multiple coulomb scattering) out to the muon chamber. A precise positional match between this extrapolation and hits in several layers of the muon chambers forms the basis for the $\tau \rightarrow \mu\overline{\nu}_\mu\nu_\tau$ selections detailed in chapter 6.

Barrel muon chambers (MB)

The barrel muon detector consists of 110 drift chambers arranged in 4 layers around HB. Four layers cover the angular range $|\cos\theta| < 0.68$, whilst one or more layers have an extended acceptance out to 0.72 for some regions in ϕ. Each chamber is 1.2 m wide and 90 mm thick, but is either 10.4, 8.4 or 6.0 m in length, depending on the physical contraints for mounting them in various ϕ regions about the detector. For example, the shortest units are used for the chambers situated between the support legs of the magnet. The geometrical acceptance of MB is studied further in appendix D using a sample of $\tau \rightarrow \mu\overline{\nu}_\mu\nu_\tau$ decays identified as such using the calorimeters.

The chambers used consist of two adjacent cells, each with a single anode wire running parallel to the z-axis along its length, so that the maximum drift length is 297 mm. The drift times within the chambers are converted to a position measurement in the r-ϕ plane with an accuracy of 1.5 mm. Corresponding z measurements are obtained with an accuracy of 2 mm using a series of diamond-shaped pads which lie opposite the anode wire along the length of each chamber.

Endcap muon chambers (ME)

The endcap chambers extend the muon detection coverage up to $|\cos\theta| \simeq 0.985$, where each endcap consists of two layers of limited streamer tubes. These layers are positioned 68 cm apart in planes that lie perpendicular to the beam axis at either end of OPAL (as shown schematically in figure 3.3(b)). Each layer consists of 4 "quadrant" chambers (6 m$\times$6 m) and 2 "patch" chambers (4 m$\times$2.5 m), which have been arranged to give maximum coverage (figure 3.3(a)), although some gaps in the acceptance are necessary to allow for the beam pipe, cables, shielding and various support structures.

Each patch or quadrant consists of two layers of streamer tubes (1 cm$\times$1 cm in cross section) containing a gas mixture of 75% isobutane and 25% argon. The ionization electrons formed in the gas by the passage of a muon, drift towards an anode wire set at 4.3 kV that runs the whole length of each tube. The cathode consists of a carbon coating on the tube's inner wall, which is held at ground. Charge signals from the streamer tubes are induced on to planes of aluminium strips located on either side of each layer of tubes, where on one side the strips are parallel to the anode wire, and on the other side they are perpendicular.

Each layer of tubes produces a fine measurement of the coordinate parallel to the wire (from the perpendicular strips) and a coarse measurement of the coordinate perpendicular to the wire (from the parallel strips). The two layers of tubes in each patch or quadrant chamber are arranged so that their anode sense wires are orthogonal, and so combining the two x-y points from each layer gives a position

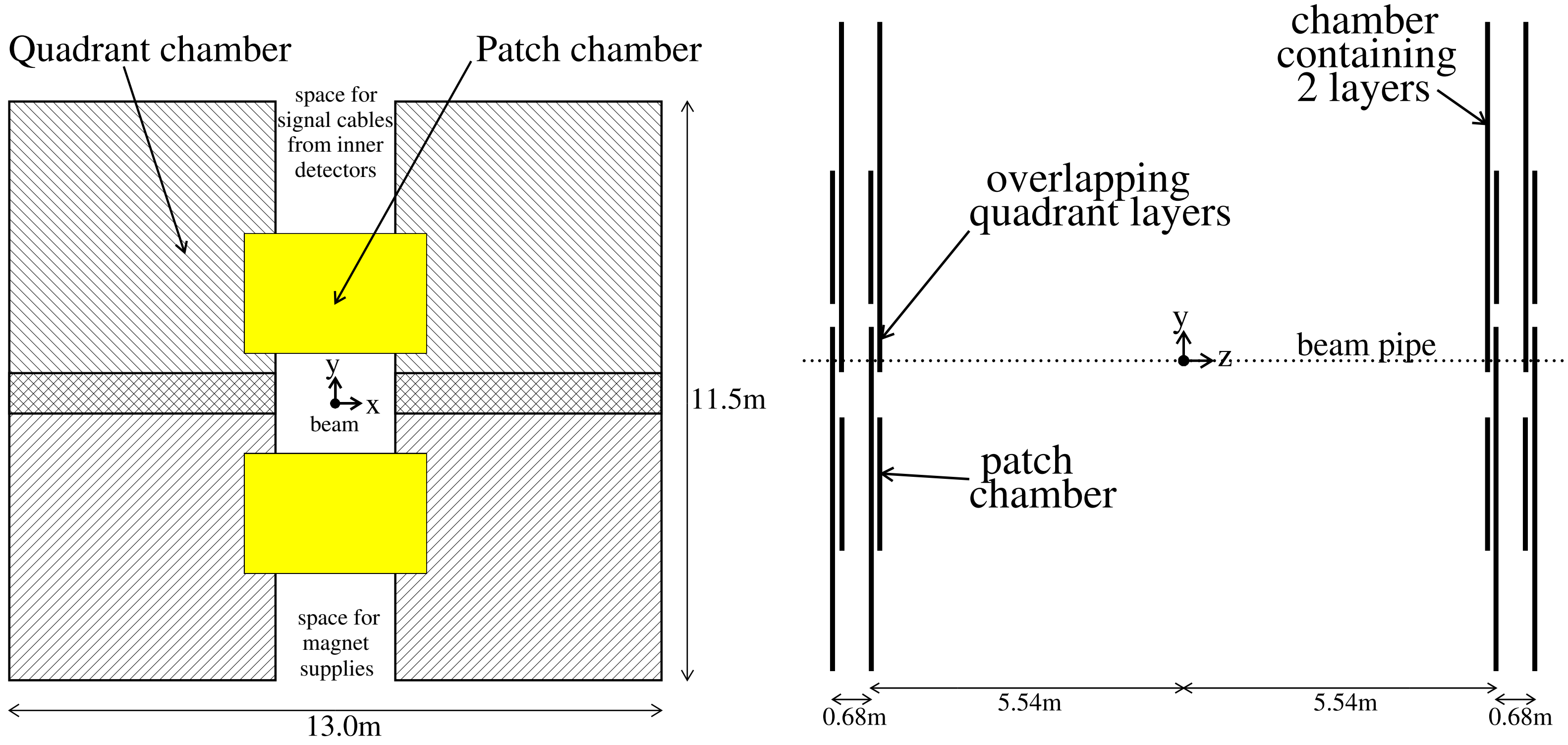

3.3(a) End view of endcap muon detector

3.3(b) Side view of endcap muon detector

Figure 3.3: Schematic diagrams showing side and end views of the endcap muon detectors (ME). For figure 3.3(a) the patches are shown by the shaded region whilst the upper and lower quadrants are distinguishable by the different hatching used. Approximate dimensions are also shown on each plot.

resolution of $\sim$1 mm.

3.3.7 Forward detector (FD) and SiW luminometer (SW)

The absolute machine luminosity at OPAL is measured by the counting of bhabha $e^+e^-\rightarrow e^+e^-$events in the forward region, a process with a QED-dominated cross section approximately proportional to $1/\theta^3$. The measurement relies critically on the precise positional reconstruction of electrons and photons in order to accurately count the events within a given acceptance.

This was originally measured at OPAL using the forward detector which is placed around the beam pipe at $z = \pm 2588$mm and covers the annular acceptance between 47 and 120 mrad from the beam axis. The forward detector is a composite detector comprising several subcomponents. A lead-scintillator sampling calorimeter providing $24X_0$ of material gives energy measurements to an accuracy of 2.7% for well-contained 45 GeV electromagnetic showers. The positional accuracy of cluster reconstruction is improved to ± 2.6 mm by the use planes of proportional tube chambers. Drift chambers were also included within FD, which were used to calibrate the tube chambers, although these were left largely unused after 1993.

A silicon-tungsten luminometer [38] was installed for use from the start of the 1993 physics run, and resulted in an improvement in the precision of the luminosity measurement from $\pm 0.6\%$ (using FD) to around $\pm 0.1\%$ after one year [39]. It consists of 18 tungsten absorber layers, interleaved with 19 sampling layers of silicon wafer diodes. The detector is constructed with an extremely well-known stable geometry (covering the annular acceptance range $31.3 \leq |\theta| \leq 51.6$ mrad), enabling it to reconstruct the radial position of a well-contained shower with a resolution of $\sim 220\,\mu$m.

3.3.8 OPAL trigger and filter

For most of the data used for this analysis, the LEP machine was running with 8 bunches of electrons crossing 8 bunches of positrons (8×8 mode) every $11\,\mu$s (a frequency of 88 kHz). However, the time taken to completely process a single event is around 20 ms, and so during each deadtime there are some 1800 beam crossings for which OPAL is inactive.

In order to ensure that every such event is a good physics event, it must first be passed by the several levels of triggering. The first of these is the deadtime-free pretrigger [40] which was introduced with the upgrade of the LEP operation from 4×4 to 8×8 mode in October 1992. This effectively reduces the 88 kHz beam crossing rate to a 1-2 kHz pretrigger rate.

The OPAL trigger [41] is the next level, which reduces the event rate to $\leq$5 Hz. To do this, the system must therefore make very rapid decisions to reject fake events that arise due to cosmic rays, synchrotron radiation and beam interactions with gas or the beampipe. At the same time it must efficiently select physics events from a variety of different processes: hadronic and leptonic decays of the Z^0, small-angle bhabha events (for luminosity measurements), two-photon processes ($\mathrm{e^+e^-}\rightarrow\gamma\gamma\rightarrow\mathrm{f\bar{f}}$), single-photon events ($\mathrm{e^+e^-}\rightarrow\nu\overline{\nu}\gamma$), as well as possible exotic events.

The trigger uses information from CV, CJ, TOF, ECAL, MB/ME and FD/SW. First there are certain "stand-alone" triggers that must be passed individually by each of the subdetectors. Then trigger signals from different parts of each subdetector are passed to a theta-phi (TPM) matrix of 144 overlapping bins (6 in θ, 24 in ϕ) covering the 4π solid angle of OPAL. By requiring correlations between subdetectors within the TPM matrix, and combining this information with the stand-alone triggers, OPAL is able to make a decision about the event before the next beam crossing arrives (in principle, at least).

Events that pass the OPAL trigger are then passed to an event filter. This partially reconstructs each event, and acts as a higher level software trigger, with around a third of all triggered events rejected as background (physics events are still retained with essentially 100% efficiency). It also performs preliminary event classification and sends events to the on-line event display for perfomance monitoring. For data taken in 1993 and 1994 (that is, with the 8×8 mode in operation), the average OPAL trigger rate was $\sim$4 Hz with deadtime fractions of $\sim$3%.

3.3.9 Data acquisition and event reconstruction

Digitized information from each subdetector is passed to a VME-based local system crate (LSC) where it is compressed and the data is partially reconstructed by the filter. The raw data from events passing the filter selection is then sent to the surface, where it is written to magnetic tape and disk. Since 1991 events have been been fully reconstructed in an on-line data farm immediately after they have been recorded. This is done using a program called ROPE [43] (**R**econstruction of **OP**AL **E**vents), which converts the raw data into a structure suitable for use in physics analyses, and stores the information on Data Summary Tapes (DSTs) and optical disks. A program GROPE [44] has been developed as a graphical interface to ROPE which enables the user to view in 3-dimensions the reconstruction of an event on the DSTs. The use of GROPE is illustrated in figure 3.4 for a typical $e^+e^-\rightarrow\tau^+\tau^-$event.

ROPE is also able to interface with the OPAL Monte Carlo detector simulation package, GOPAL [42]. This enables Monte Carlo data to be generated and stored on to DSTs using the same data structure as that used for real events. The simulation of events in OPAL is discussed further in the next chapter.

The data recorded by OPAL between the years 1990 and 1994 is given in table 3.2, where the number of multihadrons given is based on the "Gold-plated Multihadron"(GPMH) [46] selection used within the OPAL filter. Multihadron events used for analysis at OPAL use a more sophisticated selection, and so the numbers given are only a rough approximation of the actual numbers of mul-

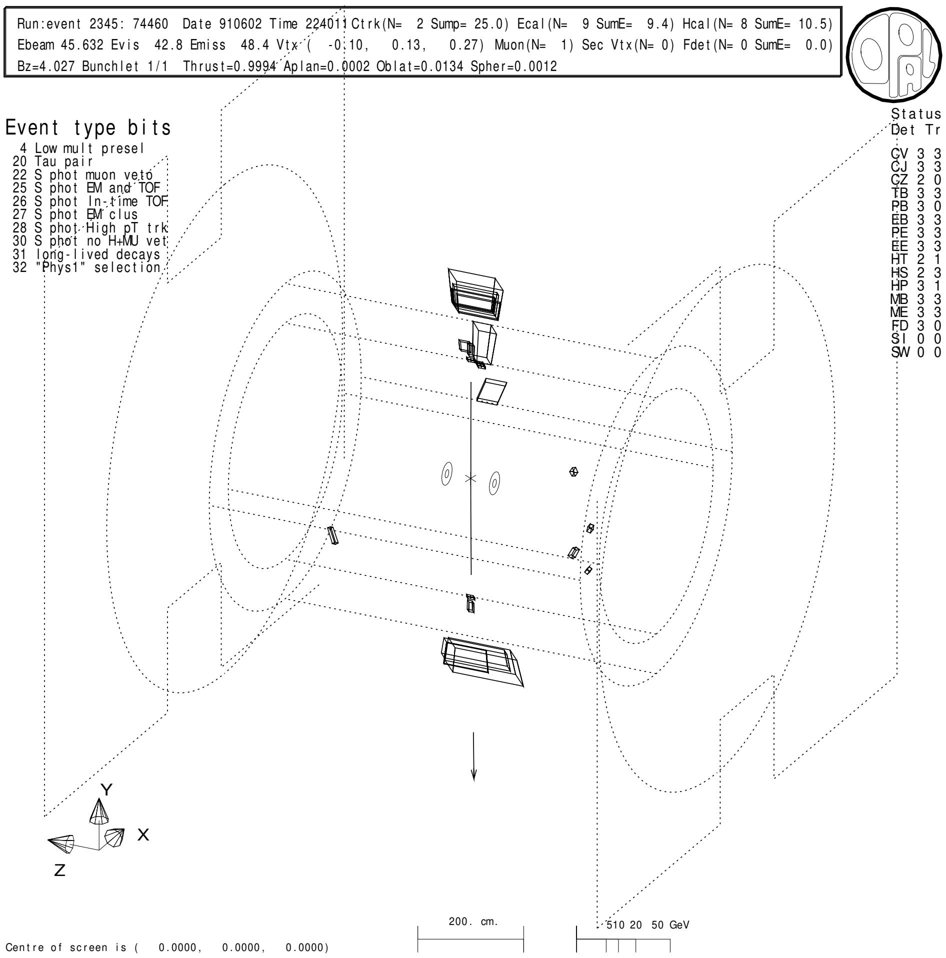

Figure 3.4: Graphical representation of a typical $e^+e^- \rightarrow \tau^+\tau^-$ event in OPAL, where this event has passed the $e^+e^- \rightarrow \tau^+\tau^-$ preselection described in chapter 5. One tau jet features a single highly penetrative charged track which passes through all layers of the detector. This is consistent with being a $\tau \rightarrow \mu\overline{\nu}_\mu\nu_\tau$ decay. The other jet contains a single charged track consistent with being a $\pi^\pm(K^\pm)$, accompanied by two distinct neutral electromagnetic clusters of roughly equal size. The two neutral clusters signify the presence of the process $\pi^0 \rightarrow \gamma\gamma$, and so this second τ jet is probably a $\tau \rightarrow \rho\nu_\tau$ decay in which the spin-1 $\rho^\pm$ particle decays rapidly in the detector by the process $\rho^\pm \rightarrow \pi^\pm\pi^0$.

tihadrons observed in OPAL. The numbers also include all events taken during energy scans, for which the centre-of-mass energy was varied either side of the Z^0 resonance.

Year	Luminosity (pb^{-1})	GPMH (1000s)
1990	6.8	147.6
1991	14.0	345.4
1992	25.1	766.9
1993	33.9	720.8
1994	58.0	1369.0

Table 3.2: The summary of OPAL data-taking for each year between 1990 and 1994, where the number of events multihadron events and the luminosity are estimated using the on-line filter.

Chapter 4

Simulation of LEP events in the OPAL detector

Monte Carlo data is used extensively in this analysis to predict the backgrounds and efficiencies when selecting $\tau\rightarrow \mu\overline{\nu}_\mu\nu_\tau$ decays from $e^+e^-\rightarrow\tau^+\tau^-$events. It is also used to predict the momentum spectra for positive and negative helicity $\tau\rightarrow \mu\overline{\nu}_\mu\nu_\tau$ decays in different angular bins. These spectra are used to extract $\langle P_\tau\rangle$ and A^{FB}_{pol}, and so it is great of importance to this analysis that charged tracks in the Monte Carlo data are well-simulated. Good track simulation is also vital for the accurate estimation of backgrounds using Monte Carlo data. This chapter gives details of the Monte Carlo data used and describes the measures taken to improve the simulation. In particular the procedures used to smear the resolution of charged tracks in the central tracking chambers are discussed at length.

4.1 Monte Carlo event generators

Several generator programs are used to produce samples of each type of physics event to be expected at LEP. All the Monte Carlo $e^+e^-\rightarrow\tau^+\tau^-$and $e^+e^-\rightarrow\mu^+\mu^-$events have been generated using KoralZ4.0 [19] where KoralZ4.0 uses another package called Tauola2.0 [21] to simulate the numerous known tau decay modes under the assumption of $V-A$ theory. In addition events generated using the following packages are also used: Babamc [22] for $e^+e^- \to e^+e^-$events, Jetset7.3/7.4 [23] for $e^+e^- \to q\bar{q}$ events, Fermisv [20] for 4-fermion events (with $e^+e^-e^+e^-$, $e^+e^-\mu^+\mu^-$ or $e^+e^-\tau^+\tau^-$ in the final state) and, finally, version 2.01 of the program by Smith, Vermaseren and Grammar [24] to generate two photon events ($\gamma\gamma \to e^+e^-, \mu^+\mu^-, \tau^+\tau^-$).

In generating $e^+e^- \to \tau^+\tau^-$events using KoralZ4.0 the relative branching ratios of the τ may be passed as inputs to Tauola2.0 to get the various decay modes produced in the correct proportions. However, the numbers used as inputs when the events used by this analysis were generated have been superceded as the branching ratios of the τ lepton have become better known experimentally. The relative branching ratios of the decay modes can therefore be made to agree with the current world averages [5] by weighting each decay on an event by event basis. This shall be done consistently throughout this analysis, where the numbers used for the branching ratios of the main τ decay channels are listed in table 4.1. The uncertainties on these numbers are considered later in evaluating the systematic errors on $\langle P_\tau \rangle$ and A^{FB}_{pol}.

Decay channel	Branching ratio
$\tau \to e\bar{\nu}_e\nu_\tau$	0.17799±0.00079
$\tau \to \mu\bar{\nu}_\mu\nu_\tau$	0.17328±0.00097
$\tau \to \pi\nu_\tau$	0.1121±0.0015
$\tau \to \rho\nu_\tau$	0.2514±0.0018
$\tau \to a_1\nu_\tau$(1-prong)	0.0914±0.0015
$\tau \to a_1\nu_\tau$(3-prong)	0.0896±0.0015
$\tau \to K\nu_\tau$	0.00714±0.00048
$\tau \to K^*\nu_\tau$	0.0137±0.0011

Table 4.1: The world average branching ratios of the main decay modes of the τ lepton are shown. These values are used to weight each Monte Carlo τ decay used within this analysis.

4.2 Simulation of the detector response in OPAL

The 4-vectors of the particles produced by the above generators are passed to a program called GOPAL [42], which stands for **G**eant at **OPAL**. Geant [45] is a package that is used to simulate the passage of different particle types through different materials, where the precise geometries and material properties of all the OPAL components must be passed to it as inputs. The modelling is further tuned within GOPAL by introducing noise, inefficiency and resolution effects for each subdetector, where detailed studies using real data events are used for calibration. Thus GOPAL tracks the passage of each particle generated in the event as it passes through successive layers of the detector. The output is simulated raw data in precisely the same format as that produced by the detector from real events, except that an additional data bank is used to store Monte Carlo generator information. The program ROPE is then used to reconstruct the events and condense the raw data on to DSTs, as is done for real data.

Over the course of LEP1 running it was possible to calibrate the response of each subdetector with increasing accuracy. This came about by the ever-improving statistics and also by the general level of understanding of the numerous detector effects that can occur within such a large multi-component apparatus. Therefore, in principle at least, each successive version of GOPAL superceded the last and was able to simulate better the different particle types over all momentum ranges.

The Monte Carlo data used for this analysis is listed in table 4.2 and was generated using GOPAL/ROPE versions 12 and 14 [42, 43] which were calibrated respectively using the 1993 and 1994 configurations of the detector. Here the analysis presented in this thesis differs from previous τ polarisation analyses performed at OPAL (the latest of which is described in [27]), since this is the first to use Monte Carlo data generated using version 14 of GOPAL/ROPE (GORO).

It is found by studying the track momentum and ECAL energy of $e^+e^- \to \mu^+\mu^-$ and $e^+e^- \to e^+e^-$ events identified in the barrel and endcap regions that the Monte Carlo consistently underestimates the resolution. A package was therefore developed to smear certain track parameters in CT and the energy response observed in the ECAL. A discussion of the ECAL smearing may be found in [27], and so shall not be dwelled upon in this thesis.

GORO version	12		14	
Event type	Luminosity	Number of events	Luminosity	Number of events
$Z^0 \rightarrow f\bar{f}$ events				
ee→ee	$4.10\,\mathrm{nb}^{-1}$	400k	$4.10\,\mathrm{nb}^{-1}$	800k
ee→$\mu\mu$	$1.54\,\mathrm{nb}^{-1}$	200k	$1.54\,\mathrm{nb}^{-1}$	600k
ee→$\tau\tau$	$1.54\,\mathrm{nb}^{-1}$	300k	$1.54\,\mathrm{nb}^{-1}$	600k
ee→$\mathrm{q\bar{q}}$	$30.4\,\mathrm{nb}^{-1}$	1987k	$30.4\,\mathrm{nb}^{-1}$	3987k
4-fermion events				
ee→ee$\mu\mu$	$3.99\,\mathrm{pb}^{-1}$	2075	-	-
ee→ee$\tau\tau$	$1.72\,\mathrm{pb}^{-1}$	1000	-	-
2-photon events				
ee→eeee	$1.02\,\mathrm{nb}^{-1}$	351k	$1.02\,\mathrm{nb}^{-1}$	400k
ee→ee$\mu\mu$	$0.866\,\mathrm{nb}^{-1}$	375k	$0.877\,\mathrm{nb}^{-1}$	400k
ee→ee$\tau\tau$	-	-	$29.5\,\mathrm{pb}^{-1}$	20k

Table 4.2: Summary of the Monte Carlo events used for this analysis, where only events generated using versions 12 and 14 of the detector reconstruction programs GOPAL/ROPE have been used. These correspond to the 1993 and 1994 configurations of the detector respectively. Note also the luminosity for the two-photon events is calculated after certain cuts have been imposed on the events before full detector reconstruction. This is to cut out the large proportion of events in which all final state particles have very low transverse momenta, and so are very unlikely to be recognized as physics events in the OPAL detector.

4.3 Monte Carlo track smearing in the barrel region

The track smearing was performed separately for the barrel ($|\cos\theta| < 0.72$) and endcap ($|\cos\theta| > 0.72$) regions since, in the barrel, all tracks have full wire coverage in CJ as well as precise z-measurement using CZ. This also means that, in principle, the track resolution in the barrel should have very little angular dependence for all but very low momentum tracks, whilst in the endcap this is not the case.

The momentum measurement in CT (see Appendix B for definitions of track parameters) is given by,

$$p = p_t\sqrt{1 + \tan^2 \lambda}$$

where $\tan\lambda = \cot\theta$ and p_t is the transverse momentum. For convenience this can be re-expressed in terms of the quantities x and x_t (respectively the total and tranverse momenta normalised to the beam energy).

$$x = \frac{p}{E_{beam}} = \frac{x_t}{\sin\theta}$$

The momentum is expressed in terms of the polar angle and transverse momentum since the two are separate measurements in CT, each with their own resolution effects. The transverse momentum is obtained from the measurement of track curvature κ in CJ, where

$$x_t \propto \frac{1}{|\kappa|}$$

Therefore, it is actually $1/x_t$, and not x_t, which is a Gaussian quantity with resolution σ_{1/x_t}. In the case of the polar angle measurement, this usually comes from the z measurement obtained in CZ. If the z-chambers lie at a constant radius R from the z-axis, then

$$\cot\theta = \frac{z}{R}$$

Therefore, for tracks with CZ hits $\cot\theta$ is a Gaussian quantity with resolution $\sigma_{\cot\theta}$, and is independent of the κ measurement in CJ. For tracks with no CZ hits the z-measurement comes from charge division on the last wire hit in CJ. Since the radius of the last wire hit is roughly constant for all tracks in the barrel region, it shall be assumed that $\cot\theta$ is still a Gaussian quantity and that the polar angle resolution ($\sigma_{\cot\theta}$) due to this measurement still has no angular dependence. It will also be assumed (although strictly this is not the case) that $\cot\theta$ and $1/x_t$ are still independent of each other for tracks with no CZ information. The total momentum resolution, σ_x, for all tracks in the barrel can be expressed as,

$$\left(\frac{\sigma_x}{x}\right)^2 = \left(\frac{\sigma_{x_t}}{x_t}\right)^2 + \left(\frac{\sigma_{\sin\theta}}{\sin\theta}\right)^2$$

$$\Rightarrow \quad \sigma_x^2 = \left(\frac{x_t^4}{\sin^2\theta}\right)\sigma_{1/x_t}^2 + \left(\cos^2\theta\sin^2\theta\right)\sigma_{\cot\theta}^2$$

In most cases, the parameters that are used for Monte Carlo momentum smearing in the barrel region are included in tables in appendix C.

4.3.1 Smearing the measurement of polar angle

The resolution of the polar angle measurement $\sigma_{\cot\theta}$ can be studied using $e^+e^- \rightarrow \mu^+\mu^-$ events. Since both muons should be back-to-back with $x \simeq 1$ one expects the distributions in $|\cot\theta_-| - |\cot\theta_+|$ for data and Monte Carlo events to have a single peak close to 0 if there are no charge-dependent systematic shifts in the z-measurement. This is indeed the case for both data and Monte Carlo events (with and without CZ hits) and so this is how resolutions are compared. The angular resolution is also studied separately for $e^\pm$ tracks using bhabha events, since it is harder to define the true curvature and direction of $e^\pm$ tracks given their higher probability of radiating a bremsstrahlung photon within CJ.

The angular smearing is applied to every good charged track in the following manner:

$$\cot\theta_{smea} = \cot\theta_{true} + \gamma_c(\cot\theta_{meas} - \cot\theta_{true})$$

where the subscript "*true*" is used to denote the true value of $\cot\theta$ as generated by the Monte Carlo; "*meas*" denotes the value after event reconstruction by GOPAL, and "*smea*" denotes the smeared value subsequently used to redefine the momentum of the track. The quantity γ_c is therefore a factor used to scale the resolution of the Gaussian quantity.

For non-radiative $e^+e^- \rightarrow \mu^+\mu^-$ events, which will contain two muons both with $x \simeq 1$, the contribution to the angular resolution from the process of Multiple Scattering (MS) is small, although for lower momentum tracks it becomes more dominant. Since it is expected that the Monte Carlo models the MS process well, it is required that the smearing only scales the contribution to $\sigma_{\cot\theta}$ brought about by the resolution of the z measurement in CZ (or charge division in CJ). This is accounted for by the fact that the scaling factor γ_c has been corrected in such a way that the expected MS contribution to $\sigma_{\cot\theta}$ is **excluded** from the smearing. This is explained as follows.

When the Monte Carlo events are generated by GOPAL/ROPE (that is, before any additional smearing is applied) the total resolution for the $\cot\theta$ measurement may be given by,

$$\begin{aligned} \overbrace{\sigma^2_{\cot\theta}}^{total} &= \overbrace{\sigma^2_{\cot\theta}}^{measurement} + \overbrace{\sigma^2_{\cot\theta}}^{MS} \\ &= c + \frac{d}{x^2_{true}\sin^5\theta_{true}} \end{aligned} \tag{4.1}$$

where the measurement component of the total $\cot\theta$ resolution should be Gaussian and independent of both momentum (x_{true}) and angle (θ_{true}). Its square may therefore be given by the constant c and it is this value that is consistently underestimated for all MC tracks. The MS component, however, is assumed to be well-described and depends on both momentum and angle where d is a constant. Clearly, for the Monte Carlo description of the $\cot\theta$ resolution to be more like that seen for data events, a constant γ (which is assumed to be independent of both x_{true} and θ_{true}) needs to be applied to the measurement component such that the total resolution becomes ($\sigma_{\cot\theta} \rightarrow \sigma'_{\cot\theta}$),

$$\begin{aligned} \overbrace{\sigma'^2_{\cot\theta}}^{total} &= \overbrace{(\gamma\sigma_{\cot\theta})^2}^{measurement} + \overbrace{\sigma^2_{\cot\theta}}^{MS} \\ &= \gamma^2 c + \frac{d}{x^2_{true}\sin^5\theta_{true}} \end{aligned} \tag{4.2}$$

However, in applying the smearing, the MS component of the resolution cannot be separated from the measurement contribution. In other words, smearing can only be applied to the total $\cot\theta$ resolution, where a corrected smearing factor ($\gamma_c = \sigma'_{\cot\theta}/\sigma_{\cot\theta}$) is used which must account for the momentum- and angular-dependence of the MS component. Equations 4.1 and 4.2 combine to give the following expression for γ_c,

$$\gamma_c(x_{true}, \theta_{true}) = \frac{\sigma'_{\cot\theta}}{\sigma_{\cot\theta}} = \sqrt{\frac{\gamma^2 c x^2_{true}\sin^5\theta_{true} + d}{c x^2_{true}\sin^5\theta_{true} + d}} \tag{4.3}$$

Hence γ_c needs to be calculated for each track using the MC generator information, although in general $\gamma_c \simeq \gamma$ for tracks in the barrel region with $x_{true} \simeq 1$.

Therefore, samples of $e^+e^- \to e^+e^-$ and $e^+e^- \to \mu^+\mu^-$ events are suitable for use in determining values for γ.

First, however, values for c and d need also to be determined as constants for equation 4.3. The MS contribution to the resolution depends on the path length for tracks in CJ, and the number of radiation lengths of gaseous material that such a path corresponds to. The same number for d is used for all tracks, where its value is estimated for tracks with momentum $x = 1$ to be,

$$d = (1.158 \pm 0.016) \times 10^{-9}$$

The constant c is evaluated for each GOPAL/ROPE version by fitting a Gaussian to the uncorrected $\cot\theta_{meas} - \cot\theta_{true}$ distributions for muon tracks from $e^+e^- \to \mu^+\mu^-$ events and correcting for the average MS contribution expected given the above value of d. Events where both tracks in the event have no CZ information are studied separately since $\sigma_{\cot\theta}$ is about a factor of 50 larger than for those with CZ hits. The process is repeated using samples of $e^+e^- \to e^+e^-$ events to get different sets of numbers for the smearing of $e^\pm$ tracks. All the values of c used in the smearing routine are shown in table C.1.

Now that c and d have been determined it remains to determine the values of γ. This needs to be done for $\mu^\pm$ tracks from $e^+e^- \to \mu^+\mu^-$ events with and without CZ hits, and then again separately for $e^\pm$ tracks from $e^+e^- \to e^+e^-$ events. In addition, it is observed that the angular resolution observed in the data (by fitting a Gaussian to the peaks of the distributions in $|\cot\theta_-| - |\cot\theta_+|$ for identified $e^+e^- \to e^+e^-$ and $e^+e^- \to \mu^+\mu^-$ events) deteriorates from one year to the next, and so, for tracks with CZ hits, γ is determined by comparing the Monte Carlo events with data from each year individually. The statistics do not allow the same to be done for tracks without CZ hits, where the data from years 1990 to 1994 is combined. In each of the above cases γ is varied and for each value a Gaussain fit is performed on the resulting Monte Carlo distribution in $|\cot\theta_-| - |\cot\theta_+|$ (using the same binning as that for the data). The value of γ that gives the best agreement between the fits to the data and Monte Carlo distributions is used for the smearing, where these numbers are listed in table C.2. It can be seen that, for tracks without CZ hits, there is no γ value given for the GORO12 Monte Carlo version. This is because the resolution in the Monte Carlo is already larger than that in the data and so no smearing is applied (see also figure 4.2).

The effect of the smearing on $e^+e^- \rightarrow \mu^+\mu^-$ and $e^+e^- \rightarrow e^+e^-$ events, where both tracks in the event have CZ hits, is shown in figure 4.1. The Monte Carlo events shown in the plots have been smeared separately for each data year and then added together with the appropriate normalisation to get a direct comparison between data and Monte Carlo. The unsmeared distributions are also shown. Figure 4.2 shows the corresponding plots for events where neither final state lepton track has CZ hits. It can be seen that the GORO12 version of the Monte Carlo does not require smearing in this case.

4.3.2 Smearing the measurement of transverse momentum

The situation in this case is slightly more complicated than that for the polar angle smearing in that two smearing parameters now have to be determined to get good agreement between real and Monte Carlo data. The smearing is performed using the following expression,

$$\frac{1}{x_t^{smea}} = \frac{1}{\beta^{\pm}\, x_t^{true}} + \alpha_c \left(\frac{1}{x_t^{meas}} - \frac{1}{x_t^{true}} \right)$$

where the superscript "$true$" is used to denote the true value of $1/x_t$ as generated by the Monte Carlo; "$meas$" denotes the value after event reconstruction by GOPAL/ROPE, and "$smea$" denotes the smeared value subsequently used to redefine the momentum of the track. The quantity $\beta^{\pm}$ is a factor that offsets the true value of x_t and, in studies of real and Monte Carlo events identified as being $e^+e^- \rightarrow \mu^+\mu^-$ or $e^+e^- \rightarrow e^+e^-$, it is seen to require separate values for positive and negatively charged tracks. Meanwhile the quantity α_c is a factor used to scale the total resolution of $1/x_t$, and has been evaluated so as to smear the Gaussian component associated with the $|\kappa|$ measurement in CJ but not the expected MS contribution to the resolution. This is done in much the same way that, in the case of the angular smearing, γ_c was determined on a track-by-track basis given

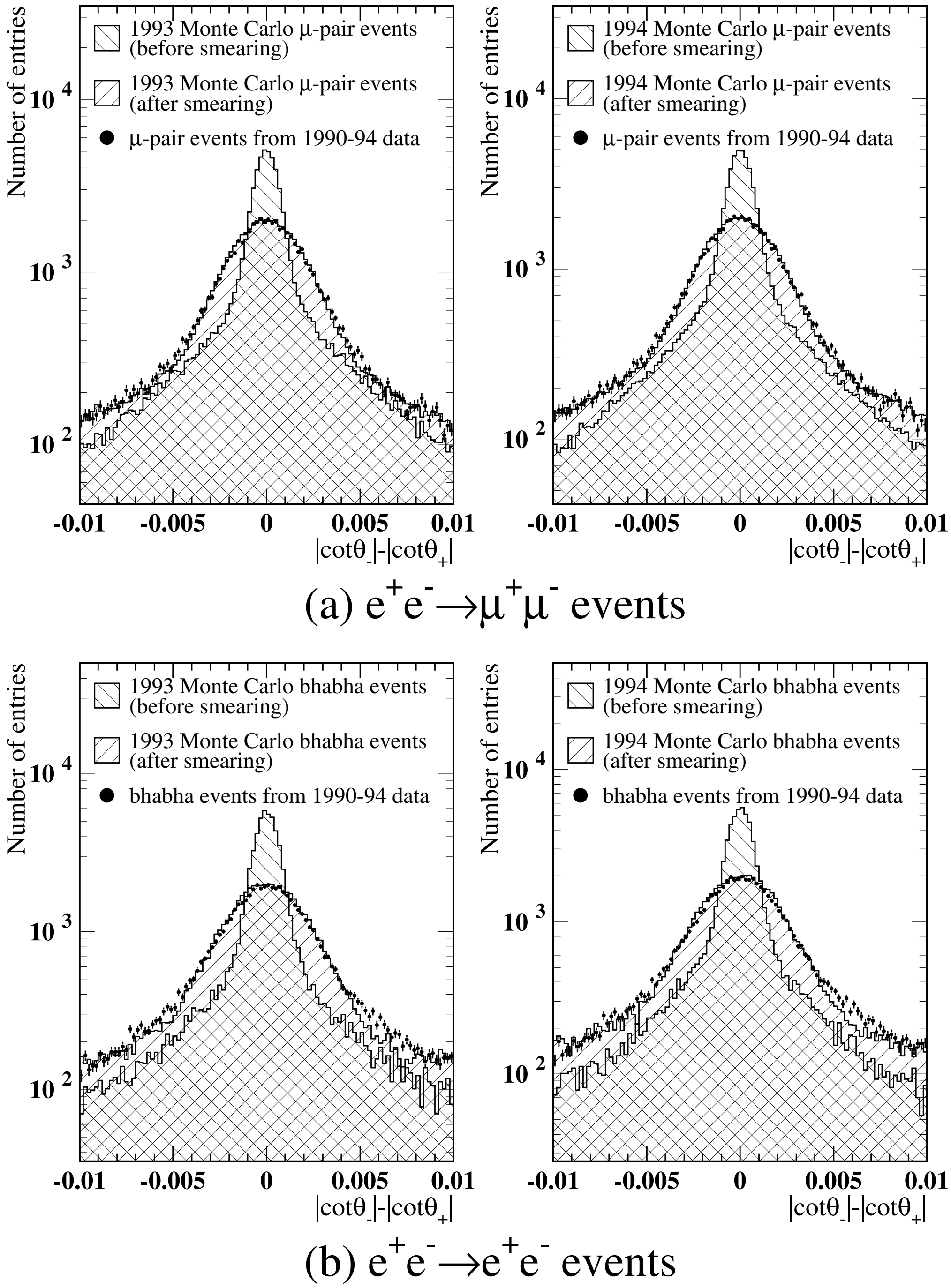

Figure 4.1: Distributions in $|\cot\theta_-| - |\cot\theta_+|$ showing the effect of smearing $\cot\theta$ resolutions in events which are identified in the barrel region as either (a) $e^+e^- \to \mu^+\mu^-$ or (b) $e^+e^- \to e^+e^-$, and in which both final state leptons have CZ hits. Monte Carlo events generated using the 1993 (GORO12) and 1994 (GORO14) detector configurations are compared separately with real data taken in years 1990 to 1994.

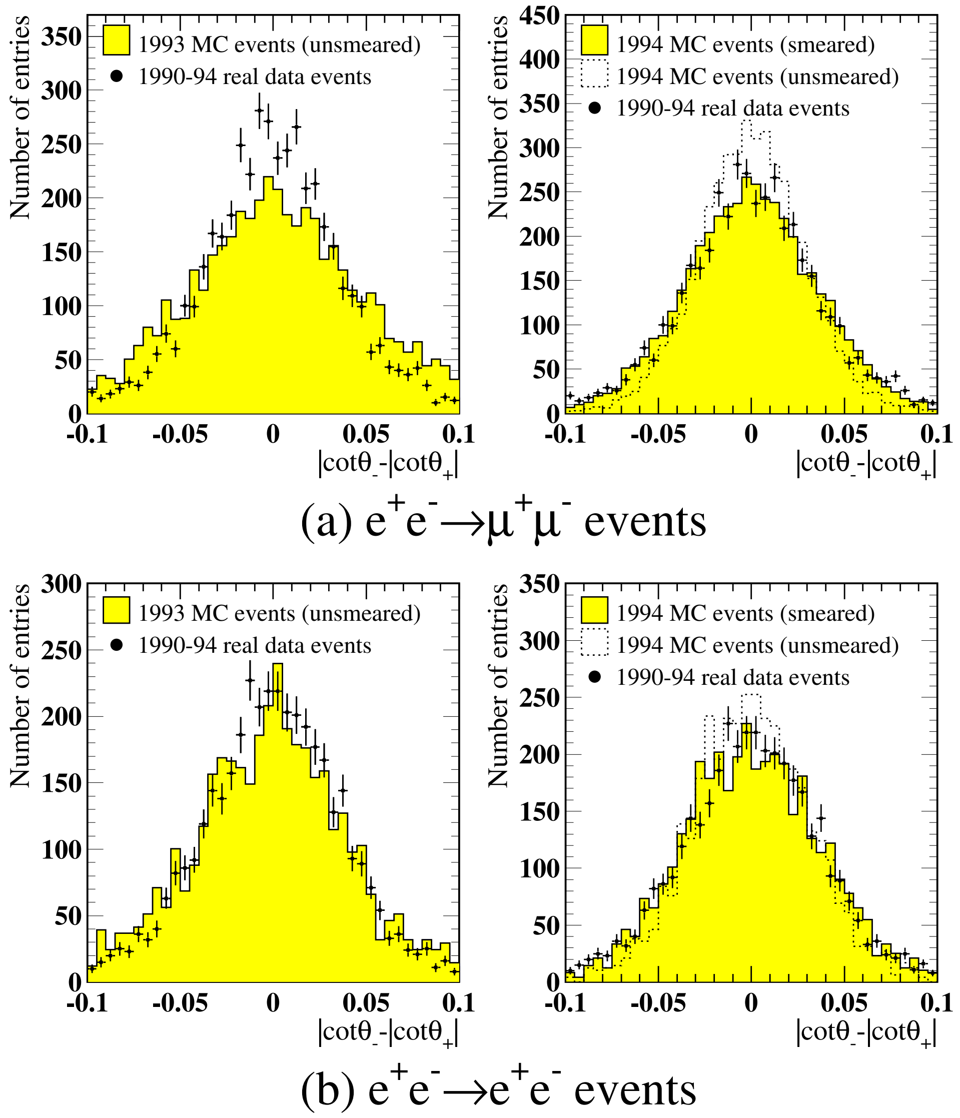

Figure 4.2: Distributions in $|\cot\theta_-|-|\cot\theta_+|$ for events which are identified in the barrel region as either (a) $e^+e^-\to\mu^+\mu^-$ or (b) $e^+e^-\to e^+e^-$, and in which neither final state lepton has CZ hits. Monte Carlo events generated using the 1993 (GORO12) and 1994 (GORO14) detector configurations are compared separately with real data taken in years 1990 to 1994. It can be seen that smearing is only required in the latter case.

constant values of γ. The MC resolution for $1/x_t$ before smearing is applied may be expressed as a quadratic sum of two components:

$$\begin{aligned}\overbrace{\sigma^2_{1/x_t}}^{total} &= \overbrace{\sigma^2_{1/x_t}}^{measurement} + \overbrace{\sigma^2_{1/x_t}}^{MS} \\ &= a + \frac{b}{x^2_{true}\sin^3\theta_{true}}\end{aligned} \tag{4.4}$$

The square of the Gaussian component of the resolution associated with the $|\kappa|$ measurement is given by the constant a, and it is this value that the MC consistently underestimates. The MS contribution, whose size is governed by the constant b, is assumed to be well-described by the MC. Therefore, we wish to apply the smearing (where $\sigma_{1/x_t} \to \sigma'_{1/x_t}$) in the following way,

$$\begin{aligned}\overbrace{\sigma'^2_{1/x_t}}^{total} &= \overbrace{\left(\alpha\sigma_{1/x_t}\right)^2}^{measurement} + \overbrace{\sigma^2_{1/x_t}}^{MS} \\ &= \alpha^2 a + \frac{b}{x^2_{true}\sin^3\theta_{true}}\end{aligned} \tag{4.5}$$

Again, since it is not possible to apply the smearing to the measurement component only in this way, a corrected scaling factor α_c must be determined for each track is therefore taken as the ratio of values for the total resolution in $1/x_t$ before and after α is applied ($\sigma'_{1/x_t}/\sigma_{1/x_t}$). Using equations 4.4 and 4.5 the following expression is obtained,

$$\alpha_c(x_{true}, \theta_{true}) = \frac{\sigma'_{1/x_t}}{\sigma_{1/x_t}} = \sqrt{\frac{\alpha^2 a x^2_{true}\sin^3\theta_{true} + b}{a x^2_{true}\sin^3\theta_{true} + b}} \tag{4.6}$$

The MS contribution is relatively very small for high momentum tracks in CJ, and so, in general for tracks in $e^+e^- \to e^+e^-$ and $e^+e^- \to \mu^+\mu^-$ events, $\alpha_c \simeq \alpha$. More importantly such tracks are used in the determination of α and $\beta^\pm$ since they are mostly produced with energies close to $x_{true} = 1$.

For the angular smearing, $e^\pm$ tracks were treated separately from other tracks. This was not essential but was done so to be consistent with what is required here in the case of the smearing in $1/x_t$. In the magnetic field OPAL $e^\pm$ tracks have a much higher probability of emitting bremsstrahlung radiation compared to other charged tracks. Whilst one expects the bremsstrahlung emission to be well simulated for $e^\pm$ tracks in Monte Carlo events, the problem that the effect creates is that there is now uncertainty as to what value to use for $1/x_t^{true}$ when performing the smearing. The Monte Carlo tree information will return the true 4-momentum at the point at which a particle is generated, but this gives an overestimation of the true $e^{\pm}$ momentum in CJ if the particle has emitted bremmsstrahlung radiation. To account for this, the absolute value of the true momentum, x_{true}, is corrected for $e^{\pm}$ tracks by subtracting the sum of all the true energies of photons emitted by the particle up to a radius of 105 cm in the xy-plane (this corresponds to the midpoint of CJ). The value of $1/x_t^{true}$ is thus only calculated after this subtraction has been made to the total momentum of the particle (one can assume the direction of the $e^{\pm}$ to remain unchanged since, in the barrel region, $1/x_t^{true}$ is relatively insensitive to small changes in $\sin\theta_{true}$).

Before the smearing parameters α and $\beta^{\pm}$ can be determined, values for a and b must be evaluated as constants for the equation 4.6. The value of b was again estimated for tracks for which $x_{true} = 1$, where the following number is used for all tracks:

$$b = (5.03 \pm 0.08) \times 10^{-5}$$

The values used for a had to be determined separately for $e^{\pm}$ tracks and for the different GOPAL/ROPE versions used in the generation of Monte Carlo events. Also the resolution of κ (and hence $1/x_t$) depends on the position of the charged track in CJ in relation to the nearest cathode and anode wire planes. In fact, the scaling factors α and $\beta^{\pm}$ are determined separately for 4 different **track types**, where each track type is defined in table 4.3 and uses a different value of a for the momentum correction. The values used for a are given in table C.3.

The smearing parameters α and $\beta^{\pm}$ are determined for tracks with $x_{true} \simeq 1$ in identified $e^+e^- \to e^+e^-$ and $e^+e^- \to \mu^+\mu^-$ events. In the case of the latter there is relatively little final state or bremsstrahlung radiation and so distributions in $x_{meas} - 1$ should be centred close to 0 with very little radiative tail. By comparing such distributions for Monte Carlo and real events (after $e^+e^- \to \mu^+\mu^-$ identification), it can be seen that there is a charge-dependent discrepancy in the central values of the two distributions, and so distributions in $1/x_t^- - 1/x_t^+$ are not suitable for the

Track type	Definition for barrel region
1	$N_{CZ} \geq 4$ and away from wire planes in CJ
2	Close to cathode plane in CJ ($\phi_{CJ} < 0.3$ or $\phi_{CJ} > 14.7$)
3	Close to anode plane in CJ ($7.0 < \phi_{CJ} < 8.0$)
4	$N_{CZ} < 4$ and away from wire planes in CJ

Table 4.3: When smearing $1/x_t$ for Monte Carlo tracks in the barrel region, every good charged track must be classified as one of these four types (where N_{CZ} is the number of z-chamber hits). The smearing parameters have a different set of values for each of these track types.

study of track resolution. Instead, α and $\beta^{\pm}$ can be satisfactorily determined by altering their values and then fitting a Gaussian distribution to the central peaks of the resulting Monte Carlo distributions in $x^{\pm}_{meas}-1$ (in determining α), $x^{+}_{meas}-1$ (for β^{+}) and $x^{-}_{meas}-1$ (for β^{-}) until the best match with fits using real data is obtained. The same is done for $e^{\pm}$ tracks in bhabha events. All the values of α and β used are listed in table 4.3.

The errors on α and β are not calculated for every value individually, since their errors arise mostly from data statistical errors only. Depending on the track type and the data year with which the Monte Carlo is being compared, estimates are made of the fractional changes to β (or α) required to cause the fitted means (or widths) that result for Monte Carlo $x^{\pm}_{meas}-1$ distributions to change by as much as the uncertainty on the fitted mean (or width) for the corresponding $x^{\pm}_{meas}-1$ distribution seen for real data. For evaluating the systematic errors in $\langle P_\tau \rangle$ and A^{FB}_{pol} arising from the modelling of track momenta in CT, these fractional uncertainties are used to scale up or down the values of α or β used for all Monte Carlo events. For $e^{\pm}$ tracks, the same values are used except that the fractional uncertainties on α and $\beta^{\pm}$ are estimated to be a factor of $\sqrt{2}$ larger by virtue of the fact that the Monte Carlo bhabha samples used for this study are comparable in size to the overall bhabha sample obtained from OPAL data taken between 1990 and 1994 (the number of MC $e^+e^- \to \mu^+\mu^-$events is around 3 times larger), and also because of the additional uncertainty associated with x_{true}. The numbers used are listed in table C.5.

For tracks close to cathode planes (type 2), it is observed for real data events that a certain fraction of high momentum tracks are badly measured, causing their momenta to be underestimated. This effect is not fully simulated in Monte Carlo events, and so a random number generator has been used to select a much higher value for α ($\sim 2.5\times$ larger than normal) for a certain proportion of tracks[1] and to subsequently smear their resolution using the following equation:

$$\frac{1}{x_t^{smea}} = \frac{1}{\beta^{\pm}\, x_t^{true}} + \alpha_c \left| \frac{1}{x_t^{meas}} - \frac{1}{x_t^{true}} \right|$$

where this equation differs in that it forces x_{smea} to always be less than x_{true}. For the evaluation of systematic errors, the random number number generator can be switched off in the smearing routine, and instead replaced by a larger than normal value for α for all type 2 tracks.

When applying the smearing of transverse momentum to the Monte Carlo events a random number generator is used to determine which data year the event should be compared with. This is done such that the number of Monte Carlo events smeared using the values of α and $\beta^{\pm}$ appropriate for a particular data-taking year reflect the fraction of events seen in the real data that were taken during that year.

4.4 Monte Carlo track smearing in the endcap region

The endcap region is generally more poorly simulated than the barrel for all Monte Carlo events. The situation is complicated by the fact that, for tracks where $|\cos\theta| > 0.72$, the number of sense wires in CJ covering the path of the track drops off with increasing $|\cos\theta|$, and also by the fact that there are no z-chambers and so the polar angle and curvature (κ) measurements are correlated. However, for

[1] 13(17)% for Monte Carlo tracks generated using GOPAL/ROPE version 14(12), where the charge of the track and its position to the left or right of the cathode plane have also been considered.

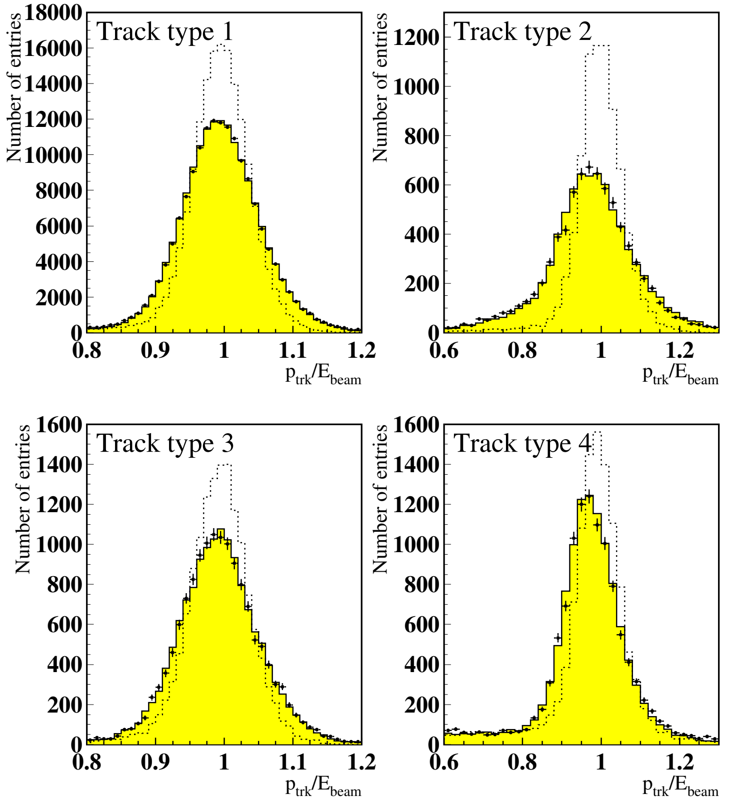

4.3(i) 1990-94 data with 1993 MC (GORO12)

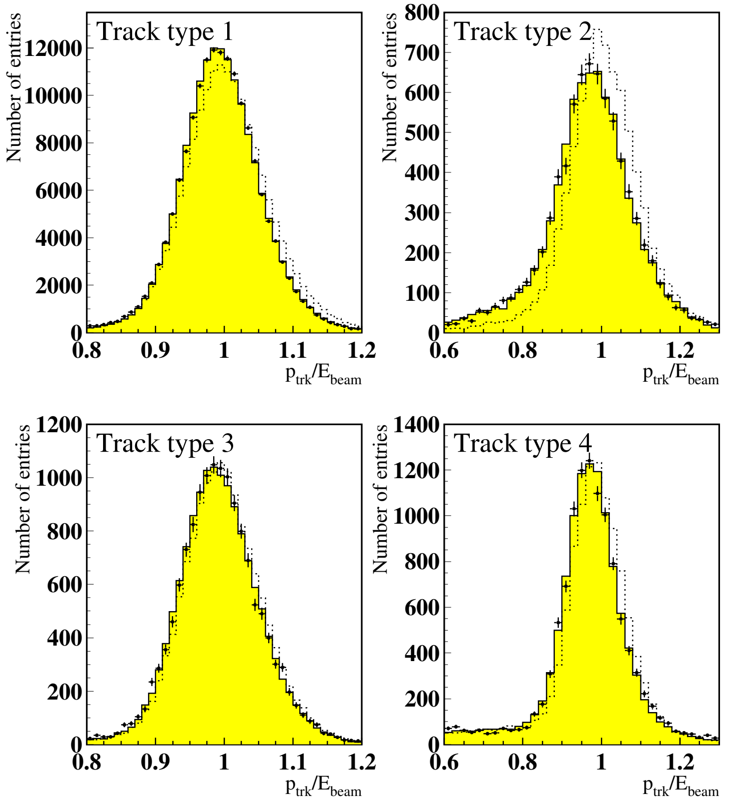

4.3(ii) 1990-94 data with 1994 MC (GORO14)

Figure 4.3: Distributions showing the effect of track smearing on the momentum distributions of $e^+e^- \rightarrow \mu^+\mu^-$ events identified in the barrel region of OPAL, where tracks are divided up into the 4 track types defined in table 4.3. The data is shown by the points whilst the Monte Carlo is shown by filled histograms (smeared spectra) or the broken lines (unsmeared spectra). Two separate sets of plots are shown for Monte Carlo events generated using GOPAL/ROPE versions 12(4.3(i)) and 14(4.3(ii)), where these correspond to the 1993 and 1994 detector configurations.

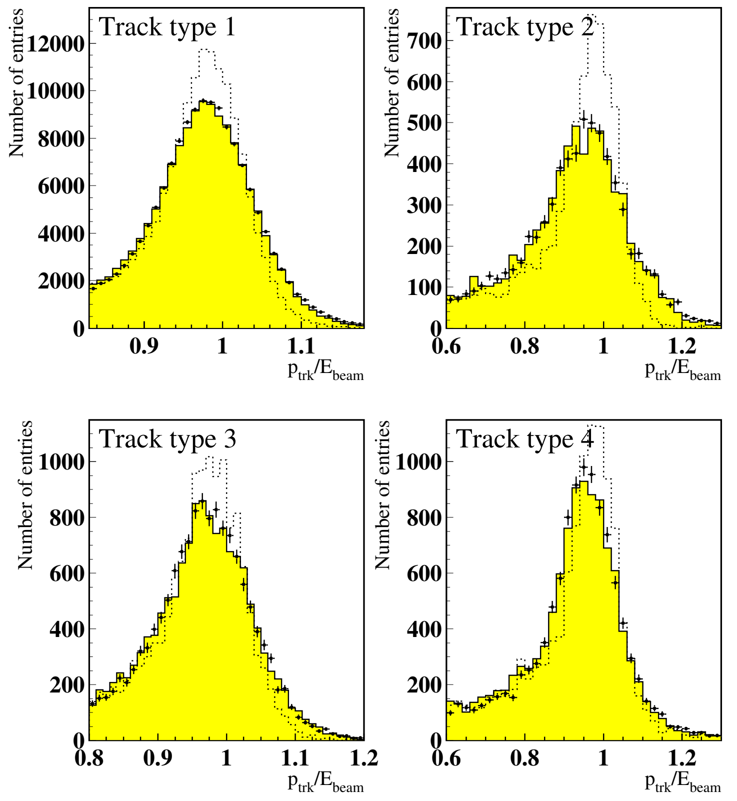

4.4(i) 1990-94 data with 1993 MC (GORO12)

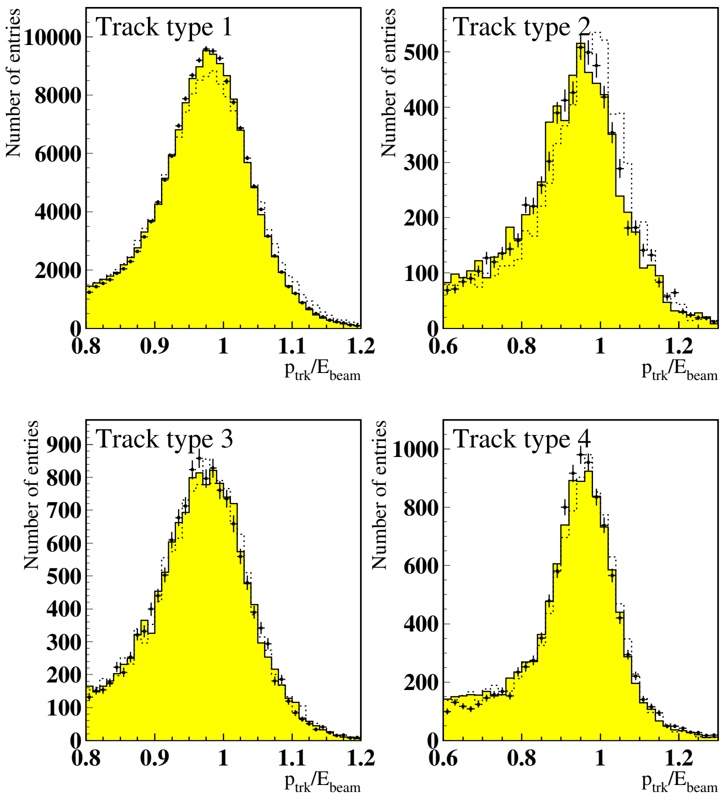

4.4(ii) 1990-94 data with 1994 MC (GORO14)

Figure 4.4: Distributions showing the effect of track smearing on the momentum distributions of $e^+e^-\rightarrow e^+e^-$events identified in the barrel region of OPAL, where tracks are divided up into the 4 track types defined in table 4.3. The data is shown by the points whilst the Monte Carlo is shown by filled histograms (smeared spectra) or the broken lines (unsmeared spectra). Two separate sets of plots are shown for Monte Carlo events generated using GOPAL/ROPE versions 12(4.4(i)) and 14(4.4(ii)), where these correspond to the 1993 and 1994 detector configurations.

tracks with good endpoints[2] in back-to-back $e^+e^- \to \mu^+\mu^-$ events identified in the endcap, distributions in $|\cot\theta_-| - |\cot\theta_+|$ (see figure 4.5) show that the simulation of the polar angle resolution in the Monte Carlo is consistent with that seen in the data to within errors. Therefore, no smearing need be applied to $|\cot\theta|$ for tracks lying beyond the barrel region.

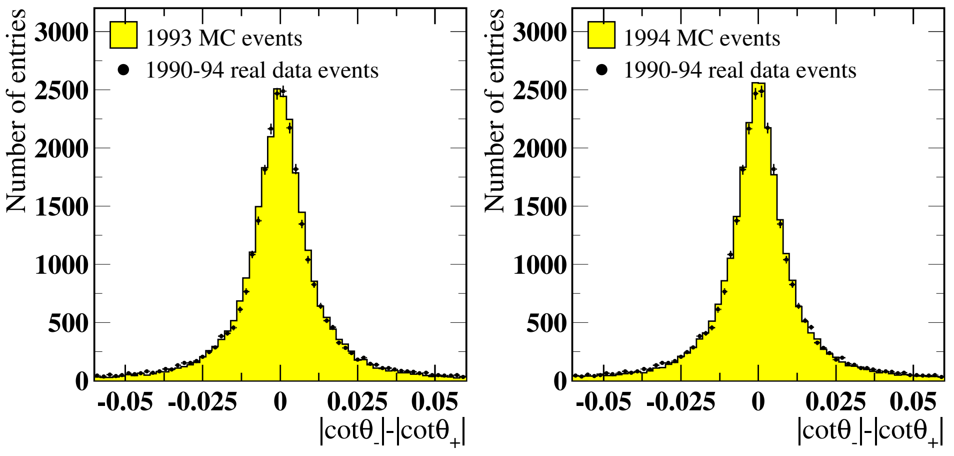

Figure 4.5: Distributions in $|\cot\theta_-| - |\cot\theta_+|$ for identified $e^+e^- \to \mu^+\mu^-$ events, where both muon tracks lie in the angular range $0.72 < |\cos\theta| < 0.90$ and have good endpoints. Monte Carlo events generated using the 1993 (GORO12) and 1994 (GORO14) detector configurations are compared separately with real data taken in years 1990 to 1994.

Hence, for Monte Carlo tracks in the endcap, the resolution of $1/x_t$ only is corrected, and this is done using the expression,

$$\frac{1}{x_t^{smea}} = \frac{\beta^{\pm}(|\cos\theta|)}{x_t^{true}} + \alpha_c(|\cos\theta|)\left(\frac{1}{x_t^{meas}} - \frac{1}{x_t^{true}}\right)$$

where, in the endcap, the smearing parameters α and $\beta^{\pm}$ now have to be considered as functions of $|\cos\theta|$.[3] Again α_c is the corrected form of α which excludes the estimated contribution of multiple scattering from the smearing. This is done using the following expression,

$$\alpha_c(|\cos\theta|) = \sqrt{\frac{\alpha^2(|\cos\theta|)a(|\cos\theta|)x_{true}^2 \sin^3\theta_{true} + b}{a(|\cos\theta|)x_{true}^2 \sin^3\theta_{true} + b}}$$

[2]Any track with a good endpoint is required to have a well-defined last-wire hit in CJ lying close to the endplate.

[3]Also the definition of $\beta^{\pm}$ has changed somewhat in that now $\beta^{\pm} \to 1/\beta^{\pm}$. This is for no particular reason.

where this is the same as equation 4.6 for smearing in the barrel, except that functions are being used in place of constants.

The values of smearing parameters are determined according to the GOPAL/ROPE version and the track type (where only the 3 track types defined in table 4.4 need now be considered). For this, samples of identified $e^+e^- \to \mu^+\mu^-$ events were used, and so the same smearing is applied to tracks regardless of particle type (in other words, there is no longer a separate set of numbers for $e^\pm$ tracks).

Track type	Definition for endcap region
1	Away from wire planes in CJ
2	Close to cathode plane in CJ ($\phi_{CJ} < 0.3$ or $\phi_{CJ} > 14.7$)
3	Close to anode plane in CJ ($7.0 < \phi_{CJ} < 8.0$)

Table 4.4: When smearing $1/x_t$ for Monte Carlo tracks in the endcap region, every good charged track with a well-defined endpoint must be classified as one of these three types. The smearing parameters have a different set of values for each of these track types. Tracks without a good endpoint are generally very poorly measured and are not considered in this analysis.

Monte Carlo and data events identified as being $e^+e^- \to \mu^+\mu^-$ were put into 6 $|\cos\theta|$ bins for values between 0.72 and 0.90. In doing this, it was necessary to combine the data from years 1990 to 1994 to ensure that the statistics were adequate. Gaussians were fitted to unsmeared distributions in $1/x_t^{meas} - 1/x_t^{true}$ for each bin, and, by fitting a polynomial function to the widths, a parameterization for $a(|\cos\theta|)$ was obtained (b is taken to be a constant and have the same value as in the barrel region).

For each $|\cos\theta|$ bin, a single Gaussian was then fitted to distributions in $1/x_t^{smea} - 1/\sin\theta$ (for Monte Carlo events) and $1/x_t^{meas} - 1/\sin\theta$ (for real data events), where $1/\sin\theta \simeq 1/x_t^{true}$ for $e^+e^- \to \mu^+\mu^-$ events. The central values obtained in these fits allowed α and $\beta^\pm$ to be determined for each bin, enabling $\beta^\pm$ to be parameterized separately for positive and negatively charged tracks as a function of $|\cos\theta|$. The same distributions (but with α_c now reset to 1 for the Monte Carlo) were then used to get binned values of σ_{1/x_t} for data and Monte Carlo. These were used to get parameterizations from which α can be determined as a function of angle using the general expression,

$$\alpha(|\cos\theta|) = \frac{\sigma^{data}_{1/x_t}(|\cos\theta|)}{\sigma^{MC}_{1/x_t}(|\cos\theta|)}$$

The binned values of $\beta^{\pm}$ and σ_{1/x_t}, and their parameterizations for all three track types are illustrated in figure 4.6. Also shown is $\alpha(|\cos\theta|)$, which has been calculated using the binned values and parameterizations of σ^{data}_{1/x_t} and σ^{MC}_{1/x_t}. Generally it was found that the parameterization of $\beta^{\pm}$ suffered when the first bin was included in the polynomial fit. This first bin ($0.72 < |\cos\theta| < 0.75$) contains tracks that lie in the so-called "overlap" region, some of which may have CZ information. Therefore this region is excluded from the $\beta^{\pm}$ parameterizations and the binned value is used instead. The parameterizations of σ_{1/x_t} used for α did include the first bin. However, the value of $\alpha(|\cos\theta| = 0.73)$ is used for tracks in the range $0.72 < |\cos\theta| < 0.73$ since the parameterizations of σ_{1/x_t} there are poor.

Figure 4.7 shows the effect of the smearing on distributions in x (where $x = p_{trk}/E_{beam}$) for each of the 3 track types and for Monte Carlo events generated using GOPAL/ROPE versions 12 and 14 (which correspond to the 1993 and 1994 detector configurations respectively). These plots include all tracks in the range $0.72 < |\cos\theta| < 0.90$. In figure 4.8, however, separate plots are shown for each of the six $|\cos\theta|$ bins to show how track momentum has been improved across the entire angular range in the endcap region for $e^+e^- \rightarrow \mu^+\mu^-$ events. All three track track types have been included in these plots.

However, figures 4.7 and 4.8 fail to show the full picture in the case of the track simulation observed for Monte Carlo generated using GOPAL/ROPE version 14. The parameterizations of β^+ and β^- shown in figure 4.6 for track types 1 and 2 show that $1/x_t^{true}$ has to be scaled considerably in equal and opposite directions for positive and negatively charged tracks (much more so than for the 1993 Monte Carlo simulation). Figure 4.9 illustrates this further, where evidently the Monte Carlo spectra for μ^+ and μ^- tracks are shifted in opposite directions with respect to equivalent distributions seen in the data. This effect is brought about by the additional simulation of field line distortions in CJ which were included in GORO14

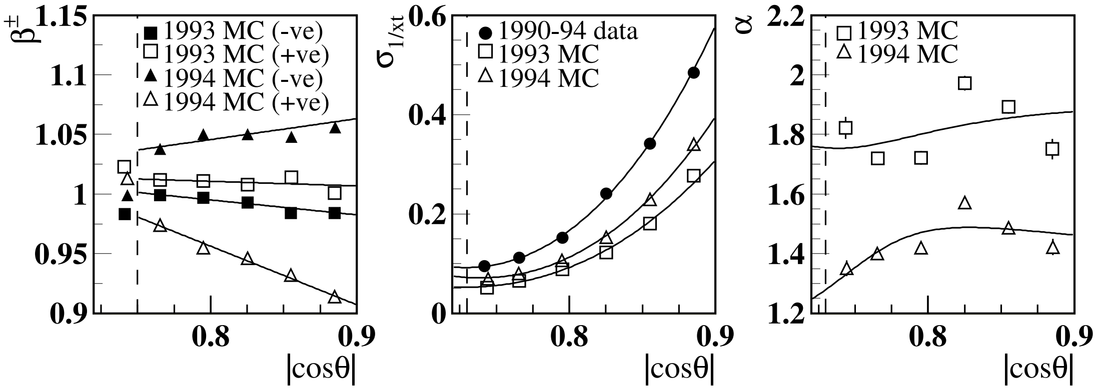

(a)Tracks with good endpoints away from wire planes in CJ

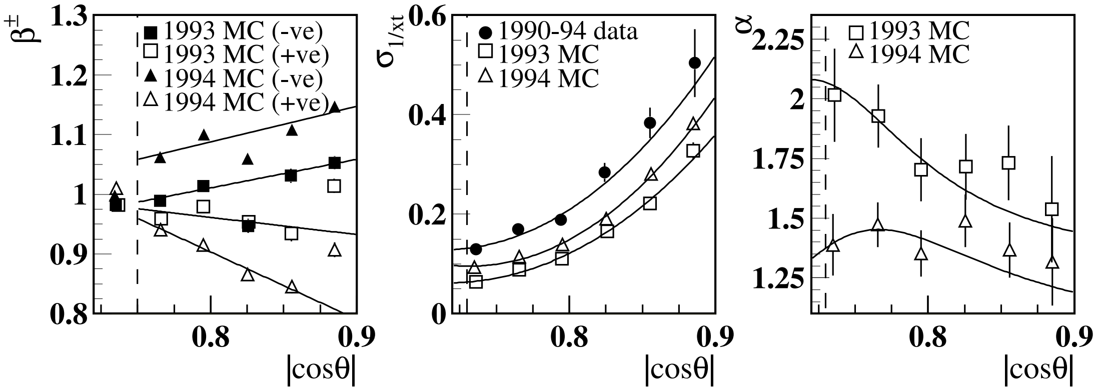

(b)Tracks with good endpoints near cathode planes in CJ

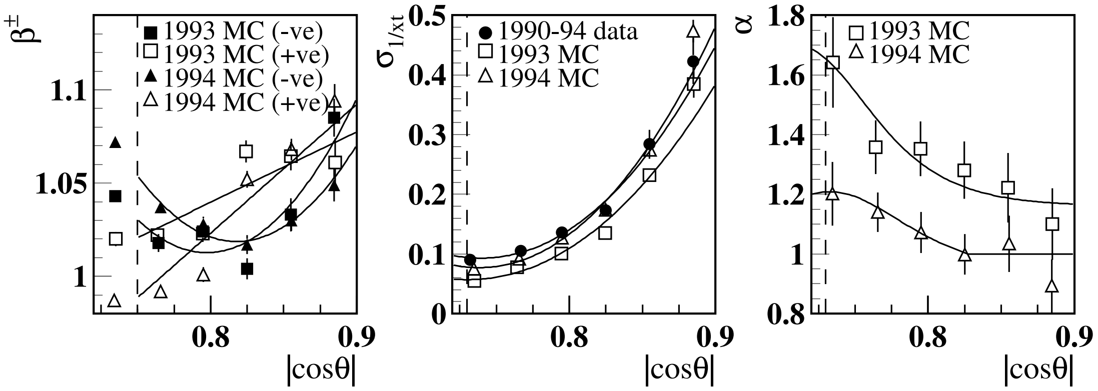

(c)Tracks with good endpoints near anode planes in CJ

Figure 4.6: Distributions showing the parameterizations used for smearing Monte Carlo tracks in the endcap. For this study events identified as $e^+e^- \to \mu^+\mu^-$ were used, where OPAL data from 1990-94 was compared with Monte Carlo samples generated using GOPAL/ROPE versions 12(1993) and 14(1994). Three sets of plots are shown, each corresponding to the three track types defined in table 4.4. The horizontal dashed lines in each plot indicate the value of $|\cos\theta|$ below which the parameterizations are not used.

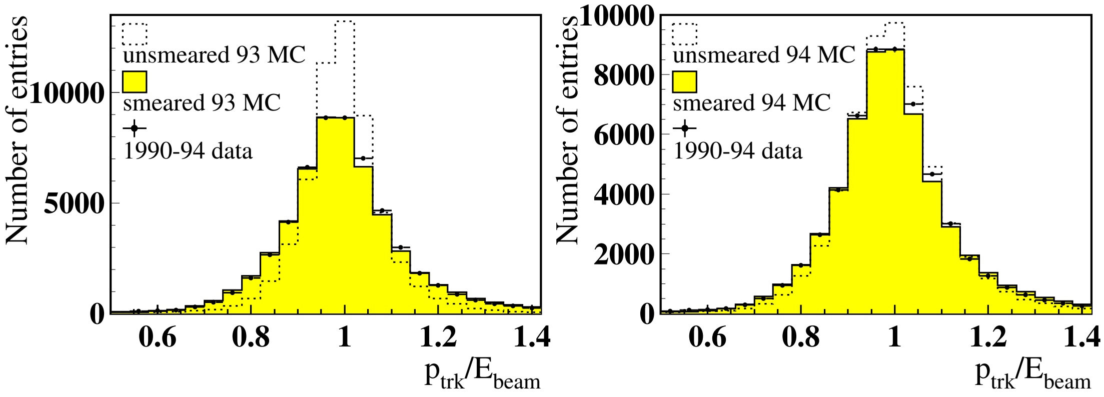

(a)Tracks with good endpoints away from wire planes in CJ

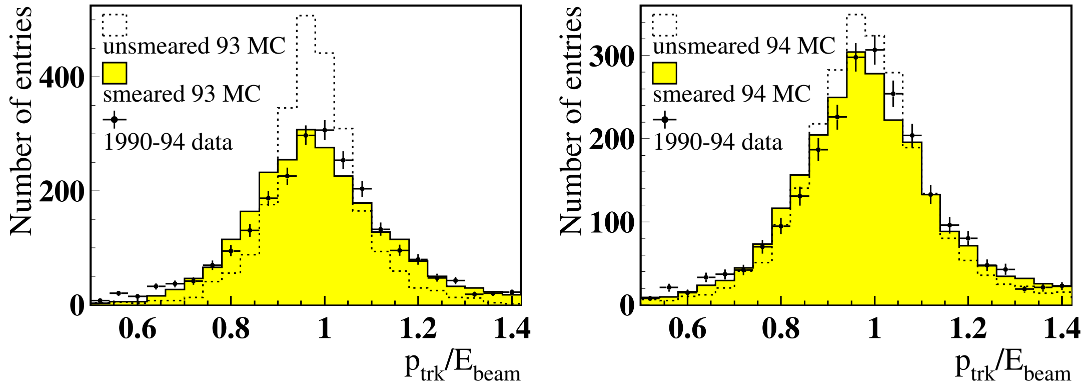

(b)Tracks with good endpoints near cathode planes in CJ

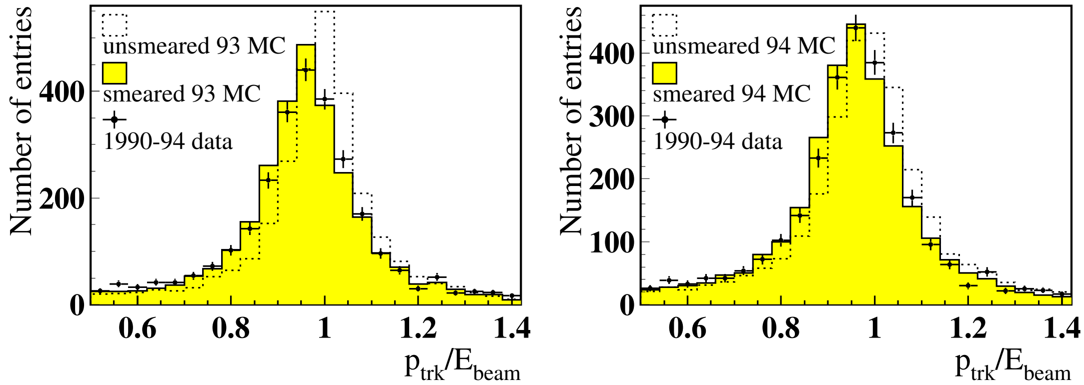

(c)Tracks with good endpoints near anode planes in CJ

Figure 4.7: The momentum distributions for muon tracks in events identified as $e^+e^- \to \mu^+\mu^-$ in the endcap region. OPAL data from years 1990-94 is compared with Monte Carlo samples generated using GOPAL/ROPE versions 12(1993) and 14(1994), where each of the three track types defined in table 4.4 are compared separately.

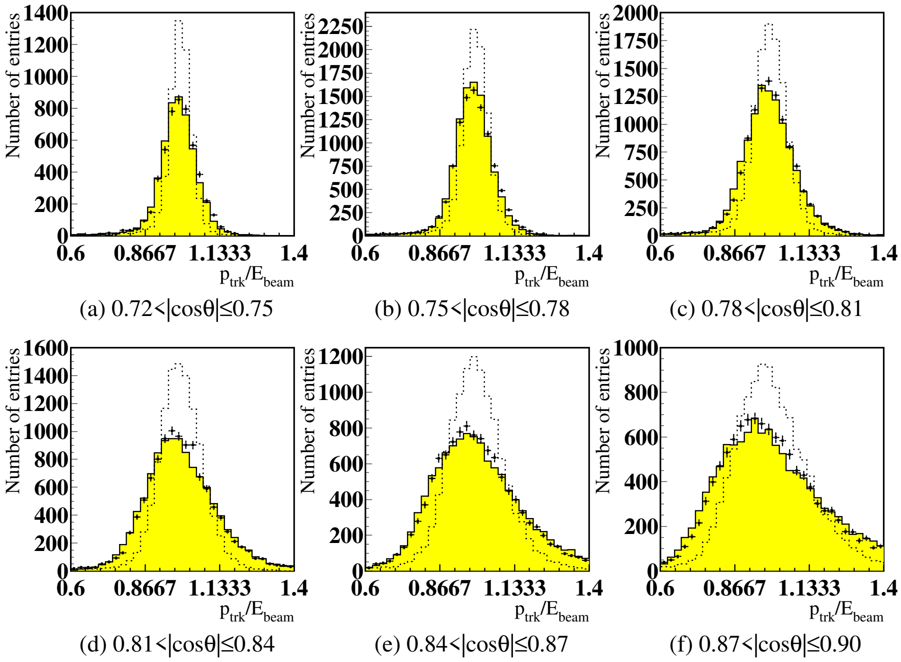

4.8(i) 1990-94 data with 1993 MC (GORO12)

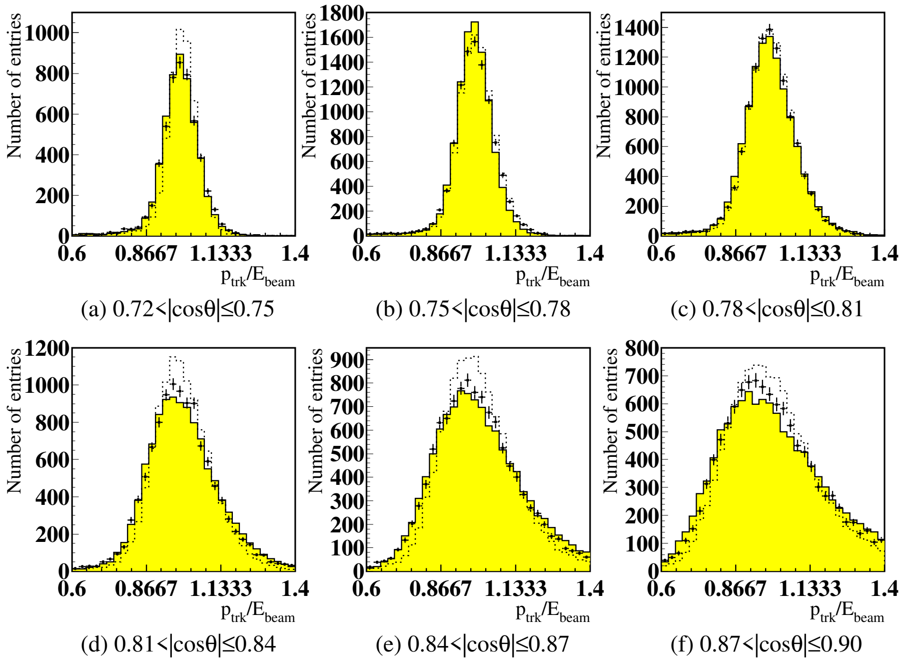

4.8(ii) 1990-94 data with 1994 MC (GORO14)

Figure 4.8: Distributions showing the effect of track smearing on the momentum distributions of $e^+e^- \rightarrow \mu^+\mu^-$ events identified in different angular ranges of the end-cap region. The data is shown by the points whilst the Monte Carlo is shown by filled histograms (smeared spectra) or the broken lines (unsmeared spectra). Two separate sets of plots are shown for Monte Carlo events generated using GOPAL/ROPE versions 12(4.8(i)) and 14(4.8(ii)), where these correspond to the 1993 and 1994 detector configurations.

but not GORO12. Whilst the inclusion of this effect in the barrel region has lead to a dramatic improvement in the simulation of track resolution, in the endcap the effect is to also introduce these large momentum shifts which get worse with increasing $|\cos\theta|$. Thus, when the μ^- and μ^+ distributions are combined as in figure 4.8(ii), the effect of the track smearing in certain angular ranges would not apparently seem to improve the simulation. However, these plots mask the fact that the momentum shifts for negative and positive tracks cancel one another out and so make the momentum resolution for unsmeared 1994 MC tracks look larger (and in better agreement with real data) than it really is.

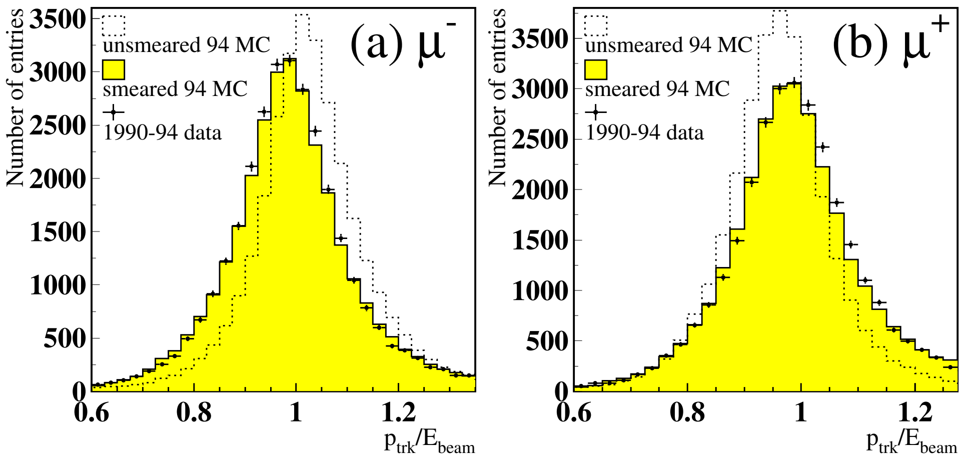

Figure 4.9: The momentum distributions for (a)$\mu^-$and (b)μ^+tracks in events identified as $e^+e^-\to\mu^+\mu^-$in the endcap region. OPAL data from years 1990-94 is compared with Monte Carlo samples generated using only GOPAL/ROPE version 14(1994) to show the charge-dependent shifts introduced as a result of the added simulation of field line distortions. All three track types defined in table 4.4 are included in the plots.

When $\langle P_\tau \rangle$ and A_{pol}^{FB} are measured using $\tau\to\mu\overline{\nu}_\mu\nu_\tau$ candidates identified in the endcap region, a systematic error must be assigned to each which estimates the uncertainty arising from the Monte Carlo modelling of tracks in CT. In the barrel region, it was assumed that the error associated with MC track measurement arises mostly from the statistical uncertainties involved in determining α and β. In the endcap region, however, the situation is made more complex by the parameterization of α and β as functions of $|\cos\theta|$. It is assumed in this case that another potentially large source of systematic error associated with track measurement in

CT arises due to uncertainties in these parameterizations. Therefore, rather than merely varying α or β up or down by a factor estimated from statistical uncertainties in the data, now the parameterized values of α or β are replaced with the **average** parameterized value of each in the endcap. The changes observed in the measured values of $\langle P_\tau \rangle$ and A_{pol}^{FB} are taken as the systematic errors. In addition, the average values of α and β themselves are also varied. For replacing the parametizations of α, separate averages are used for the overlap $(0.72 < |\cos\theta| < 0.75)$ and endcap $(0.75 < |\cos\theta| < 0.90)$ regions. For β, since the parameterizations are not used in the overlap regions anyway, an average value is used for $0.75 < |\cos\theta| < 0.90$, whilst the binned value in the overlap region is varied up or down by 5%.

Chapter 5

Preselection of $e^+e^- \to \tau^+\tau^-$ events

The reader should now be familiar with the OPAL detector, and how it may be used to select certain types of event and discriminate against others. This chapter shall go on to describe how the sample of $e^+e^- \to \tau^+\tau^-$ events used for this analysis is obtained. Beyond this chapter this procedure will be referred to as the "preselection" to distinguish it from the $\tau \to \mu\overline{\nu}_\mu\nu_\tau$ selections described in the next chapter.

In order to perform a study of final state polarisation in $e^+e^- \to \tau^+\tau^-$ events a sample of such events must first be obtained which is clean and unbiased. The selection used in this analysis is done in several stages. First every event must be selected as a good low multiplicity physics event within ROPE [43]. The second stage rejects events likely to come from sources other than $e^+e^- \to \ell^+\ell^-$ events. Finally cuts are made on the remaining $e^+e^- \to \ell^+\ell^-$ sample to suppress the backgrounds from $e^+e^- \to e^+e^-$ and $e^+e^- \to \mu^+\mu^-$ events. The preselection efficiency is estimated by Monte Carlo $e^+e^- \to \tau^+\tau^-$ events to be 91.5% in the barrel region ($|\overline{\cos\theta}| < 0.72$, where $|\overline{\cos\theta}|$ is averaged for the two τ jets in the event), and 75.4% in the endcap region ($0.72 < |\overline{\cos\theta}| < 0.90$). These estimates will discussed further at the end of the chapter.

5.1 Low Multiplicity Selection

The data used in this analysis was collected from LEP runs between the years 1990 and 1994. The branching ratios for the possible decay modes of the Z^0 at LEP1 energies are predicted by the Standard Model to be approximately as follows: $Z^0 \rightarrow q\overline{q}(70\%)$, $Z^0 \rightarrow \nu\overline{\nu}(20\%)$, $Z^0 \rightarrow e^+e^-(3\%)$, $Z^0 \rightarrow \mu^+\mu^-(3\%)$, $Z^0 \rightarrow \tau^+\tau^-(3\%)$. The $Z^0 \rightarrow \nu\overline{\nu}$ decays are undetectable (in the absence of initial or final state radiation) since neutrinos do not interact with any of the material in the detector, which means that any Z^0 decay observed in OPAL will either be from $Z^0 \rightarrow \ell^+\ell^-$ or $Z^0 \rightarrow q\overline{q}$ decays.

The number of detectable particles in the hadronisation accompanying the formation of a $q\overline{q}$ pair rises rapidly with energy ($\propto \ln E$), such that at LEP1 energies a multihadronic event typically would have ten or more charged tracks. Hence, multiplicity, based on the number of charged tracks or electromagnetic clusters observed in OPAL, is a very powerful way of distinguishing $Z^0 \rightarrow q\overline{q}$ from $Z^0 \rightarrow \ell^+\ell^-$ decays.

Based on this knowledge, the OPAL low multiplicity selection [46] applies a loose high multiplicity veto which suppresses the number of $Z^0 \rightarrow q\overline{q}$ decays in the sample whilst removing very few $Z^0 \rightarrow \ell^+\ell^-$ decays. Events are rejected if:

$$N_{trk} + N_{clus} > 18$$

where N_{trk} is the number of tracks in the central detector and N_{clus} is the number clusters in the electromagnetic calorimeter. Tracks are only considered if they have (see Appendix B for definitions of track parameters): $p_t > 1.0\,\mathrm{GeV}/c$, $|d_0| < 1\,\mathrm{cm}$, $|z_0| < 20\,\mathrm{cm}$, and at least 20 hits in the central detector (that is, CV,CJ and CZ combined), the first of which must be within within a radius of 75 cm. Barrel electromagnetic clusters are only considered if they are above a certain raw energy, $E_{raw} > 0.1\,\mathrm{GeV}$, whereas a cluster in the endcap is required to have $E_{raw} > 0.2\,\mathrm{GeV}$, contain at least two blocks and not have more 99% of its energy contained within the highest energy block.

In addition, the low multiplicity selection requires that events satisfy ANY one of the following conditions:

- A good track with $p_t > 0.7\,\mathrm{GeV}/c$, $|d_0| < 1\,\mathrm{cm}$, $|z_0| < 20\,\mathrm{cm}$ and at least 20 hits in the central detector. The first of these 20 or more hits must be within a radius of 75 cm.
- A track in the endcap muon chambers (ME) that, when projected back to the $z = 0$ plane, is within 20 cm of the beam spot. Only endcap events containing less than five tracks are considered.
- At least two electromagnetic clusters with total corrected energy $> 6\,\mathrm{GeV}$.
- Two electromagnetic clusters that are back to back within 25°, one of which has total corrected energy $> 2\,\mathrm{GeV}$.

5.2 Selection of $e^+e^- \to \ell^+\ell^-$ events

A sample of $e^+e^- \to \ell^+\ell^-$ events is now made from the low multiplicity strip, by making tighter contraints on the multihadronic signal, as well as suppressing the backgrounds from two photon and cosmic ray events. Unless otherwise mentioned the rest of the preselection is based upon the standard selection of $e^+e^- \to \tau^+\tau^-$ events used within the Tau Platform package [48], where the Tau Platform has been developed in order to standardize τ analyses at OPAL and to be consistent with similar packages used by the Lepton Pair group [47].

5.2.1 Good track, cluster and cone definitions

Since $e^+e^- \to \tau^+\tau^-$ events contain two roughly back-to-back jets often containing more than one charged track it is convenient to consider each event in terms of two distinct cones, to which all good electromagnetic clusters and good charged tracks within a certain half-angle are assigned. Within the Tau Platform the following definitions are used:-

Good charged tracks must satisfy the following requirements:

- number of jet chamber wires hit, $N_{hits}^{CJ} \geq 20$
- tranverse momentum of track, $p_t \geq 0.1\,\mathrm{GeV}/c$
- impact parameter in the xy plane, $|d_0| \leq 2\,\mathrm{cm}$
- separation in z between track and vertex at point of closest approach, $|z_0| \leq 75\,\mathrm{cm}$
- radius of the innermost wire hit in jet chamber, $R_{min} \leq 75\,\mathrm{cm}$

Good electromagnetic clusters must satisfy the following requirements:

- number of blocks within the cluster, $N_{blk} \geq 1$
- uncorrected electromagnetic cluster energy, $E_{raw} \geq 100\,\mathrm{MeV}$

Good charged cones are defined using a jet finding algorithm which associates charged tracks and clusters to a cone of half-angle 35° as follows. The highest momentum good track or good cluster in the event defines an initial cone direction. The next highest energy good track or cluster whose momentum vector points to within 35° of the cone direction is assigned to the cone, whose direction is then redefined by taking the sum of two vectors. The process continues until all the tracks and clusters in the event are checked to see if they are assigned to this cone. Of the good tracks and good clusters that remain unassigned after this, the one with the highest energy is used to define the direction of a second cone, and so the process repeats until all good tracks and clusters in the event are assigned to a cone. A charged cone is one that contains at least one charged track; otherwise it is a considered a neutral cone. Furthermore only those cones containing greater than 1% of the beam energy are considered as good cones. For this analysis, a candidate lepton pair must contain exactly two good charged cones.

5.2.2 Rejection of multihadronic events

The suppression of the multihadron background in $e^+e^- \to \ell^+\ell^-$ events on the basis of event multiplicity is improved further by applying the following two cuts:

- the total number of good charged tracks in the event, $N^{tot}_{chrg} \leq 6$
- the total number of good clusters in the event, $N^{tot}_{clus} \leq 10$

5.2.3 Rejection of two photon events

Not every event at LEP occurs as a result of e^+e^- annihilation. QED predicts that the process illustrated in figure 5.1 can occur where the exchange of virtual photons between the incoming e^- and e^+ lead to the formation of a lepton pair.

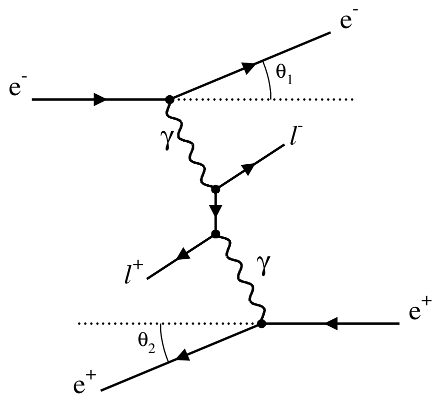

Figure 5.1: The production of a lepton pair by the two photon process.

The form of the differential cross section for such a process means that relatively very few of the leptons from the $\gamma\gamma \to \ell^+\ell^-$ process have large transverse momentum and that mostly the two beam particles remain down the beam pipe (θ_1 and θ_2 are low). However, there are still two-photon events for which the transverse momenta of the particles in the $\gamma\gamma \rightarrow \ell^+\ell^-$system is sufficient for them to get well into the OPAL detector whilst the beam particles remain undetected.

One virtual photon in such an event will be of higher energy than the other, and so the rest frame in which $\gamma\gamma \rightarrow \ell^+\ell^-$process occurs is Lorentz boosted with respect to the laboratory frame (preferentially in a direction very close to the beam axis). Therefore lepton pairs getting into the OPAL detector from the process $\gamma\gamma \rightarrow \ell^+\ell^-$will be characterised by their not being back-to-back and by having a low **net** transverse momentum. Furthermore, most of the energy in the event will remain with the undetected beam particles so that the amount of energy actually observed in OPAL will always be lower than the total centre of mass energy. The following cuts are applied to suppress the background from two photon events:

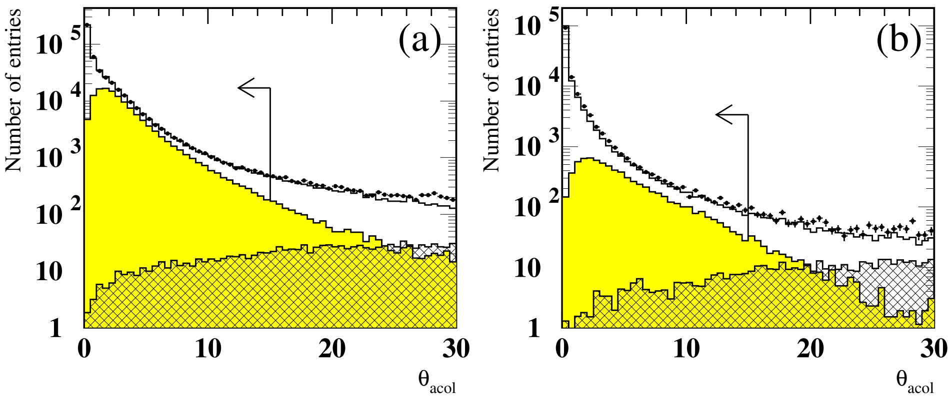

Figure 5.2: The effect of cutting on the acollinearity distribution in rejecting two-photon events from the sample of lepton pairs (after all other cuts have been applied). The points represent the 90-94 data whilst the Monte Carlo events are shown by the solid histograms. The shaded regions show the contribution from Monte Carlo $e^+e^- \rightarrow \tau^+\tau^-$events , whilst the hatched region repesents the two-photon background. Plot (b) differs from (a) in that both sides in the event are loosely identified as muons according to the selection described in section 5.3.2. This is to observe the effect the cut might have on $\tau^+\tau^-$ events in which both sides are possible $\tau \rightarrow \mu\overline{\nu}_\mu\nu_\tau$ decays.

- the acollinearity of the two cones (whose unit momentum vectors, $\hat{\mathbf{p}}_1$ and $\hat{\mathbf{p}}_2$, are defined using good charged tracks and clusters) in the event (see figure 5.2),

$$\theta_{acol} = \cos^{-1}(-\hat{\mathbf{p}}_{\mathbf{1}}\cdot\hat{\mathbf{p}}_{\mathbf{2}}) < 15^\circ$$

• total visible energy (where for every cone in the event, the visible energy is taken as the total raw cluster energy or the scalar sum of the track momenta, whichever is the larger),

$$E_{vis} \equiv \sum_{cones} \max(\sum_{clus} E_{raw}, \sum_{trk} p_{trk}) \geq 0.03\, E_{CM}$$

• if the total visible energy is less than $20\% E_{CM}$, the event is rejected if the **net** transverse energy of the charged tracks and clusters are both less than 2 GeV.

5.2.4 Rejection of cosmic ray background

OPAL can be triggered by high energy cosmic rays (such as muons), which are constantly passing through it, and which are uniformly distributed throughout the apparatus. The passage of such particles through the detector will be inconsistent with those particles coming from $e^+e^- \to \ell^+\ell^-$ events which are generated in the interaction region and whose subsequent trajectories can therefore be traced back towards the beam spot. To suppress the background from cosmic rays it is required that within each event there is at least one good charged track with:

$$|d_0|_{min} \leq 0.5\,\mathrm{cm}$$

$$|z_0| \leq 20\,\mathrm{cm}$$

$$|z_{0,ave}| \leq 20\,\mathrm{cm}$$

where $|d_0|_{min}$ and $|z_0|_{min}$ are the minimum $|d_0|$ and $|z_0|$ respectively of good tracks in the event, and $|z_{0,ave}|$ is the average z_0 of a set of tracks with a good $|z_0|_{min}$.

Also there should be at least one TOF signal associated with each track within 10 ns of the expected value. Furthermore an event is rejected if all pairs of TOF signals separated by more than 165° in azimuth have time differences greater than 10 ns.

5.2.5 Detector/trigger status requirements

It is possible within a given physics run for one or more of the subdetectors within OPAL to not be fully functioning whilst data events are still being accumulated. This effect is not fully included in the Monte Carlo simulation, and so requirements on the detector and trigger statuses are applied to both to ensure consistency between the two.

Within ROPE a word is assigned for each subdetector which specifies its detector status as follows:

0 = Status unknown.

1 = Subdetector not on.

2 = Detector only partially on (low voltage or readout problems).

3 = Everything appears to be as normal.

A similar word is assigned to each to describe its status in the OPAL trigger (again with a value between 0 and 3). Table 5.1 shows the subdetectors to which detector and trigger status cuts are applied, and the cuts used for this analysis (some of which differ from the standard ones used in the Tau Platform). The numbers correspond to the minimum value required for each of the status words in order that the event be included in the $e^+e^-\to \ell^+\ell^-$ sample.

Subdetector:	CV	CJ	TB	PB	EB	PE	EE	HS	MB
Detector status:	3	3	3	2	3	3	3	3	3
Trigger status:	0	2	0	0	2	0	3	0	0

Table 5.1: The detector and trigger status cuts used for the preselection.

5.3 Classification of $e^+e^-\to \ell^+\ell^-$ events

To get the final $e^+e^-\to \tau^+\tau^-$ sample it is necessary to distinguish them from the $e^+e^-\to e^+e^-$ and $e^+e^-\to \mu^+\mu^-$ events within the $e^+e^-\to \ell^+\ell^-$ sample that now remains after all the above cuts have been applied. The $e^+e^-\to e^+e^-$ and $e^+e^-\to \mu^+\mu^-$ events are classified using the selections detailed below, whilst the remaining events in the $e^+e^-\to \ell^+\ell^-$ sample are therefore taken as being $e^+e^-\to \tau^+\tau^-$ events.

5.3.1 Classification of $e^+e^-\to e^+e^-$ events

Bhabha events are classified within the $e^+e^-\to \ell^+\ell^-$ sample by imposing cuts on the total energy in the calorimeter, $\sum E_{clus}$, and the total scalar momentum of all charged tracks, $\sum p_{trk}$. The cut used depends upon the average $|\cos\theta|$ of the cones in the event, where tracks and clusters in the cone are used to define its $|\cos\theta|$. In the endcap region the resolution for both tracks and clusters is poorer, and also bhabhas from the t-channel process are dominant in the more forward regions. Hence looser selection cuts are applied there.

In the **barrel** region ($\overline{|\cos\theta|} \leq 0.7$):

$$R_{clus} < 0.7 \quad \textbf{OR} \quad R_{clus} + 0.3R_{trk} < 1$$

In the **endcap** region ($\overline{|\cos\theta|} \geq 0.7$):

$$R_{clus} < 0.25 \quad \textbf{OR} \quad R_{clus} + R_{trk} < 1.05$$

where $R_{clus} = \sum E_{clus}/E_{CM}$ and $R_{trk} = \sum p_{trk}/E_{CM}$.

The effect of applying these cuts in the barrel and endcap regions is illustrated by the scatter plots in figures 5.3 and 5.4 respectively.

5.3.2 Classification of $e^+e^- \to \mu^+\mu^-$ events

The identification of muon pair events is more important to this analysis as muon pairs are one of main sources of background in the selection of $\tau \to \mu\overline{\nu}_\mu\nu_\tau$ candidates. To be considered as a possible $e^+e^- \to \mu^+\mu^-$ event each of the cones must pass a loose muon identification, using the ECAL, HCAL and muon chambers. Since there are regions where one or more of these subdetectors may be inactive, each side is required to pass only one of these cuts to be considered as a muon.

- The total electromagnetic cluster energy assigned to the cone, $E_{clus} < 2$GeV
- The following combination of HCAL requirements for the cone:
  ◦ Number of layers containing strip hits, $N_{lyr}^{HC} \geq 4$
  ◦ Number of layers (outermost 3) containing strip hits, $N_{lyr}^{HCo3} \geq 1$
  ◦ Average number of strip hits per layer, $N_{hits}^{HC}/N_{lyr}^{HC} < 2$
- At least 2 layers in the muon chamber contain a signal, $N_{lyr}^{MU} \geq 2$

Once both cones have been identified as muons a cut on R_{total} is used to separate $e^+e^- \to \mu^+\mu^-$ from $e^+e^- \to \tau^+\tau^-$ events, where R_{total} is defined as the scalar sum of the highest energy cluster and highest momentum track for each of the two cones divided by E_{CM}. Since $e^+e^- \to \tau^+\tau^-$ events with a loosely **identified** muon on either side will usually contain at least three, usually four, missing neutrinos, the total visible energy measured in the event will in general be somewhat less than E_{CM}.

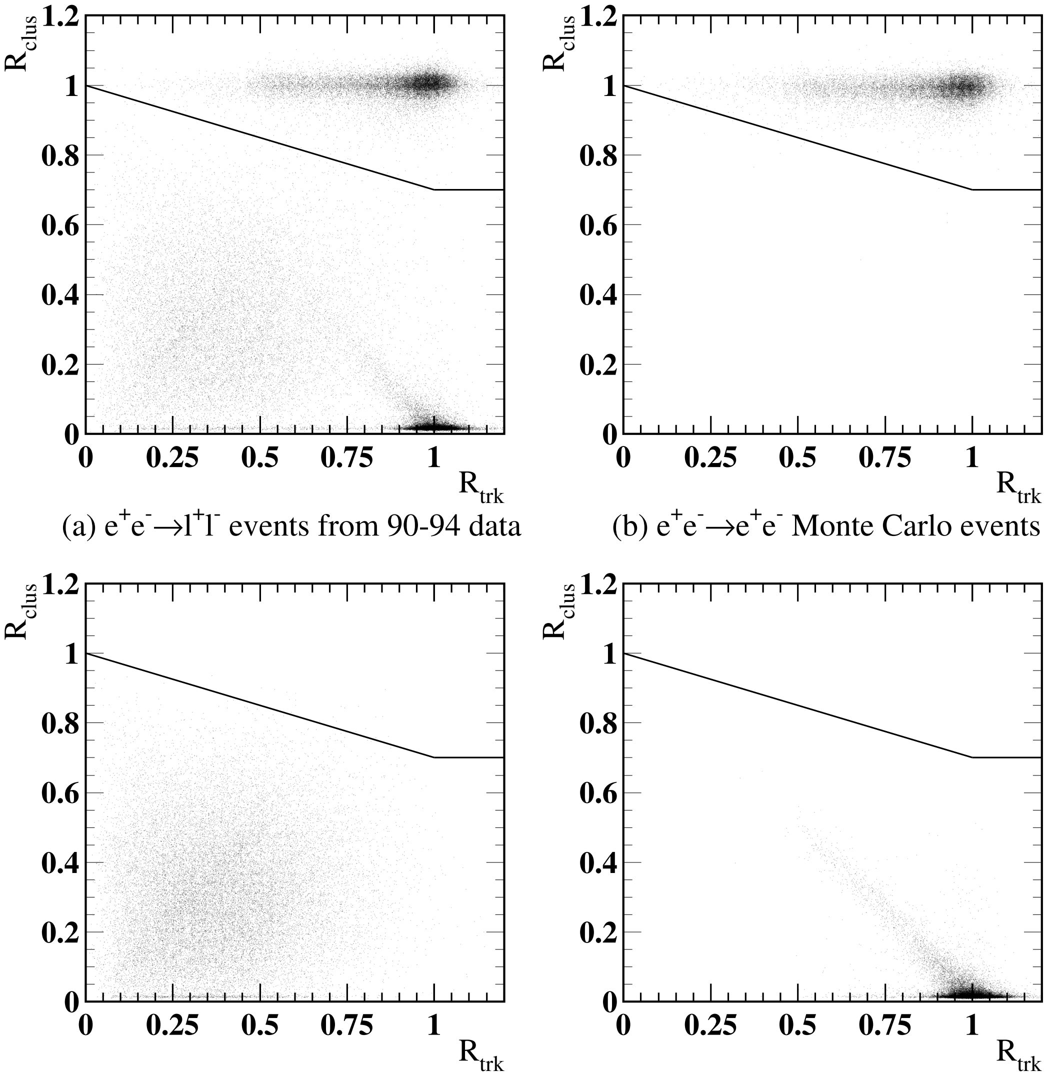

(a) $e^+e^- \to l^+l^-$ events from 90-94 data

(b) $e^+e^- \to e^+e^-$ Monte Carlo events

(c) $e^+e^- \to \tau^+\tau^-$ Monte Carlo events

(d) $e^+e^- \to \mu^+\mu^-$ Monte Carlo events

Figure 5.3: The classification of bhabha events in the barrel ($\overline{|\cos\theta|} \leq 0.7$) region.

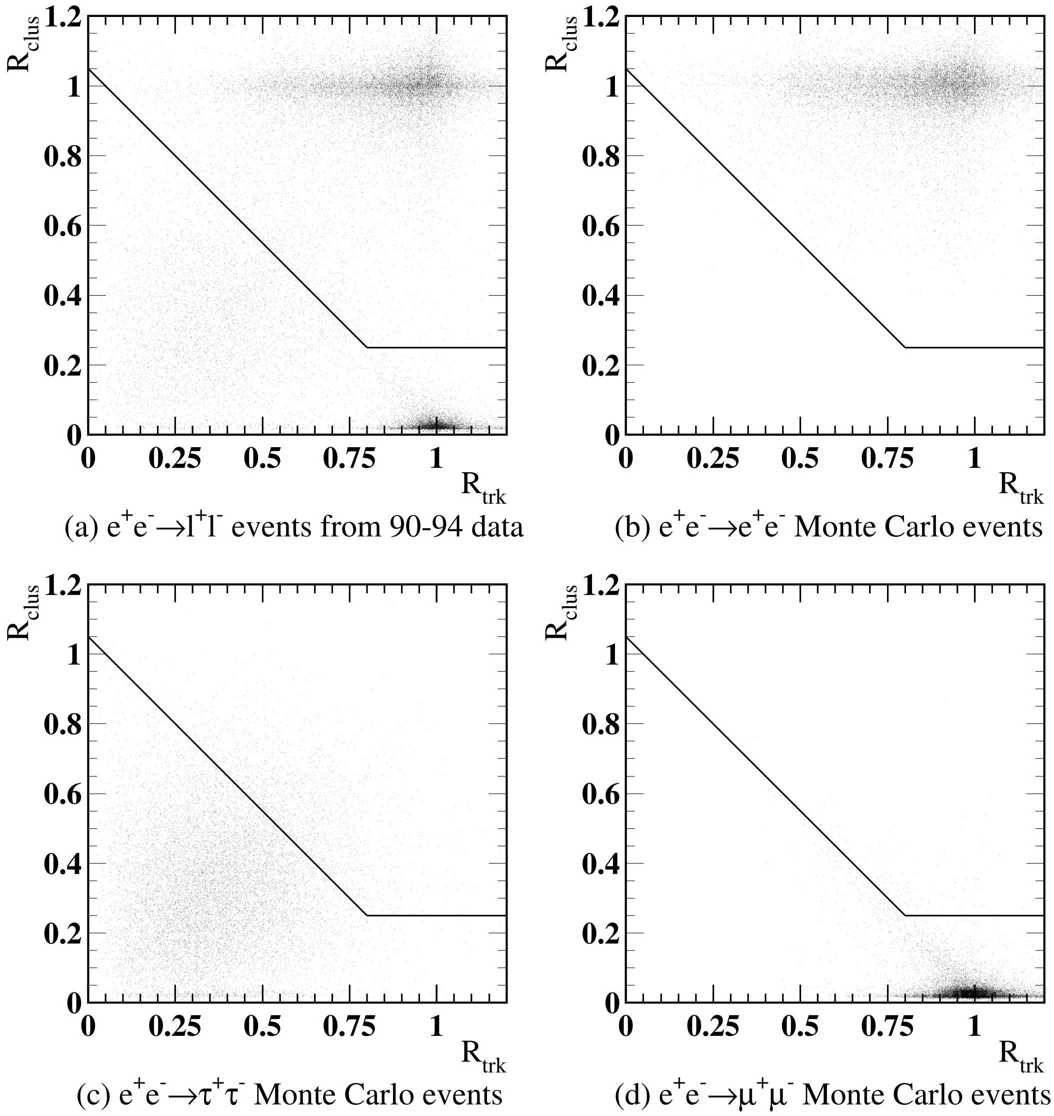

Figure 5.4: The classification of bhabha events in the endcap ($0.7 < \overline{|\cos\theta|} < 0.9$) region.

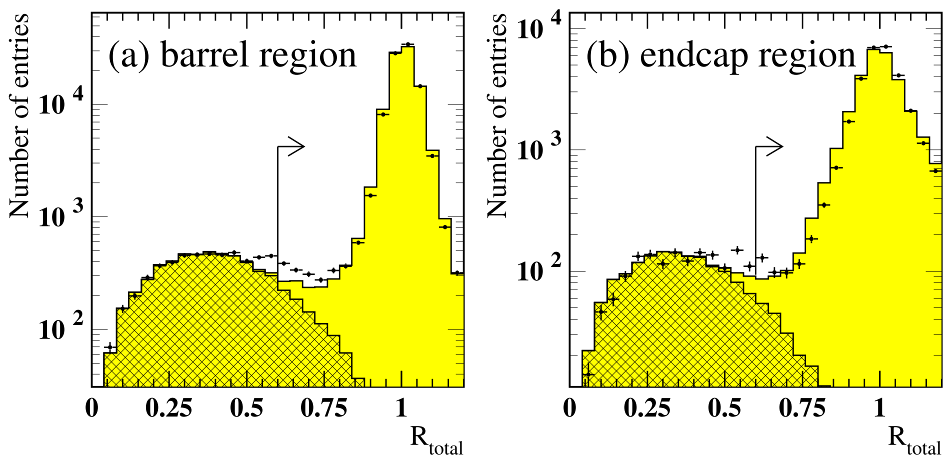

Figure 5.5: The classification of $e^+e^- \rightarrow \mu^+\mu^-$ events in (a) the barrel region ($\overline{|\cos\theta|} < 0.72$) and (b) the endcap region ($0.72 \geq \overline{|\cos\theta|} < 0.90$) where the points are data from 1990-94 runs and the solid regions are Monte Carlo. The hatched region shows the Monte Carlo background to $e^+e^- \rightarrow \mu^+\mu^-$ events from τ-pair and two-photon events.

Thus any events for which

$$R_{total} > 0.6$$

are classified as $e^+e^- \rightarrow \mu^+\mu^-$ events.

Figure 5.5 shows a sample of events which have passed the $e^+e^- \rightarrow \ell^+\ell^-$ selection and have been loosely identified as a muon on both sides. The Monte Carlo events were taken from an overall sample containing 400000 $e^+e^- \rightarrow \tau^+\tau^-$ and 400000 $e^+e^- \rightarrow \mu^+\mu^-$ events with two-photon backgrounds also included at the appropriate luminosity. The data sample uses all the data taken from 1990 to 1994, whilst the Monte Carlo sample is composed of events generated using the 1993 (50%) and 1994 (50%) configurations of the detector. The effect of the $e^+e^- \rightarrow \mu^+\mu^-$ classification on $e^+e^- \rightarrow \tau^+\tau^-$ events was studied further using the same sample of MC $\tau^+\tau^-$ events. The R_{total} distributions for various τ-decay combinations are shown in figure 5.6 before and after the loose muon identification has been applied to both sides. In addition, the efficiency with which both τ's in such events pass the muon identification is plotted as a function of R_{total} for each decay combination in figure 5.7.

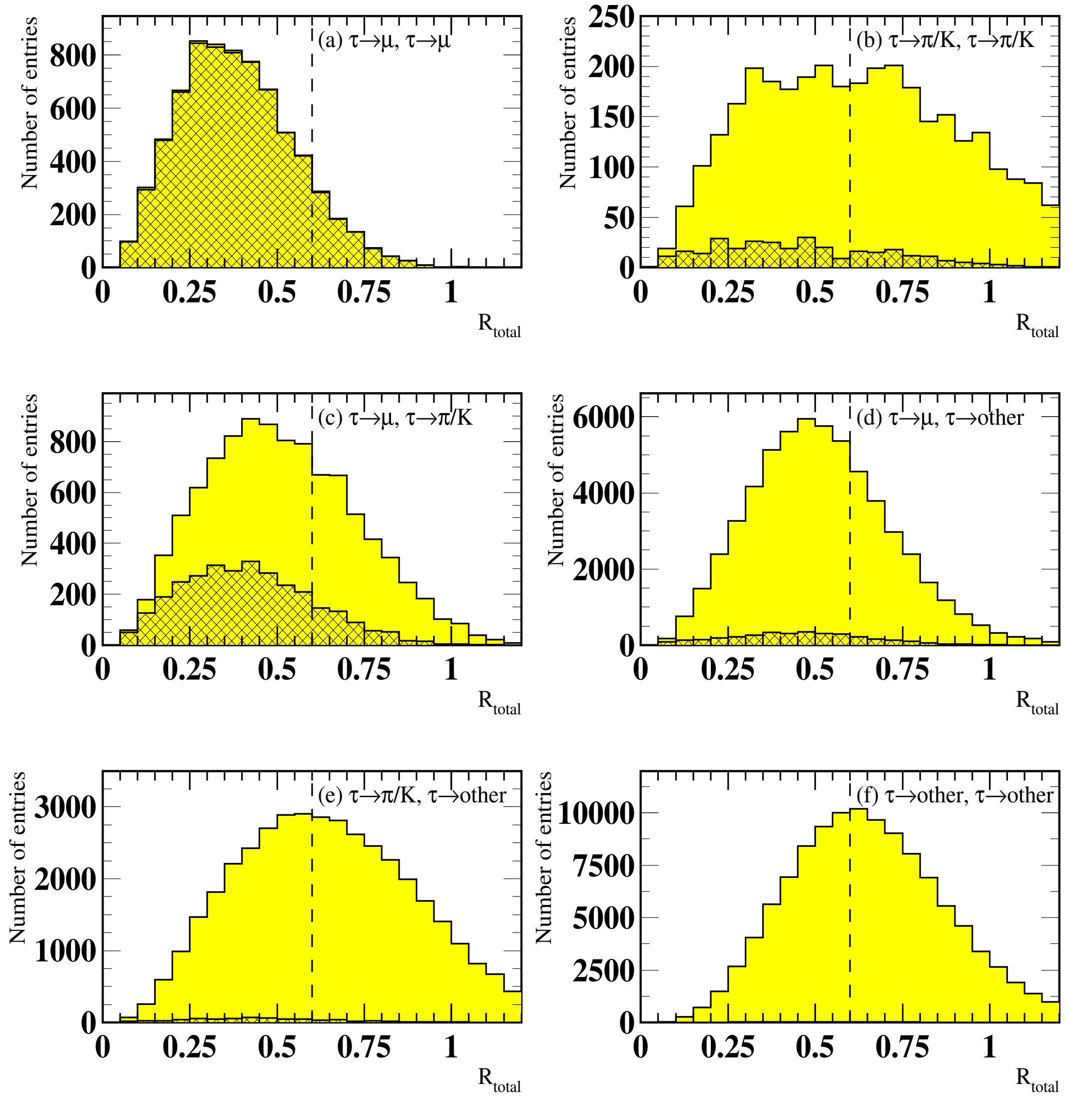

Figure 5.6: The distribution of R_{total} for $e^+e^- \to \tau^+\tau^-$events in the barrel region ($|\cos\theta| < 0.72$) after the $e^+e^- \to \ell^+\ell^-$selection. Only Monte Carlo events are used where the $e^+e^- \to \tau^+\tau^-$sample is subdivided into six possible decay combinations. The hatched regions show the events for which both sides have passed the loose muon identification.

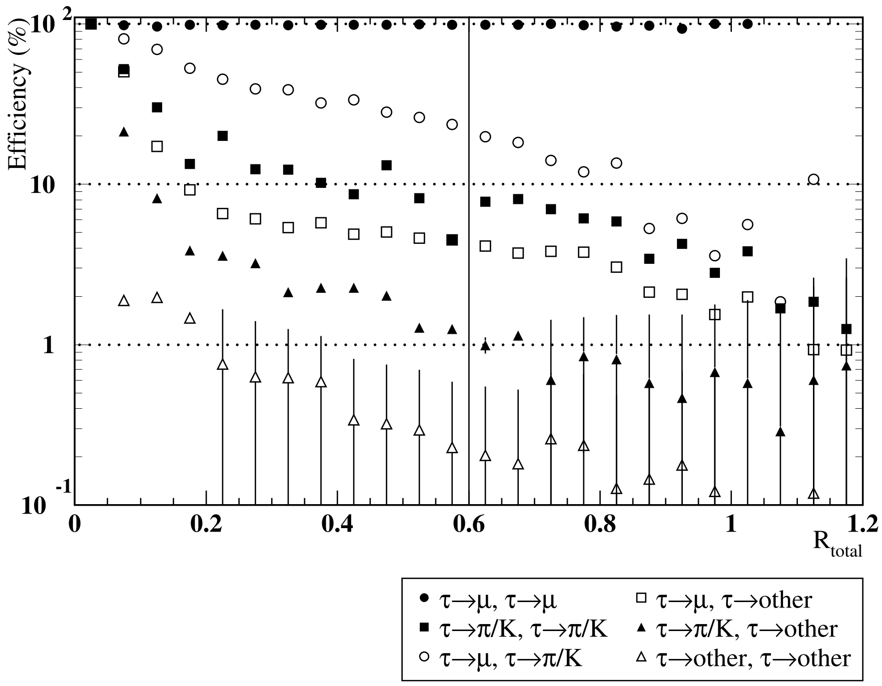

Figure 5.7: The efficiency of different decay combinations for passing the loose muon pair identification as a function of R_{total}. From a total sample of 400000 Monte Carlo τ-pairs only events for which $\overline{|\cos\theta|} < 0.90$ were used.

5.3.3 Rejection of mismeasured $e^+e^- \to \mu^+\mu^-$ events

It can be seen in figure 5.5 that, whilst the Monte Carlo predicts that there are very few $e^+e^- \to \mu^+\mu^-$ events for which $R_{total} < 0.6$, there is a clear excess of events in the data in the region just below the cut. This effect is more clearly demonstrated in figure 5.8. This shows events from the same data and Monte Carlo samples for which $R_{total} < 0.6$ and for which both cones in the event have passed the loose muon identification cuts and lie in the barrel region.

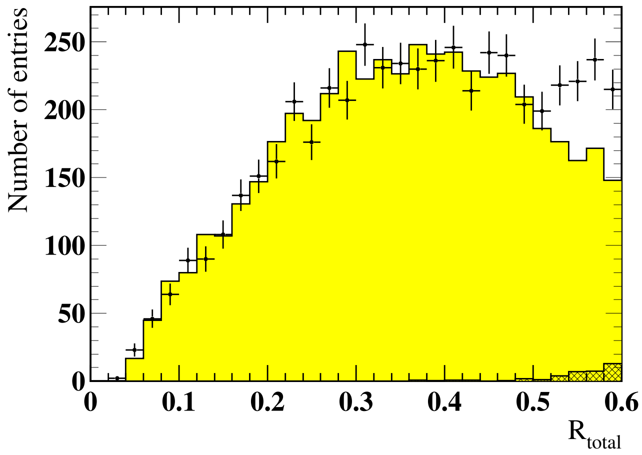

Figure 5.8: Events in the barrel region ($\overline{|\cos\theta|} < 0.72$) with both sides loosely identified as muons and for which $R_{total} < 0.6$. The points are data from 1990-94 runs and the solid regions are Monte Carlo. The hatched region shows the Monte Carlo background from $e^+e^- \to \mu^+\mu^-$ events.

This excess arises from an effect that is clearly not adequately modelled in the Monte Carlo simulation, namely the mismeasurement of momentum for straight tracks travelling close to an anode plane in CJ. If the trajectory of such a track lies either side of an anode plane then its curvature, κ, can be overestimated, causing its measured momentum to be much lower than the true value.[1] Such an effect thus leads to the presence of mismeasured $e^+e^- \to \mu^+\mu^-$ events for which $R_{total} < 0.6$, and the relative number of these observed in real data events is much higher than is the case for Monte Carlo events. Therefore a number of cuts have

[1] Also this can lead to *track splitting*, where there appears to be two tracks instead of one. An algorithm to identify and remove such ghost tracks from data and Monte Carlo events has been incorporated into this analysis.

been developed to ensure that most of these events have been removed from the $e^+e^- \rightarrow \tau^+\tau^-$sample used for this analysis (note that these events are not removed in the standard Tau Platform $e^+e^- \rightarrow \tau^+\tau^-$preselection [48]). To help in the removal of such events one relies on the fact that, despite any momentum mismeasurement, tracks from $e^+e^- \rightarrow \mu^+\mu^-$events will still be more collinear in ϕ compared to back-to-back muons from $e^+e^- \rightarrow \tau^+\tau^-$events. The effect is charge-dependent also since the direction in which the track curves determines whether the track bends away from a wire plane (thus keeping to one side of it) or passes through it (leading to a possible mismeasurement).

The coordinate system in OPAL is such that a **sector** in CJ is defined as a region in ϕ bounded by two adjacent cathode planes, and the variable ϕ_{CJ} that will be used here is defined as the measured value of ϕ of a track with respect to a sector in CJ. Hence, since like-charged wire planes are placed in CJ at every 15° in ϕ, ϕ_{CJ} will always have a value between 0° and 15° and a value of 7.5° corresponds to the position of an anode plane.

Generally for $e^+e^- \rightarrow \mu^+\mu^-$events in the range $0.4 < R_{total} < 0.6$, if one track has its momentum badly mismeasured it is the opposite track with higher momentum that it is measured to be travelling closer to an anode plane (usually for this track ϕ_{CJ} is observed to be not more than 0.5° away from the position of an anode plane). It also found that for rejecting these events any charge dependence is best introduced by making cuts based upon the charge of the highest momentum track in the event. Since the cuts used are symmetric about $\phi_{CJ} = 7.5$ for the different charges of the higher momentum track, the variable Φ_{CJ} is defined for both muon tracks to simplify the selection:

$$\Phi_{CJ} = 15 - \phi_{CJ} \quad (Q^{hi} = +1)$$

$$\Phi_{CJ} = \phi_{CJ} \quad (Q^{hi} = -1)$$

where Q denotes the measured electric charge and from now on the superscripts *hi* and *lo* will be used to denote the higher and lower momentum tracks in the event respectively.

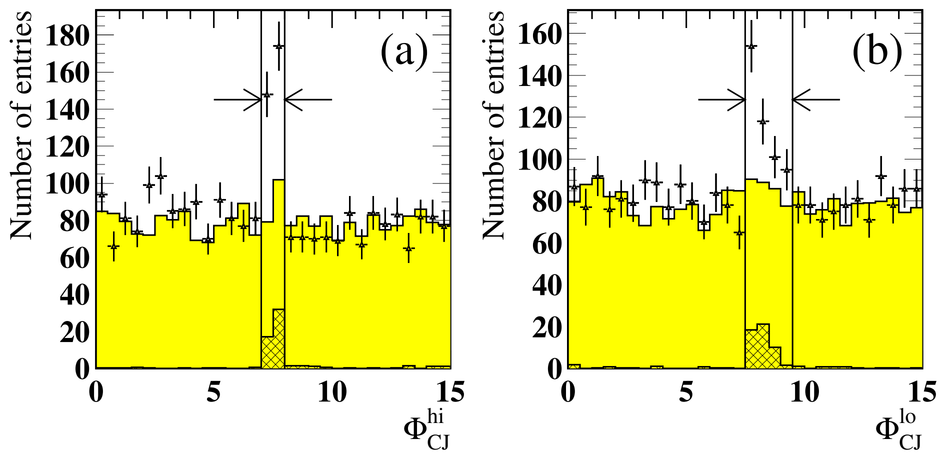

Figure 5.9: Events in the region $\overline{|\cos\theta|} < 0.90$ and in the range $0.4 < R_{total} < 0.6$, where both sides are loosely identified muons whose electric charges are measured to be of opposite sign. The distributions in CJ sectors (see text) are shown for the muon with (a) the highest and (b) the lowest momentum in the event. The points are data from 1990-94 runs and the solid regions are Monte Carlo. The hatched regions show the Monte Carlo background from $e^+e^- \to \mu^+\mu^-$ events.

Thus distributions of Φ^{hi}_{CJ} and Φ^{lo}_{CJ} were studied for events with two loosely identified muons for which $0.4 < R_{total} < 0.6$ and $\overline{|\cos\theta|} \leq 0.9$. These events were from the same lepton pair samples used to describe the standard $e^+e^- \to \mu^+\mu^-$ selection described above, where the total number of leptons observed in the region $\overline{|\cos\theta|} \leq 0.9$ after bhabha rejection was used to normalise the Monte Carlo to the data. Figure 5.9 shows the more usual case where $Q^{hi} = -Q^{lo}$ and the cuts used to reject the excess observed in the data. Figure 5.10 shows the case where $Q^{hi} = Q^{lo}$ and the cuts used, where here the excess in the data is even larger.

In summary events are rejected from the $e^+e^- \to \tau^+\tau^-$ sample if the event passes all of the following cuts:

- both sides are loosely identified as a muon (see above)
- the total visible energy lies in the range, $0.4 < R_{total} < 0.6$
- the ϕ of the higher momentum track is measured to be within 0.5° of an anode plane, ie. $7.0 < \Phi^{hi}_{CJ} < 8.0$

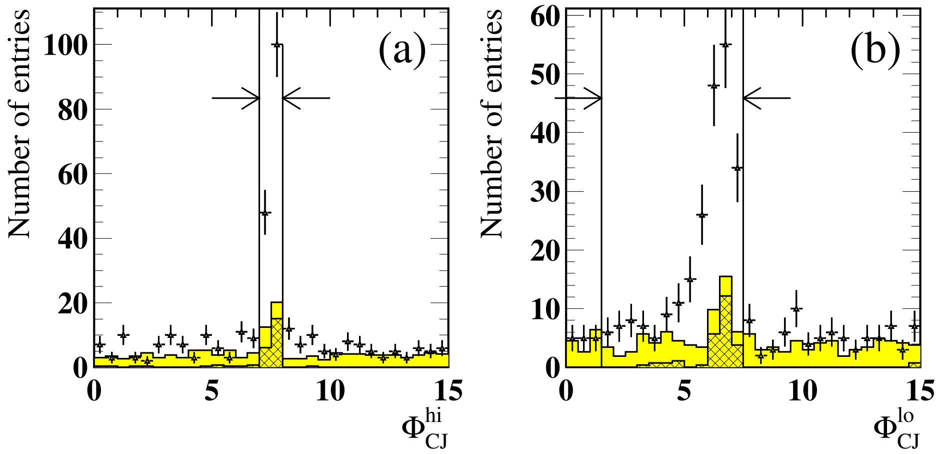

Figure 5.10: Events in the region $\overline{|\cos\theta|} < 0.90$ and in the range $0.4 < R_{total} < 0.6$, where both sides are loosely identified muons whose electric charges are measured to be equal. The distributions in CJ sectors (see text) are shown for the muon with (a) the highest and (b) the lowest momentum in the event. The points are data from 1990-94 runs and the solid regions are Monte Carlo. The hatched regions show the Monte Carlo background from $e^+e^- \rightarrow \mu^+\mu^-$ events.

- if $Q^{hi} = Q^{lo}$ then $1.5 < \Phi^{lo}_{CJ} < 7.5$, otherwise $7.5 < \Phi^{lo}_{CJ} < 9.5$

5.4 The $e^+e^- \rightarrow \tau^+\tau^-$ sample

Table 5.2 shows the number of Monte Carlo $e^+e^- \rightarrow \tau^+\tau^-$ events rejected at each stage of the preselection, and hence the Monte Carlo estimate of the preselection efficiency for $e^+e^- \rightarrow \tau^+\tau^-$ events. The preselection has been applied to all 900k on-peak $e^+e^- \rightarrow \tau^+\tau^-$ events generated using GOPAL/ROPE versions 12 and 14 [42, 43] have been used for this study. The track momenta of all particles in the event have been smeared but no weighting has been applied to the events to correct for the input values of the τ branching ratios used in the event generation.

In collecting together the Monte Carlo sample of $e^+e^- \rightarrow \tau^+\tau^-$ events which is then used for the polarisation analysis, the preselection is applied to all the Monte Carlo events listed in table 4.2. Table 5.3 shows the contribution made by each event type to the total Monte Carlo $e^+e^- \rightarrow \tau^+\tau^-$ sample. Events passing the prese-

	no $\tau \to \mu\overline{\nu}_\mu\nu_\tau$ decays			1 $\tau \to \mu\overline{\nu}_\mu\nu_\tau$ decay			2 $\tau \to \mu\overline{\nu}_\mu\nu_\tau$ decays		
	barrel	endcap	farfwd	barrel	endcap	farfwd	barrel	endcap	farfwd
TOTAL	388533	137217	87431	164128	58196	36979	17341	6180	3994
fail LowMS	2003	1393	13302	173	178	8149	6	14	865
fail $N_{cone} = 2$	7756	4471	29436	2667	1492	9565	191	109	1024
multihadron rej.	10123	6183	1399	755	462	84	0	0	0
2γ rejection	9591	3527	2146	4885	1915	991	1244	527	232
cosmic ray rej.	404	2339	1765	193	281	257	7	2	0
IDd $e^+e^- \to \ell^+\ell^-$	358656	119304	39383	155455	53868	17933	15893	5528	1873
IDd $e^+e^- \to e^+e^-$	2562	23862	7463	109	1673	1021	2	0	1
IDd $e^+e^- \to \mu^+\mu^-$	1072	100	103	2940	434	467	1747	646	428
anode plane rej.	12	0	4	79	7	5	93	19	3
IDd $e^+e^- \to \tau^+\tau^-$	355010	95342	31813	152327	51754	16440	14051	4863	1441
Efficiency(%)	91.37	69.48	36.39	92.81	88.93	44.46	81.03	78.69	36.08
$\pm$(%)	0.04	0.12	0.16	0.06	0.13	0.26	0.30	0.52	0.76

Table 5.2: Table showing the number of Monte Carlo $e^+e^- \to \tau^+\tau^-$ events rejected at each stage of the preselection, and the final numbers remaining in the sample out of the initial 900k events generated using the 1993 and 1994 detector configurations. Each event is put into one of nine possible categories depending on $\overline{|\cos\theta|}$ and on how many actual $\tau \to \mu\overline{\nu}_\mu\nu_\tau$ decays there are in each event. The Monte Carlo generator information is used to obtain the τ directions and hence define $\overline{|\cos\theta|}$. The barrel, endcap and far forward regions are defined as $\overline{|\cos\theta|} < 0.72$, $0.72 \geq \overline{|\cos\theta|} < 0.9$ and $0.9 \geq \overline{|\cos\theta|} < 1.0$ respectively. The errors shown for the final preselection efficiencies are the statistical (binomial) errors.

lection have been subdivided into those identified in the barrel ($\overline{|\cos\theta|} < 0.72$) and endcap ($0.72 \leq \overline{|\cos\theta|} < 0.9$) regions, where these are defined using the average $|\cos\theta|$ for the two cones in the event. The non-τ events that are included are weighted so that the total integrated luminosity for a particular type of event is the same as that for $e^+e^- \to \tau^+\tau^-$events generated using the same GORO (GOPAL/ROPE) version. If a certain type of event for a particular GORO version does not exist, then events generated using the other GORO version are used for the background estimate. This method of normalisation is used throughout this analysis, except where explicitly mentioned. In evaluating the numbers shown in table 5.3 the relative branching fractions of the different decay modes have been corrected to agree with the current world averages [5]. This is done by weighting each event, where this event weight is taken to be the average of the individual weights for the two τ decays in the event.

The numbers given in table 5.3 provide an estimate of the background content for $e^+e^- \to \tau^+\tau^-$samples identified from real OPAL data collected at the Z^0 resonance. Studies may be performed to test these Monte Carlo background estimates using control samples. This is necessary in the case of a branching ratio measurement but for this analysis it is sufficient to only perform such tests on the final sample of $\tau \to \mu\overline{\nu}_\mu\nu_\tau$ decays used to extract $\langle P_\tau \rangle$ and A^{FB}_{pol}. The selection of such decays and the subsequent tests that are performed to test the validity of the Monte Carlo background estimates for such a sample are discussed in the following two chapters.

Whilst all the Monte Carlo events used for this analysis are generated with centre-of-mass energies very close to the Z^0 resonance (typically, $\sqrt{s}$=91.21 GeV), the real LEP1 data-set includes events collected either side of the resonance. The beam optics of the LEP machine are such that $\sqrt{s}$ can be displaced either side of the Z^0 peak in units of $\sim$0.88 GeV. Off-peak data has been collected during LEP1 running at ± 1, ± 2 and ± 3 units with respect to the peak energy value, where, averaging over the years 1990-1994, the average centre-of-mass energy during on-

Event type	Content (%) in barrel region	Content (%) in endcap region
$Z^0 \rightarrow f\bar{f}$ events:		
ee$\rightarrow\tau\tau$	98.20$\pm$0.14	94.30$\pm$0.24
ee$\rightarrow\mu\mu$	0.674$\pm$0.011	4.087$\pm$0.051
ee$\rightarrow$ee	0.1155$\pm$0.0047	0.367$\pm$0.015
ee$\rightarrow$q$\bar{\text{q}}$	0.794$\pm$0.012	0.500$\pm$0.017
2-photon events:		
ee$\rightarrow$ee$\tau\tau$	0.0438$\pm$0.0029	0.0846$\pm$0.0073
ee$\rightarrow$ee$\mu\mu$	0.0595$\pm$0.0033	0.292$\pm$0.013
ee$\rightarrow$eeee	0.0103$\pm$0.0044	0.360$\pm$0.015
4-fermion events:		
ee$\rightarrow$ee$\tau\tau$	0.0120$\pm$0.0015	0.0091$\pm$0.0024
ee$\rightarrow$ee$\mu\mu$	0.00212$\pm$0.00063	0.0016$\pm$0.0010

Table 5.3: The content of different Monte Carlo event types within the sample of identified $e^+e^-\rightarrow\tau^+\tau^-$events used for this analysis.

peak running is,

$$\sqrt{s} = 91.205 \pm 0.071\,\text{GeV} \tag{5.1}$$

The numbers of $e^+e^-\rightarrow\tau^+\tau^-$events identified at each energy and for each year are shown in table 5.4. Only the on-peak events ($\sim$91% of the total data set) are used for this analysis due to the energy-dependence of the background from 2-photon events, as well as the implications that different values of $\sqrt{s}$ have upon $\langle P_\tau \rangle$ and A^{FB}_{pol}.

Data year	Number of $e^+e^- \to \tau^+\tau^-$ events at each $\sqrt{s}$							Total
	-3	-2	-1	on-peak	+1	+2	+3	
1990	111	241	321	4509	485	339	207	6203
1991	229	360	666	11701	851	509	422	14738
1992	0	0	0	32265	0	0	0	32265
1993	0	4312	0	20895	0	5582	0	30789
1994	0	0	0	71794	0	0	0	71794
Total	340	4913	987	141164	1336	6430	629	155789

Table 5.4: The number of $e^+e^- \to \tau^+\tau^-$ events identified during each data-taking year between 1990 and 1994 at the different centre-of-mass energies, where these are expressed for off-peak data in units of $\sim$880 GeV with respect to the on-peak energy setting.

Chapter 6

Selection of $\tau \rightarrow \mu \overline{\nu}_\mu \nu_\tau$ decays

This chapter details the selection of $\tau \rightarrow \mu \overline{\nu}_\mu \nu_\tau$ decays from the sample of τ pairs described in the previous chapter. Separate selections are applied to obtain $\tau \rightarrow \mu \overline{\nu}_\mu \nu_\tau$ samples in both the barrel ($|\cos\theta| < 0.72$) and endcap regions ($0.72 < |\cos\theta| < 0.90$) of the OPAL detector. Both selections rely primarily on the muon chambers since the Monte Carlo modelling of the hadron calorimeters is less well-understood. This is possible through the use of a variable that matches the trajectory of tracks in the tracking chamber with hits in the muon chambers. Previous analyses using $\tau \rightarrow \mu \overline{\nu}_\mu \nu_\tau$ decays at OPAL [25, 26, 27] have not used information of this kind and so involved selection procedures which were more heavily reliant upon the use of the HCAL. However, the selections used for this analysis have clear advantages which will be made apparent as the chapter progesses. In addition the selections developed in both regions of the detector are applied twice, with and without an invariant mass cut used in conjunction with the muon chamber identification. The reasons for this will also be explained later.

Throughout the chapter various figures will illustrate the effect of the cuts used, where in each case the 1990-94 on-peak data is represented by the points and the simulated Monte Carlo data by shaded histograms. The Monte Carlo data used includes every on-peak run generated using the 1993 and 1994 configurations of the detector, where, for illustrative purposes only, the Monte Carlo has been normalised to the data using the final numbers remaining in each $\tau\to\mu\overline{\nu}_\mu\nu_\tau$ sample. The backgrounds are shown by the hatched regions where the type of background (τ and/or non-τ) being highlighted varies from figure to figure.

6.1 Selection of $\tau\to\mu\overline{\nu}_\mu\nu_\tau$ decays in the barrel region

The selection of $\tau\to\mu\overline{\nu}_\mu\nu_\tau$ decays in the barrel region is based around the identification of muons using the muon chambers. This is mainly because the response of the hadronic calorimeters to minimum ionizing particles is less well understood in the Monte Carlo simulation than that for the muon chambers. However, further motivations for making the selection of $\tau\to\mu\overline{\nu}_\mu\nu_\tau$ decays more reliant upon the muon chambers will be discussed in greater depth after the selections have been defined.

The Monte Carlo events used to test the selection were generated using GOPAL/ROPE(GORO) versions 12 and 14, which are the detector simulations which correspond to the configuration of OPAL in 1993 and 1994 respectively. The latter of these versions (which has not been used in previous OPAL τ polarsation measurements) is seen to model the response of the HCAL to muon tracks much better. However, the modelling for both GORO versions is observed to be worse when tested using control samples of **hadronic** τ-decays. To reduce the uncertainty in the background from such decays in the $\tau\to\mu\overline{\nu}_\mu\nu_\tau$ sample, the selection outlined here uses the HCAL (and ECAL) to detect muons only when the candidate $\mu^\pm$ track points to a region outside the acceptance of the muon chambers. This also allows for a selection efficiency that is roughly flat across the chosen $|\cos\theta|$ range, and allows us to use the HCAL to cross-check certain aspects of the muon chamber selection **within** the geometrical acceptance of MB/ME. For this analysis, a study of the acceptance of MB using a test sample of $\tau\to\mu\overline{\nu}_\mu\nu_\tau$ decays was performed and is detailed in appendix D.

- Only decays for which $|\cos\theta| < 0.72$ are considered for a sample in the barrel region, where $|\cos\theta|$ is defined using the track only. This means that the sample is identified in a region which is almost completely covered by the acceptance of the z-chambers (CZ) and with most tracks travelling the full radius of CJ in the xy-plane tracks (ie. momentum is measured by all 159 sense wires in the adjacent anode and cathode wire planes). One therefore expects the momentum resolution in this sample to be nearly constant with $|\cos\theta|$, except for those few which escape past the ends of CZ or which pass through one of the regions where it is inactive.

- The variable used to determine the energy spectrum for $\tau\to\ \mu\overline{\nu}_{\mu}\nu_{\tau}$ decays (and hence extract $\langle P_{\tau}\rangle$) is merely the track momentum normalised to the value of the beam energy,

$$x_{\mu} \equiv x_{trk} = \frac{p_{trk}}{E_{beam}}$$

At low energies the efficiency for muons reaching the outer detectors becomes lower due to the large amount of material in OPAL that they must pass through, and this drop in efficiency cannot be reliably predicted. The true energy of muons from $\tau\to\ \mu\overline{\nu}_{\mu}\nu_{\tau}$ decays is physically contrained to be no greater than E_{beam}, but a limit to the observed energy is employed here which allows for the effects of momentum resolution. Therefore, only candidates within the following kinematic range are considered:

$$0.05 < x_{\mu} < 1.20$$

- The $\tau\to\ \mu\overline{\nu}_{\mu}\nu_{\tau}$ decay contains only one charged track, although for radiative muons the conversion of photons into e^+e^-pairs can occur, and more frequently so in the data. This fact is borne out in figure 6.1 although one can see that this discrepancy amounts to only a very small fraction of the total sample. Split tracks can occur at wire planes (see section 5.3.3) but an algorithm has been used to efficiently detect and remove the second ghost track. Therefore the number of good tracks assigned to a cone, N_{trk}, must satisfy:

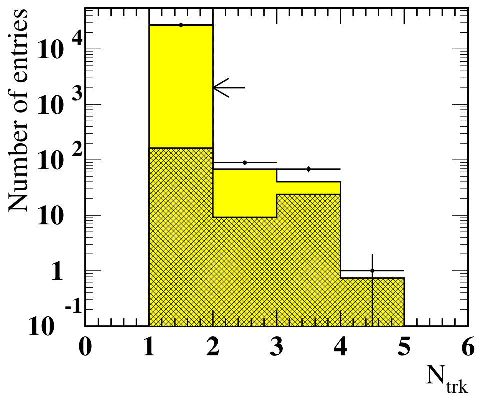

Figure 6.1: Distribution of N_{trk} for $\tau \rightarrow \mu\overline{\nu}_\mu\nu_\tau$ candidates in the barrel region where all are other selection cuts have been applied. The hatched area illustrates the background from other τ decays only.

$$N_{trk} = 1$$

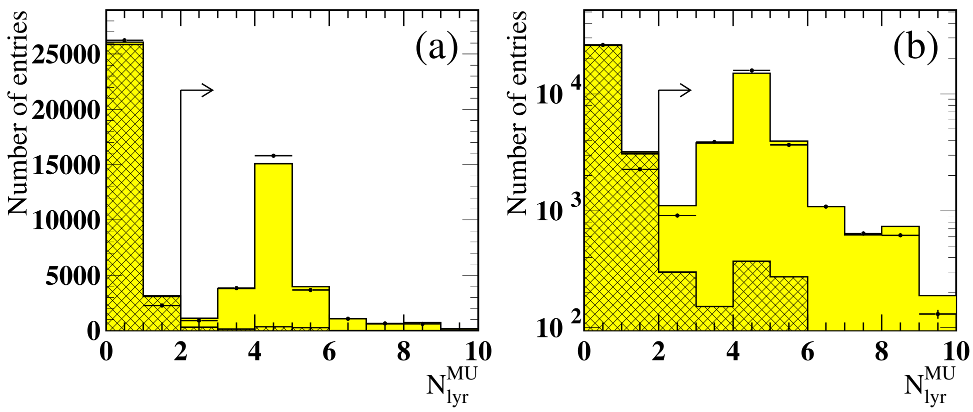

Figure 6.2: Distribution of N_{lyr}^{MU} for $\tau \rightarrow \mu\overline{\nu}_\mu\nu_\tau$ candidates in the barrel region and within the geometrical acceptance of MB or ME, where all are other selection cuts have been applied (except the χ_{match} variable). The plot is shown with both (a) linear and (b) logarithmic scales on the y-axis. The hatched area illustrates the background from other τ decays only.

- For a $\tau \rightarrow \mu\overline{\nu}_\mu\nu_\tau$ candidate to pass the muon chamber identification, **MCHID**, it has to pass two cuts. The first is a requirement on N_{lyr}^{MU}, the number of muon layers containing hits loosely associated to the track. The second cut is made on a matching variable called χ_{match}, where χ_{match} is a measure of the probability that the average position of hits in the muon chambers is matched to that of the track when its path is extrapolated out to MB or ME. χ_{match} is calculated within OPAL's software package ID [49] and is used here to suppress the background from hadronic τ decays. If a charged particle from a $\tau \rightarrow \pi(\mathrm{K})\nu_\tau$ decay manages to reach the muon chambers then it is either through late hadronic showering not being fully contained by the calorimeters (the **punchthrough** effect) or by the production of a muon. The latter can occur within the hadronic showering or simply by the decay process $\pi(\mathrm{K}) \rightarrow \mu\overline{\nu}_\mu$. Given the nature in which a charged particle from a hadronic decay can penetrate the muon chambers, the match between the track and muon chamber hits is generally poor and this results in a large value of χ_{match}.

Thus the muon chamber identification, **MCHID**, requires that:

$$N_{lyr}^{MU} \geq 2 \quad \text{(see figure 6.2)}$$

$$\chi_{match} < 5 \quad \text{(see figure 6.3)}$$

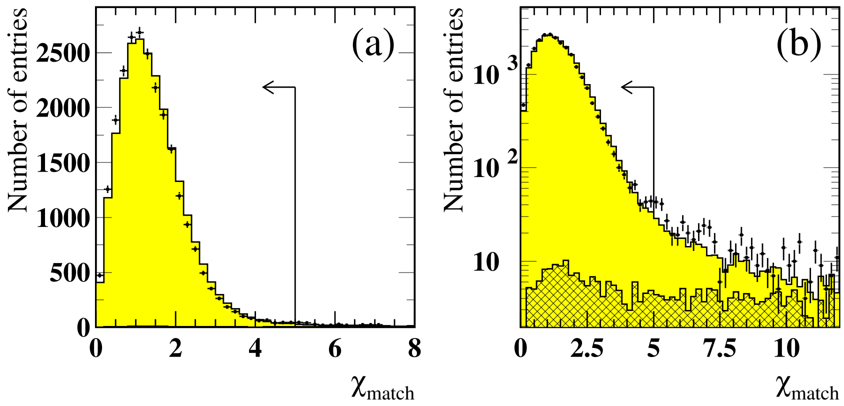

Figure 6.3: Distribution of χ_{match} for $\tau \rightarrow \mu\overline{\nu}_\mu\nu_\tau$ candidates in the barrel region and within the geometrical acceptance of MB or ME, where all are other selection cuts have been applied. The plot is shown with both (a) linear and (b) logarithmic scales on the y-axis. The hatched area illustrates the background from other τ decays only, where most of these have a very high χ_{match} value and so are not shown.

- If a candidate in the barrel region fails MCHID but passes all the other cuts and points to a region outside the geometrical acceptance of both MB and

ME, then it may be accepted if it passes the certain requirements in the ECAL and HCAL (see figure 6.4). These requirements are listed below and collectively will be referred to as the calorimeter identification, **CALID**, where any $\tau\rightarrow \mu\overline{\nu}_\mu\nu_\tau$ candidate in the barrel must therefore pass either MCHID or CALID to be selected. Note that cut (c) provides the greatest discrimination against hadronic decays of the four used. Figure 6.4(c) would indicate that a looser requirement might be used here. However, it must be remembered that the plots are made using samples with no requirements on the muon chambers. Those $\tau\rightarrow \mu\overline{\nu}_\mu\nu_\tau$ candidates which are allowed to enter the final sample using the below requirements must first have **failed** the muon chamber cuts and so a tight set of cuts is used to suppress the hadronic background.

The calorimeter identification, **CALID**, requires that:

(a) the number of HCAL layers containing strip hits,

$$N_{lyr}^{HC} \geq 4$$

(b) the number of HCAL layers from the outermost 3 containing strip hits,

$$N_{lyr}^{HCo3} \geq 1$$

(c) the average number of strip hits per layer in the HCAL,

$$\frac{N_{hits}^{HC}}{N_{lyr}^{HC}} < 2$$

(d) the total ECAL cluster energy assigned to the cone,

$$E_{clus} < 2\,\mathrm{GeV}$$

(e) the candidate fails MCHID and points outside the full acceptance of MB and ME.

- The $\tau\rightarrow \mu\overline{\nu}_\mu\nu_\tau$ selection uses a cut on M_{inv}, the total invariant mass of the cone containing the candidate muon. M_{inv} is calculated by combining the

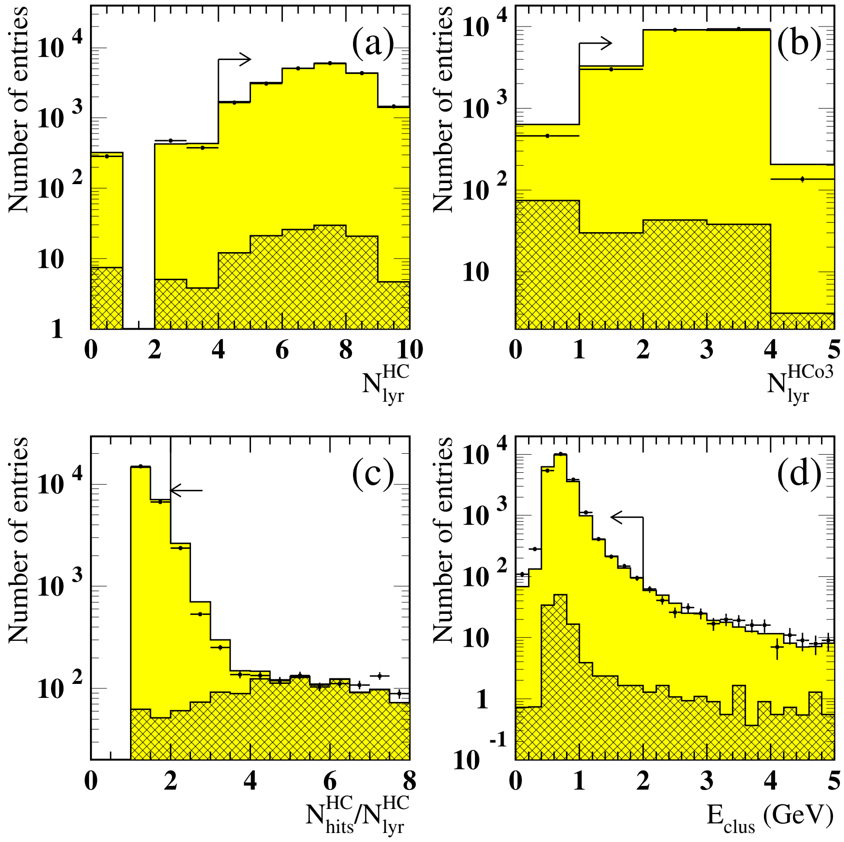

Figure 6.4: Distributions of (a)N_{lyr}^{HC}, (b)N_{lyr}^{HCo3}, (c)$N_{hits}^{HC}/N_{lyr}^{HC}$ and (d)E_{clus}, for an HCAL/ECAL selection in the barrel region. The samples used for the plots were made using the cuts shown as well as those involving N_{trk}, x_{μ} and M_{inv}. The hatched area illustrates the background from other τ decays only.

4-momenta of all tracks (assuming $\pi^{\pm}$ masses) with the 4-momenta of all clusters in the cone (where those clusters to which a track is assigned are corrected for the average energy deposition of a minimum ionizing particle). The cut is used to suppress the background from $\tau \to \rho \nu_\tau$ and 1-prong $\tau \to \mathrm{a}_1 \nu_\tau$ decays, where the $\rho^{\pm}$ and $\mathrm{a}_1^{\pm}$ particles decay by the processes $\rho^{\pm} \to \pi^{\pm}\pi^{0}$ and $\mathrm{a}_1^{\pm} \to \pi^{\pm}\pi^{0}\pi^{0}$ respectively. The π^0s formed during the decays then themselves decay rapidly by the process $\pi^0 \to \gamma\gamma$. Therefore both of these decays are seen in the detector as a single charged pion with a number of photons. If well-measured (and the ECAL is able to resolve the clusters from each of the photons), M_{inv} should reproduce the mass of the original resonance (M_ρ or M_{a_1}). The plots in figure 6.5 clearly show the rise in the invariant mass spectrum due the background from such decays. The cut used for this analysis is:

$$M_{inv} < 0.3\,\mathrm{GeV}/c^2$$

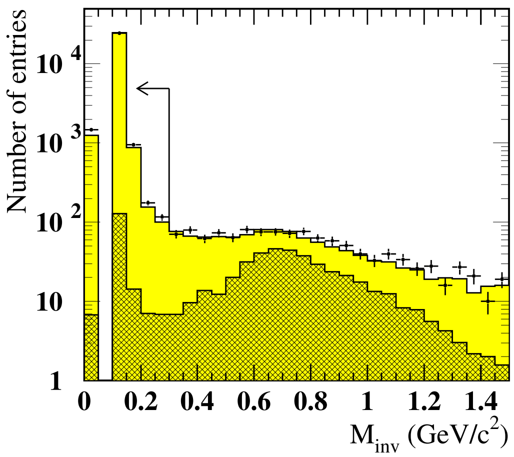

Figure 6.5: Distribution of M_{inv} for $\tau \to \mu\overline{\nu}_\mu\nu_\tau$ candidates in the barrel region after all other selection cuts have been applied. The hatched area illustrates the background from other τ decays only.

- Nearly all of the muons from $\mathrm{e^+e^-} \to \mu^+\mu^-$ events that still remain in the $\tau \to \mu\overline{\nu}_\mu\nu_\tau$ sample are there because one or other of the muons fails to pass the loose muon identification applied to both sides during the preselection

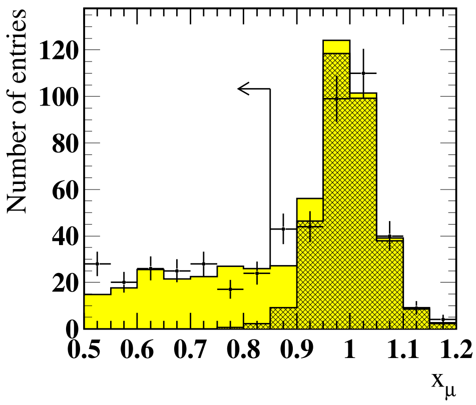

Figure 6.6: Distribution of x_μ for $\tau \to \mu\overline{\nu}_\mu\nu_\tau$ candidates in the barrel region after all other selection cuts have been applied apart from the muon pair rejection. The candidates shown are those from events with $R_{total} > 0.9$ and for which the highest energy track in the opposite cone satisfies at least one of the following 3 conditions: **EITHER** it lies outside the full geometrical acceptance of the HCAL **OR** lies outside the geometrical acceptance of the muon chambers **OR** has associated muon chamber hits in only one layer, N_{lyr}^{MU}(opp)= 1. The hatched area illustrates the background from $e^+e^- \to \mu^+\mu^-$ events only.

(see section 5.3.2). Under this loose detection scheme a particle is identified as a muon if it is consistent with being such in either the ECAL, HCAL or muon chambers. Clearly the candidate muon for the $\tau \to \mu\overline{\nu}_\mu\nu_\tau$ sample cannot have failed the loose muon identification, so it remains to look at the opposite cone in the event, which must have failed the requirements in each of the three subdetectors. The opposite muon track in possible $e^+e^- \to \mu^+\mu^-$ background events is likely to lie outside the full geometrical acceptance of the HCAL for it to fail the HCAL requirements in the $e^+e^- \to \mu^+\mu^-$ preselection. Similarly for the muon chambers, although it's possible also that it can leave hits in the muon chambers but only in one layer. Also the $e^+e^- \to \mu^+\mu^-$ background will be characterised by events with high total visible energy, with both sides having a measured track momentum close to E_{beam}. Therefore any $\tau \to \mu\overline{\nu}_\mu\nu_\tau$ candidate which passes all of the following cuts is **rejected** (see figure 6.6):

(a) the total visible energy in the event,

$$R_{total} > 0.9$$

(b) the momentum of the candidate $\tau \to \mu\overline{\nu}_\mu\nu_\tau$ track (normalised to E_{beam}),

$$x_\mu > 0.85$$

(c) the highest energy track in the opposite cone is **EITHER** outside the full geometrical acceptance of the HCAL **OR** outside the geometrical acceptance of the muon chambers **OR** has muon chamber hits in only one layer, N_{lyr}^{MU}(opp)= 1.

Whilst the cut used on the invariant mass, M_{inv}, is very effective in reducing the background from certain τ decay channels, it also slightly biases the momentum spectrum of the $\tau \to \mu\overline{\nu}_\mu\nu_\tau$ candidates left in the sample since higher momentum muons pass the cut with greater efficiency. Therefore, if the Monte Carlo data does not model this bias correctly, it will lead to systematic shifts in the final values of $\langle P_\tau \rangle$ and A_{pol}^{FB} obtained. The Monte Carlo modelling of the cut relies on good simulation for the response of the ECAL and the track parameters in the central detector. However, the fact that the M_{inv} uses information from the ECAL also means that it is more difficult to find suitable control samples with which to test the selection. Therefore, **the analysis is repeated with the invariant mass cut switched off if the candidate is identified by MCHID**, since it is then also possible to use the ECAL and HCAL to select a control sample of $\tau \to \mu\overline{\nu}_\mu\nu_\tau$ decays with which to test MCHID. Note that it is not necessary to drop the M_{inv} cut from the selection involving CALID, since CALID itself uses cuts in the ECAL. The two barrel selections will be referred to as B1 and B2, where both are summarised in table 6.1 to clarify the difference between them.

The main reason behind keeping the two separate barrel selections B1 and B2, is that, at this stage, the size of the systematic errors on $\langle P_\tau \rangle$ and A_{pol}^{FB} that arise from uncertainties in selection efficiency and background are unknown. Selection B1 is expected to have a larger selection efficiency error but its τ background

Selection B1	Selection B2
$\|\cos\theta\| < 0.72$	
$0.05 < x_\mu < 1.20$	
$N_{trk} = 1$	
(MCHID or CALID) & $M_{inv} < 0.3\,\mathrm{GeV}/c^2$	MCHID or (CALID & $M_{inv} < 0.3\,\mathrm{GeV}/c^2$)
μ-pair rejection	

Table 6.1: Summary of the two selections used to obtain samples of $\tau \rightarrow \mu\overline{\nu}_\mu\nu_\tau$ decays in the barrel region.

will be much smaller, and so the error associated with knowing the extent of this background will be smaller than that for B2. Essentially the decision whether or not to combine the M_{inv} cut with MCHID comes down to a play-off between two potentially large sources of systematic error. This decision is avoided by merely retaining both selections.

The selection efficiency and backgrounds for selections B1 and B2 have been estimated by applying them to all Monte Carlo events which have passed the $e^+e^- \rightarrow \tau^+\tau^-$preselection. The non-$\tau$ background events in the $e^+e^- \rightarrow \tau^+\tau^-$sample are weighted to the same integrated luminosity as the generated $e^+e^- \rightarrow \tau^+\tau^-$events, whilst the generated $e^+e^- \rightarrow \tau^+\tau^-$events themselves are weighted to account for the latest world average values [5] of the τ branching ratios as described in chapter 4. The Monte Carlo estimates of the various τ and non-τ backgrounds are shown in table 6.2, where the total numbers of $\tau \rightarrow \mu\overline{\nu}_\mu\nu_\tau$ candidates found in the Monte Carlo and real data sets are also included. The numbers identified using selections B1 and B2 are subdivided into those identified using MCHID or CALID, where the MCHID and CALID identifications are mutually exclusive. The momentum distributions for all data and MC events selected using the two selections are also displayed (including the major backgrounds) in figure 6.7.

The number of $\tau \rightarrow \mu\overline{\nu}_\mu\nu_\tau$ decays within the sample, before and after the $\tau \rightarrow \mu\overline{\nu}_\mu\nu_\tau$ selection has been applied, is used to estimate the selection efficiency as a function of x_μ (see figure 6.8). These plots show that the overall efficiency is

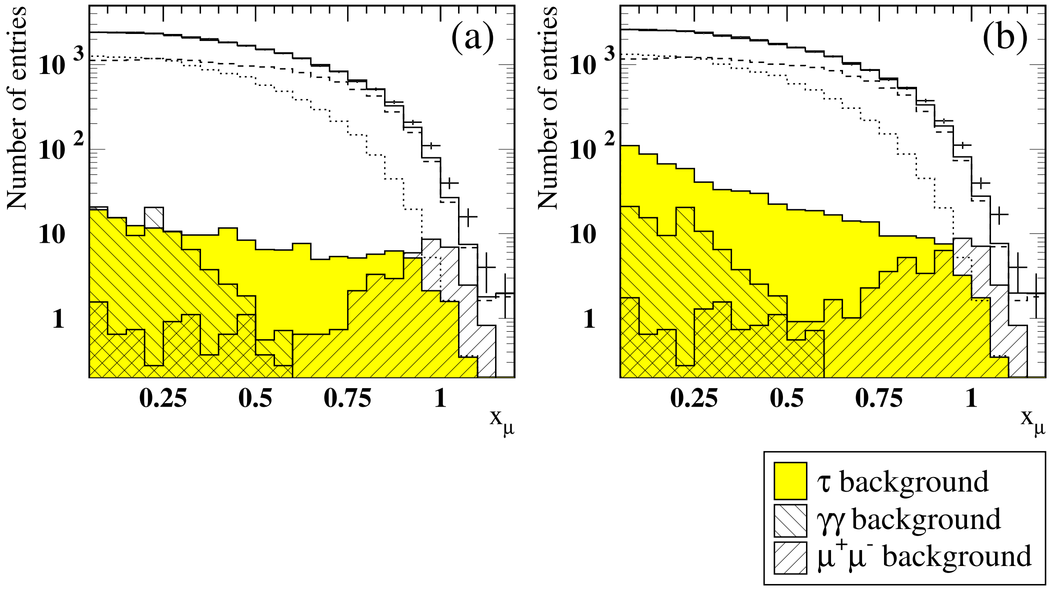

Figure 6.7: Distributions of x_μ for all $\tau \rightarrow \mu\overline{\nu}_\mu\nu_\tau$ candidates selected using (a) selection B1 and (b) selection B2. All Monte Carlo events (histograms) are weighted to give the same total number as that seen in the data (points). The backgrounds from other τ decays are shown, along with the major non-τ backgrounds from $e^+e^- \rightarrow \mu^+\mu^-$ and $\gamma\gamma \rightarrow \ell^+\ell^-$ events. The contributions from the negative and positive helicity MC $\tau \rightarrow \mu\overline{\nu}_\mu\nu_\tau$ decays are also included, and are represented by the dashed and dotted lines respectively.

slightly better for the 94 MC version. This is a result of differences in the muon chamber calibrations used by two versions of GOPAL/ROPE (12 and 14), which cause the muons in the 94 MC to pass the MCHID cut on N_{lyr}^{MU} more efficiently. This might be potentially worrisome but for the fact that this cut has very little momentum-dependence, and so the difference in efficiency for the two MC versions appears to be constant across the entire momentum range.

The Monte Carlo estimates of efficiency and background quoted at this stage are before the corrections made using control sample studies. These are discussed in the following two chapters.

Comparison with previous $\tau \rightarrow \mu\overline{\nu}_\mu\nu_\tau$ selections used for OPAL analyses

The basis of the $\tau \rightarrow \mu\overline{\nu}_\mu\nu_\tau$ selections used in previous analyses [25, 26, 27] is that a muon candidate had to pass selection criteria in at least two of the three subdetectors: the ECAL, HCAL and muon chambers. In the muon chambers it was merely required that $N_{MU}^{lyr} \geq 2$, whilst the ECAL and HCAL requirements are identical to the cuts used within CALID. The MC estimate [27] of the τ background in such a sample is given at just over 1%, which is smaller than that for selection B2 (but larger than that for B1). However, whilst the background for selection B2 is larger, it has an advantage over previous methods in that no selection requirements are made in the ECAL or HCAL. Studies [50] show that, for muons, there is only a very weak correlation between the detector responses measured in the muon chambers and those measured in the calorimeters. Therefore, the MC selection efficiency of those muons selected using the MCHID within B2 can be tested using a sample of $\tau \rightarrow \mu\overline{\nu}_\mu\nu_\tau$ decays identified using cuts made in the HCAL and ECAL.

Furthermore, chapter 7 will explain how an independent sample of $\tau \rightarrow \rho\nu_\tau$ decays can be used to check the MC estimate of the τ background for selection B2, thereby reducing the systematic error associated with this estimate. Since the previous selections used the ECAL, HCAL and muon chambers simultaneously, it

EVENT TYPE	MCHID (Selection B1)	MCHID (Selection B2)	CALID (Selections B1 (& B2)
Identified $\tau \rightarrow \mu \overline{\nu}_\mu \nu_\tau$:			
90-94 data	25295	26867	1863
all 93/94 MC	142010	150282	8896.36
MC τ-decays:			
$\tau \rightarrow \mu \overline{\nu}_\mu \nu_\tau$	98.916±0.263%	97.329±0.254%	98.632±0.485%
$\tau \rightarrow \pi(\mathrm{K}) \nu_\tau$	0.542±0.019%	0.575±0.019%	0.585±0.080%
$\tau \rightarrow \rho \nu_\tau$	0.014±0.003%	1.015±0.026%	0.011±0.011%
$\tau \rightarrow \mathrm{a}_1 \nu_\tau$	0.001±0.001%	0.329±0.015%	0
others	0.046±0.005%	0.250±0.013%	0
MC $\mathrm{e}^+\mathrm{e}^- \rightarrow f\overline{f}$ bgnd:			
$\mathrm{e}^+\mathrm{e}^- \rightarrow \mu^+\mu^-$	0.145±0.011%	0.174±0.011%	0.236±0.054%
$\mathrm{e}^+\mathrm{e}^- \rightarrow q\overline{q}$	0	0.012±0.005%	0.033±0.033%
MC 2-photon bgnd:			
$\gamma\gamma \rightarrow \mu^+\mu^-$	0.293±0.012%	0.277±0.011%	0.473±0.059%
$\gamma\gamma \rightarrow \tau^+\tau^-$	0.030±0.003%	0.029±0.003%	0.029±0.012%
MC 4-fermion bgnd:			
$e^+e^-\mu^+\mu^-$	0.002±0.001%	0.002±0.001%	0
$e^+e^-\tau^+\tau^-$	0.008±0.001%	0.008±0.001%	0

Table 6.2: The Monte Carlo estimates of the relative contributions from all possible sources to the $\tau \rightarrow \mu \overline{\nu}_\mu \nu_\tau$ sample identified in the barrel region. The terms MCHID and CALID indicate whether the $\tau \rightarrow \mu \overline{\nu}_\mu \nu_\tau$ candidates were selected using the muon chambers (with (B1) and without (B2) the use of the M_{inv} cut), or the hadron and electromagnetic calorimeters respectively. Selections B1 and B2 are summarised in table 6.1. The non-τ backgrounds are corrected for total integrated luminosity and the relative branching ratios of the τ-decays are corrected to agree with the current world averages 4.1.

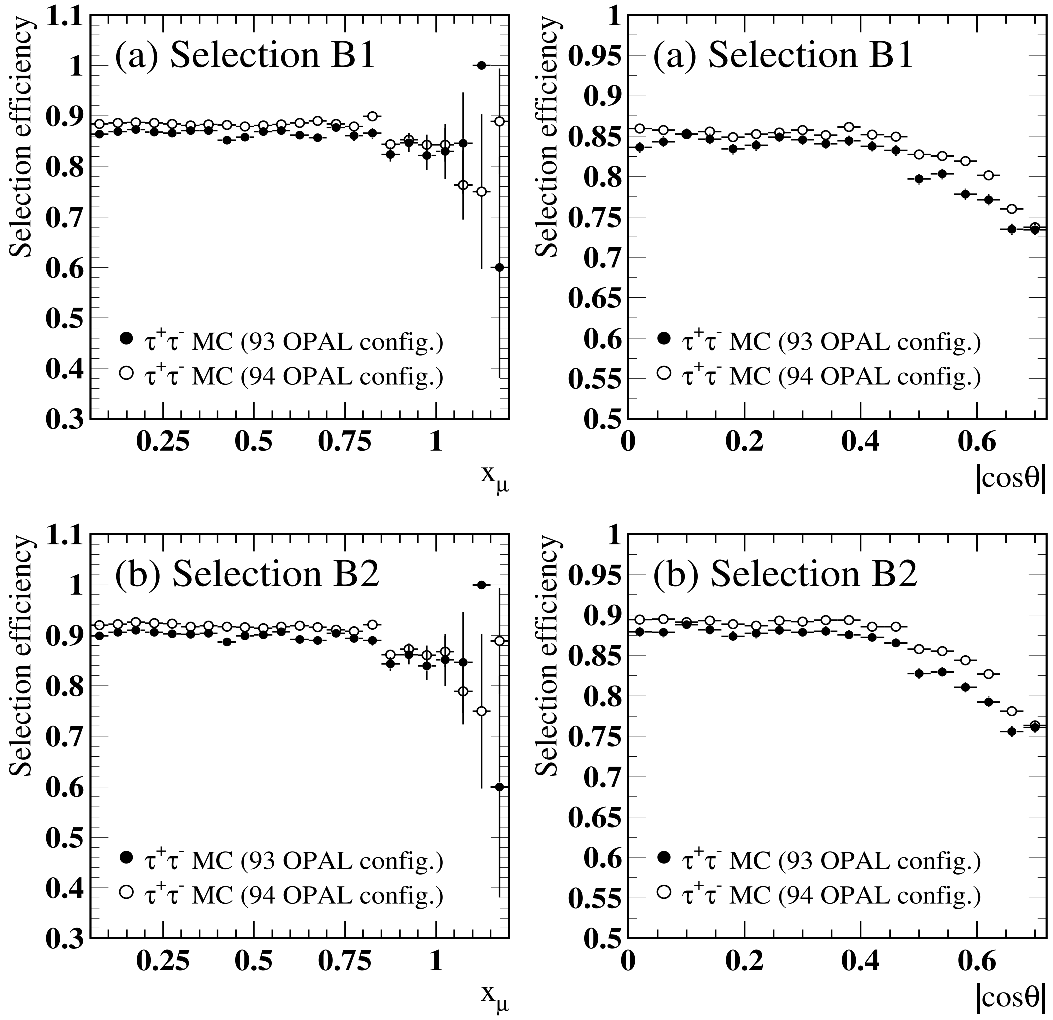

Figure 6.8: The uncorrected selection efficiency for Monte Carlo $\tau \rightarrow \mu\overline{\nu}_\mu\nu_\tau$ decays in the barrel region (after $e^+e^- \rightarrow \tau^+\tau^-$ preselection). The selection efficiency is shown as a function of both momentum and $|\cos\theta|$, and for the cases where (a) Selection B1 and (b) Selection B2 are used.

was impossible to get an entirely **independent** control sample of isolated hadronic tracks with which to test the MC background estimates. In addition, due to a heavier reliance upon the HCAL, previous uncertainties in these MC estimates were larger for the fact that there are known inadequacies in the simulation of minimum ionizing hadrons in the HCAL.

Comparing selection B1 to previous selections, it can be seen that the hadronic τ background has been reduced by nearly half. Having such a small background means that the fitted values of $\langle P_\tau \rangle$ and A_{pol}^{FB} will be relatively insensitive to possible uncertainties arising from the MC estimate of this background. Also the methods used to test the selection efficiency of B1 (see chapter 8) are more extensive than used in other OPAL polarisation analyses involving $\tau \rightarrow \mu \overline{\nu}_\mu \nu_\tau$ decays.

The most recent global τ polarisation analysis [27], whilst retaining the older $\tau \rightarrow \mu \overline{\nu}_\mu \nu_\tau$ selection, attempts to reduce the systematic errors associated with poor HCAL simulation by extending the use of smearing that is applied to MC events. Therefore, in addition to applying the momentum smearing described in chapter 4, corrections are applied to the detector responses observed in the ECAL, HCAL and muon chambers. This extension of the smearing procedure is not used for this analysis, and is less necessary due to the relatively low reliance of the selection procedures used here upon the HCAL. However, such smearing could be used to further improve the results presented in this thesis.

6.2 Selection of $\tau \rightarrow \mu \overline{\nu}_\mu \nu_\tau$ decays in the endcap region

The simulation of the HCAL in the endcap region is poor and so is not used at all in this selection, which is based on the muon chamber detection scheme (MCHID) that is used in the barrel region. Some of the figures included in this section include separate plots for the regions $0.72 < |\cos\theta| < 0.81$ and $0.81 < |\cos\theta| < 0.90$ in order to observe how the Monte Carlo simulation might possibly worsen for events further forward into the endcap.

- Only decays for which $0.72 < |\cos\theta| < 0.90$ are used since, beyond 0.90, the track resolution deteriotes badly and the non-τ backgrounds (particularly from $\gamma\gamma \to \mu^+\mu^-$events) become less manageable. Since tracks in this region miss the edge of the z-chambers, it is required also that the charged track in every candidate $\tau \to \mu\overline{\nu}_\mu\nu_\tau$ cone has a well-defined endpoint in CJ so that its z-measurement is reasonable.

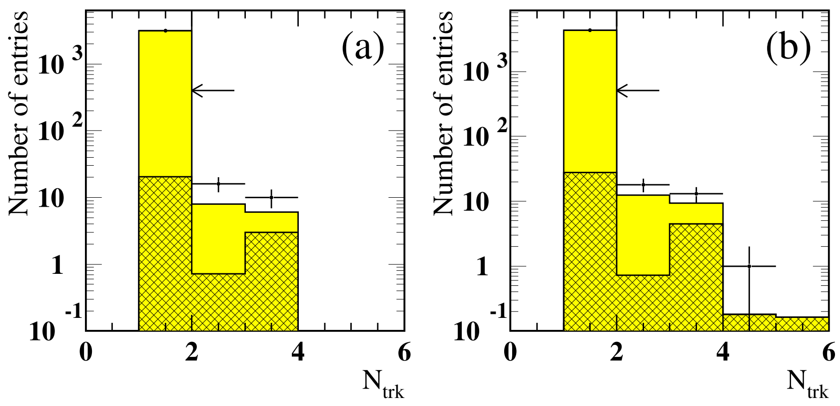

Figure 6.9: Distribution of N_{trk} for $\tau \to \mu\overline{\nu}_\mu\nu_\tau$ candidates in the endcap region where all are other selection cuts have been applied. The distributions are shown separately for candidate muon tracks in the regions (a) $0.72 < |\cos\theta| < 0.81$ and (b) $0.81 < |\cos\theta| < 0.90$. The hatched area illustrates the background from other τ decays only.

- Only candidates within the following kinematic range are considered:

$$0.05 < x_\mu < 1.20$$

- As in the barrel region the number of good tracks assigned to a cone, N_{trk}, must satisfy the following for it to be considered as a $\tau \to \mu\overline{\nu}_\mu\nu_\tau$ candidate (see figure 6.9):

$$N_{trk} = 1$$

- The muon chamber selection, MCHID, is identical to that used for the barrel region, where the candidate is required to pass the following two cuts:

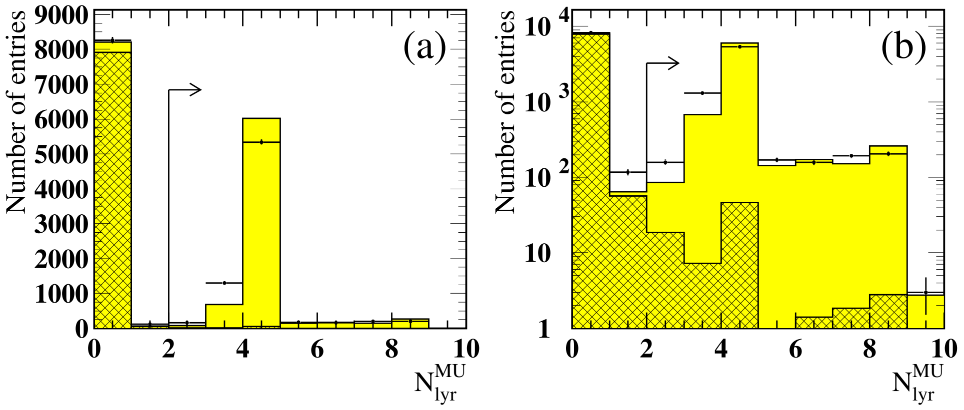

Figure 6.10: Distribution of N_{lyr}^{MU} for $\tau\rightarrow\ \mu\overline{\nu}_\mu\nu_\tau$ candidates in the endcap region where all are other selection cuts have been applied (except on χ_{match}). The distributions are shown with both (a) linear and (b) logarithmic scales on the y-axes. The hatched area illustrates the background from other τ decays only.

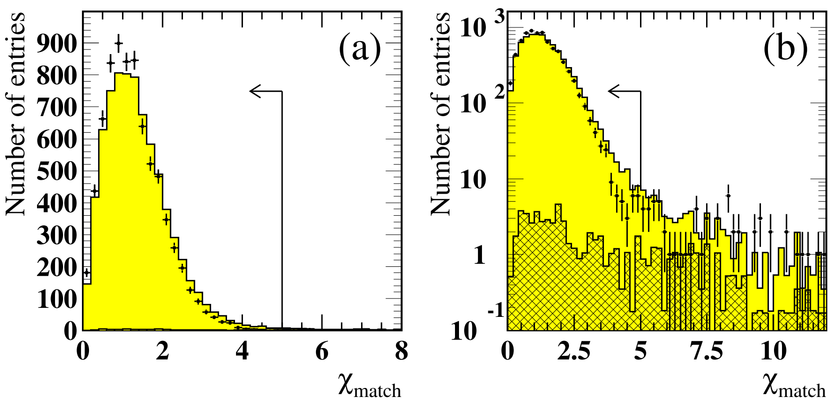

Figure 6.11: Distribution of χ_{match} for $\tau\rightarrow\ \mu\overline{\nu}_\mu\nu_\tau$ candidates in the endcap region where all are other selection cuts have been applied. The distributions are shown with both (a) linear and (b) logarithmic scales on the y-axes. The hatched area illustrates the background from other τ decays only, where most of these have a very high χ_{match} value and so are not shown.

$$N_{lyr}^{MU} \geq 2 \quad \text{(see figure 6.10)}$$

$$\chi_{match} < 5 \quad \text{(see figure 6.11)}$$

- An invariant mass cut is used to suppress the background from $\tau \rightarrow \rho\nu_\tau$ and $\tau \rightarrow a_1\nu_\tau$ decays (see figure 6.12). The analysis in the endcap (as in the barrel) is repeated with this cut omitted, where the cut used is:

$$M_{inv} < 0.3\,\mathrm{GeV}/c^2$$

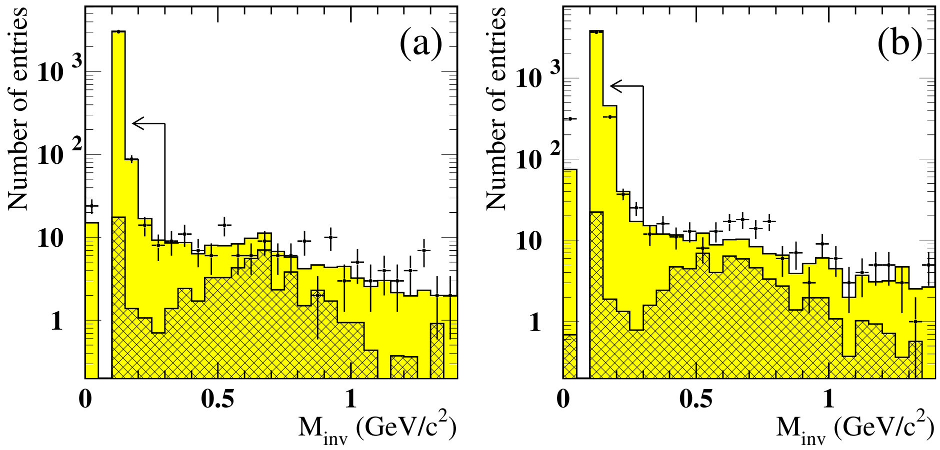

Figure 6.12: Distribution of M_{inv} for $\tau \rightarrow \mu\overline{\nu}_\mu\nu_\tau$ candidates in the endcap region where all are other selection cuts have been applied. The distributions are shown separately for candidate muon tracks in the regions (a) $0.72 < |\cos\theta| < 0.81$ and (b) $0.81 < |\cos\theta| < 0.90$. The hatched area illustrates the background from other τ decays only.

- Those $\tau \rightarrow \mu\overline{\nu}_\mu\nu_\tau$ candidates for which the opposite track in the event is a muon pointing to a far-forward region ($|\cos\theta| > 0.90$) are likely to contain a high non-τ background content (as illustrated in figure 6.13). The most significant contribution to this background is from $\gamma\gamma \rightarrow \mu^+\mu^-$events which are heavily peaked in the far forward direction by virtue of their differential cross section. Momentum mismeasurement becomes a more significant problem for tracks with $|\cos\theta| > 0.90$, and so poorly measured $e^+e^- \rightarrow \mu^+\mu^-$events also contribute to this background. The combined background contribution from the two non-τ sources is significant and so $\tau \rightarrow \mu\overline{\nu}_\mu\nu_\tau$ candidates are discarded if:

$$N_{lyr}^{MU}(opp) \geq 2 \quad \textbf{AND} \quad |\cos\theta_{opp}| > 0.90$$

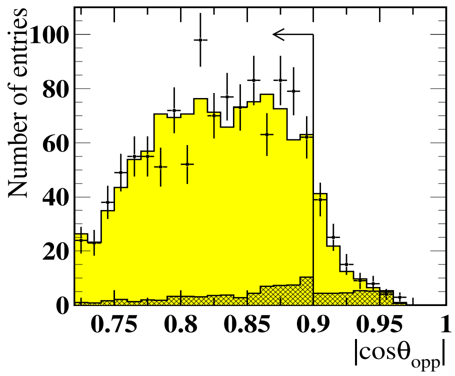

Figure 6.13: The angular distribution, $|\cos\theta_{opp}|$, of the highest energy track from cones opposite to $\tau \rightarrow \mu\overline{\nu}_\mu\nu_\tau$ endcap candidates and for which there are associated muon chamber hits in at least two layers. The hatched area illustrates the non-$\tau^+\tau^-$ background.

- The final cut is to suppress the $e^+e^- \rightarrow \mu^+\mu^-$ background and is very similar to the $e^+e^- \rightarrow \mu^+\mu^-$ rejection employed in the barrel selection. Events are likely to be $e^+e^- \rightarrow \mu^+\mu^-$ background if they have high visible energy, and contain a high momentum $\tau \rightarrow \mu\overline{\nu}_\mu\nu_\tau$ candidate from one cone and a single track from the other which points outside the geometrical acceptance of the muon chambers. Hence $\tau \rightarrow \mu\overline{\nu}_\mu\nu_\tau$ candidates are **rejected** if (see figure 6.14):

  (a) the total visible energy in the event,

  $$R_{total} > 0.8$$

  (b) the momentum of the candidate $\tau \rightarrow \mu\overline{\nu}_\mu\nu_\tau$ track (normalised to E_{beam}),

  $$x_\mu > 0.7$$

  (c) the highest energy track in the opposite cone is outside the geometrical acceptance of the muon chambers.

The selection of $\tau \rightarrow \mu\overline{\nu}_\mu\nu_\tau$ decays in the endcap is less complicated than that in the barrel since there is no separate calorimeter identification. A brief summary

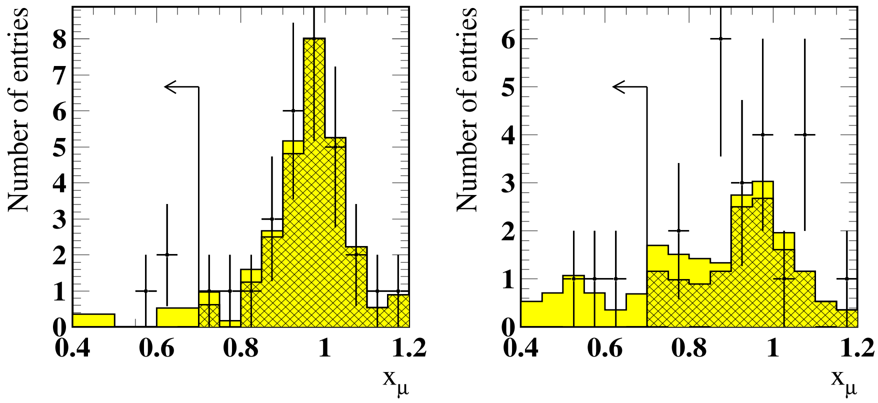

Figure 6.14: Distribution of x_μ for $\tau \rightarrow \mu\overline{\nu}_\mu\nu_\tau$ candidates in the endcap region from events with $R_{total} > 0.8$ and where the highest momentum track from the opposite cone points outside the geometrical acceptance of the muon chambers. All other selection cuts have been applied. The distributions are shown separately for candidate muon tracks in the regions (a) $0.72 < |\cos\theta| < 0.81$ and (b) $0.81 < |\cos\theta| < 0.90$. The hatched area illustrates the background from $e^+e^- \rightarrow \mu^+\mu^-$ events only.

of the cuts used is given in table 6.3, where, as for the barrel selection, the analysis is repeated with the cut on M_{inv} switched off to give two separate selections. This is done for the same reasons as those described earlier in justifying the use of two separate barrel selections, B1 and B2. The two analogous endcap selections will be referred to as E1 and E2 in later chapters.

Monte Carlo simulation data has again been used to estimate the selection efficiency and backgrounds, as was done for the barrel selection. The uncorrected selection efficiency for Monte Carlo $\tau \rightarrow \mu\overline{\nu}_\mu\nu_\tau$ decays in the endcap region can be seen in figure 6.15, and the Monte Carlo estimates of the various τ and non-τ backgrounds are shown in table 6.4, where the only corrections to be have been applied at this stage are for luminosity (for the non-τ background) and for the relative τ branching ratios (the input values used in KoralZ4.0 are corrected for using the current world averages [5]). The total numbers of $\tau \rightarrow \mu\overline{\nu}_\mu\nu_\tau$ candidates obtained from the Monte Carlo and real data sets after all selection cuts are also included in the table. The momentum distributions for all data and MC events selected using the two selections are also displayed (including the major backgrounds) in

Selection E1	Selection E2
$\lvert\cos\theta\rvert < 0.72$	
$0.05 < x_\mu < 1.20$	
$N_{trk} = 1$	
MCHID	
$M_{inv} < 0.3\,\mathrm{GeV}/c^2$	-
μ-pair rejection using θ_{acol}	
rejection of dimuon events, one far forward	
high momentum μ-pair rejection	

Table 6.3: Summary of the two selections used to obtain samples of $\tau \rightarrow \mu\overline{\nu}_\mu\nu_\tau$ decays in the endcap region.

figure 6.16.

Event type	Selection E1	Selection E2
Identified $\tau\rightarrow\mu\overline{\nu}_\mu\nu_\tau$:		
90-94 data	7509	7936
all 93/94 MC	42053.1	44109.9
MC τ-decays:		
$\tau\rightarrow\mu\overline{\nu}_\mu\nu_\tau$	97.884±0.481%	96.563±0.467%
$\tau\rightarrow\pi(\mathrm{K})\nu_\tau$	0.592±0.037%	0.626±0.037%
$\tau\rightarrow\rho\nu_\tau$	0.024±0.008%	0.898±0.045%
$\tau\rightarrow\mathrm{a}_1\nu_\tau$	0.002±0.002%	0.274±0.026%
others	0.023±0.007%	0.169±0.019%
MC $\mathrm{e}^+\mathrm{e}^-\rightarrow f\overline{f}$ bgnd:		
$\mathrm{e}^+\mathrm{e}^-\rightarrow\mu^+\mu^-$	0.328±0.029%	0.349±0.030%
$\mathrm{e}^+\mathrm{e}^-\rightarrow q\overline{q}$	0.007±0.007%	0.020±0.012%
MC 2-photon bgnd:		
$\gamma\gamma\rightarrow\mu^+\mu^-$	1.068±0.041%	1.029±0.039%
$\gamma\gamma\rightarrow\tau^+\tau^-$	0.068±0.008%	0.066±0.008%
MC 4-fermion bgnd:		
$e^+e^-\mu^+\mu^-$	0	0.001±0.001%
$e^+e^-\tau^+\tau^-$	0.004±0.002%	0.005±0.002%

Table 6.4: The Monte Carlo estimates of the relative contributions from all possible sources to the $\tau\rightarrow\mu\overline{\nu}_\mu\nu_\tau$ sample identified in the endcap region. The numbers are shown for the cases where the cut on M_{inv} is (E1) and is not (E2) used. Selections E1 and E2 are summarised in table 6.3. The non-τ backgrounds are corrected for total integrated luminosity and the relative branching ratios of the τ-decays are corrected to agree with the current world averages 4.1.

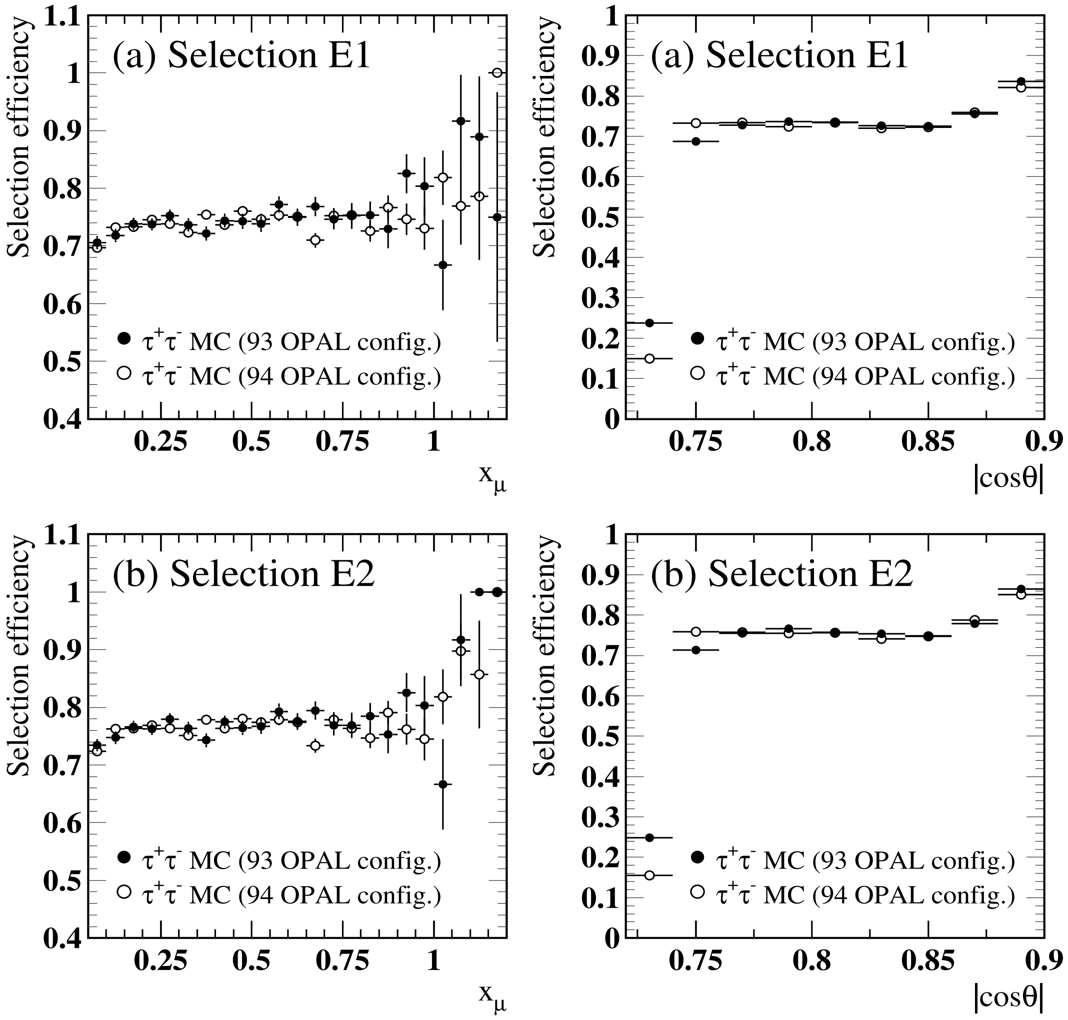

Figure 6.15: The uncorrected selection efficiency for Monte Carlo $\tau \to \mu\overline{\nu}_\mu\nu_\tau$ decays in the endcap region (after $e^+e^- \to \tau^+\tau^-$ preselection). The selection efficiency is shown as a function of both momentum and $|\cos\theta|$, and for the cases where (a) Selection E1 and (b) Selection E2 are used.

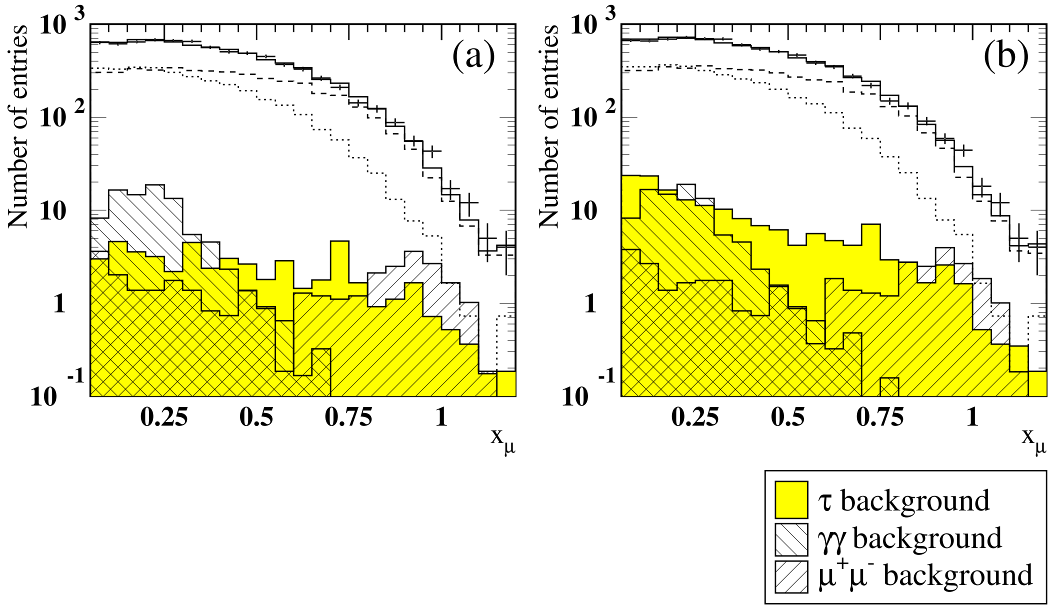

Figure 6.16: Distributions of x_μ for all $\tau \rightarrow \mu\overline{\nu}_\mu\nu_\tau$ candidates selected using (a) selection E1 and (b) selection E2. All Monte Carlo events (histograms) are weighted to give the same total number as that seen in the data (points). The backgrounds from other τ decays are shown, along with the major non-τ backgrounds from $e^+e^- \rightarrow \mu^+\mu^-$ and $\gamma\gamma \rightarrow \ell^+\ell^-$ events. The contributions from the negative and positive helicity MC $\tau \rightarrow \mu\overline{\nu}_\mu\nu_\tau$ decays are also included, and are represented by the dashed and dotted lines respectively.

Chapter 7

Monte Carlo background estimates

Monte Carlo events are used to estimate the background content from both $\tau^+\tau^-$ and non-$\tau^+\tau^-$ sources. The uncorrected estimates have been given for B1, B2, E1 and E2 in tables 6.2 and 6.4. However, a Monte Carlo simulation can never be perfect and so a number of checks must be performed to ensure that the extent of each background source is well-known when the final values of $\langle P_\tau \rangle$ and A^{FB}_{pol} are extracted. This chapter describes a number of studies that have been performed to check these background estimates, all of which differ (most substantially so) from previous methods used within OPAL τ polarisation studies for estimating the backgrounds in $\tau \rightarrow \mu\overline{\nu}_\mu\nu_\tau$ samples.

7.1 Background from other τ decays

If the $\tau \rightarrow \mu\overline{\nu}_\mu\nu_\tau$ sample is selected by the muon chambers (MCHID) but without using the cut on M_{inv} (Selections B2 and E2), then the background from other τ-decays mostly comes from 1-prong hadronic channels, where their relative contributions are approximately proportional to their relative branching ratios. If the cut on M_{inv} is now combined with the muon chamber identification cuts (as for Selections B1 and E1), the number of decays accompanied by one or more π^0s (such as $\tau \rightarrow \rho\nu_\tau$ and $\tau \rightarrow a_1\nu_\tau$) becomes negligible, whilst the number of $\tau \rightarrow \pi(K)\nu_\tau$ decays is not significantly reduced, making it the dominant τ background in the $\tau \rightarrow \mu\overline{\nu}_\mu\nu_\tau$ sample. Within the $\tau \rightarrow \mu\overline{\nu}_\mu\nu_\tau$ samples selected by Selections B1, E1, B2 and E2 there are three possible cases for which the background from hadronic τ decays must be considered, these being:-

CASE A

Those $\tau \rightarrow \mu\overline{\nu}_\mu\nu_\tau$ candidates identified using MCHID but which are not required to pass the invariant mass requirement (Selections B2 and E2).

CASE B

Those $\tau \rightarrow \mu\overline{\nu}_\mu\nu_\tau$ candidates identified using the muon chamber identification (MCHID) and with the invariant mass cut included in the selection (Selections B1 and E1).

CASE C

Those $\tau \rightarrow \mu\overline{\nu}_\mu\nu_\tau$ candidates identified using the calorimeter identification (CALID) and with the invariant mass cut included in the selection (Selections B1 and B2).

7.1.1 CASE A

For $\tau \rightarrow \mu\overline{\nu}_\mu\nu_\tau$ candidates identified using MCHID, but with no constraints applied to the invariant mass (M_{inv}), the background from hadronic τ decay amounts to $\sim$2% (see the Monte Carlo background estimates for Selections B2 and E2 in tables 6.2 and 6.4). The background is therefore considerably larger than is the case for when M_{inv} is used and so the MC estimate requires further study using an independent control sample of hadronic τ decays.

Since $\tau \rightarrow \mu\overline{\nu}_\mu\nu_\tau$ candidates identified using the MCHID within Selections B2 and E2 do not rely on any information from the calorimeters, the ECAL can be used to discriminate between leptonic and hadronic decays, and hence obtain a sample with which the response of the muon chambers to $\pi^{\pm}(\mathrm{K}^{\pm})$ tracks can be tested. However, for $\pi^{\pm}(\mathrm{K}^{\pm})$ tracks, the responses in the ECAL and muon chambers are correlated, and so, to get as unbiased a sample as possible, little or no direct ECAL constraints are applied to the $\pi^{\pm}(\mathrm{K}^{\pm})$track itself. Instead, it is possible to select a highly pure, unbiased sample of $\pi^{\pm}(\mathrm{K}^{\pm})$tracks by looking for 1-prong hadronic decays accompanied by a well-defined and unambiguous signal in the ECAL from at least one π^0. Therefore, the control sample used consists of mostly $\tau\rightarrow\rho\nu_\tau$ and $\tau\rightarrow \mathrm{a}_1\nu_\tau$ decays, where any $\pi^0\rightarrow\gamma\gamma$ decays are clearly separated from the single charged track in the cone.

After the $\mathrm{e}^+\mathrm{e}^-\rightarrow\tau^+\tau^-$preselection, any cone is considered in which there is one good charged track and at least 3 good clusters ($N_{clus}\geq 3$). By considering the momentum vector of each cluster with respect to the interaction region, it is required that one cluster is assigned to the charged track (within 40 mrad), whilst the others are at least 60 mrad from the assigned cluster. This ensures that the signatures of the charged track and any photons from $\pi^0\rightarrow\gamma\gamma$ decays are reasonably well defined in the ECAL. The selection of the control sample uses a new invariant mass variable, $M^{'}_{inv}$, which is defined using only the 4-momenta of the track and unassigned clusters in the cone, and which must be non-zero for the cone to be considered. In addition, the fact is used that, in decays such as $\rho^{\pm}\rightarrow\pi^{\pm}\pi^0$, the angle seen in the detector between the $\pi^{\pm}$ and π^0 is kinematically constrained, whilst this is not the case for leptonic decays accompanied by bremsstrahlung radiation. Thus the following cuts are applied to the sample:-

- The track momentum normalised to the beam energy,

$$x_\pi \equiv \frac{p_{trk}}{E_{beam}} > 0.05$$

- The angle between the charged track and the vector sum of the unassigned ECAL clusters (see figure 7.1),

$$\theta_{trk-\pi^0} < 180\,\mathrm{mrad}$$

- If $N_{clus}=3$, requirements are made on the highest energy cluster in the cone and on M'_{inv},

$$\frac{E^{hi}_{clus}}{p_{trk}} > 0.1$$

$$0.5 < M'_{inv} < 1.4\mathrm{GeV}/c^2 \text{ (see figure 7.1)}$$

The same cuts are used to select samples in both the barrel ($|\cos\theta| < 0.68$) and endcap ($0.72 < |\cos\theta| < 0.90$) regions of the detector. The total numbers in each sample are shown in table 7.1, where the data sample is taken from LEP runs between 1990 and 1994, and the Monte Carlo sample uses the 900k $e^+e^- \to \tau^+\tau^-$ events generated using the 1993 and 1994 detector configurations.

	Before muon chamber cuts		After muon chamber cuts	
	Barrel	Endcap	Barrel	Endcap
data sample	15084	3723	79	15
MC sample	60416.19	14200.96	351.44	60.27
MC $\tau\to e\overline{\nu}_e\nu_\tau$ bgd	70.59	13.91	0	0
MC $\tau\to \mu\overline{\nu}_\mu\nu_\tau$ bgd	14.92	5.99	12.94	5.00

Table 7.1: The samples of hadronic τ decays used to test the efficiency with which $\pi^\pm(K^\pm)$ tracks pass the muon chamber identification.

Each control sample is then subjected to the muon chamber cuts used in the $\tau\to \mu\overline{\nu}_\mu\nu_\tau$ selections (MCHID: $N^{MU}_{lyr} \geq 2$ and $\chi_{match} < 5$) to observe the efficiency with which $\pi^\pm(K^\pm)$ tracks in data and Monte Carlo pass the cuts. The Monte Carlo is used to correct the data sample for the background from leptonic channels before its efficiency is calculated. The data and Monte Carlo efficiencies (ε_{data} and ε_{MC} respectively) are then combined to get a correction factor, C_{had}, which can be used to weight the hadronic τ background in the $\tau\to \mu\overline{\nu}_\mu\nu_\tau$ samples identified using the muon chambers (only when the M_{inv} cut is not used).

- The correction obtained for the **barrel** region is,

$$C_{had} = \frac{\varepsilon_{data}}{\varepsilon_{MC}} = \frac{0.503 \pm 0.059\%}{0.561 \pm 0.030\%} = 0.897 \pm 0.116$$

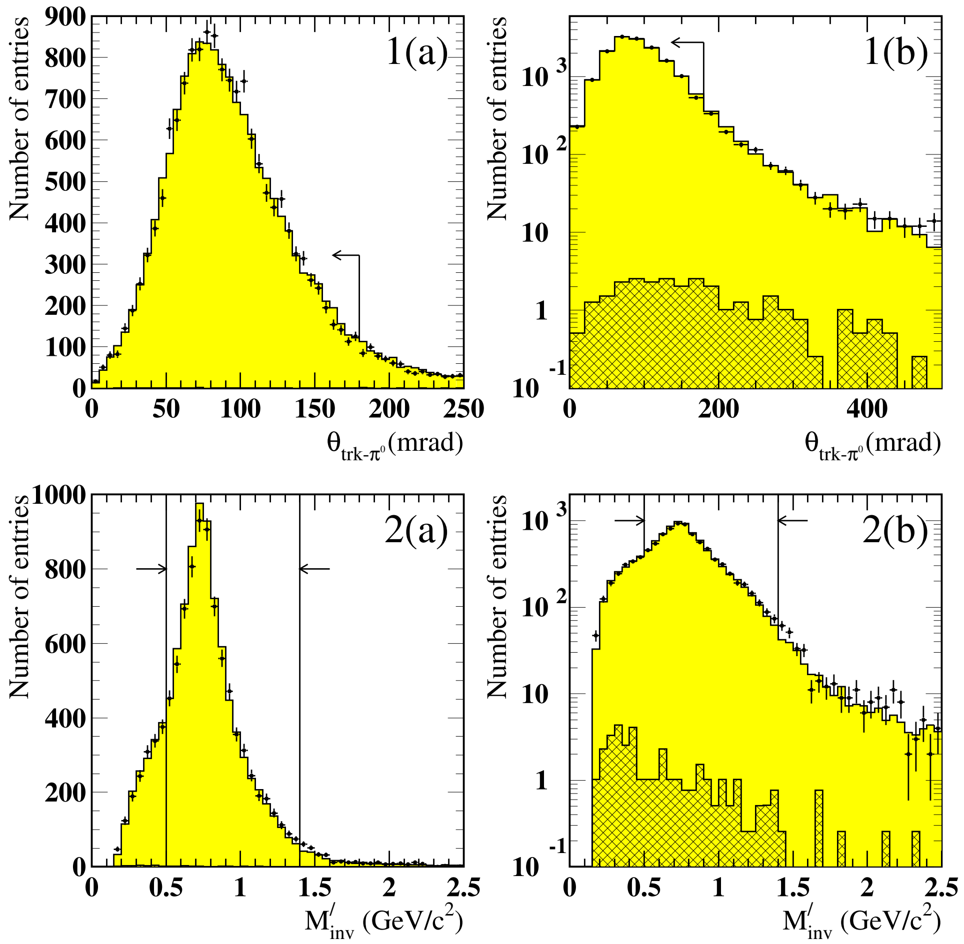

Figure 7.1: The effect of cutting on the variables $\theta_{trk-\pi^0}$ (1(a) and 1(b)) and $M^{'}_{inv}$ (2(a) and 2(b)) in selecting a pure sample of hadronic τ decays in the barrel region. All are other selection cuts have been applied, with the $M^{'}_{inv}$ distributions only featuring cones for which $N_{clus} = 3$. The distributions are shown with both linear (a) and logarithmic (b) scales on the y-axes. The hatched area illustrates the background from leptonic τ decays.

- The correction obtained for the **endcap** region is,

$$C_{had} = \frac{\varepsilon_{data}}{\varepsilon_{MC}} = \frac{0.368 \pm 0.105\%}{0.390 \pm 0.052\%} = 0.945 \pm 0.298$$

The corrections for both the barrel and endcap are statistically consistent with unity and so are not used to weight the background from hadronic τ decays by default. However, these corrections are used in evaluating the systematic errors on $\langle P_\tau \rangle$ and A_{pol}^{FB} due to uncertainties on the τ background fraction.

7.1.2 CASE B

In the case where M_{inv} is combined with MCHID, the τ background is very small in both the barrel and endcap $\tau \rightarrow \mu \overline{\nu}_\mu \nu_\tau$ samples and comes largely from just the $\tau \rightarrow \pi(\mathrm{K})\nu_\tau$ channel. The background can enter the sample by several different processes. The sneakthrough process is where the $\pi^\pm(\mathrm{K}^\pm)$ simply fails to interact strongly within the calorimeters and so is able to reach muon chambers with little deviation. The punchthrough process is where the $\pi^\pm(\mathrm{K}^\pm)$ does interact but the hadronic showering is not fully contained in the calorimetry, thus causing hits to be observed in the muon chambers. Lastly, background from $\tau \rightarrow \pi(\mathrm{K})\nu_\tau$ decays can arise through the production of a muon, either during the hadronic showering or by the decay-in-flight process $\pi(\mathrm{K}) \rightarrow \mu \overline{\nu}_\mu$. The Monte Carlo is expected to simulate the decay-in-flight process very precisely, but the accurate simulation of the remaining effects rely on the Monte Carlo modelling of hadronic showering in the ECAL and HCAL, and so this may not be done satisfactorily.

A study was performed using the tree information of the Monte Carlo to estimate what fraction of $\tau \rightarrow \pi(\mathrm{K})\nu_\tau$ decays identified as muons fall into each category. A sample of actual $\tau \rightarrow \pi(\mathrm{K})\nu_\tau$ decays was taken from all on-peak $e^+e^- \rightarrow \tau^+\tau^-$events generated using the 1993 and 1994 detector configurations. In addition they must come from events passing the $\tau^+\tau^-$ preselection, and pass the following cuts to select only those $\tau \rightarrow \pi(\mathrm{K})\nu_\tau$ decays which look like muons (most of the selection B1 cuts are used):-

- the number of charged tracks in the cone, $N_{trk}=1$
- the decay is identified in the barrel, $|\cos\theta|<0.72$
- the $\pi^\pm$ track momenta (normalised to E_{beam}) must lie in the range, $0.05 < x_\pi < 1.20$
- the invariant mass of the cone, $M_{inv} < 0.3\,\mathrm{GeV}/c^2$
- the number of loosely associated muon chamber hits must come from at least two layers, $N^{MU}_{lyr} \geq 2$

From a total of 900k $e^+e^- \to \tau^+\tau^-$events, 8328 $\tau \to \pi(K)\nu_\tau$ decays are found to enter this sample, and, of these, there are only 31.7% for which a daughter $\mu^\pm$ was found in the Monte Carlo particle tree. Thus the rest one can assume to be there due to the punchthrough and sneakthrough processes. However, if the $\tau \to \mu\overline{\nu}_\mu\nu_\tau$ selection cut on the χ_{match} variable is now applied to the sample (that is, we require $\chi_{match} < 5$), the number of punchthrough/sneakthrough $\tau \to \pi(K)\nu_\tau$ decays is reduced from 5690 to 402 (an efficiency of $\sim$7%), whilst the number in the sample with muon production is reduced from 2638 to 504 (a larger efficiency of $\sim$19%). In the case of the punchthrough and sneakthrough pions which pass the muon chamber cuts, there is little to distinguish between the signals in the detector from the two processes. Some pions clearly enter the final sample by one process or the other, but there are also others (for example, those pions which only begin to interact deep into the HCAL) for which it is ambiguous as to whether the response in the muon chambers is due to shower particles or due to the pion itself. However, in general, one would expect the weakly-interacting sneakthrough pions to pass the χ_{match} cut with a high efficiency.

Figure 7.2 shows the distribution of R_{xy} for those decays in the sample containing muon production before and after the χ_{match} cut is applied, where R_{xy} is defined as the radial distance from the $z=0$ axis at which the daughter $\mu^\pm$ is produced. Muons produced from hadronic showering typically have low energies ($\leq$1 GeV) and are likely to have a starting radius lying within the ECAL or HCAL (roughly $200 < R_{xy} < 440\,\mathrm{cm}$) where showering usually begins. This explains the peak shown in the R_{xy} distribution seen before the χ_{match} cut is applied. Afterwards, however, this peak is largely removed since the direction in which the muons are produced is not heavily biased towards that of the $\pi^{\pm}(\mathrm{K}^{\pm})$ track.

Most of the muons produced in the region $R_{xy} < 183.5\,\mathrm{cm}$ (that is, in CJ, the jet chamber) are likely to come from the process $\pi(\mathrm{K})\rightarrow\mu\overline{\nu}_{\mu}$, since hadronic showering from $\pi^{\pm}(\mathrm{K}^{\pm})$ tracks is highly unlikely to occur until they reach the edge of the CT pressure vessel and OPAL magnet. The process $\pi(\mathrm{K})\rightarrow\mu\overline{\nu}_{\mu}$ is only a two body decay whose rest frame is highly Lorentz-boosted with respect to the laboratory frame, and so the daughter muons should still travel in a direction close to that of the $\pi^{\pm}(\mathrm{K}^{\pm})$ with a reasonable share of its energy. This explains why most of the muons produced in $\pi(\mathrm{K})\rightarrow\mu\overline{\nu}_{\mu}$ decays in CJ still remain even after the χ_{match} cut has been applied.

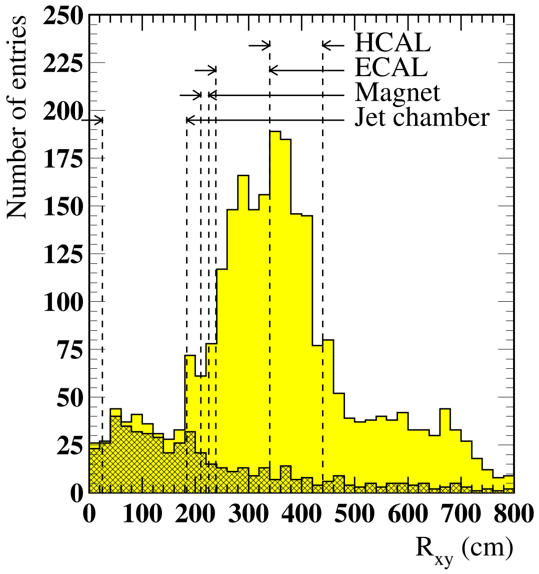

Figure 7.2: Distribution of R_{xy}, the starting radius of muons produced from $\tau\rightarrow\pi(\mathrm{K})\nu_{\tau}$ decays in the barrel. The shaded region is for those $\mu^{\pm}$s which leave hits in at least two layers of the muon chambers (see text), and the hatched region shows the number remaining in the sample after the cut on χ_{match} has been applied. The radii of various OPAL subdetectors are superimposed to indicate where in the detector the muons are being produced.

Figure 7.3 shows the true Monte Carlo energy distributions for the daughter

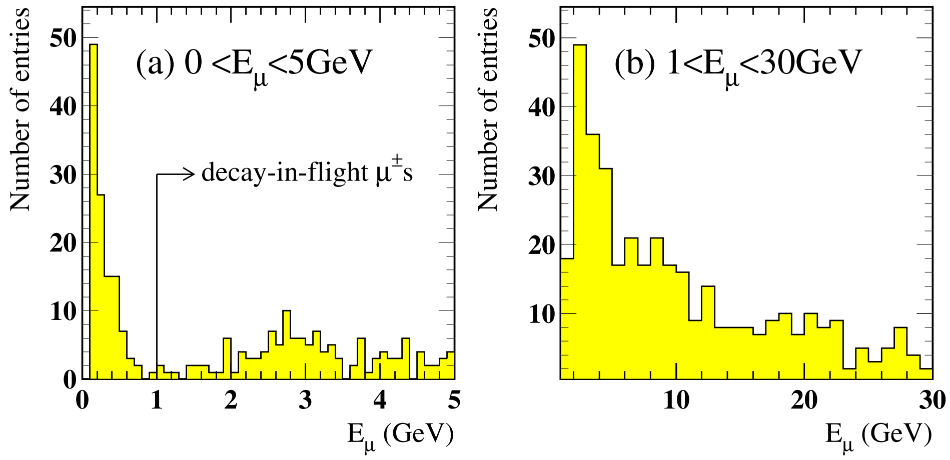

Figure 7.3: Distribution of E_μ, the true energy of muons produced from $\tau \rightarrow \pi(\mathrm{K})\nu_\tau$ decays in the barrel, where the requirements on N^{MU}_{lyr} and χ_{match} in the muon chambers have both been satisfied. The plots (a) and (b) show the same variable but for different ranges in E_μ to illustrate the contributions of the two possible processes to the final sample.

muons in the sample after the χ_{match} cut. There is a clear peak in the distribution below 1 GeV which can be attibuted to the muons produced during hadronic showering. A cut has been arbitrarily placed at 1 GeV to distinguish between these and the muons produced by the decay-in-flight process. Thus estimates have been made of the contributions from each of the three processes to the sample of "muon-like" $\tau \rightarrow \pi(\mathrm{K})\nu_\tau$ decays left after the χ_{match} cut (see table 7.2).

Process	Number in sample	Fraction of sample(%)
punchthrough/ sneakthrough	402±40	44.4±4.4
decay-in-flight	385±39	42.5±4.3
μ from showering	119±22	13.1±2.4
total	906	100

Table 7.2: The contributions from the four possible processes to a sample of Monte Carlo $\tau \rightarrow \pi(\mathrm{K})\nu_\tau$ decays which pass the muon chamber requirements used in the barrel and endcap $\tau \rightarrow \mu\overline{\nu}_\mu\nu_\tau$ selections. To account for systematic effects involved in the method used to estimate these numbers, the errors are quoted as being twice the statistical error.

From this study it is concluded that, for the MC $\tau\rightarrow \mu\overline{\nu}_\mu\nu_\tau$ samples selected using the MCHID within B1 and E1 (that is, in conjunction with a M_{inv} cut), the fraction of the $\tau\rightarrow \pi(\mathrm{K})\nu_\tau$ background arising from the combined punchthrough and sneakthrough contributions is less than half. Of these, HCAL distributions indicate that there will be a significant proportion for which the $\pi^\pm(\mathrm{K}^\pm)$ track simply fails to shower in the calorimetry. It is expected that the Monte Carlo should predict this fraction well, given also that the amount of material that the track must pass through is very well-known. The Monte Carlo is expected to predict the decay-in-flight process very precisely as well, and so the overall MC τ-background estimate can be well-trusted for around half of the decays.

The main point to the above study, apart from to understand more how the τ backgrounds arise for case B, is to show that the background for which we might consider the Monte Carlo simulation suspect represents only around 0.3 % of the samples in the barrel and endcap. Given the size of such a background it can therefore be reasonably assumed that the final fit values of $\langle P_\tau\rangle$ and A_{pol}^{FB} will be relatively insensitive to inaccuracies in the MC estimations of these backgrounds. No correction is applied to the MC τ background events for case B although the values of C_{had} obtained for case A in the barrel and endcap are used again to test the sensitivity of $\langle P_\tau\rangle$ and A_{pol}^{FB} during the fit and to assign a systematic error accordingly.

7.1.3 CASE C

For $\tau\rightarrow \mu\overline{\nu}_\mu\nu_\tau$ decays identified in the barrel region using the calorimeter identification, CALID, combined with the M_{inv} cut, the Monte Carlo estimates the small τ background to come almost entirely from $\tau\rightarrow \pi(\mathrm{K})\nu_\tau$ decays (see table 6.2). When checking this background estimate, the situation is slightly complicated by the fact, within Selections B1 and B2, MCHID must be failed for candidates to be selected by CALID and that the candidates have to point outside the muon chambers. It was found that, very more so than for muons, the responses seen in the ECAL, HCAL and muon chambers for minimum ionizing $\pi^{\pm}(\mathrm{K}^{\pm})$ tracks are highly correlated. It is therefore impossible to get a meaningful control sample with which to test the background from hadronic τ decays. However, since $\tau\to\mu\overline{\nu}_{\mu}\nu_{\tau}$ candidates identified using CALID and the M_{inv} cut constitute less than 7% of the total $\tau\to\mu\overline{\nu}_{\mu}\nu_{\tau}$ sample in the barrel region (using Selections B1 or B2), the Monte Carlo estimates the hadronic τ content under consideration here to be only about 0.038% of the total barrel sample. This is very small and unlikely to have a noticeable effect on the measured values of $\langle P_{\tau}\rangle$ or A_{pol}^{FB} if incorrectly estimated. No correction is therefore applied to this background.

7.2 Background from $e^+e^-\to\mu^+\mu^-$ events

The method used to check the Monte Carlo estimate of the $e^+e^-\to\mu^+\mu^-$ background is as follows. The $e^+e^-\to\mu^+\mu^-$ content of the signal $\tau\to\mu\overline{\nu}_{\mu}\nu_{\tau}$ sample is enhanced by only considering those decays for which $x_{\mu}>0.9$. The acoplanarity of $\tau\to\mu\overline{\nu}_{\mu}\nu_{\tau}$ candidates from background $e^+e^-\to\mu^+\mu^-$ events should be low compared to those from $e^+e^-\to\tau^+\tau^-$ events. The Monte Carlo is used to estimate the distributions from each contribution, and then a binned maximum likelihood fit using the program MINUIT [18] fits linear combinations of them to the corresponding acoplanarity distribution observed in the data. Each of these distributions (before the fit is performed) can be seen in figure 7.4 for both the barrel and endcap selections.

The fit involves the use of a single parameter ($C_{\mu\mu}$) which scales the size of the $e^+e^-\to\mu^+\mu^-$ contribution to the background-enhanced $\tau\to\mu\overline{\nu}_{\mu}\nu_{\tau}$ sample. At the same time, $C_{\mu\mu}$ is then used to alter the normalisation of the τ contribution in such a way that the total number of Monte Carlo events for which $x_{\mu}>0.9$ remains constant with each iteration of the fit. The total number in this Monte Carlo sample is then normalised to equal the corresponding number in the background-enhanced sample obtained from real data events. The value of $C_{\mu\mu}$ extracted from the fit can then be used as a correction factor which can be used to weight the $e^+e^-\to\mu^+\mu^-$ background in $\tau\to\mu\overline{\nu}_{\mu}\nu_{\tau}$ decays used in the final analysis.

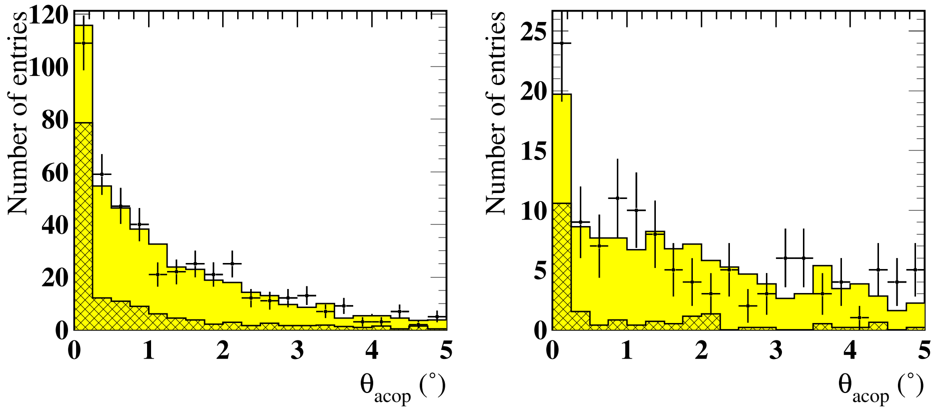

Figure 7.4: The acoplanarity distributions for $\tau\to\mu\bar{\nu}_\mu\nu_\tau$ candidates with $x_\mu>0.9$ identified in (a) the barrel and (b) the endcap regions of the detector. These candidates have also had the mu-pair rejection cut loosened to increase the $e^+e^-\to\mu^+\mu^-$ background content, which is shown as the hatched region in each plot.

The method is performed twice, the second time with Monte Carlo statistical fluctuations taken into account using the method described in [9]. Of the two fitted values of $C_{\mu\mu}$ obtained, this second value is used. The error due to the data statistics is taken to be the MINUIT error returned from the first fit. When the fit is repeated with the Monte Carlo statistics incorporated a larger error from MINUIT is returned, and this is taken to be the quadratic sum of the individual data and Monte Carlo statistical errors.

Using the method as it stands leads to numbers which are consistent with unity but which have large errors. Therefore, to improve the statistics and hence make the corrections more meaningful, the cuts used in Selections B1, B2, E1 and E2 to reject high momentum muons from $e^+e^-\to\mu^+\mu^-$ events need to be relaxed, but in such a way so as to not make the correction invalid. This is done by loosening the cut on the visible energy to $R_{total}>1.0$ (see the μ-pair rejection cuts detailed in chapter 6). This leads to the following results:

- The correction obtained for the **barrel** region is,

$$C_{\mu\mu} = 0.907 \pm 0.107(\text{data stat.})\pm 0.072(\text{MC stat.}) = 0.907 \pm 0.129$$

- The correction obtained for the **endcap** region is,

$$C_{\mu\mu} = 1.28 \pm 0.33(\text{data stat.})\pm 0.25(\text{MC stat.}) = 1.28 \pm 0.41$$

Both of these corrections are consistent with unity, and so no correction is applied. As before, however, both the barrel and endcap values were used in the assignment of systematic errors on $\langle P_\tau \rangle$ and A^{FB}_{pol}.

7.3 Background from $\gamma\gamma \to \mu^+\mu^-$ events

For evaluating the MC background from $\gamma\gamma \to \mu^+\mu^-$events there are two possible methods. The first is very similar to the one adopted for evaluating the $e^+e^- \to \mu^+\mu^-$background. The second involves relaxing the cut on acollinearity (θ_{acol}) used in the $e^+e^- \to \tau^+\tau^-$preselection to suppress $\gamma\gamma \to \ell^+\ell^-$events, and observing the number of identified $\tau \to \mu\overline{\nu}_\mu\nu_\tau$ candidates in an region of θ_{acol} adjacent ($15^\circ < \theta_{acol} < 25^\circ$) to that for the signal $\tau \to \mu\overline{\nu}_\mu\nu_\tau$ candidates. One can expect the Monte Carlo to accurately predict for both $e^+e^- \to \tau^+\tau^-$and $\gamma\gamma \to \mu^+\mu^-$events the fraction that lie in this range, and for this number to accurately reflect the relative numbers seen in the signal region. The justification for this lies in the fact that most of the control sample from $e^+e^- \to \tau^+\tau^-$events that lie in this measured range are genuinely acollinear (due to the missing momenta of the neutrinos), and are not merely there due to mismeasurement in the tracking chambers.

The rest frame of lepton pairs from the $\gamma\gamma \to \ell^+\ell^-$process is preferentially boosted in the detector along a direction close to the beam axis, particularly for events where the beam particles remain untagged. This means that, whilst the typical 3D acollinearity of the two cones in 2-photon events events is larger than that from $e^+e^- \to \tau^+\tau^-$events, the acoplanarity will usually remain low.

Thus the method used to test the Monte Carlo estimate of the $e^+e^- \to \mu^+\mu^-$ background can be adapted to obtain corrections for the MC $\gamma\gamma \to \mu^+\mu^-$background estimate. The only difference to the method used for the $e^+e^- \to \mu^+\mu^-$background is in choosing a subsample from the barrel and endcap $\tau\to\mu\overline{\nu}_\mu\nu_\tau$ samples in which the $\gamma\gamma\to\mu^+\mu^-$ content is enhanced. This is done by choosing events in which **both** sides were identified as $\tau\to\mu\overline{\nu}_\mu\nu_\tau$ candidates, and requiring that $R_{total} < 0.3$, where R_{total} is defined in section 5.3.2. The uncorrected acoplanarity distributions for the background-enhanced subsamples can be seen in figure 7.5. It can be seen that for the barrel region that the background does not represent a significant proportion of the events in the first bin, and so, given also the limited statistics, any measurement obtained this way is essentially meaningless as a test of the background content. Therefore, another method must be used to test the $\gamma\gamma\to\mu^+\mu^-$ background for the barrel selections. For the endcap, however, the Monte Carlo predicts that roughly half of the events in the first acoplanarity bin are from the $\gamma\gamma\to\mu^+\mu^-$ background, and so a more meaningful test of the background content can be expected, despite the large statistical error:

$$C_{\gamma\gamma}^{e1} = 0.931 \pm 0.486(\text{data stat.}) \pm 0.327(\text{MC stat.}) = 0.931 \pm 0.586$$

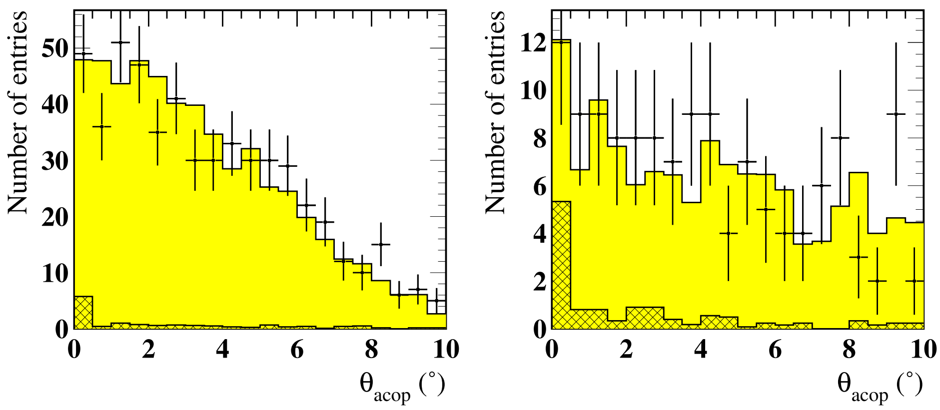

Figure 7.5: The acoplanarity distributions for events with $R_{total} < 0.3$ and two $\tau\to\mu\overline{\nu}_\mu\nu_\tau$ candidates identified in (a) the barrel and (b) the endcap regions of the detector. The hatched area shows the uncorrected contribution from the $\gamma\gamma\to\mu^+\mu^-$ background.

For the second method, the acollinearity cut used in the preselection is relaxed to 25° to allow in extra $\gamma\gamma\to\mu^+\mu^-$ (and $\gamma\gamma\to\tau^+\tau^-$) events, and then the $\tau\to\mu\overline{\nu}_\mu\nu_\tau$ selections B1 and E1 are applied to both sides. In evaluating the correction, the two-photon content of the samples is further enriched by requiring only events for which both sides are candidate $\tau \rightarrow \mu\overline{\nu}_{\mu}\nu_{\tau}$ decays. The correction is then obtained by considering the fraction,

$$f = \frac{N_2}{N_1 + N_2}$$

where N_1 is the number of events in the range $5^\circ < \theta_{acol} < 15^\circ$ whilst N_2 is the number for which $15^\circ < \theta_{acol} < 25^\circ$. The correction factor is taken to be the weight that must be applied to two-photon events in the MC sample in order that $f_{MC} = f_{data}$. The following results are thus obtained:

- The correction obtained for the **barrel** region is,

$$C^{b}_{\gamma\gamma}{=}1.122{\pm}0.236$$

- The second correction obtained for the **endcap** region is,

$$C^{e2}_{\gamma\gamma}{=}1.048{\pm}0.541$$

If it is assumed that the two endcap corrections $C^{e1}_{\gamma\gamma}$ and $C^{e2}_{\gamma\gamma}$ are independent, then they can be combined to give a single overall correction for the endcap:

$$C^{e}_{\gamma\gamma} = 0.994 \pm 0.398$$

The numbers for both the barrel and endcap are both consistent with unity. Also it is believed that the theoretical description of $\gamma\gamma \rightarrow \mu^+\mu^-$ events is well-known from QED calculations and that, for the energy range in which two-photon muons enter the $\tau \rightarrow \mu\overline{\nu}_{\mu}\nu_{\tau}$ samples, the Monte Carlo detector simulation should agree well with the data. Therefore, no correction is applied to MC 2-photon events in either the barrel or endcap by default. However, since $\gamma\gamma \rightarrow \ell^+\ell^-$ events represent a substantial proportion of the background, especially in the endcap regions (~1.0% compared to ~0.3% in the barrel region), the sensitivity of the fitted values of $\langle P_\tau \rangle$ and A^{FB}_{pol} to the MC estimate of the $\gamma\gamma \rightarrow \mu^+\mu^-$ background is tested by weighting all $\gamma\gamma \rightarrow \ell^+\ell^-$ events by the above values for $C^{b}_{\gamma\gamma}$ and $C^{e}_{\gamma\gamma}$. Systematic errors on the τ asymmetries are assigned accordingly.

Chapter 8

Monte Carlo selection efficiency

It is essential for this analysis to ensure that any momentum-dependence in the efficiencies of the $\tau\rightarrow \mu\overline{\nu}_{\mu}\nu_{\tau}$ selections B1, B2, E1 and E2 is accurately replicated by the Monte Carlo simulation. If the Monte Carlo fails to predict the momentum-dependence correctly systematic effects will arise in the measurement of $\langle P_{\tau}\rangle$ and A^{FB}_{pol}. This chapter describes the control samples used to compare selection efficiencies between real data and Monte Carlo events. It also details the resulting steps that are taken to correct the Monte Carlo estimates of the $\tau\rightarrow \mu\overline{\nu}_{\mu}\nu_{\tau}$ selection efficiencies.

8.1 Selection of non-τ control samples

Three non-τ control samples of $\mu^{\pm}$ tracks in different momentum ranges are used to correct the Monte Carlo estimate of the $\tau\rightarrow \mu\overline{\nu}_{\mu}\nu_{\tau}$ efficiency for passing certain selection cuts used in the barrel and endcap. The selection of each of these samples is outlined below, where each selection has been carefully optimized to produce a highly pure sample of muon tracks. Within selections B1, B2, E1 and E2 (see tables 6.1 and 6.3) the main cuts that need testing are those using the variables N^{MU}_{lyr}, χ_{match} and M_{inv}, and so control samples are chosen which contain muons whose distributions in these variables should reproduce those for muons of similar energies from $\tau \rightarrow \mu\overline{\nu}_\mu\nu_\tau$ decays. In order that the samples remain unbiased, the selections used rely on tightly identifying muons in the cone opposite to the one used for the sample. Thus in describing the selections the super(sub)script *opp* is used to denote the opposite cone.

8.1.1 Selection of a $e^+e^- \rightarrow \mu^+\mu^-$ control sample

The sample is taken from events which have passed the OPAL low multiplicity selection with the cosmic ray rejection cuts used by the Lepton Pair group [47]. The cuts listed below are then applied to get the final sample, where the cone to be used for the sample is taken to be the one containing the **lower** momentum track of the two. The data and Monte Carlo samples are split up into those identified in the barrel ($|\cos\theta| < 0.72$) and endcap ($0.72 < |\cos\theta| < 0.9$) regions.

- The event is required to contain two good charged cones, $N_{cone} = 2$
- Each cone is required to contain one good charged track, $N_{trk} = N^{opp}_{trk} = 1$
- The opposite cone is required to contain a high momentum muon identified in the barrel or endcap using the muon chambers and a cut on the total electromagnetic cluster energy in the cone,

$$x^{opp}_\mu \equiv \frac{p^{opp}_{trk}}{E_{beam}} > 0.95$$

$$|\cos\theta_{opp}| < 0.9$$

$$N^{MU,opp}_{lyr} \geq 4$$

$$E^{opp}_{clus} < 2\mathrm{GeV}$$

- The control sample only contains tracks which point to a region within the geometrical acceptance of the muon chambers, and for which,

$$0.8 < x_\mu < 1.2$$

$$|\cos\theta| < 0.9$$

- To suppress the background from $e^+e^-\to\tau^+\tau^-$ events the two muon tracks in the event are required to have a low acoplanarity (see figure 8.1),

$$\theta_{acop} < 0.2$$

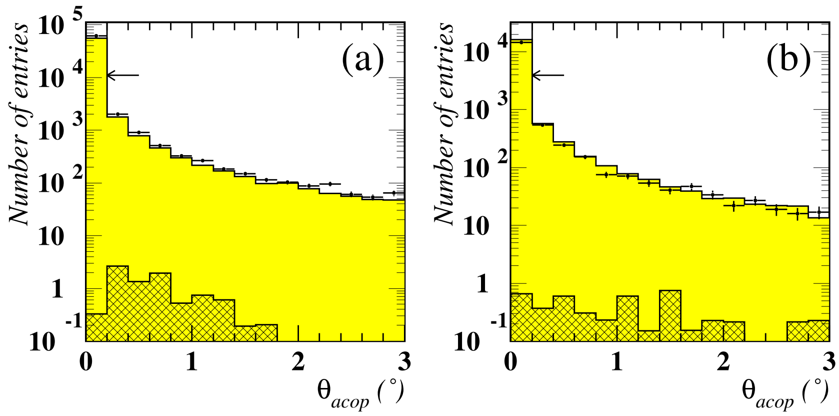

Figure 8.1: Distributions showing the effect of the cut on θ_{acop} in selecting a control sample of muons from $e^+e^-\to\mu^+\mu^-$ events in (a) the barrel and (b) the endcap regions of the detector. The hatched area shows the contribution from the $e^+e^-\to\tau^+\tau^-$ background.

The data sample is taken from all 1990-1994 LEP runs and the Monte Carlo sample uses the 800k $e^+e^-\to\mu^+\mu^-$ and 900k $e^+e^-\to\tau^+\tau^-$ events generated using the 1993 and 1994 configurations of the detector. The final numbers obtained are given in table 8.1.

	Barrel	Endcap
data sample	62053	14353
MC sample	273028.6	69610.6
MC τ-bgd	1.6	2.9

Table 8.1: The control samples of $e^+e^-\to\mu^+\mu^-$ events used to test the selection efficiency for high momentum $\mu^\pm$ tracks.

8.1.2 Selection of a $\gamma\gamma \to \mu^+\mu^-$ control sample

A sample of low energy muons is obtained from $\gamma\gamma \to \mu^+\mu^-$events, identified again using the OPAL low multiplicity selection with the Lepton Pair group's cosmic ray rejection applied [47]. The cuts listed below are then applied to get the final sample, where the cone to be used for the sample is taken to be the one containing the **higher** momentum track of the two. The data and Monte Carlo samples are split up into those identified in the barrel ($|\cos\theta| < 0.72$) and endcap ($0.72 < |\cos\theta| < 0.9$) regions.

- The event is required to contain two good charged cones with no neutral or badly measured charged cones, $N^{TOT}_{cone} = 2$
- Each cone is required to contain one good charged track, $N_{trk} = N^{opp}_{trk} = 1$
- The opposite cone is required to contain a muon identified using the muon chambers and a cut on the total electromagnetic cluster energy in the cone,

$$|\cos\theta_{opp}| < 0.97$$

$$N^{MU,opp}_{lyr} \geq 2$$

$$E^{opp}_{clus} < 2\,\mathrm{GeV}$$

- The control sample only contains tracks which point to a region within the geometrical acceptance of the muon chambers, and for which,

$$0.05 < x_\mu < 0.45$$

$$|\cos\theta| < 0.9$$

- Since the centre of mass frame for muon pairs from $\gamma\gamma \to \mu^+\mu^-$events is Lorentz boosted with respect to the detector frame, a cut is placed on the 3D acollinearity of the event to suppress the $e^+e^- \to \tau^+\tau^-$background (see figure 8.2),

$$\theta_{acol} > 18^\circ \text{ (barrel)}$$

$$\theta_{acol} > 16^\circ \text{ (endcap)}$$

- Since the beam particles in the $\gamma\gamma \to \mu^+\mu^-$events used remain untagged, the **net** transverse momentum of the two muon tracks seen in the event should be low. The following cut is therefore used to suppress the $e^+e^- \to \tau^+\tau^-$background (see figure 8.2),

$$\Delta p_t < 3.0\,\mathrm{GeV}/c \text{ (barrel)}$$

$$\Delta p_t < 1.6\,\mathrm{GeV}/c \text{ (endcap)}$$

- To suppress the background from $\tau \to e, \tau \to \mu$ events it is necessary to make a requirement on the total cluster energy seen in the near-side cone (see figure 8.2),

$$\frac{E_{clus}}{p_{trk}} < 0.6$$

- Most of the $\ell^+\ell^-$ pairs produced in $\gamma\gamma \to \ell^+\ell^-$events remain very close to the beam axis. Therefore, during the generation of Monte Carlo $\gamma\gamma \to \ell^+\ell^-$events, a number of cuts were used before detector reconstruction to select only those $\gamma\gamma \to \ell^+\ell^-$events which are likely to be observed in the detector. To ensure consistency between the data and Monte Carlo samples used here, the same cuts are reapplied after full detector reconstruction as follows. First there must be one particle with $p_{trk} > 4$ GeV and $|\cos\theta| < 0.95$. Second there must be two particles each with $p_{trk} > 0.5$ GeV and $|\cos\theta| < 0.95$, where the angle between them, θ_{12}, must satisfy $\cos\theta_{12} < -0.9$.

The data sample is taken from all 1990-1994 LEP runs and the Monte Carlo sample uses all the events generated using the 1993 and 1994 configurations of the detector. The final numbers obtained are given in table 8.2.

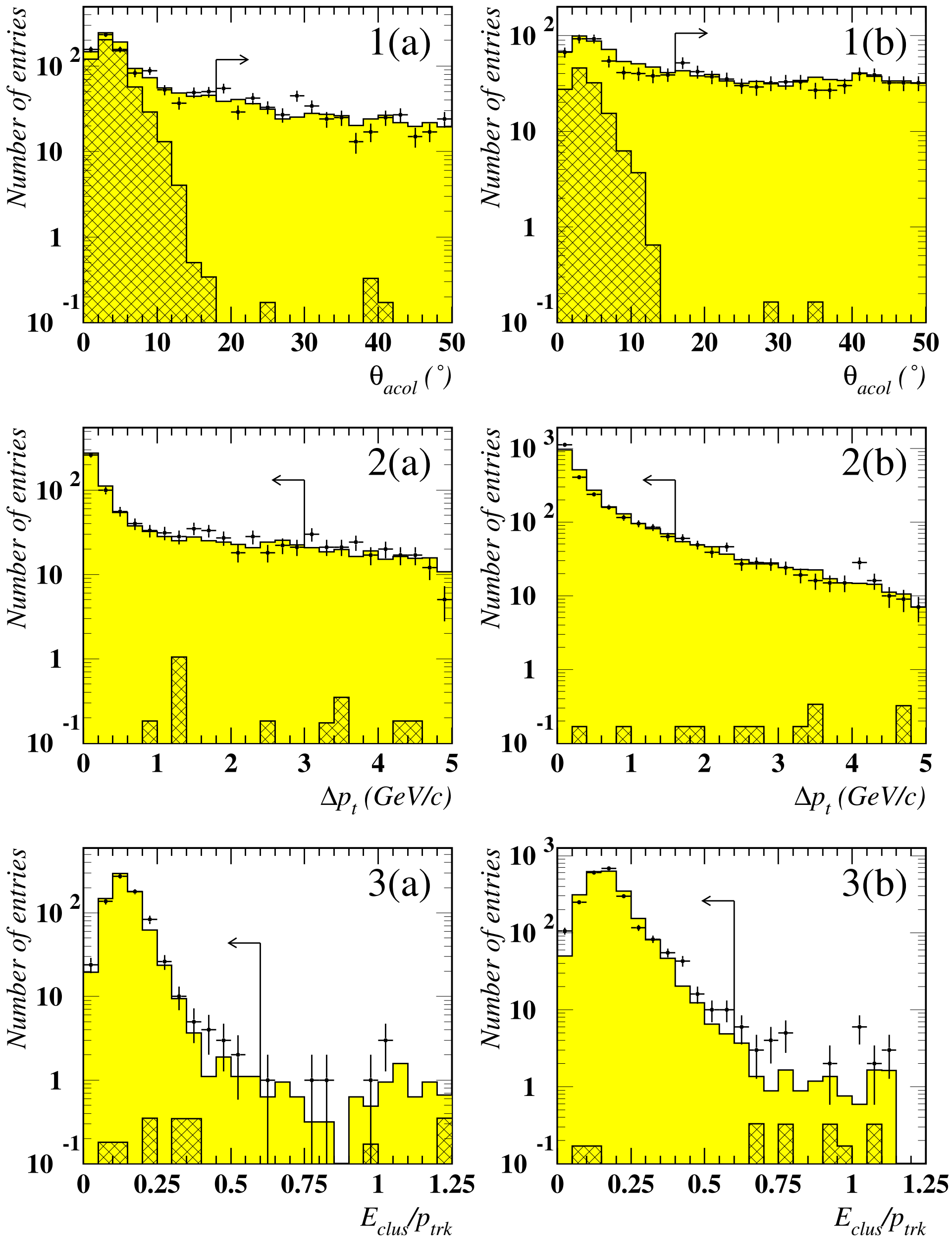

Figure 8.2: Distributions showing the effects of the cuts on θ_{acol} (1(a),1(b)), Δp_t (2(a),2(b)) and $\frac{E_{clus}}{p_{trk}}$ (3(a),3(b)) in selecting a control sample of muons from $\gamma\gamma \rightarrow \mu^+\mu^-$ events in (a) the barrel and (b) the endcap regions of the detector. The hatched area shows the contribution from the $e^+e^- \rightarrow \tau^+\tau^-$ background.

	Barrel	Endcap
data sample	744	2264
MC sample	4775.9	15572.0
MC τ-bgd	8.9	2.3

Table 8.2: The control samples of $\gamma\gamma \rightarrow \mu^+\mu^-$events used to test the selection efficiency for $\mu^\pm$ tracks.

8.1.3 Selection of a $e^+e^- \rightarrow \mu^+\mu^-$control sample accompanied by a hard bremsstrahlung photon

The two control samples obtained so far contain very few tracks in the momentum range, $0.3 < x_\mu < 0.8$. It is possible to get an independent sample of $\mu^\pm$ tracks in this range by looking for $e^+e^- \rightarrow \mu^+\mu^-$events in which a high energy bremsstrahlung photon is emitted by one of the muons. The muon in the event which has emitted the photon is therefore of lower energy and so is used as the control sample candidate in this case.

The sample is taken from events which have passed the OPAL low multiplicity selection with the cosmic ray rejection cuts used by the Lepton Pair group [47]. The cuts listed below are then applied to get the control sample. The data and Monte Carlo samples are split up into those identified in the barrel ($|\cos\theta| < 0.72$) and endcap ($0.72 < |\cos\theta| < 0.9$) regions.

- The event is required to contain two good charged cones, $N_{cone} = 2$
- Each cone is required to contain one good charged track, $N_{trk} = N_{trk}^{opp} = 1$
- The opposite cone is required to contain a high momentum muon identified in the barrel or endcap using the muon chambers and a cut on the total electromagnetic cluster energy in the cone,

$$x_\mu^{opp} \equiv \frac{p_{trk}^{opp}}{E_{beam}} > 0.95$$

$$|\cos\theta_{opp}| < 0.9$$

$$N_{lyr}^{MU,opp} \geq 2$$

$$E^{opp}_{clus} < 2\,\mathrm{GeV}$$

- There must be an electromagnetic cluster observed with no charged track assigned to it and a minimum raw energy of $E_\gamma > 4\,\mathrm{GeV}$. It must be within the same hemisphere as the candidate muon track, but (by considering its 3-momentum vector with respect to the origin) not lie within 5° of the track or any good electromagnetic cluster assigned to the cone. If more than one such photon is observed, then the one with the highest energy is taken to give E_γ.

- The control sample only contains tracks which point to a region within the geometrical acceptance of the muon chambers, and for which,

$$\frac{p_{trk}+E_\gamma}{E_{beam}} > 0.9 \text{ (barrel)}$$

$$\frac{p_{trk}+E_\gamma}{E_{beam}} > 0.8 \text{ (endcap)}$$

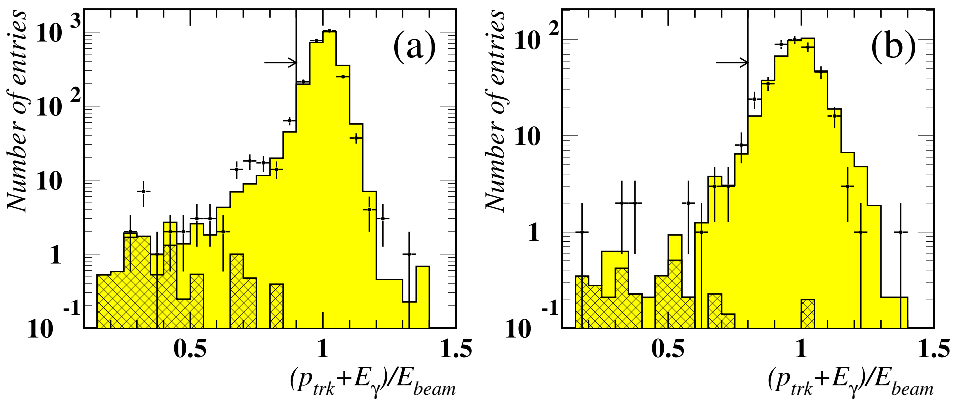

Figure 8.3: Distributions showing the effect of the cut on $\frac{p_{trk}+E_\gamma}{E_{beam}}$ in selecting a control sample of muons with hard bremsstrahlung radiation from $e^+e^- \to \mu^+\mu^-$ events in (a) the barrel and (b) the endcap regions of the detector. The hatched area shows the contribution from the $e^+e^- \to \tau^+\tau^-$ background. Note also that the plot includes all events in the momentum range $0.05 < x_\mu < 1.05$.

- The muon control sample uses only tracks in the momentum range, $0.25 < x_\mu < 1.05$

By only considering events in which the hard photon is isolated within the ECAL by an angle of at least 5°, it is hoped that all the other clusters in the cone containing the candidate muon remain entirely unaffected by its presence. This is particularly important since the invariant mass of the cone, M_{inv}, must be recalculated excluding the contribution of the bremsstrahlung photon if the photon is assigned to the cone. The M_{inv} variable is one of the ones to be tested using the control sample, and so it must remain unbiased.

The data sample is taken from all 1990-1994 LEP runs and the Monte Carlo sample uses all the events generated using the 1993 and 1994 configurations of the detector. The final numbers obtained are given in table 8.3.

	Barrel	Endcap
data sample	2145	381
MC sample	9606	1637
MC τ-bgd	0	0

Table 8.3: The control samples of $e^+e^-\to\mu^+\mu^-$events with hard bremsstrahlung radiation used to test the selection efficiency for $\mu^\pm$ tracks.

8.2 Combining the control samples

The momentum spectra of the data samples obtained for the three types of event are shown in figure 8.4 to give an idea of the statistical limitations to be expected for the bin-by-bin efficiency calculations. For each sample a number of the $\tau\to\mu\overline{\nu}_\mu\nu_\tau$ identification cuts are applied to the data and Monte Carlo, and a ratio of the efficiencies is obtained in each x_μ bin, taking into account also the small background. For the i^{th} bin,

$$C_\varepsilon^i = \frac{\varepsilon^i_{data}}{\varepsilon^i_{MC}}$$

The three samples are used to check the muon chamber identification (MCHID); first on its own (for correcting selection efficiencies for B2 and E2), and then in

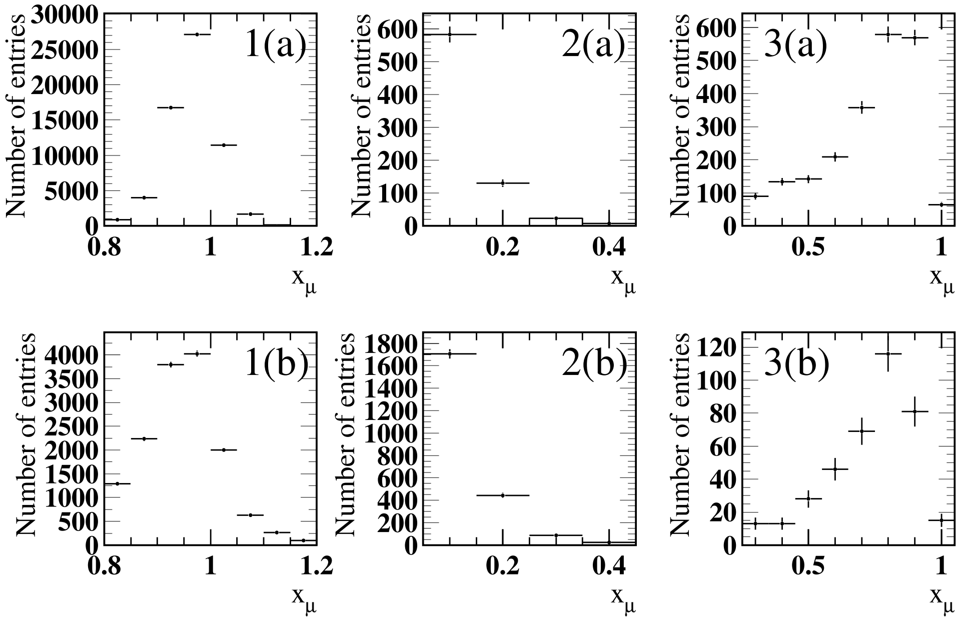

Figure 8.4: Momentum distributions for the control samples obtained from the data. Plots 1(a) and 1(b) are $e^+e^-\to\mu^+\mu^-$events identified in the barrel and endcap regions respectively; 2(a) and 2(b) are $\gamma\gamma\to\mu^+\mu^-$events, and 3(a) and 3(b) are radiative $e^+e^-\to\mu^+\mu^-$events.

combination with the M_{inv} cut (for testing selections B1 and E1). Figure 8.5 shows the variation in C_ε^i with x_μ for each of the samples in the barrel and endcap, and for the two sets of cuts being tested.

The C_ε^i numbers from each sample are combined to get an average for each of the 10 bins in x_μ, corresponding to the range 0.05 to 1.05. However, the statistical errors on C_ε^i from the $e^+e^-\to\mu^+\mu^-$sample are much smaller than those from the other two samples, since the sample itself is very much larger. Therefore, when $\langle C_\varepsilon\rangle^i$ is calculated, all events from the $e^+e^-\to\mu^+\mu^-$sample are considered to contribute to the final momentum bin $(0.95 < x_\mu < 1.05)$ only.

The justification for this can be clearly seen by considering the scenario in which values of $\langle C_\varepsilon\rangle^i$ are calculated with events from the $e^+e^-\to\mu^+\mu^-$sample being allowed to contribute to several momentum bins. The gradient of any subsequent straight-line fits applied to these binned values of $\langle C_\varepsilon\rangle^i$ as a function of x_μ, would be dominated by muons for which $x_\mu > 0.8$. This would be unsatisfactory for

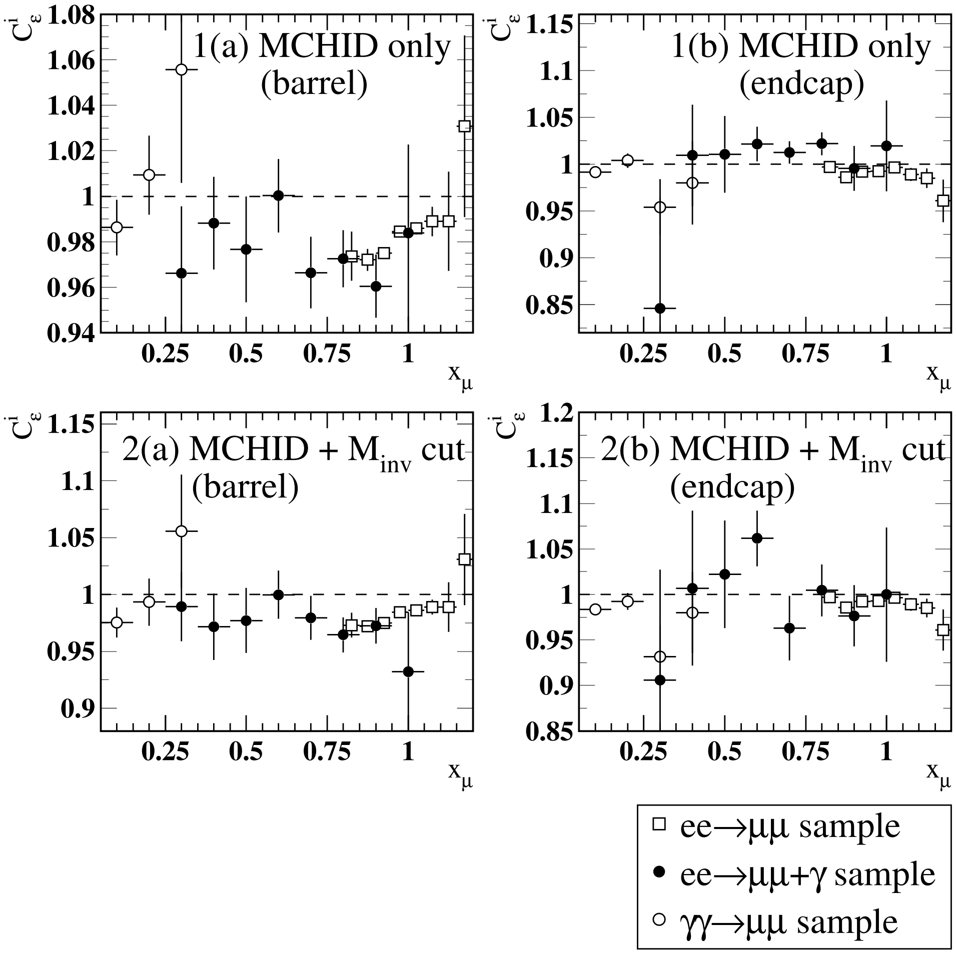

Figure 8.5: The C^i_ε distributions for muons from the control samples identified in (a) the barrel (b) the endcap region, where $C^i_\varepsilon = \varepsilon^i_{data}/\varepsilon^i_{MC}$. Plots 1(a) and 1(b) are obtained using the efficiencies for muons passing the muon chamber identification (MCHID) only (to test selections B2 and E2), whereas MCHID combined with a M_{inv} cut is used for plots 2(a) and 2(b) (to test selections B1 and E1).

two reasons. First, the true momenta of the muons from the $e^+e^- \to \mu^+\mu^-$ sample should all be nearly equal to E_{beam} with a small radiative tail. This implies that the measured momentum bias in C^i_ε would actually be dominated by events whose true momenta are very nearly the same ($x_{true} \simeq 1$). Second, such a straight-line fit would be relatively insensitive to muons from the other two samples in the momentum range $x_\mu < 0.75$, which is the region where the large majority of $\tau \to \mu\overline{\nu}_\mu\nu_\tau$ decays lie.

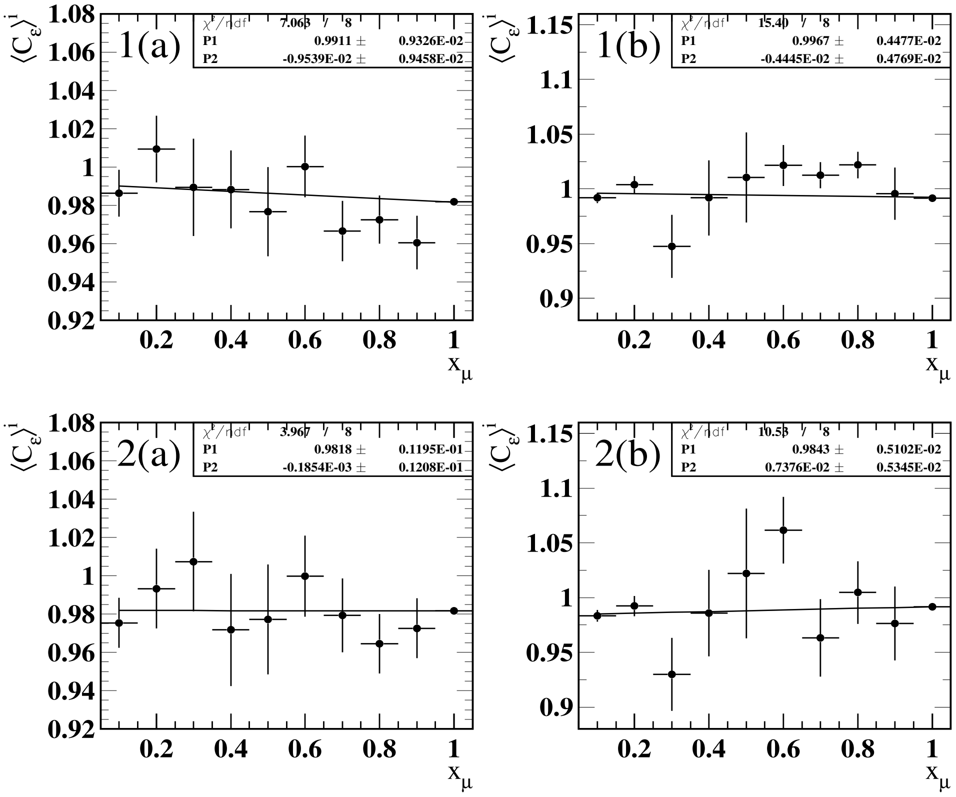

Figure 8.6: The $\langle C_\varepsilon \rangle^i$ distributions for muons from the control samples identified in (a) the barrel (b) the endcap region. Plots 1(a) and 1(b) are obtained using the efficiencies for muons passing the muon chamber identification (MCHID) only (to correct selections B2 and E2), whereas MCHID combined with a M_{inv} cut is used for plots 2(a) and 2(b) (to test selections B1 and E1). Furthermore a straight-line fit is applied to each distribution, the results of which are displayed in the top right hand corner of each plot.

Figure 8.6 shows the variation of $\langle C_\varepsilon \rangle^i$ with x_μ for the barrel and endcap samples, and for the two sets of cuts being tested (that is, the muon chamber identification (MCHID) on its own, and then MCHID combined with a cut on the invariant mass, M_{inv}).

8.3 Correcting the Monte Carlo selection efficiency

This section details how the binned corrections shown in figure 8.6 (and others) are used in this analysis. The main concern here is that the Monte Carlo correctly simulates the momentum spectra observed for positive and negative helicity $\tau \rightarrow \mu\overline{\nu}_{\mu}\nu_{\tau}$ decays after the selection criteria have been applied. Any discrepancies between data and Monte Carlo in estimating the overall efficiency with which muons pass the $\tau \rightarrow \mu\overline{\nu}_{\mu}\nu_{\tau}$ selection procedure are therefore less important than ensuring that the Monte Carlo correctly predicts how the selection efficiency may vary with momentum. Therefore, if linear fits are applied to the distributions shown in figure 8.6 to get momentum-dependent correction factors of the form,

$$C_{\varepsilon}(x_{\mu}) = P1 + P2 \cdot x_{\mu}$$

then it is the parameter $P2$ which is significant in altering the momentum spectra for MC $\tau \rightarrow \mu\overline{\nu}_{\mu}\nu_{\tau}$ decays.

This is the method adopted here, where the momentum-dependent correction functions $C_{\varepsilon}(x_{\mu})$ are obtained by fitting a straight line to correction factors binned in x_{μ}. These are used as weighting factors for MC $\tau \rightarrow \mu\overline{\nu}_{\mu}\nu_{\tau}$ decays when applying the selections B1, B2, E1 and E2 to $e^{+}e^{-} \rightarrow \tau^{+}\tau^{-}$events. The number of events subject to a particular correction is (in most cases) subsequently rescaled such that the overall normalisation remains unaffected. The one exception to this is the case in which corrections are applied to MC $\tau \rightarrow \mu\overline{\nu}_{\mu}\nu_{\tau}$ decays identified using the CALID part of selections B1 and B2, for reasons to be explained later in this section.

The first case to consider is that in which $\tau \rightarrow \mu\overline{\nu}_{\mu}\nu_{\tau}$ decays are identified using the muon chambers as part of selections B1 and E1. Here the M_{inv} cut is combined with MCHID and so the correction functions used are taken from the fits shown in plots 2(a) and 2(b) of figure 8.6:

$$C_\varepsilon(x_\mu) = \begin{cases} 0.98184 - 0.0001854 \cdot x_\mu & (\text{barrel - B1}) \\ 0.98430 - 0.0073763 \cdot x_\mu & (\text{endcap - E1}) \end{cases}$$

By default, both these corrections are applied to the relevant MC $\tau\rightarrow \mu\overline{\nu}_\mu\nu_\tau$ decays. As already stated, it is the gradient parameter $P2$ that is significant in correcting the Monte Carlo momentum spectra. Therefore, a systematic error is assigned on the fitted values of $\langle P_\tau \rangle$ and A_{pol}^{FB} according to the changes that occur when the value of $P2$ used is altered. If $P2$ is consistent with 0 (as is the case above for B1) the correction is merely set to 1 for all x_μ; otherwise $P2$ is varied according to the size of its error. This same treatment applies to the remaining efficiency corrections detailed in this chapter.

8.3.1 Testing the muon chamber selection using a $\tau\rightarrow\mu\overline{\nu}_\mu\nu_\tau$ sample

The remaining plots in figure 8.6 (1(a) and 1(b)) show the efficiency corrections for MCHID only (that is, not in combination with the M_{inv} cut), and so these are used to correct those MC $\tau\rightarrow \mu\overline{\nu}_\mu\nu_\tau$ decays which are identified using the muon chambers as part of selections B2 and E2. However, since this part of the B2/E2 selection procedures uses no information from the calorimeters, the MC efficiency estimate for muons detected this way may be further checked using control samples of $\tau\rightarrow \mu\overline{\nu}_\mu\nu_\tau$ decays identified using the ECAL and HCAL. This produces a separate set of binned correction factors which can be combined with those shown in figures 8.6.1(a) and 8.6.1(b). The two sets of numbers are combined before the straight-line fit is applied to obtain the correction functions.

The $\tau\rightarrow \mu\overline{\nu}_\mu\nu_\tau$control samples used to test the MCHID selection are identified in the barrel and endcap regions using a set of calorimeter cuts identical to those used for the CALID mentioned in chapter 6. In addition, it is required that the invariant mass,

$$M_{inv} < 0.3\,\mathrm{GeV}$$

The background from other τ decays for such a sample is estimated (using Monte Carlo events) to be about 0.5 (1.0)% in the barrel (endcap) region of the detector. Although the control sample is not completely independent of the main $\tau \rightarrow \mu\overline{\nu}_\mu\nu_\tau$ sample used to extract $\langle P_\tau \rangle$ and A^{FB}_{pol}, studies [50] show that for muons the correlation between the response in the calorimetery and that in the muon chambers can be neglected. Therefore, this $\tau \rightarrow \mu\overline{\nu}_\mu\nu_\tau$ sample can be used to obtain momentum-dependent corrections to the Monte Carlo MCHID efficiency, which can then be combined with those obtained using the $\gamma\gamma \rightarrow \mu^+\mu^-$ and $e^+e^- \rightarrow \mu^+\mu^-$ samples mentioned in the previous section. As before, the correction factor (C^i_μ) is calculated in the i^{th} momentum bin as the ratio of the data and MC efficiencies, where the data has first been corrected for its estimated background content. Figure 8.7 shows the binned values of C^i_μ for samples in the barrel and endcap regions, where a linear fit has been applied to each set of values.

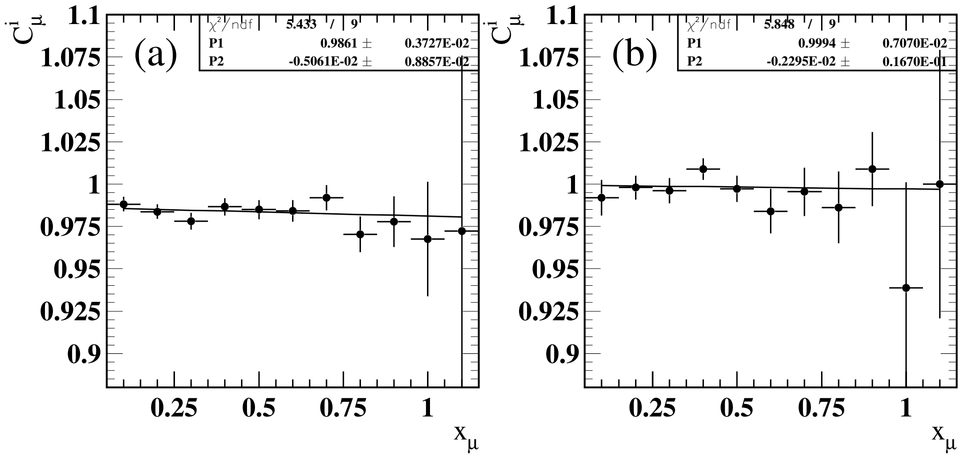

Figure 8.7: The C^i_μ distributions for the $\tau \rightarrow \mu\overline{\nu}_\mu\nu_\tau$ samples identified in (a) the barrel and (b) the endcap regions. A straight-line fit is applied to each distribution, the results of which are displayed in the top right hand corner of each plot.

As previously mentioned, the values of C^i_μ shown are comparable with the values of $\langle C_\varepsilon \rangle^i$ obtained by applying MCHID to the $\gamma\gamma \rightarrow \mu^+\mu^-$, $e^+e^- \rightarrow \gamma\mu^+\mu^-$ and $e^+e^- \rightarrow \mu^+\mu^-$ samples discussed in the previous section. Therefore, the binned values of $\langle C_\varepsilon \rangle^i$ are redefined by combining them with the values of C^i_μ to give a weighted mean. Figure 8.8 shows the variation of $\langle C_\varepsilon \rangle^i$ with momentum for the barrel and endcap regions, where C^i_μ has now also been incorporated. A correction function is obtained by performing a straight-line fit to these binned values of $\langle C_\varepsilon \rangle^i$, the results of which are included in the plots shown in figure 8.8 and give the following corrections:

$$C_\varepsilon(x_\mu) = \begin{cases} 0.98633 - 0.0047901 \cdot x_\mu & \text{(barrel - B2)} \\ 0.99897 - 0.0066374 \cdot x_\mu & \text{(endcap - E2)} \end{cases}$$

It is these functions that are then used to weight Monte Carlo $\tau \rightarrow \mu \overline{\nu}_\mu \nu_\tau$ decays identified by MCHID within the selections B2 and E2. The evaluation of systematic errors arising from uncertainties in selection efficiency is treated as in the case for selections B1 and E1.

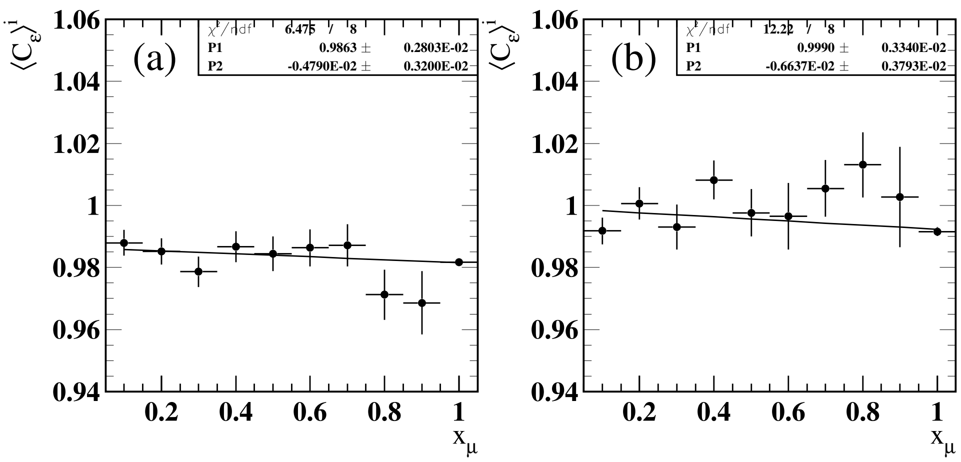

Figure 8.8: Distributions in $\langle C_\varepsilon \rangle$ obtained by applying MCHID to data and MC muon control samples in (a) the barrel and (b) the endcap regions. The values of $\langle C_\varepsilon \rangle$ are obtained by taking the mean of the values of $\langle C_\varepsilon \rangle$ (obtained using the non-τ samples) with the values of C_μ (obtained using the $\tau \rightarrow \mu \overline{\nu}_\mu \nu_\tau$ control sample). A straight-line fit is applied to each distribution, the results of which are displayed in the top right hand corner of each plot and are used as corrections functions for selections B2 and E2.

8.3.2 Testing the ECAL/HCAL selection cuts used in the barrel region

The $\tau \rightarrow \mu\overline{\nu}_\mu\nu_\tau$ selections B1 and B2 in the barrel region accept candidates which have failed the muon chamber cuts (MCHID), if they instead pass cuts made using the ECAL and HCAL (CALID). Since one of the requirements of CALID is that such τ decays must be only selected outside the geometrical acceptance of the muon chambers, the $\tau \rightarrow \mu\overline{\nu}_\mu\nu_\tau$ decays selected inside the geometrical acceptance using MCHID can therefore be used as an independent sample of muons with which to test the response of the ECAL and HCAL. These decays are divided into those which pass through a fully active region of the HCAL, and those which do not. The ECAL/HCAL cuts used in selection B1 and B2 are then applied to both (including the cut on M_{inv}) and the efficiencies for data and Monte Carlo events are compared in the usual way (that is, correcting for the hadronic background before evaluating the efficiencies). The ratios of the efficiencies are shown in figure 8.9, where C^{in}_{HC} and C^{out}_{HC} are the bin-by-bin ratios ($\varepsilon^i_{dat}/\varepsilon^i_{MC}$) for those tracks within the sample which are inside and outside the geometrical acceptance of the HCAL respectively.

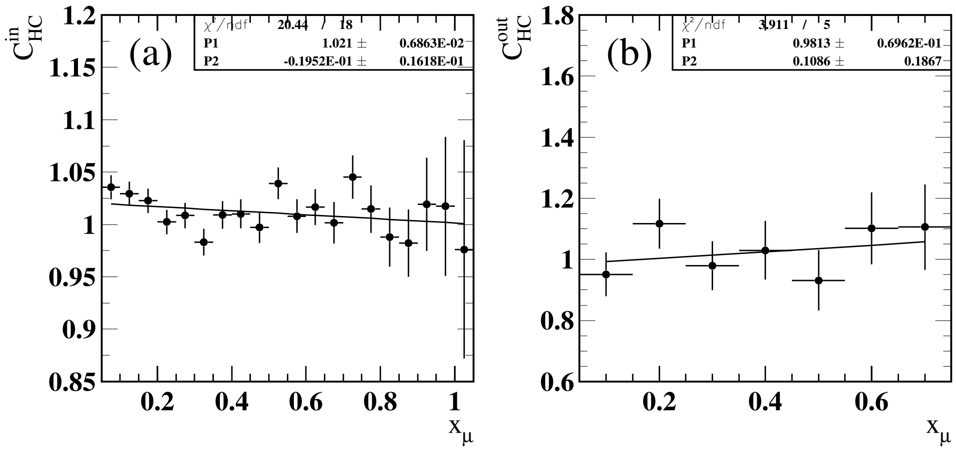

Figure 8.9: The distributions for (a)C^{in}_{HC} and (b)C^{out}_{HC} obtained using a $\tau \rightarrow \mu\overline{\nu}_\mu\nu_\tau$ samples identified in the barrel within the geometrical acceptance of the muon chambers. A 1st order polynomial fit is applied to each distribution, the results of which are displayed in the top right hand corner of each plot.

Figure 8.9 shows that, when a straight-line is fitted to C_{HC}^{in}, the gradient is not consistent with being 0 to within 1σ, suggesting that there is a momentum bias in the Monte Carlo simulation of the ECAL and HCAL response to muons. A momentum-dependent correction based upon the results of the fit is therefore used to weight Monte Carlo $\tau \rightarrow \mu\overline{\nu}_\mu\nu_\tau$ decays which are identified by CALID within selections B1 and B2, and which point to an fully active region of the HCAL. This is,

$$C_{HC}^{in}(x_\mu) = 1.020980 - 0.019522 \cdot x_\mu$$

For the C_{HC}^{out} distribution, statistical evidence of a momentum bias in the MC efficiency is less conclusive due to the small number of events in the samples, particularly for $x_\mu > 0.75$. The gradient obtained from the fit is consistent with 0, and has a large error. Therefore those $\tau \rightarrow \mu\overline{\nu}_\mu\nu_\tau$ decays passing the CALID selection in the barrel whose trajectories do not point to an fully active region of the HCAL are not corrected.

However, it should be noted that, if C_{HC}^{in} and C_{HC}^{out} are determined for all x_μ (that is, ignoring momentum-dependence), the following numbers are obtained:

$$\langle C_{HC}^{in} \rangle = 1.0135 \pm 0.0075$$

$$\langle C_{HC}^{out} \rangle = 1.030 \pm 0.038$$

where this implies that the muons in the data pass the CALID criteria with greater efficiency than those in Monte Carlo events. If anything, the opposite is observed for tests involving the cuts used in MCHID, and so this partly accounts for the fact that the fraction of $\tau \rightarrow \mu\overline{\nu}_\mu\nu_\tau$ candidates in the barrel identified by CALID as opposed to MCHID is larger for data events compared to the Monte Carlo. A contribution to this discrepancy is also brought about by muon chamber efficiency near the edges of MB dropping off slightly more quickly for events in the data (see figure D.1). The CALID detection scheme is there to counteract this very problem, and so it is important that the overall CALID efficiency (for all x_μ) is well simulated. Therefore, after the $C_{HC}^{in}(x_\mu)$ weighting has been applied to MC $\tau \rightarrow \mu\overline{\nu}_\mu\nu_\tau$ candidates identified using CALID, the overall normalisation of such events is allowed to have changed. This effect is considered in the evaluation of systematic errors on $\langle P_\tau \rangle$ and A^{FB}_{pol} in addition to the effect of altering the value of $P2$.

Chapter 9

Extraction of $\langle P_\tau \rangle$ and A_{pol}^{FB}

This chapter describes the analysis that has been performed to extract values for $\langle P_\tau \rangle$ and A_{pol}^{FB} from the $\tau \rightarrow \mu \overline{\nu}_\mu \nu_\tau$ samples obtained using selections B1, B2, E1 and E2 (see tables 6.1 and 6.3 in chapter 6). First the binned maximum likelihood fit that is used will be described at length, followed by descriptions of several other methods that have been used to ensure that the errors arising from all potential systematic effects may be determined. The results of the fits for each of the four selections are given, and then the results for selection B1 are combined with those from E1, and similarly for B2 and E2. The combination that gives the lowest errors for $\langle P_\tau \rangle$ and A_{pol}^{FB} is quoted as the final result, whilst the remaining combination exists to provide a useful cross check. In the conclusions at the end of the chapter these final numbers are discussed in the light of previous measurements of $\langle P_\tau \rangle$ and A_{pol}^{FB} made using $\tau \rightarrow \mu \overline{\nu}_\mu \nu_\tau$ decays at OPAL.

9.1 The binned maximum likelihood fit

The basic principle behind the method used to simultaneously extract $\langle P_\tau \rangle$ and A_{pol}^{FB} is as follows. Linear combinations of binned distributions for positive and negative helicity Monte Carlo τ decays are fitted to the corresponding real data distribution, where the real and simulated data events have undergone exactly the same $\tau \rightarrow \mu\overline{\nu}_\mu\nu_\tau$ selection procedures. This fitting method was briefly introduced earlier (in chapter 2), and, although based on similar procedures used by OPAL and other LEP experiments, has been developed independently for this analysis.

The same method is applied to samples obtained in the barrel and endcap regions, where the fitting procedure only permits any one of selections B1, B2, E1 or E2 to be used at any one time. The chosen $\tau \rightarrow \mu\overline{\nu}_\mu\nu_\tau$ selection is applied to $e^+e^- \rightarrow \tau^+\tau^-$events identified from on-peak data taken in the years 1990 to 1994 and all on-peak Monte Carlo events generated using the 1993 and 1994 detector configurations.

Any $\tau \rightarrow \mu\overline{\nu}_\mu\nu_\tau$ candidates thus identified from the real data samples are binned according to x_μ (the track momentum normalised to the beam energy) and $\cos\theta$ (defined using the track in CT only). The variable d_{ij} is defined to be the number of real data candidates in the ij^{th} $(\cos\theta, x_\mu)$-bin. During the process of binning the charge of the tracks must be considered. By convention $\langle P_\tau \rangle = \langle P_{\tau^-} \rangle$, and to a very good approximation $\langle P_{\tau^-} \rangle = -\langle P_{\tau^+} \rangle$ using the arguments outlined in chapter 2. Therefore the sign of $\cos\theta$ must be reversed for all $\tau^+ \rightarrow \mu^+\overline{\nu}_\mu\nu_\tau$ candidates before binning, where henceforth in this section we shall mostly only refer to the τ^-. Naturally the method relies on there being very few tracks with mismeasured charge in the data, and this problem is addressed later in the chapter.

Consider now the number of $\tau \rightarrow \mu\overline{\nu}_\mu\nu_\tau$ candidates within the ij^{th} bin. According to Poisson statistics the probability of observing d_{ij} data events in each bin is given as

$$e^{-f_{ij}} \frac{f_{ij}^{d_{ij}}}{d_{ij}!}$$

where f_{ij} is the predicted number in a given bin and is appropriately normalised such that $\sum_{ij} f_{ij} = \sum_{ij} d_{ij}$. The principle behind the binned maximum likelihood method used here is that if f_{ij} depends on some input parameter (like $\langle P_\tau \rangle$, for example), then this parameter can be varied until the total probability summed over all i and j (the likelihood) is maximised. For convenience, the logarithm of the probabilities can be taken and so (omitting constant factorials) the function that needs to be maximimised within the fit is the (log-)likelihood given by,

$$\ln \mathcal{L} = \sum_{ij} d_{ij} \ln f_{ij} - f_{ij} \tag{9.1}$$

For the fit under consideration here the values of f_{ij} are evaluated by using Monte Carlo events to predict the number of candidates that should be seen in the ij^{th} bin, given different input values of $\langle P_\tau \rangle$. Monte Carlo $\tau \rightarrow \mu \overline{\nu}_\mu \nu_\tau$ candidates come from three possible sources, and so a further bin index k is used to denote each of these, where,

$$k = \begin{cases} 1 & \text{candidate from } \tau^\mp \text{ with helicity}=\mp\frac{1}{2} \\ 2 & \text{candidate from } \tau^\mp \text{with helicity}=\pm\frac{1}{2} \\ 3 & \text{candidate from non-}\tau\text{-pair event} \end{cases}$$

The following naming conventions are thus used for the total number of Monte Carlo events arising from each possible source k after applying the $\tau \rightarrow \mu \overline{\nu}_\mu \nu_\tau$ selection to all types of event:

$$N_k = \sum_{ij} W_{ijk} a_{ijk} \quad \text{and} \quad N_{MC} = \sum_{k}^{3} N_k \tag{9.2}$$

The weighting of events has been included in the calculation of these numbers and enters through the bin-averaged terms W_{ijk}. For instance, non-τ events have to be weighted to give the same integrated luminosity as τ events, whilst the τ events themselves are weighted to correct for the obsolete branching ratios used as inputs during event generation. In addition, the background and efficiency corrections described in chapters 7 and 8 have also used to weight events. The terms a_{ijk} represent the unweighted number of events in a given bin. It is important know the unweighted numbers a_{ijk} since they are subject to statistical fluctuations, the treatment of which will be discussed in the next section.

Returning to equation 9.1 we may define the general form for the f_{ij} terms as,

$$f_{ij} = \left(\frac{N_D}{N_{MC}} \right) \sum_{k=1}^{3} P_k F_{ijk} \tag{9.3}$$

where the quantity F_{ijk} is the probability density function for source k, and so represents the fraction of MC events from source k that lie in the ij^{th} bin:

$$F_{ijk} = \frac{W_{ijk}a_{ijk}}{\sum_{ij} W_{ijk}a_{ijk}} = \frac{W_{ijk}a_{ijk}}{N_k} \tag{9.4}$$

However, more important in equation 9.3 is the quantity P_k, which is the total number of Monte Carlo events from source k that is expected given the overall size of the Monte Carlo sample (N_{MC}) and the current fit value for $\langle P_\tau \rangle$.[1] The values of f_{ij} are normalised to the overall size of the real data sample by the factor in brackets outside the summation. With each iteration of the fit, therefore, it can be seen that only P_k in equation 9.3 should change, and is defined as follows for the three possible values of k:

$$P_k = \begin{cases} \frac{1}{2}\left[1 - (\langle P_\tau \rangle + \Delta P_\tau^\varepsilon)\right] \cdot (N_1 + N_2) & (k=1) \\ \frac{1}{2}\left[1 + (\langle P_\tau \rangle + \Delta P_\tau^\varepsilon)\right] \cdot (N_1 + N_2) & (k=2) \\ N_3 & (k=3) \end{cases} \tag{9.5}$$

It is the underlying polarisation, $\langle P_\tau \rangle$, which gives the following expressions for the relative cross sections of positive and negative helicity τ^- particles before selection criteria are applied:

$$\frac{1}{2}(1 - \langle P_\tau \rangle) = \frac{\sigma_-}{\sigma_+ + \sigma_-} \quad \text{and} \quad \frac{1}{2}(1 + \langle P_\tau \rangle) = \frac{\sigma_+}{\sigma_+ + \sigma_-} \tag{9.6}$$

However, since the momentum spectra of the two helicity states are markedly different and since also the efficiencies of the various $\tau \rightarrow \mu\overline{\nu}_\mu\nu_\tau$ selections used are momentum-dependent, one expects the actual polarisation present in the final data samples of $\tau \rightarrow \mu\overline{\nu}_\mu\nu_\tau$ decays to be different from the underlying fit value, $\langle P_\tau \rangle$. This effect is corrected for by the inclusion of the term $\Delta P_\tau^\varepsilon$ seen in equations 9.5, where this is calculated using MC events (with all efficiency corrections applied). The value of $\Delta P_\tau^\varepsilon$ is typically about -0.014, and so a systematic error on the final fit value of $\langle P_\tau \rangle$ must be assigned to account for the error on $\Delta P_\tau^\varepsilon$.

In order to make the fitting procedure sensitive to A_{pol}^{FB}, one can assume that the detector is symmetric about $\cos\theta = 0$, and bin all Monte Carlo τ decays ($k \leq 2$)

[1] In other words, P_k is defined such that $\sum_k P_k = \sum_k N_k = N_{MC}$.

according to $|\cos\theta|$. Consider the following expression for the differential cross section of the τ^- in the improved Born approximation:

$$\frac{d\sigma^{\pm}}{d\cos\theta} = C\left[(1 \pm \langle P_\tau \rangle) \cdot \left(1+\cos^2\theta\right) + \frac{8}{3}\left(A^0_{FB} \pm A^{FB}_{pol}\right)\cos\theta\right] \qquad (9.7)$$

where the $\pm$ indicate the negative and positive helicity states of the τ^-. From this equation it can be seen that for τ^- decays of a given helicity state and in a given $|\cos\theta|$ bin, the anti-symmetric $\cos\theta$ terms in equation 9.7 cancel for the forward ($\cos\theta > 0$) and backward ($\cos\theta < 0$) hemispheres (under the symmetric detector assumption). Therefore, to a good approximation, distributions binned in $|\cos\theta|$ for MC τ decays of a given helicity state are independent of the value of A^{FB}_{pol} used by the MC program KoralZ4.0 during event generation. The current fit value of A^{FB}_{pol} may therefore be imposed instead by using equation 9.7 to predict, for MC $\tau \rightarrow \mu\overline{\nu}_\mu\nu_\tau$ decays of a given helicity and within a particular $|\cos\theta|$ bin, the relative fractions that exist in the forward and backward hemispheres. Note that, within equation 9.7, the value used for the pole forward-backward asymmetry, A^0_{FB}, is constant throughout the fit and is taken to be the measured value in the $\mathrm{Z}^0 \rightarrow \tau^+\tau^-$ channel [10] at $\sqrt{s} = M_{\mathrm{Z}}$.

It is now appropriate to define the probability densities $G_{|i|jk}$ for negative (k=1) and positive (k=2) helicity MC τ decays when binned in $|\cos\theta|$ rather than $\cos\theta\,(F_{ijk})$,

$$G_{|i|jk} = \frac{W_{|i|jk}\,a_{|i|jk}}{\sum_{|i|j} W_{|i|jk}\,a_{|i|jk}} = \frac{W_{|i|jk}\,a_{|i|jk}}{N_k} \qquad (9.8)$$

where $|i|$ is used to denote the appropriate $|\cos\theta|$ bin. These probability densities may be used in redefining the expression for f_{ij}, where now,

$$f_{\pm ij} = \left(\frac{N_D}{N_{MC}}\right)\left[\sum_{k=1}^{2} P_k \left(\frac{\sigma_{\pm ik}}{\sigma_{+ik}+\sigma_{-ik}}\right) G_{|i|jk} + P_3 F_{\pm ij3}\right] \qquad (9.9)$$

Here $\pm$ has been placed in front of the index i to distinguish between $\cos\theta$ bins in the forward and backward directions. Average values of $\cos\theta$ and $\cos^2\theta$ for τ MC decays in $|\cos\theta|$ bin $|i|$ are used in calculating the values of $\sigma_{\pm ik}$ from equation 9.7. In addition, the corrections which account for the effects of γ exchange, γZ interference and QED photonic corrections are taken into account in evaluating the values of $f_{\pm ij}$. This will be discussed again in section 9.5.

In discussing how the effects of Monte Carlo statistical fluctuations are included in the fit, it is desirable that a more general form than equation 9.9 is used for $f_{\pm ij}$. If the density functions $G_{|i|j}$ and $F_{\pm ij3}$ are substituted using equations 9.4 and 9.8, then we may write:

$$f_{\pm ij} = \left(\frac{N_D}{N_{MC}}\right)\left[\sum_{k=1}^{2} P_k \left(\frac{\sigma_{\pm ik}}{\sigma_{+ik}+\sigma_{-ik}}\right)\frac{W_{|i|jk}a_{|i|jk}}{N_k} + P_3 \frac{W_{\pm ij3}a_{\pm ij3}}{N_3}\right] \tag{9.10}$$

This may now be written in the following more general form in which the $a_{|i|jk}$ and $a_{\pm ijk}$ terms (which are subject to the Monte Carlo statistical fluctuations) are separated from the other terms.

$$f_{\pm ij} = \sum_{k=1}^{2}(w_{\pm ijk}a_{|i|jk}) + w_{\pm ij3}a_{\pm ij3} \tag{9.11}$$

Thus all the other terms present in equation 9.10 are collected together into single weighting terms w_{ijk} which vary with each iteration of the fit.

Now that the evaluation of f_{ij} and d_{ij} used in equation 9.1 have been fully discussed, it remains to briefly describe how the $\ln \mathcal{L}$ function is maximized. This is done using a package called MINUIT [18], where in fact it is $(-\ln \mathcal{L})$ that is used by MINUIT since the program only allows for minimization. Starting values for $\langle P_\tau \rangle$ and A^{FB}_{pol}, as well as step sizes for varying them during the fit, are specified and then MINUIT calculates the values of $\langle P_\tau \rangle$ and A^{FB}_{pol} for which $(-\ln \mathcal{L})$ was minimized, along with their statistical errors.

9.2 Incorporating Monte Carlo statistics

The fitting method as it stands assumes that the values of f_{ij} are not subject to statistical fluctuations, and so the errors on $\langle P_\tau \rangle$ and A^{FB}_{pol} returned from the fit by MINUIT only account for statistical fluctuations in the real data. However, it can seen from Equation 9.11 that the predicted values in each bin rely on $a_{|i|jk}(a_{\pm ijk})$, the unweighted number of Monte Carlo events from source k in bin $|i|j$ (or $\pm ij$). There will be some bins where the value of $a_{|i|jk}$ or $a_{\pm ijk}$ is low (or even zero), and so a second fit is performed where the effects of Monte Carlo statistical fluctuations have been incorporated into the likelihood function using methods based on those described in [9] (the necessary changes made to $\ln\mathcal{L}$ are discussed in appendix E). The error returned by MINUIT for this second fit is larger, and is taken to be the quadratic sum of the data and MC statistical errors, where the former is known from the first fit. Thus the MC statistical error can be evaluated and included as part of the overall systematic error. The final values used for $\langle P_\tau \rangle$ and A^{FB}_{pol} are also taken from this second fit.

From [9] the general expression for a maximum likelihood function with the effects of Monte Carlo statistical fluctuations incorporated, is given by:

$$\ln\mathcal{L} = \sum_{ij} (d_{ij} \ln f_{ij} - f_{ij}) + \sum_{ij} \sum_{k=1}^{3} (a_{ijk} \ln A_{ijk} - A_{ijk}) \tag{9.12}$$

where the number predicted to be in each bin f_{ij} is now taken to be,

$$f_{ij} = \sum_{k=1}^{3} w_{ijk} A_{ijk} \tag{9.13}$$

A_{ijk} is the expected number of MC events and, in general, differs from the actual unweighted number of MC events observed in that bin, a_{ijk}. For the case in question here, however, the situation is complicated by the fact that the Monte Carlo samples used in the forward and backward hemispheres for $k \leq 2$ are the same. Therefore, equation 9.12 is rewritten to treat the $\cos\theta < 0$ and $\cos\theta > 0$ bins simultaneously:

$$\begin{aligned} \ln\mathcal{L} &= \sum_{|i|j} [\, (d_{+ij} \ln f_{+ij} - f_{+ij} + d_{-ij} \ln f_{-ij} - f_{-ij}) \\ &+ \sum_{k=1}^{2} \left(a_{|i|jk} \ln A_{|i|jk} - A_{|i|jk} \right) \\ &+ (a_{+ij3} \ln A_{+ij3} - A_{+ij3} + a_{-ij3} \ln A_{-ij3} - A_{-ij3}) \,] \end{aligned} \tag{9.14}$$

The indices $|i|$ and $\pm i$ have again been used to distinguish between quantities binned in $|\cos\theta|$ and $\cos\theta$ respectively, whilst the $f_{\pm ij}$ values are now given by,

$$f_{\pm ij} = \sum_{k=1}^{2} (w_{\pm ijk} A_{|i|jk}) + w_{\pm ij3} A_{\pm ij3} \tag{9.15}$$

This function, as it stands, contains too many unknowns for MINUIT to handle. As is described for the general case in [9], analytical methods are applied to solve for the terms $A_{|i|jk}$ and $A_{\pm ij3}$, thereby reducing the number of unknowns. The method for this is outlined in Appendix E, where these have been adapted from those used in [9] to handle the problem of treating the forward and backward hemispheres simultaneously.

9.3 Charge misassignment

It is important for $\tau \rightarrow \mu\overline{\nu}_\mu\nu_\tau$ candidates identified from real data events to have correctly measured charge, since the sign of $\cos\theta$ for candidates coming from τ^+ decays must be reversed before binning. Charge mismeasurement would therefore result in the measured value of $\langle P_\tau \rangle$ being closer to zero. The effect is momentum-dependent since higher momentum tracks are straighter and therefore more likely to have their curvature mismeasured. This will lead to the biasing of the momentum spectra, and hence also changes in the measured value of $\langle P_\tau \rangle$. It is dangerous, however, to merely exclude events in which both cones would appear to have the same measured charge. This is because such events occur with less frequency in the Monte Carlo, and so the extent to which momentum spectra might be biased by their omission would be different for data and Monte Carlo events. Instead, for events where both cones contain single tracks with the same charge, it is possible to construct a probability for each track that its measured charge is incorrect, P^q_{mism}. The charge of a candidate $\tau \rightarrow \mu\overline{\nu}_\mu\nu_\tau$ decay may therefore be reversed on the basis that its value of P^q_{mism} is higher that of the opposite track in the event.

There are a certain number of reasons why charged tracks in the central tracking detector (CT) have mismeasured charges. Usually it is because the track is travelling across an anode plane in CJ or because it passes through an inactive region of CV and/or CZ. In the endcap, none of the tracks have CZ hits of course, and additionally there is the problem that the wire coverage in CJ drops off with increasing $|\cos\theta|$. By using the likelihood measurement, all these factors can be combined into a single probability that the charge is mismeasured.

The basis of the likelihood method is as follows. Suppose that the variable x_i is the i^{th} one of N_{var} possible variables that could be used to construct this probability. It is then possible to determine probability density functions $f_j^i(x_i)$ for the different track types j (j is 1 for tracks with mismeasured charge or 2 for all other tracks) where these must all be normalised to unity and are assumed to be uncorrelated:

$$\int f_j^i(x_i)\mathrm{d}x_i = 1$$

For each variable, the probability $e_j^i(x_i)$ that the track is of type j is given by,

$$e_j^i(x_i) = \frac{f_j^i(x_i)}{\sum_{j=1}^{2} f_j^i(x_i)}$$

These single-variable probabilities can then be combined into a single quantity, $E_j(\vec{x})$:

$$E_j(\vec{x}) = \prod_{i=1}^{N_{var}} e_j^i(x_i)$$

Finally the probability $P_j(\vec{x})$ that the track is of type j using all N_{var} variables is given by,

$$P_j(\vec{x}) = \frac{E_j(\vec{x})}{\sum_{j=1}^{2} E_j(\vec{x})}$$

where here we require $P^q_{mism} = P_1(\vec{x})$, the probability that the charge has been misassigned. For determining the probabilities $P_j(\vec{x})$ variables must be chosen which give good discrimination between tracks with correct charge measurement and those where the charge is mismeasured. For tracks in the barrel region, the following variables are used:

- the number of axial CV hits, N^a_{CV}
- the number of stereo CV hits, N^s_{CV}
- the number of CZ hits, N_{CZ}
- the variable, ϕ^q_{CJ}, which is defined as,

$$\phi^q_{CJ} = \frac{7.5 + Q_{meas}(\phi_{CJ} - 7.5)}{1.5}$$

where ϕ^q_{CJ} gives a measurement of the track position within a CJ sector, and includes charge dependence to optimize the difference in the density functions between tracks with correct and incorrect charge assignments. For tracks in the endcap region the number of CJ hits, N_{CJ}, is used in place of N_{CZ}.

Discrete values of the normalised probability density functions are determined for each variable using 1-prong decays from Monte Carlo $e^+e^- \to \tau^+\tau^-$ events. Using the MC tree information to pick out those tracks with misassigned charge, the τ decays are also further subdivided into loosely identified muons (using the "loose" muon identification mentioned throughout this thesis), electrons (for which the highest energy cluster in the cone, $E_{clus} > 0.8 p_{trk}$) or hadrons (any other cones containing a single charged track). A separate set of functions is therefore determined for each particle type, and in different regions of the detector (the barrel and endcap regions being defined in the usual way).

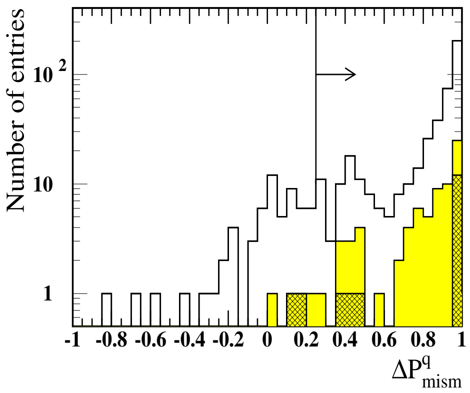

Figure 9.1: Distributions in ΔP^q_{mism} for MC $e^+e^- \to \tau^+\tau^-$ events in the range $|\cos\theta| < 0.90$), where both cones contain a single track of the same charge. In addition at least one of the tracks is identified as a $\tau \to \mu\overline{\nu}_\mu\nu_\tau$ decay by either selection B1 or E1. The shaded region shows the subset of events for which it is the muon track whose charge is misassigned, whilst the hatched region shows events where both cones are identified as muons.

Figure 9.1 shows the difference in probability ΔP^q_{mism} for MC $e^+e^- \to \tau^+\tau^-$ events in which both cones contain a single track of the same measured charge, and where at least one of the cones is identified as a $\tau \to \mu\overline{\nu}_\mu\nu_\tau$ candidate (combining the barrel and endcap selections B1 and E1). The variable ΔP^q_{mism} is defined such that,

$$\Delta P^q_{mism} = P^{qBAD}_{mism} - P^{qOK}_{mism}$$

where P^{qBAD}_{mism} is the probability of charge misassignment for the track in the event whose measured charge is actually incorrect, whilst P^{qOK}_{mism} is the misassigment probability for the track that is well measured. If the method works, it would therefore be expected that $P^{qBAD}_{mism} > P^{qOK}_{mism}$ for nearly all tracks, and, apart from a handful of tracks that are mostly in the endcap, this is indeed the case. For Monte Carlo $e^+e^- \rightarrow \tau^+\tau^-$events, the method is 100% efficient at picking out the misassigned charge in events containing two identified $\tau \rightarrow \mu\overline{\nu}_\mu\nu_\tau$ candidates with the same measured charge (although only 11 (6) such events were observed in the barrel (endcap) region out of 900k generated events). For events containing a single $\tau \rightarrow \mu\overline{\nu}_\mu\nu_\tau$ candidate, the charge of the muon track is reassigned if,

$$\Delta P^q_{mism} > 0.25$$

This results in 27 of the 28 (barrel) MC $\tau \rightarrow \mu\overline{\nu}_\mu\nu_\tau$ candidates with charge misassignment having their charges correctly reassigned (31 out of 32 in the endcap). Conversely there are 3 events out of 267 in the barrel in which the $\tau \rightarrow \mu\overline{\nu}_\mu\nu_\tau$ candidate is mistakenly chosen to be the track in the event with misassigned charge (this occurs 3 times out of 159 events in the endcap).

In the data, the fraction of events with wrongly assigned charge is larger by a factor of $\sim$2 for all momenta, and, although this still represents a very small fraction of the data set, the method formulated above is applied to all real data $\tau \rightarrow \mu\overline{\nu}_\mu\nu_\tau$ candidates before binning. This is done as the default action, whilst the charge misassignent tagging is swtiched off in the assessment of systematic errors.

9.4 The symmetry of the OPAL detector

Since the extraction of $\langle P_\tau \rangle$ and A^{FB}_{pol} assumes that the OPAL detector is symmetric about $\cos\theta = 0$, a simple study was performed to ensure that this was the case for both data and Monte Carlo events.

The selections used for both the barrel and endcap regions rely mostly on the use of the muon chambers, and so the check is to see that the efficiency of the muon chamber selection (MCHID, see chapter 6) is symmetric for all muons in OPAL. This is done using a sample of $\tau \rightarrow \mu\overline{\nu}_\mu\nu_\tau$ decays selected using the ECAL and HCAL (the selection uses similar cuts to those used in previous sections). The efficiency with which such a sample passes MCHID in the forward (ε_μ^F) and backward (ε_μ^B) hemispheres is observed as a function of $|\cos\theta|$ of the muon track in CJ (where only muons in the acceptance of the muon chambers are considered). Figure 9.2 shows ε_μ^F and ε_μ^B for both the data and Monte Carlo samples in five bins of $|\cos\theta|$, as well as the the ratio $\varepsilon_\mu^F/\varepsilon_\mu^B$.

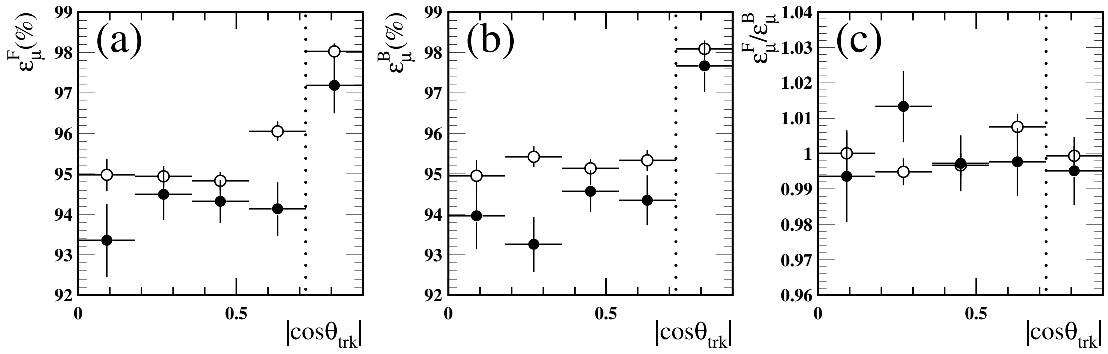

Figure 9.2: The efficiency of muon chamber selection in (a) the forward (ε_μ^F) and (b) the backward hemispheres (ε_μ^B) for a sample of $\tau \rightarrow \mu\overline{\nu}_\mu\nu_\tau$ decays identified using the hadron and electromagnetic calorimeters in the region $|\cos\theta| < 0.90$. Figure 9.2(c) shows the ratio $\varepsilon_\mu^F/\varepsilon_\mu^B$. In all diagrams the 1990-94 data is represented by the points shown as filled circles, whilst the empty circles represent the Monte Carlo data. The vertical dotted line is to distinguish between the barrel ($|\cos\theta| < 0.72$) and endcap regions of the detector.

The four bins in the barrel region show no overall trend in the case of either the data or Monte Carlo distributions in $\varepsilon_\mu^F/\varepsilon_\mu^B$, and so these bins are combined into a single value for the barrel. The overall efficiencies for both the barrel and endcap regions are given in table 9.1.

The Monte Carlo numbers indicate that the efficiencies in the forward and backward hemispheres are consistent with each other. However, since MC τ events

	Barrel region		Endcap region	
	1990-94 data	Monte Carlo	1990-94 data	Monte Carlo
ε_μ^F	0.9417±0.0033	0.9519±0.0013	0.9719±0.0069	0.9803±0.0019
ε_μ^B	0.9410±0.0032	0.9524±0.0013	0.9767±0.0064	0.9809±0.0018

Table 9.1: Values of ε_μ^F and ε_μ^B for samples of $\tau \to \mu\overline{\nu}_\mu\nu_\tau$ events identified in the barrel and endcap regions using the ECAL and HCAL.

are in bins of $|\cos\theta|$, a discrepancy would have no systematic effect on the values of $\langle P_\tau \rangle$ and A_{pol}^{FB}. If, in the case of real data, ε_μ^F and ε_μ^B were inconsistent with one another then some correction would have to applied within the fit to take this effect into account. In neither the barrel or endcap regions is this the case (ε_μ^F and ε_μ^B **are** consistent to within errors for both regions of OPAL), and so no correction need be applied. Nevertheless the values for ε_μ^F and ε_μ^B can be used to evaluate the size of the systematic errors on $\langle P_\tau \rangle$ and A_{pol}^{FB} that arise from the detector symmetry assumption. First it is necessary to make a few definitions. Recall that the τ asymmetries are defined as follows,

$$\begin{aligned} P_\tau &= \frac{\sigma_R^F + \sigma_R^B - \sigma_L^F - \sigma_L^B}{\sigma_{tot}} \\ A_{pol}^{FB} &= \frac{(\sigma_R^F - \sigma_L^F) - (\sigma_R^B - \sigma_L^B)}{\sigma_{tot}} \\ A_{FB} &= \frac{(\sigma_R^F + \sigma_L^F) - (\sigma_R^B + \sigma_L^B)}{\sigma_{tot}} \end{aligned} \tag{9.16}$$

With some rearranging the following set of equations are obtained,

$$\begin{aligned} \sigma_R^F &= \frac{\sigma_{tot}}{4}\left(1 + P_\tau + A_{pol}^{FB} + A_{FB}\right) \\ \sigma_R^B &= \frac{\sigma_{tot}}{4}\left(1 + P_\tau - A_{pol}^{FB} - A_{FB}\right) \\ \sigma_L^F &= \frac{\sigma_{tot}}{4}\left(1 - P_\tau - A_{pol}^{FB} + A_{FB}\right) \\ \sigma_L^B &= \frac{\sigma_{tot}}{4}\left(1 - P_\tau + A_{pol}^{FB} - A_{FB}\right) \end{aligned} \tag{9.17}$$

One can now estimate the change that occurs in the observed value of A_{pol}^{FB} that results from the introduction of different muon chamber efficiencies in the forward

(ε_μ^F) and backward (ε_μ^B) hemispheres:

$$\begin{aligned}\Delta A_{pol}^{FB} &= A_{pol}^{FB'} - A_{pol}^{FB} \\ &= \frac{\varepsilon_\mu^F(\sigma_R^F - \sigma_L^F) - \varepsilon_\mu^B(\sigma_R^B - \sigma_L^B)}{\varepsilon_\mu^F(\sigma_R^F + \sigma_L^F) + \varepsilon_\mu^B(\sigma_R^B + \sigma_L^B)} - A_{pol}^{FB}\end{aligned} \tag{9.18}$$

Substituting in equations 9.17 leads to the expression,

$$\Delta A_{pol}^{FB} = \frac{(\varepsilon_\mu^F - \varepsilon_\mu^B)}{2}\left[\frac{\sigma_{tot}}{\varepsilon_\mu^F(\sigma_R^F + \sigma_L^F) + \varepsilon_\mu^B(\sigma_R^B + \sigma_L^B)}\right]\left(P_\tau - A_{pol}^{FB} A_{FB}\right)$$

This expression can be simplified if the assumption is made that $\varepsilon_\mu^F \simeq \varepsilon_\mu^B$,

$$\Delta A_{pol}^{FB} \simeq \left(\frac{\varepsilon_\mu^F - \varepsilon_\mu^B}{\varepsilon_\mu^F + \varepsilon_\mu^B}\right)\left(P_\tau - A_{pol}^{FB} A_{FB}\right) \tag{9.19}$$

Using a similar derivation, it possible to obtain an analogous equation for the evaluating the sensitivity of $\langle P_\tau \rangle$ to an asymmetric selection efficiency:

$$\Delta P_\tau \simeq \left(\frac{\varepsilon_\mu^F - \varepsilon_\mu^B}{\varepsilon_\mu^F + \varepsilon_\mu^B}\right)\left(A_{pol}^{FB} - P_\tau A_{FB}\right) \tag{9.20}$$

The expressions 9.19 and 9.20 are used in section 9.7.1 in the evaluation of systematic errors.

9.5 QED, photonic and mass corrections

The measured values of $\langle P_\tau \rangle$ and A_{pol}^{FB} must be corrected for certain effects in order that the following expressions become exact:

$$\langle P_\tau \rangle = -\mathcal{A}_\tau \quad \text{and} \quad A_{pol}^{FB} = -\frac{3}{4}\mathcal{A}_e \tag{9.21}$$

where the coupling combinations $\mathcal{A}_\ell$ are given by,

$$\mathcal{A}_\ell = \frac{\hat{a}_\ell \hat{v}_\ell}{\hat{v}_\ell^2 + \hat{a}_\ell^2} \tag{9.22}$$

As explained in chapter 2, the couplings of leptons to the Z^0 boson are subject to weak corrections. In the improved Born approximation, which takes the leading weak corrections into account, this results in the lowest-order vector and axial couplings being replaced by the effective quantities given in equation 9.22. However, in order that the effective couplings can be obtained from the $\langle P_\tau \rangle$ and A^{FB}_{pol} measurements using expressions 9.21 the following effects must first be corrected for (see also [11]):

- Direct Born-level γ and γZ^0 terms, which are dependent upon $\sqrt{s}$. The results, therefore, are corrected to correspond to $\langle P_\tau \rangle$ and A^{FB}_{pol} at $\sqrt{s}{=}M_Z$ with no γ-exchange in the s-channel.

- Electomagnetic radiative corrections for initial and final state radiation from the beam particles and $\tau^\pm$ respectively.

- Born-level mass terms leading to helicity-flip configurations.

In doing this it is necessary to make use of the program ZFITTER [17]. Certain Standard Model electroweak parameters may be passed to the program ($M_{\rm top}, M_{\rm Z}, M_{\rm H}$ and α_s), which can then be used to calculate various asymmetries and cross sections at specified values of $\sqrt{s}$. Within the calculations the effects of initial and final-state QED radiation can be included up to $\mathcal{O}(\alpha^2)$, or alternatively switched off to get instead the underlying values for the asymmetries in the improved Born approximation. In fact, the weak corrections are implemented through an effective form-factor approach which extends the improved Born approximation to also account for the imaginary parts of couplings and the non-factorisability of some corrections between initial and final states. The effects of the photon propagator can also be investigated by switching off s-channel γ exchange and/or γZ interference within the calculations.

The effects which it is necessary to correct for are switched on or off within ZFITTER to calculate the combined effect that they have upon the values of A_{FB} (in bins of $|\cos\theta|$) and $\langle P_\tau \rangle$ (in bins of $\cos\theta$). These changes are applied on a bin-by-bin basis to the τ Monte Carlo "strengths" σ_{ik} in equation 9.9, where these have first been predetermined for the negative and positive helicity states using the current fit values of $\langle P_\tau \rangle$ and A^{FB}_{pol} within the improved Born approximation (expression 9.7). Typically, the inclusion of these corrections as part of the fitting procudure results in the following changes in the measured values of $\langle P_\tau \rangle$ and A_{pol}^{FB},

$$\Delta P_\tau \simeq -0.003 \quad \text{and} \quad \Delta A_{pol}^{FB} \simeq -0.002$$

A systematic error of 0.001 is assigned to each measurement to account for uncertainties in the corrections calculated by ZFITTER. Both the above changes in the asymmetries and the assignment of the systematic errors are consistent with those used for other LEP measurements of the τ polarisation asymmetries.

A further point to mention is that the program ZFITTER requires the user to specify different kinematical cuts which are used in the calculation of QED photonic corrections. These are chosen to be consistent with the $e^+e^- \rightarrow \tau^+\tau^-$ preselection and $\tau \rightarrow \mu\overline{\nu}_\mu\nu_\tau$ selections detailed in previous chapters. Figure 9.3 illustrates, for example, the sensitivity of the $\langle P_\tau \rangle$ values calculated by ZFITTER to different acollinearity cuts.

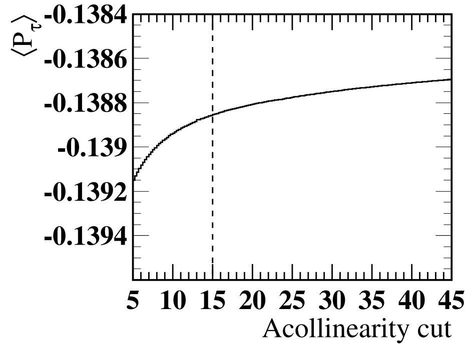

Figure 9.3: The variation of $\langle P_\tau \rangle$ at the Z^0 resonance for different acollinearity cuts as calculated by ZFITTER (using M_Z=91.1863 GeV, M_{top}=175 GeV, M_H=300 GeV and α_s=0.118). The actual kinematic cut used in the analysis is shown as a vertical dashed line.

9.6 Tests of the fitting procedure

Before applying the polarisation fit to real data a simple test was performed to check that the fitting procedure was working. If the individual MC distributions for the two helicity states and non-τ background are actually fitted to the summed MC distributions (in place of real data), then the values of $\langle P_\tau \rangle$ and A_{pol}^{FB} extracted should correspond to similar values calculated by counting the actual numbers of negative and positive helicity τ decays in the forward and backward hemispheres. This was done for all four selections, and in each case it was found that the statistical errors on the fitted values of $\langle P_\tau \rangle$ and A_{pol}^{FB} were substantially larger than the difference between the values obtained by fitting and those obtained by the counting method.

9.7 Results

By applying the fitting procedure to $\tau \rightarrow \mu \overline{\nu}_\mu \nu_\tau$ samples collected using each of the four selections described in chapter 6, the following results for the τ asymmetries were obtained (see also the plots in figure 9.4):

$$\langle P_\tau \rangle = \begin{cases} -0.143 \pm 0.030\,(stat.) \pm 0.018(syst.) & \text{- selection B1} \\ -0.157 \pm 0.030\,(stat.) \pm 0.020(syst.) & \text{- selection B2} \\ -0.141 \pm 0.061\,(stat.) \pm 0.036(syst.) & \text{- selection E1} \\ -0.153 \pm 0.061\,(stat.) \pm 0.038(syst.) & \text{- selection E2} \end{cases} \tag{9.23}$$

$$A_{pol}^{FB} = \begin{cases} -0.126 \pm 0.034\,(stat.) \pm 0.005(syst.) & \text{- selection B1} \\ -0.125 \pm 0.034\,(stat.) \pm 0.006(syst.) & \text{- selection B2} \\ -0.039 \pm 0.047\,(stat.) \pm 0.013(syst.) & \text{- selection E1} \\ -0.042 \pm 0.047\,(stat.) \pm 0.013(syst.) & \text{- selection E2} \end{cases} \tag{9.24}$$

Before analyzing these results further, the evaluation of the systematic errors quoted above is discussed below.

9.7.1 Evaluation of systematic errors

The assignment of systematic errors to $\langle P_\tau \rangle$ and A_{pol}^{FB} have been mentioned where appropriate throughout this thesis. The sources of systematic error and their

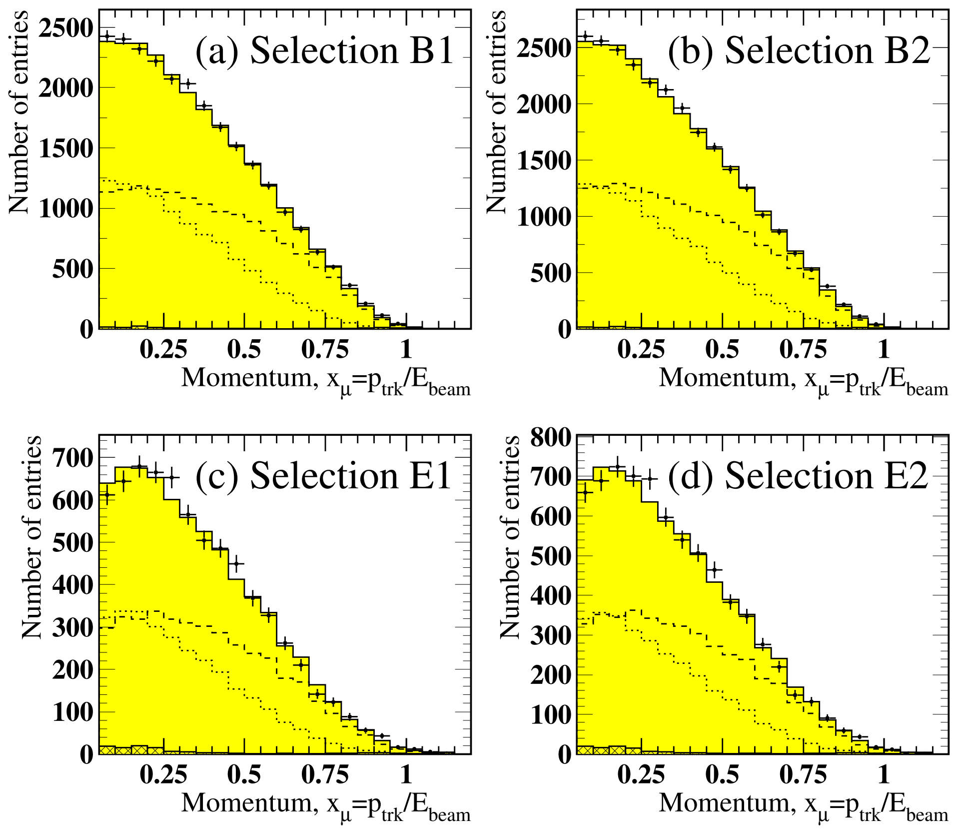

Figure 9.4: Final distributions in x_μ for each of the four $\tau \rightarrow \mu\overline{\nu}_\mu\nu_\tau$ selections after performing the polarisation fit, where each distribution is summed over all $\cos\theta$ bins used during the fit. The Monte Carlo distributions from all sources have been corrected for statistical fluctuations and added together (given the final fit values for $\langle P_\tau \rangle$ and A^{FB}_{pol}) to give the shaded histograms, whilst the points represent data collected at the Z^0 resonance between 1990 and 1994. The hatched region shows the non-τ background, whilst the broken lines show the MC contributions from all tau leptons identified as $\tau \rightarrow \mu\overline{\nu}_\mu\nu_\tau$ decays. The positive helicity taus are shown by the dotted lines, and the negative helicity taus are shown by the dashed lines.

evaluation may be summarized as follows:

- **MC statistics** - The MC statistical error is combined with the systematic errors in accordance with the latest OPAL polarisation analysis [27].

- **MC momentum simulation** - The momenta of all MC particles have been smeared according to the procedures described in chapter 4, where the systematics are dominated by the smearing applied to the transverse momentum (rather than the $\cot\theta$ measurement). Systematic errors are assigned for selections B1 and B2 by varying the smearing parameters α and β, and by switching off the random number generator used in applying extra smearing to tracks near the cathode plane. For selections E1 and E2 additional uncertainty arises due to the use of parameterisations for the smearing parameters. For systematic studies these parameterised values are replaced by fixed values to observe the effect on $\langle P_\tau \rangle$ and A^{FB}_{pol}, and then these fixed values themselves are then varied.

- **Selection efficiency** - By default the selection efficiencies are corrected by weighting signal MC decays by a momentum-dependent factor of the general form, $C_\varepsilon(x_\mu) = P_1 + P_2 \cdot x_\mu$. If the gradient term is inconsistent with zero then it is varied by the size of its error to assign the systematic error, otherwise the correction is merely switched off. In the barrel region an error is obtained using this method for the MCHID correction, and this is combined quadratically with a similar error obtained by turning off the correction applied to the events selected using the CALID identification. The error associated with the corrections $\Delta P^\varepsilon_\tau$ used in equations 9.5 are also included as part of the selection efficiency error, since changes made to the $C_\varepsilon(x_\mu)$ functions are correlated with the values used for $\Delta P^\varepsilon_\tau$.

- **Non-τ background** - The factors described in chapter 7 for correcting the MC backgrounds from $\gamma\gamma \rightarrow \mu^+\mu^-$ and $e^+e^- \rightarrow \mu^+\mu^-$ events were all found to be consistent with one, and so were not used during the fitting procedures by default. However, they may be used in the evaluation of systematic errors by applying them to each background type separately, and taking the observed changes seen in $\langle P_\tau \rangle$ and A^{FB}_{pol} to be the size of the systematic error. This was done for all four selections and for both $\gamma\gamma \rightarrow \mu^+\mu^-$and $e^+e^- \rightarrow \mu^+\mu^-$background events. This error is particularly important in the case of the $e^+e^- \rightarrow \mu^+\mu^-$background since the values returned from the polarisation fit are relatively sensitive to changes in the size of the MC background estimate. This is because the background events lie in a momentum range in which there are few $\tau \rightarrow \mu\overline{\nu}_\mu\nu_\tau$ decays. It is also important to note that the size of the $e^+e^- \rightarrow \mu^+\mu^-$background is not that sensitive to changes in the smearing parameters α and β mentioned above since many of the residual $e^+e^- \rightarrow \mu^+\mu^-$background events have not entered the sample through momentum mismeasurement. It is insufficient therefore to take the error on the size of the MC $e^+e^- \rightarrow \mu^+\mu^-$background to be simply part of the error assigned for the MC momentum simulation.

- **Hadronic τ-decay background** - For selections B2 and E2 (for which such backgrounds are larger than those for B1 and E1) an error is assigned by applying the background corrections described in chapter 7. Since the corrections themselves are consistent with unity in every case, they are again not applied by default. For selections B1 and E1, which have very small τ backgrounds, the errors are obtained by applying the same corrections used for B2 and E2.

- **MC branching ratios** - Chapter 4 detailed how weights could be applied to MC $e^+e^- \rightarrow \tau^+\tau^-$events to correct for the now obsolete branching ratios used in their generation. The weights can be adjusted to account for the error on the each branching ratio. Since, for the hadronic decays, this has a similar effect to applying the background corrections obtained in chapter 7, the systematic error is taken as the larger effect out of altering the branching ratio by the size of its error or by applying a background correction. The branching ratio of the $\tau \rightarrow \mu\overline{\nu}_\mu\nu_\tau$ channel itself is not varied since this too would amount to counting the same error twice.

- **A^0_{FB} value** - There is an error on the measured value of the pole asymmetry A^0_{FB} used in equation 9.7. The systematic uncertainties on $\langle P_\tau \rangle$ and A^{FB}_{pol} that arise from the use of this measured value are evaluated by varying A^0_{FB} by the size of its error.

- **Charge misassignment** - The algorithm used to look for and correct misassigned charges is switched off and the systematic errors on $\langle P_\tau \rangle$ and A^{FB}_{pol} are assigned accordingly.

- **Detector symmetry** - The fitting routine makes the assumption that the OPAL detector is symmetric about $\cos\theta{=}0$. A systematic error associated with this assumption is assigned using equations 9.19 and 9.20 and numbers given in table 9.1.

- **ZFITTER** - To be consistent with other polarisation measurements (see [11]), an error is assigned based on the use of ZFITTER to correct for the effects described in 9.5.

The individual contributions to the overall systematic error for each of the four $\tau \rightarrow \mu\overline{\nu}_\mu\nu_\tau$ selections are shown in table 9.2:

9.8 Interpretation of results

As it stands there are four separate measurements for both $\langle P_\tau \rangle$ and A^{FB}_{pol}. The measurements made using selections B1 and B2 are highly correlated with one another, as are those made with selections E1 and E2. However, since endcap selections rely on particles being identified in an entirely different part of the detector from those identified in the barrel region, the measurements made using B1 are independent of those obtained using E1. Therefore the results made using these two selections are combined to give weighted means for $\langle P_\tau \rangle$ and A^{FB}_{pol}. Similarly the measurements made using selections B2 and E2 are also combined.

Source of error	Barrel selections		Endcap selections	
	B1	B2	E1	E2
Monte Carlo statistics	0.0154 0.0046	0.0172 0.0052	0.0343 0.0122	0.0361 0.0117
Momentum simulation	0.0070 0.0018	0.0083 0.0014	0.0074 0.0043	0.0086 0.0039
Selection efficiency	0.0038 0.0004	0.0031 0.0001	0.0053 0.0001	0.0039 0.0002
Two-photon background	0.0014 0.0001	0.0014 0.0001	0.0003 0.0000	0.0002 0.0000
Muon pair background	0.0017 0.0001	0.0020 0.0001	0.0080 0.0023	0.0085 0.0020
Branching ratios/ τ background	0.0009 0.0004	0.0023 0.0007	0.0010 0.0002	0.0003 0.0004
Input A_{FB} value	0.0003 0.0009	0.0003 0.0010	0.0001 0.0009	0.0001 0.0009
Charge assignment	0.0001 0.0015	0.0001 0.0013	0.0002 0.0015	0.0004 0.0002
OPAL symmetry	0.0000 0.0001	0.0000 0.0001	0.0001 0.0003	0.0001 0.0003
ZFITTER error	0.0010 0.0010	0.0010 0.0010	0.0010 0.0010	0.0010 0.0010
TOTAL ΔP_τ	0.0175	0.0197	0.0364	0.0383
TOTAL ΔA^{FB}_{pol}	0.0053	0.0058	0.0133	0.0126

Table 9.2: The individual systematic errors on $\langle P_\tau \rangle$ and A^{FB}_{pol} (where ΔP_τ is written before ΔA^{FB}_{pol} in each case), which arise from each potential source for the four $\tau \rightarrow \mu\overline{\nu}_\mu\nu_\tau$ selections used in this analysis. Sources of error which lead to a change in $\langle P_\tau \rangle$ and A^{FB}_{pol} of $<$0.00005 are entered as zero.

The two pairs of selections lead to the following results:

$$\langle P_\tau \rangle = \begin{cases} -0.142 \pm 0.031 & \text{- } \textbf{selection B1/E1} \\ -0.157 \pm 0.032 & \text{- selection B2/E2} \end{cases} \tag{9.25}$$

$$A_{pol}^{FB} = \begin{cases} -0.097 \pm 0.028 & \text{- } \textbf{selection B1/E1} \\ -0.098 \pm 0.028 & \text{- selection B2/E2} \end{cases} \tag{9.26}$$

In each case, it is the combination B1/E1 that provides marginally lower errors on the final values and so it is these that are taken to be the final results of this analysis. The results made using selections B2/E2 provide a useful cross-check of the final quoted values.

The measurements of $\langle P_\tau \rangle$ and A_{pol}^{FB} given above can be used to obtain the coupling combinations $\mathcal{A}_\tau$ and $\mathcal{A}_\mathrm{e}$ according to equation 9.21. These expressions are exact since the fitting procedure has used ZFITTER to take the effects of QED bremsstrahlung, photonic corrections and mass effects into account. Therefore, using only the results for $\langle P_\tau \rangle$ and A_{pol}^{FB} obtained by combining selections B1 and E1, the following values are calculated for the coupling combinations:

$$\begin{aligned} \mathcal{A}_\tau &= 0.142 \pm 0.031 \\ \mathcal{A}_\mathrm{e} &= 0.129 \pm 0.037 \end{aligned} \tag{9.27}$$

According to equation 9.22 these results may also interpreted in terms of the ratios of the effective couplings of the τ and e leptons to the Z^0 boson:

$$\begin{aligned} \frac{\hat{v}_\tau}{\hat{a}_\tau} &= 0.072 \pm 0.016 \\ \frac{\hat{v}_\mathrm{e}}{\hat{a}_\mathrm{e}} &= 0.065 \pm 0.019 \end{aligned} \tag{9.28}$$

These values are consistent with one another and therefore with the hypothesis of lepton universality. Hence the results for the e and τ leptons may be combined under the assumption of lepton universality to give a single measurement for leptons:

$$\frac{\hat{v}_\ell}{\hat{a}_\ell} = 0.069 \pm 0.012 \tag{9.29}$$

This combination of values for the e and τ leptons assumes also that the $\langle P_\tau \rangle$ and A_{pol}^{FB} measurements are independent. In [27, 25] it was found that, for the binned maximum likelihood method, this is a good approximation, and so the assumption of independence is made here.

Finally, the ratio of the effective vector and axial-vector couplings for leptons may be reinterpreted using equation 2.29 as a measurement of the effective electroweak mixing angle for leptons,

$$\sin^2 \theta_{\mathrm{eff}}^{\mathrm{lept}} = 0.2328 \pm 0.0030 \tag{9.30}$$

9.9 Discussion and conclusions

Throughout most of this thesis two selections have been developed in parallel for both the barrel (B1 and B2) and endcap (E1 and E2) regions. This was mainly because it was difficult to predict initially which would lead to the smaller systematic errors in each case. As it turned out, there is little to choose between selections B1 and B2 (both are improvements on previously-used selections), and between selections E1 and E2. As predicted in chapter 6, selections B1 and E1 have lower τ background uncertainties, whereas B2 and E2 have lower errors associated with the MC estimates of selection efficiency. The play-off between these two possible sources of error is in the end relatively insignificant since the final systematic error for each selection is dominated more by the individual errors assigned to account for MC statistical fluctuations and the MC estimate of the $e^+e^- \to \mu^+\mu^-$ background. In quoting the final values for $\langle P_\tau \rangle$ and A_{pol}^{FB} selections B1 and E1 have been used since their errors are fractionally lower, whilst the results from B2 and E2 provide a useful cross check.

The results obtained using $\tau \to \mu \overline{\nu}_\mu \nu_\tau$ decays identified in the barrel region compare favourably with previous measurements made at OPAL using the same decay channel. The latest analysis (detailed in [27]) gives the following numbers for the $\tau \rightarrow \mu\overline{\nu}_\mu\nu_\tau$ decay channel ($|\cos\theta| < 0.68$):

$$\begin{aligned} \langle P_\tau \rangle &= -0.138 \pm 0.033\,(stat.) \pm 0.022\,(syst.) \\ A_{pol}^{FB} &= -0.143 \pm 0.038\,(stat.) \pm 0.005\,(syst.) \end{aligned} \tag{9.31}$$

The individual measurements of $\langle P_\tau \rangle$ made using selections B1 and B2 (see equations 9.23 and 9.24) improve on the systematic errors quoted above, whilst the systematic errors on A_{pol}^{FB} (which are much smaller anyway) are of roughly the same size in each case. The statistical errors are also of comparable size since the analysis presented in this thesis and the measurements made in [27] use data samples of similar sizes. However, the use of the endcap selections E1 and E2 here means that the measurements made using selections B1 and B2 can also be combined with another independent measurement to further reduce the overall error in comparison with existing measurements. The endcap values, however, have large statistical and systematic errors and so by themselves are less useful as measurements.

The systematic studies associated with the τ asymmetry measurements made using $\tau \rightarrow \mu\overline{\nu}_\mu\nu_\tau$ decays form a substantial part of this thesis. This has lead to a greater understanding of the various systematic effects that may arise in such a measurement, thus enabling lower errors to be quoted on the final results. In particular, improvements have been made in the following areas of study:

- **Selection efficiency** - Previous $\tau \rightarrow \mu\overline{\nu}_\mu\nu_\tau$ measurements made at OPAL have used $\gamma\gamma \rightarrow \mu^+\mu^-$events and $e^+e^- \rightarrow \mu^+\mu^-$events at low and high momenta respectively to estimate the momentum bias in the Monte Carlo estimate of selection efficiency. However, this analysis uses in addition a sample of muons lying in the momentum range $0.25 < x_\mu < 0.8$ (from $e^+e^- \rightarrow \gamma\mu^+\mu^-$ events) to allow the studies using control samples to be extended over all momentum ranges. In addition, the fact that selections B2 and E2 rely only on the central tracking detector (CT) and the muon chambers (MB and ME) means that it has also been possible to use a separate sample of $\tau \rightarrow \mu\overline{\nu}_\mu\nu_\tau$ decays, selected using the calorimeters, to check the Monte Carlo simulation.

This was not possible for previous analyses.

- **Momentum simulation** - It has been emphasized throughout this thesis that it is important for the final measurements that the Monte Carlo simulates momentum resolution well. Chapter 4 went into some detail to describe the smearing methods devised by the author to make sure that this was the case. The same momentum smearing package was used for the analysis detailed in [27].

- **Tau-pair background** - New methods have been devised for this analysis to check the Monte Carlo estimates of the τ-pair background. In the case of selections B2 and E2, a highly pure and unbiased sample of $\tau \rightarrow \rho\nu_\tau$ decays has been used to assign a systematic error for the Monte Carlo estimate of the background from hadronic decays. The correction factors derived from this sample are also used for evaluating the background errors for selections B1 and E1, where these selections have much lower τ-pair backgrounds. This fact ultimately leads to the lower systematic errors quoted for the background uncertainties in selections B1 and E1 compared to B2 and E2.

- **Non-tau backgrounds** - Systematic errors are quoted on $\langle P_\tau \rangle$ and A_{pol}^{FB} which account for uncertainties in the non-τ backgrounds. In particular the $e^+e^- \rightarrow \mu^+\mu^-$background must be well-known since (after mismeasured tracks travelling close to anode planes in the jet chamber are removed - see section 5.3.3) most of the background lies in a momentum range in which there are few $\tau \rightarrow \mu\overline{\nu}_\mu\nu_\tau$ decays present. Therefore, the fitting procedure is particularly sensitive to any discrepancies that might exist in the $e^+e^- \rightarrow \mu^+\mu^-$background content between data and Monte Carlo events. The analysis in [27] does not quote an individual systematic error associated with the $e^+e^- \rightarrow \mu^+\mu^-$background estimate, even though it is considered for this analysis to be numerically quite significant. Instead, the $e^+e^- \rightarrow \mu^+\mu^-$error is included as part of more general systematic errors concerning the Monte Carlo simulation of the various subcomponents of the detector.

  It is of note to mention that the use of the endcap region has lead to an increased need for checks to be made which ensure that the $\gamma\gamma \rightarrow \mu^+\mu^-$ background is correctly predicted (since, in the endcap, the background from such events is a factor of $\sim$3 larger). Again, the methods used for this analysis in checking this background for all four selections are different to those used in previous analyses.

- **Other systematics** - The methods used to evaluate the systematic errors arising from the effects of charge mismeasurement and detector symmetry are also useful, since neither error has been quantified in previous OPAL polarisation studies made using the binned maximum likelihood method. In particular, it is the inclusion of the charge mismeasurement error that partly leads to the slightly higher systematic error on A^{FB}_{pol} for selection B2 when compared to the OPAL result in equation 9.31.

The final values obtained for $\langle P_\tau \rangle$ and A^{FB}_{pol} lead to values for $\hat{v}_\tau/\hat{a}_\tau$ and $\hat{v}_e/\hat{a}_e$ that are consistent with each other, and so are consistent also with the hypothesis of lepton universality. Combining these values for the e and τ leptons leads to the final result for the effective weak mixing angle:

$$\sin^2\theta^{\mathrm{lept}}_{\mathrm{eff}} = 0.2328 \pm 0.0030$$

which is entirely consistent with the Standard Model predictions displayed in figure 2.10 for different input values of m_{top} and m_{H} (the Higgs boson mass). This value also agrees with the world experimental average to well within errors, where, from all electroweak measurements (see [10]), this value is taken to be,

$$\sin^2\theta^{\mathrm{lept}}_{\mathrm{eff}} = 0.23165 \pm 0.00024$$

Appendix A

OPAL coordinate systems

A standard right-handed Cartesian system is used at OPAL, the origin of which lies at the centre of the jet chamber and which approximately coincides with the interaction point in e^+e^- events. The z axis defined by the direction of the e^- beam as it passes through OPAL (anti-clockwise around LEP when viewed from above); the x axis is taken as pointing towards the centre of the LEP ring, and the y axis is therefore pointing approximately vertically. It is not exactly so since the LEP beam passes through the axis of the detector at an angle of 13.9 mrad relative to the horizontal.

A spherical polar coordinate system (r, θ, ϕ) is also frequently used, where this is defined in relation to the Cartesian coordinate system in the usual way. Hence, the azimuthal angle, ϕ, is measured about the z axis, with the positive x axis defining $\phi = 0$. The polar angle is measured from the positive z axis, and r is the spherical radius from the origin.

Appendix B

OPAL track parameters

Several OPAL Central Detector track parameters are used in determining the momenta of charged tracks and are also used in describing certain preselection requirements in Chapter 5 Note that the term "PCA" is used to denote the point of closest approach to the origin in the $r - \phi$ plane.

- κ is the curvature where
$$|\kappa| = \frac{1}{2\rho}$$
where ρ is the radius of curvature of the charged track and the sign of κ is such that, if positive, then ϕ is **increasing** along the path of the track from the PCA. For the axial magnetic field within OPAL (with a positive z component of the field strength, B_z) $\kappa > 0$ corresponds to a particle with negative electric charge.

- ϕ_0 is the azimuthal angle made by the tangent of the track at the PCA.

- d_0 is the impact parameter which equals the distance from the origin to the PCA. Formally it is defined by the following equation,
$$d_0 = \hat{\phi} \wedge \vec{d} \cdot \hat{z}$$
where $\vec{d}$ is defined to be the position vector of the PCA with respect to the origin; $\hat{\phi}$ is the unit vector tangential to the track at the PCA, and $\hat{z}$ is the

unit vector along the z axis.

- $\tan\lambda = \cot\theta$, where θ is the polar angle of the track in the spherical polar coordinate system described in Appendix A.

- z_0 is defined as the z coordinate of the track at the PCA. If s is defined as the $r-\phi$ path integral from the PCA, then the $s-z$ projection of the helix is given by,

$$z = z_0 + s\tan\lambda$$

The physics track momentum is calculated using the following parameter,

$$p_t = a|\frac{B_z}{\kappa}|$$

where p_t is the modulus of the momentum transverse to the beam direction. If p_t is measured in GeV/c, B_z in kG and κ in cm, then,

$$a = \frac{c}{2}\times 10^{-14} \simeq 1.5\times 10^{-4}$$

Hence, the momentum, p, and charge, q, are defined as follows,

$$p_x = p_t\cos\phi_0$$

$$p_y = p_t\sin\phi_0$$

$$p_z = p_t\tan\lambda$$

$$p = p_t\sqrt{1+\tan^2\lambda}$$

$$q = -\frac{B_z/\kappa}{|B_z/\kappa|}$$

Appendix C

Parameters for MC track smearing in the barrel region

Chapter 4 details how, for Monte Carlo data, the momentum resolution for charged tracks in CT is smeared. A large number of parameters are required for this purpose, most of which are included in this appendix for the case of track smearing in the barrel region. The track smearing is decomposed into smearing of the polar angle measurement ($\cot\theta$) and smearing of transverse momentum ($1/x_t$).

MC type	c
GORO12 (with CZ hits)	1.548±0.007 $\times 10^{-7}$
GORO14 (with CZ hits)	1.646±0.006 $\times 10^{-7}$
GORO14 (w/o CZ hits)	4.297±0.049 $\times 10^{-4}$

C.1(a): $e^+e^- \to \mu^+\mu^-$ events

MC type	c
GORO12 (with CZ hits)	1.706±0.019 $\times 10^{-7}$
GORO14 (with CZ hits)	1.816±0.014 $\times 10^{-7}$
GORO14 (w/o CZ hits)	4.494±0.118 $\times 10^{-4}$

C.1(b): $e^+e^- \to e^+e^-$ events

Table C.1: The values of c used in the polar angle smearing of charged tracks, where c is effectively the contribution to $\sigma^2_{\cot\theta}$ arising from the measurement of the z-coordinate for tracks in the barrel region of CT. The numbers have been determined for tracks in identified (a) $e^+e^- \to \mu^+\mu^-$ and (b) $e^+e^- \to e^+e^-$ events. The terms GORO12 and GORO14 indicate the Gopal/Rope versions used to generate Monte Carlo events (these correspond to the 1993 and 1994 configurations of the OPAL detector respectively). There is no value of c given for tracks generated using GORO12 and without CZ hits. This is because the resolution observed for the Monte Carlo in this case is larger than that seen in the data and so no smearing is applied.

Gopal/ Rope MC version	Uncorrected scaling factor, γ, for each data year (with CZ hits) 1990	1991/92	1993	1994	γ (w/o CZ hits) 1990-94
12 (1993)	2.74	2.87	3.03	3.23	-
14 (1994)	2.69	2.83	3.00	3.17	1.29

C.2(a): $e^+e^- \to \mu^+\mu^-$ events

Gopal/ Rope MC version	Uncorrected scaling factor, γ, for each data year (with CZ hits) 1990	1991/92	1993	1994	γ (w/o CZ hits) 1990-94
12 (1993)	3.21	3.04	3.19	3.40	-
14 (1994)	3.15	3.00	3.13	3.34	1.23

C.2(b): $e^+e^- \to e^+e^-$ events

Table C.2: The values of γ used in the polar angle smearing of charged tracks are shown, where γ is the scaling factor that would be applied to the polar angle resolution $\sigma_{\cot\theta}$ in the absense of multiple scattering. The numbers have been determined for Monte Carlo (MC) tracks in events identified in the barrel as (a) $e^+e^- \to \mu^+\mu^-$ or (b) $e^+e^- \to e^+e^-$, where Gopal/Rope versions 12 and 14 (corresponding to the 1993 and 1994 detector configurations respectively) have been used. For each MC version, separate values of γ for tracks with CZ hits are determined according to the data year with which their resolution is being compared.

Gopal/Rope MC version	Value of a used for each track type			
	1	2	3	4
12 (1993)	1.868 ± 0.006 $\times10^{-3}$	2.843 ± 0.047 $\times10^{-3}$	1.799 ± 0.027 $\times10^{-3}$	2.920 ± 0.055 $\times10^{-3}$
14 (1994)	4.219 ± 0.010 $\times10^{-3}$	7.164 ± 0.143 $\times10^{-3}$	3.756 ± 0.027 $\times10^{-3}$	4.019 ± 0.056 $\times10^{-3}$

C.3(a): $e^+e^-\rightarrow\mu^+\mu^-$ events

Gopal/Rope MC version	Value of a used for each track type			
	1	2	3	4
12 (1993)	2.178 ± 0.018 $\times10^{-3}$	3.138 ± 0.139 $\times10^{-3}$	2.323 ± 0.072 $\times10^{-3}$	3.332 ± 0.124 $\times10^{-3}$
14 (1994)	4.537 ± 0.039 $\times10^{-3}$	8.203 ± 0.451 $\times10^{-3}$	4.466 ± 0.105 $\times10^{-3}$	5.009 ± 0.175 $\times10^{-3}$

C.3(b): $e^+e^-\rightarrow e^+e^-$ events

Table C.3: The values of a used in smearing the resolution of $1/x_t$ for charged Monte Carlo (MC) tracks in the barrel region. The numbers have been determined using events identified as (a) $e^+e^-\rightarrow\mu^+\mu^-$ or (b) $e^+e^-\rightarrow e^+e^-$, where Gopal/Rope versions 12 and 14 (corresponding to the 1993 and 1994 detector configurations respectively) have been used. For each MC version, there are separate values of a for each of 4 different track types, where these are defined in table 4.3.

MC version	year	β^-	β^+	α
12 (1993 OPAL config.)	1990	1.0044(1.0092)	0.9966(1.0007)	1.48(1.41)
	91/92	1.0004(1.0052)	0.9995(1.0030)	1.35(1.27)
	1993	0.9950(0.9986)	0.9996(1.0024)	1.43(1.39)
	1994	0.9991(1.0016)	1.0001(1.0040)	1.43(1.36)
14 (1993 OPAL config.)	1990	1.0050(1.0106)	0.9835(0.9900)	0.99(0.89)
	91/92	1.0009(1.0064)	0.9872(0.9925)	0.90(0.86)
	1993	0.9956(0.9997)	0.9867(0.9913)	0.96(0.94)
	1994	0.9996(1.0026)	0.9872(0.9929)	0.96(0.92)

C.4(a): Type 1 tracks

MC version	year	β^-	β^+	α
12 (1993 OPAL config.)	1990	0.9990(1.015)	0.9954(1.003)	1.67(1.61)
	91/92	1.0031(1.002)	0.9967(0.998)	1.37(1.36)
	1993	1.0003(1.000)	0.9967(0.999)	1.45(1.38)
	1994	1.0048(1.008)	0.9896(0.996)	1.44(1.44)
14 (1993 OPAL config.)	1990	0.9994(1.016)	0.9873(0.997)	1.18(1.13)
	91/92	1.0039(1.004)	0.9891(0.993)	0.96(0.99)
	1993	1.0011(1.001)	0.9888(0.993)	1.01(0.99)
	1994	1.0060(1.010)	0.9824(0.989)	1.01(0.99)

C.4(b): Type 3 tracks

MC version	year	β^-	β^+	α
12 (1993 OPAL config.)	1990	0.999(0.990)	0.988(1.000)	1.56(1.57)
	91/92	0.992(0.998)	0.983(0.991)	1.28(1.37)
	1993	0.984(0.980)	0.980(0.986)	1.35(1.36)
	1994	0.983(0.986)	0.978(0.987)	1.41(1.47)
14 (1994 OPAL config.)	1990	0.963(0.959)	1.030(1.041)	1.33(1.26)
	91/92	0.963(0.971)	1.019(1.028)	1.11(1.09)
	1993	0.954(0.954)	1.017(1.023)	1.16(1.09)
	1994	0.952(0.958)	1.016(1.026)	1.22(1.19)

C.4(c): Type 4 tracks

Table C.4: The values of α and $\beta^{\pm}$ used to smear all Monte Carlo tracks in the barrel are shown. The numbers in brackets are the numbers obtained using $e^+e^- \rightarrow e^+e^-$events and which are used to smear the momenta of $e^{\pm}$ tracks. The rest have been determined using tracks from $e^+e^- \rightarrow \mu^+\mu^-$events. The numbers for track types 1,3 and 4 only (see table 4.3) are given since the case for type 2 tracks is complicated by the charge-dependent use of a random generator to choose a certain fraction of tracks near cathode wire planes for extra smearing.

Track type (see Table 4.3	Value of σ_α/α used for comparison with each data-taking year			
	1990	1991/92	1993	1994
1	±0.013	±0.010	±0.010	±0.010
2	±0.050			
3	±0.057	±0.020	±0.023	±0.014
4	±0.082	±0.025	±0.032	±0.025

C.5(a): σ_α/α

Track type (see Table 4.3	Value of σ_β/β used for comparison with each data-taking year			
	1990	1991/92	1993	1994
1	±0.0007	±0.0002	±0.0003	±0.0002
2	±0.0022			
3	±0.0032	±0.0010	±0.0011	±0.0007
4	±0.0042	±0.0012	±0.0016	±0.0012

C.5(b): σ_β/β

Table C.5: The uncertainties on α and $\beta^\pm$ largely arise from the statistical errors on the fitted means and widths obtained from $x_{meas}-1$ distributions in the data. For use in systematic studies, the fractional uncertainties (a) σ_α/α and (b) σ_β/β are therefore estimated for Monte Carlo comparisons with each data-taking year, as shown, where the different track types (as defined in table 4.3) need also to be considered.

Appendix D

The geometrical acceptance of the muon chambers

The $\tau \rightarrow \mu\overline{\nu}_\mu\nu_\tau$ selection procedures in the barrel region (described further in section 6.1) allow the hadron and electromagnetic calorimeters to be used in the detection of muons in regions where the muon chamber is either much less efficient or does not exist. Therefore a study was made to investigate which areas of MB were inefficient and to observe the edge effects of muons travelling near the extremities of the detector.

Data and Monte Carlo samples of $\tau \rightarrow \mu\overline{\nu}_\mu\nu_\tau$ decays selected using the HCAL and ECAL were used to test the geometrical acceptance of MB. The calorimeter cuts used in identifying this sample are listed below and make up the calorimeter identification, **CALID**. CALID is also used as part of the main $\tau \rightarrow \mu\overline{\nu}_\mu\nu_\tau$ selections in the barrel region and so a fuller description of CALID can be found in section 6.1.

(a) the number of HCAL layers containing strip hits,

$$N_{lyr}^{HC} \geq 4$$

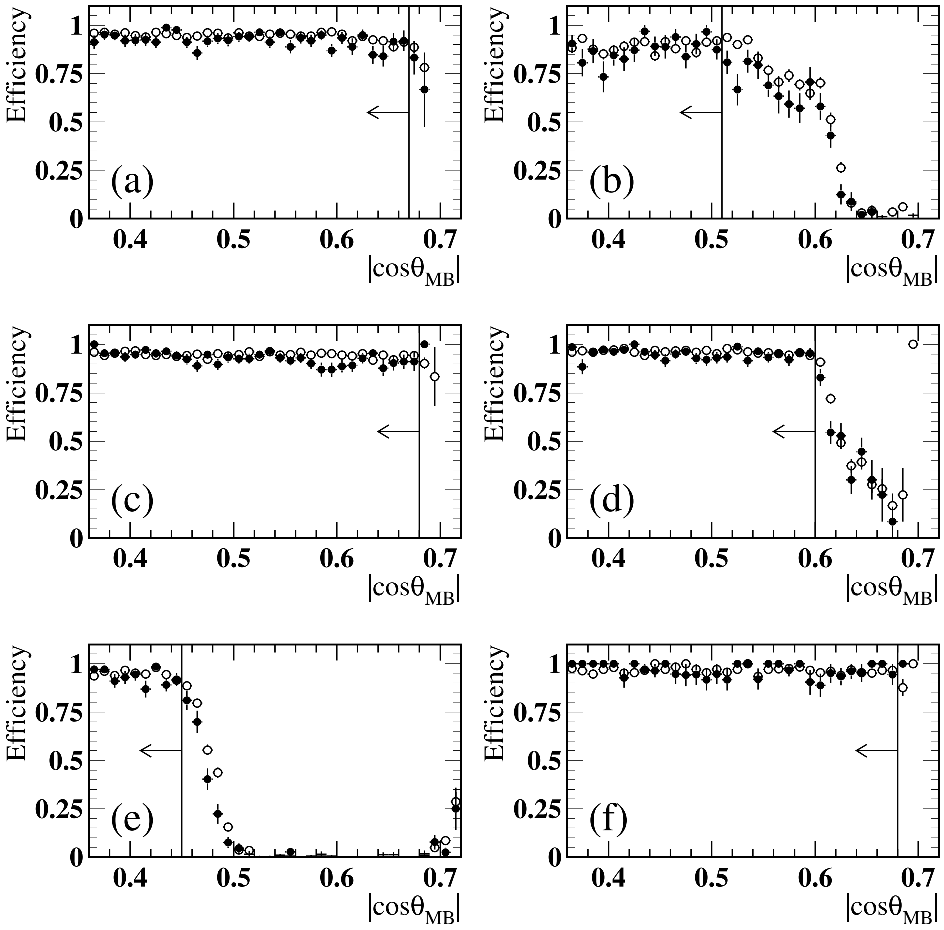

Figure D.1: The efficiency of muon chamber selection for a sample of $\tau \rightarrow \mu\overline{\nu}_\mu\nu_\tau$ decays indentified in the barrel region ($|\cos\theta_{MB}| < 0.72$) using the hadron and electromagnetic calorimeters. The 1990-94 data is represented by the points shown as filled circles, whilst the empty circles represent the Monte Carlo data. Each sample has been subdivided into different regions of ϕ_{MB}: (a) $\phi_{MB} \leq 72°$, (b) $72° < \phi_{MB} \leq 108°$, (c) $108° < \phi_{MB} \leq 205°$, (d) $205° < \phi_{MB} \leq 238°$ and $302° < \phi_{MB} \leq 340°$, (e) $238° < \phi_{MB} \leq 302°$, and (f) $340° < \phi_{MB} \leq 360°$.

(b) the number of HCAL layers from the outermost 3 containing strip hits,

$$N_{lyr}^{HCo3} \geq 1$$

(c) the average number of strip hits per layer in the HCAL,

$$\frac{N_{hits}^{HC}}{N_{lyr}^{HC}} < 2$$

(d) the total ECAL cluster energy assigned to the cone,

$$E_{clus} < 2\,\mathrm{GeV}$$

In addition the muons used for this acceptance study were required to come from good charged cones containing a single charged track whose momentum must be at least $5\% E_{beam}$. The full Monte Carlo and real data (1990-94) sets were used (including off-peak data) for this study, where the Monte Carlo predicts the background from hadronic τ decays in this test sample to be $\sim$0.5 %.

The variables $|\cos\theta_{MB}|$ and ϕ_{MB} are calculated for each track by extrapolating its path to the intersection point with the barrel muon chambers. Figure D.1 shows the efficiency with which the test sample of muons passes the muon chamber identification (**MCHID**) as a function of $|\cos\theta|_{MB}$ for different sections in ϕ_{MB}. Like CALID, MCHID is used in the main $\tau\rightarrow\mu\overline{\nu}_{\mu}\nu_{\tau}$ selections used for the polarisation analysis and so full descriptions of the two cuts it uses can be found in sections 6.1 and 6.2. However, since this study is performed to test the acceptance of MB, the efficiencies considered here are based on the MCHID cuts applied to MB only (elsewhere the responses of MB and ME are combined).

Both real data and Monte Carlo data events are shown on the plots in figure D.1. However, it is the MCHID efficiency of the real data sample that is used to define the acceptance of MB. For each section in ϕ_{MB}, the value of $|\cos\theta|_{MB}$ above which the efficiency starts to drop is taken as the limit of the acceptance of MB, as shown. Therefore, any muon track is taken to be within the geometrical acceptance of MB if lies in one of the following ranges:

$$0^\circ < \phi_{MB} \leq 72^\circ \ : |\cos\theta_{MB}| < 0.67$$
$$72^\circ < \phi_{MB} \leq 108^\circ : |\cos\theta_{MB}| < 0.51$$
$$108^\circ < \phi_{MB} \leq 205^\circ : |\cos\theta_{MB}| < 0.68$$
$$205^\circ < \phi_{MB} \leq 238^\circ : |\cos\theta_{MB}| < 0.60$$
$$238^\circ < \phi_{MB} \leq 302^\circ : |\cos\theta_{MB}| < 0.45$$
$$302^\circ < \phi_{MB} \leq 340^\circ : |\cos\theta_{MB}| < 0.60$$
$$340^\circ < \phi_{MB} \leq 360^\circ : |\cos\theta_{MB}| < 0.68$$

Appendix E

Determining A_{ijk} and A'_{ijk} in the log-likelihood function

The binned likelihood function used for the extraction of $\langle P_\tau \rangle$and $A_{pol}^{FB}$is given by

$$
\begin{aligned}
\ln \mathcal{L} &= \sum_{|i|j} \left[\left(d_{+ij} \ln f_{+ij} - f_{+ij} + d_{-ij} \ln f_{-ij} - f_{-ij} \right) \right. \\
&+ \sum_{k=1}^{2} \left(a_{|i|jk} \ln A_{|i|jk} - A_{|i|jk} \right) \\
&+ \left. \left(a_{+ij3} \ln A_{+ij3} - A_{+ij3} + a_{-ij3} \ln A_{-ij3} - A_{-ij3} \right) \right] \qquad \text{(E.1)}
\end{aligned}
$$

where

$$
f_{\pm ij} = \sum_{k=1}^{2} (w_{\pm ijk} A_{|i|jk}) + w_{\pm ij3} A_{\pm ij3} \qquad \text{(E.2)}
$$

and where the indices $|i|$ and $\pm i$ have been used to distinguish between quantities binned in $|\cos\theta|$ and $\cos\theta$ respectively. All the other quantities have been defined previously in Sections 9.1 and 9.2. To reduce the number of unknowns in this equation it is necessary to solve for $A_{|i|jk}$ and $A_{\pm ij3}$ for each $|i|j$ bin using the methods outlined below.

For maximization of the log likelihood function it is first required that the derivative of $\ln \mathcal{L}$ with respect to A_{ijk} vanishes. Differentiating for each value of k

therefore gives,

$$\frac{d_{+ij}}{f_{+ij}}w_{+ijk} - w_{+ijk} + \frac{d_{-ij}}{f_{-ij}}w_{-ijk} - w_{-ijk} + \frac{a_{|i|jk}}{A_{|i|jk}} - 1 = 0 \qquad (\text{for } k \leq 2)$$

$$\frac{d_{\pm ij}}{f_{\pm ij}}w_{\pm ijk} - w_{\pm ijk} + \frac{a_{\pm ij3}}{A_{\pm ij3}} - 1 = 0 \qquad (\text{for } k = 3)$$

At this point, it is necessary to introduce the quantities $t_{\pm ij} = 1 - d_{\pm ij}/f_{\pm ij}$, which allow the last set of equations to be rearranged as follows:

$$\begin{aligned} t_{+ij}w_{+ijk} + t_{-ij}w_{-ijk} &= \frac{a_{|i|jk}}{A_{|i|jk}} - 1 \quad \Rightarrow \quad A_{|i|jk} = \frac{a_{|i|jk}}{1 + t_{+ij}w_{+ijk} + t_{-ij}w_{-ijk}} \qquad (k=1,2) \\ t_{\pm ij}w_{\pm ij3} &= \frac{a_{\pm ij3}}{A_{\pm ij3}} - 1 \quad \Rightarrow \quad A_{\pm ij3} = \frac{a_{\pm ij3}}{1 + t_{\pm ij}w_{\pm ij3}} \end{aligned} \qquad \text{(E.3)}$$

Therefore, if it is possible to solve for t_{+ij} and t_{-ij}, the values of $A_{|i|jk}$ and $A_{\pm ij3}$ can be determined from these expressions. To do this, Equations E.3 are first used to substitute for $A_{|i|jk}$ and $A_{\pm ij3}$ in the definition of $f_{\pm ij}$ (equations E.2):

$$f_{\pm ij} = \frac{d_{\pm ij}}{1 - t_{\pm ij}} = \sum_{k=1}^{2} \left(\frac{w_{\pm ijk}a_{|i|jk}}{1 + t_{+ij}w_{+ijk} + t_{-ij}w_{-ijk}} \right) + \frac{w_{\pm ij3}a_{\pm ij3}}{1 + t_{\pm ij}w_{\pm ij3}} \qquad \text{(E.4)}$$

There exists now a system of equations with two variables $t_{\pm ij}$, which must be solved for every $|i|j$ bin for each iteration of the fit. The equations are non-linear and so must be solved analytically. First we define,

$$g_{\pm ij} = \frac{d_{\pm ij}}{1 - t_{\pm ij}} - \sum_{k=1}^{2} \left(\frac{w_{\pm ijk}a_{|i|jk}}{1 + t_{+ij}w_{+ijk} + t_{-ij}w_{-ijk}} \right) - \frac{w_{\pm ij3}a_{\pm ij3}}{1 + t_{\pm ij}w_{\pm ij3}} \qquad \text{(E.5)}$$

The Newton Method is now used, which proceeds as follows. Arbitrary starting values of t_{+ij} and t_{-ij} are chosen (usually 0) and then we look for $\delta_{\pm ij}$ such that both $g_{+ij}(t_{+ij} + \delta_{+ij}, t_{-ij} + \delta_{-ij}) = 0$ and $g_{-ij}(t_{+ij} + \delta_{+ij}, t_{-ij} + \delta_{-ij}) = 0$. For this, Taylor expansions are used:

$$\begin{aligned} 0 &= g_{\pm ij}(t_{+ij} + \delta_{+ij}, t_{-ij} + \delta_{-ij}) \\ &= g_{\pm ij}(t_{+ij}, t_{-ij}) + \delta_{+ij}\frac{\partial g_{\pm ij}}{\partial t_{+ij}} + \delta_{-ij}\frac{\partial g_{\pm ij}}{\partial t_{-ij}} + \ldots \end{aligned} \qquad \text{(E.6)}$$

If higher terms are neglected, the following two approximations for δ_{+ij} and δ_{-ij} are thus obtained:

$$\delta_{\pm ij} = \frac{-g_{\pm ij}\frac{\partial g_{\mp ij}}{\partial t_{\mp ij}} + g_{\mp ij}\frac{\partial g_{\pm ij}}{\partial t_{\mp ij}}}{\frac{\partial g_{+ij}}{\partial t_{+ij}}\frac{\partial g_{-ij}}{\partial t_{-ij}} - \frac{\partial g_{+ij}}{\partial t_{-ij}}\frac{\partial g_{-ij}}{\partial t_{+ij}}} \tag{E.7}$$

Values for $\delta_{\pm ij}$ are calculated using these equations and added to the corresponding starting values of $t_{\pm ij}$. The resulting values of $g_{\pm ij}$ (evaluated using the new values of $t_{\pm ij}$) are not exactly zero, since Equations E.7 do not account for higher order terms from the Taylor expansions in Equation E.6. Therefore, the process is done repeatedly, with new values of $\delta_{\pm ij}$ determined and added to $t_{\pm ij}$, until the resulting values of $g_{\pm ij}$ are very close to 0 ($|g_{\pm ij}| < 10^{-12}$). The final values of $t_{\pm ij}$ are then used in Equations E.3 to evaluate the values of $A_{|i|jk}(k \leq 2)$ and $A_{\pm ij3}$.

Bibliography

[1] S.L. Glashow, Nucl. Phys. **22** (1961) 579;
A. Salam, in "Elementary Particle Theory", edit. N. Svartholm (Almqvist and Wikell, Stockholm, 1968) 361;
S. Weinberg, Phys. Rev. Lett. **19** (1967) 1264.

[2] F. Halzen and A.D. Martin, "Quarks and Leptons: An Introductory Course in Modern Particle Physics", (John Wiley and Sons, New York, 1984).

[3] I.J.R. Aitchison and A.J.G. Hey, "Gauge Theories in Particle Physics", (Adam Hilger, Bristol, 1982).

[4] D. Miller, "Events spring surprises as Moon stretches LEP", Physics World Vol. 6 No. 1 (Jan 1993).

[5] Particle Data Group, L. Montanet *et al.*, Phys. Rev. **D54** (July 1996) 1.

[6] P.W. Higgs, Phys. Rev. Lett. **12** (1964) 132; Phys. Rev. Lett. **13** (1964) 508; Phys. Rev. **145** (1966) 1156.

[7] G.'t Hooft, Nucl. Phys. **B33** (1971) 173; Nucl. Phys. **B35** (1971) 167; Utrecht Preprint THU-92/25 (1992).

[8] T. Appelquist and J. Carazzone, Phys. Rev. **D11** (1975) 2856.

[9] R. Barlow and C. Beeston, Comm. Phys. Comm., **77** (1993) 219.

[10] The LEP Electroweak Working Group and the SLD Heavy Flavour Group, LEPEWWG/96-02.

[11] Tau Polarisation Subgroup of the LEP Electroweak Working Group, LEPTAU/94-01; LEPTAU/94-02.

[12] CDF Coll., "Measurement of the Top Quark Mass at CDF", contr. to ICHEP 96, **PA-08-018**;
DØ Coll., "Measurement of the top mass from events with two isolated leptons·", contr. to ICHEP 96, **PA-05-027**;
DØ Coll., "Measurement of the top mass from events with single isolated leptons·", contr. to ICHEP 96, **PA-05-028**;
P. Grannis, talk pres. at ICHEP96, to appear in proceedings.

[13] M. Consoli and W. Hollik, in "Z physics at LEP", edit. G. Altarelli, R. Kleiss and C. Verzegnassi, Vol. 1 (1989) 7.

[14] G. Burgers and F. Jegerlehner, in "Z physics at LEP", edit. G. Altarelli, R. Kleiss and C. Verzegnassi, Vol. 1 (1989) 55.

[15] M. Böhm and W. Hollik, in "Z physics at LEP", edit. G. Altarelli, R. Kleiss and C. Verzegnassi, Vol. 1 (1989) 203.

[16] S. Jadach and Z. Wąs, in "Z physics at LEP", edit. G. Altarelli, R. Kleiss and C. Verzegnassi, Vol. 1 (1989) 235.

[17] D. Bardin *et al.*,"Zfitter: An analytical Program for Fermion Pair Production in e^+e^- Annihilation", CERN-TH-6443/92

[18] M.Goosens *et al.*, CERN Program Library Long Writeup D506, Vers. 92.1 (March 1992).

[19] S. Jadach, L.H. Kühn and Z. Wąs, Comm. Phys. Comm., **64** (1991) 275;
(Vers. 3.8) Comm. Phys. Comm., **66** (1991) 276;
(Vers. 4.0) Comm. Phys. Comm., **79** (1994) 503.

[20] J.M. Hilgart, R. Kleiss and F. le Diberder, Comm. Phys. Comm., **75** (1993) 191;

[21] S. Jadach, L.H. Kühn and Z. Wąs, Comm. Phys. Comm., **64** (1991) 275; R. Decker, S. Jadach, L.H. Kühn and Z. Wąs, Comm. Phys. Comm., **76** (1993) 361.

[22] M. Böhm, A. Denner and W. Hollik, Nucl. Phys. **B304** (1988) 687; F.A. Berends, R. Kleiss, and W. Hollik, Nucl. Phys. **B304** (1988) 712.

[23] M. Bengtsson and T. Sjöstrand, Nucl. Phys. **B289** (1987) 810.

[24] R. Battacharya, J. Smith and G. Grammar, Phys. Rev. **D15** (1977) 3267; J. Smith, J.A.M. Vermaseren and G. Grammar, Phys. Rev. **D15** (1977) 3280.

[25] R. Akers *et al.*, OPAL Coll., Z. Phys. **C65** (1995) 1.

[26] R. Akers *et al.*, OPAL Coll., Z. Phys. **C66** (1995) 543.

[27] G. Bella *et al.*, OPAL Coll., OPAL Physics Note PN-172 (March 1995); Preprint CERN-PPE/96-078 (June 1996), to be submitted to Z. Phys.

[28] D. Buskulic *et al.*, ALEPH Coll., Z. Phys. **C69** (1996) 183.

[29] P. Abreu *et al.*, DELPHI Coll., Z. Phys. **C67** (1995) 183.

[30] M. Acciari *et al.*, L3 Coll., Phys. Rev. Lett. **B341** (1994) 245; "A Preliminary Update of $\mathcal{A}_\tau$ and $\mathcal{A}_e$ Using 1994 Data", contr. to EPS-HEP Brussels, **eps0094**.

[31] K. Abe, SLD Coll., Phys. Rev. Lett. **73** (1994) 25; M. Woods, "The SLD A_{LR} Result and Review of Weak Mixing Angle Results at LEP and SLC", talk at EPS-HEP-95 Conf., to appear in proceedings.

[32] S. Myers, "The LEP collider, from design to approval and commissioning", CERN 91-08.

[33] K. Ahmet *et al.*, OPAL Coll., Nucl. Instr. and Meth. **A305** (1991) 275.

[34] D. Decamp *et al.*, ALEPH Coll., Nucl. Instr. and Meth. **A294** (1990) 121.

[35] D. Aarnio *et al.*, DELPHI Coll., Nucl. Instr. and Meth. **A303** (1991) 233.

[36] B. Adeva *et al.*, L3 Coll., Nucl. Instr. and Meth. **A289** (1990) 35.

[37] P.P. Allport *et al.*, OPAL Coll., Nucl. Instr. and Meth. **A313** (1992) 103.

[38] B.E. Anderson *et al.*, "The OPAL Silicon-tungsten Calorimeter Front-end Electronics", CERN/ECP 93-20.

[39] R. Akers *et al.*., OPAL Coll., OPAL Physics Note PN-142 (July 1994).

[40] M. Arignon *et al.*, Nucl. Instr. and Meth. **A333** (1993) 330.

[41] M.Z. Akrawy *et al.*, OPAL Coll., "The Trigger System of the OPAL Experiment at LEP", CERN-PPE/91-32.

[42] J. Allison *et al.*, OPAL Coll., Nucl. Instr. and Meth. **A317** (1992) 47;
D. Ward, "A GOPAL Primer", OPAL Internal Note (January 1995).

[43] C. Hawkes *et al.*, "ROPE4.09 Users Guide", OPAL Offline Note 16/OFFL-0487 (August 1995).

[44] D. Ward and J. Banks, "A Grope Primer", OPAL Internal Note (March 1995).

[45] R. Brün *et al.*, "GEANT3", CERN DD/EE/84-1 (1987).

[46] S.L. LLoyd, "The OPAL Primer", OPAL Internal Note, Vers. 3.2 (June 1995).

[47] T. Smith, "The LL Processor in Rope", OPAL Internal Note, Vers. LL202 (June 1995); "The Lepton Pair Analysis Code: LA", OPAL Internal Note, Vers. LA202 (June 1995).

[48] M. Sasaki, "The Tau Platform (TP) Version 1.02", OPAL Internal Note, (1992).

[49] J.F. Kral, R. Van Kooten and P. Wells, "ID114 Users' Guide", OPAL Internal Note, Vers. ID114/06 (June 1996).

[50] D.A. Rigby *et al.*,"Updated Measurement of the $\tau\rightarrow\ \mu\overline{\nu}_{\mu}\nu_{\tau}$ Branching Ratio", to be published.